TIME-RESOLVED SPECTROSCOPY BETWEEN NANOSECONDS AND HOURS: POLYMER PHOTOCROSSLINKING, 1,6-DIPHENYL-1,3,5-HEXATRIENE EMISSION AND GUANOSINE HYDROGEN TRANSFER

INAUGURAL-DISSERTATION

zur Erlangung des Doktorgrades
der Mathematisch-Naturwissenschaftlichen Fakultät
der Heinrich-Heine-Universität Düsseldorf

vorgelegt von

KATHARINA HUNGER
aus Clausthal-Zellerfeld

Düsseldorf, 2013

aus dem Institut für Physikalische Chemie I
der Heinrich-Heine Universität Düsseldorf

Gedruckt mit der Genehmigung der
Mathematisch-Naturwissenschaftlichen Fakultät der
Heinrich-Heine-Universität Düsseldorf

Referent: Prof. Dr. Karl Kleinermanns
1. Korreferent: Prof. Dr. Michael Schmitt
2. Korreferent: Prof. Dr. Jürgen Köhler

Tag der mündlichen Prüfung: 23.01.2013

Contents

1. Introduction

Polymers are omnipresent in our everyday life as well as in almost every industrial branch. Functional polymers like polymethyl methacrylate (PMMA) and polyimides (PI) are often used as membrane materials, for water cleaning, in food and life science, and especially for petrochemical purposes.[1–4] Since the introduction of EU directive 98/70/EG,[5] the benzene percentage in motor fuels is limited to 1 vol %, and thus development of effective and economic separation processes gained much interest. Recently, established processes for separation of chemicals, which are based on osmosis or nanofiltration are superseded by pervaporation techniques.[6–9] These are most suitable for separation of aromatic and aliphatic compounds.[10;11] The mechanism for separation by pervaporation is long known.[12] It is based on sorption, diffusion and desorption and therefore takes advantage of differences in solubility and diffusion rates of the different compounds, rather than their different sizes.[13–15] When the mixture of compounds which shall be separated ("feed") is led over the membrane, the compound with the higher sorption rate (in most cases the aromatic compound) passes through the membrane under phase change ("permeate"). Driving force for permeation is the difference of the chemical potential between feed and permeate. The required enthalpy of vaporization is supplied as heat, which constitutes a major percentage of the operating costs.[16] The final amount of permeate (flow) and the fraction of the desired species in the permeate (selectivity) are the factors by which a membrane is rated. Both parameters are desired to be high, to make a high quality membrane.[16;17]

The materials used for pervaporation membranes have to fulfill a number of additional requirements, like stability against chemicals, insolubility, mechanical durability, UV stability *etc.* These requirements are met by PMMA, which finds application in innumerable areas since its introduction in 1960.[18] The physical and chemical properties of PMMA can easily be controlled by temperature and duration of the polymerisation process, as well as by functionalisation of the acid groups.[19] The PMMAs used in this work where provided by BASF and functionalised by N. Schmeling.[20]

The same properties can be found in most polyimides, which are not only used as membrane materials in the chemical industries, but also in aviation, microelectronics and medicine.[21] Polyimides are based on the imide sequence -R-CO-NR'-CO-R-, and usually exhibit a polycyclic structure. They were first synthesized in 1908,[22] in the style of the well known nylon synthesis.[23] Nowadays, a two-step synthesis is used, with dianhydrides or tetracarbonacids as one and diamines as the other monomer.[24;25] The polyimides used in this work where synthesized by N. Schmeling.[17]

Both PIs and PMMAs are linear polymers at first, without intersections or crosslinks, which is a major disadvantage regarding the application as membrane material for pervaporation. The permeating compounds cause the polymer to swell by accumulating in the micropores of the membrane.[26] This eventually leads to dissolution of the polymer strands in the feed. Crosslinking the polymer strands can prevent this undesirable effect, but usually decreases the flow and may also influence the selectivity.

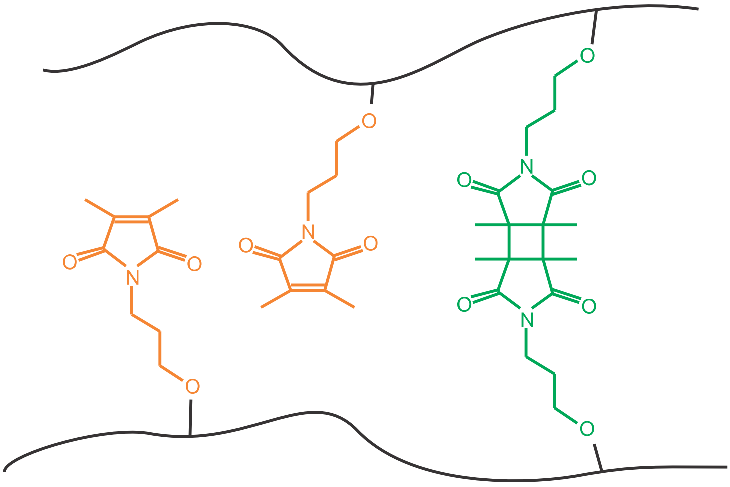

FIGURE 1.1: Schematic drawing of a polymer crosslinked with maleimide. Depicted in orange are the non-crosslinked dimethylmaleimide moieties, in green the maleimide-cyclobutane-dimer after photocrosslinking, which now connects the two polymer strands.

Crosslinking can easily be done in polymers containing functional groups like carboxylic acids. While PMMA contains carboxylic acid groups as a matter of principle, polyimides have to be specially designed in this way. The polyimide used in this work is based on the monomers 4,4'-hexafluoroisopropylidene diphthalic anhydride (6FDA), 4,4'-diaminodiphenyl ether (ODA) and 3,5-diamino benzoic acid (DABA), with the latter of the three providing the carboxylic acid (6FDA-ODA/6FDA-DABA 4:1). By esterification with diols, diamines, aluminium acetyl acetonate, *etc.*, the polymer strands are crosslinked covalently or ionically.[27–29] To enable the crosslinking in this approach, catalysts are needed, which later can be elutriated by the feed and thus contaminate the permeate. Additionally, the membrane properties and performance are influenced by these secondary compounds. Another approach is the application of photocrosslinkers, like the maleimide derivate used in this work (see figure 1.1). This way, there are no catalysts required, also the crosslinking degree can be controlled easily. Here, the crosslinking of the polymer is a photoreaction and thus only proceeds as long as the polymer is irradiated. By varying the crosslinking degree or length and stiffness of the crosslinking moiety, flow and selectivity of the membrane can be altered and thus adjusted to the mixture of compounds desired to be separated.

Therefore, it is of major interest to find methods to trace the crosslinking reaction, resolve the reaction path kinetics and to determine the crosslinking yield. With knowledge of these parameters, the ideal membrane can be designed for each purpose. Spectroscopy is obviously suitable for this purpose, since it allows for investigation of the photocrosslinking reaction without destroying the membranes. Time dependent spectroscopy methods can be used to determine the reaction kinetics and to identify transient species or intermediates. Photoproducts can be identified with the help of Fourier Transform Infrared (FTIR) spectroscopy in combination with quantum mechanical calculations.

Photo-induced inter- and intramolecular processes are of interest in a variety of fields, not only in material sciences but also in biochemistry and medicine. Ultraviolet (UV) radiation is known to induce skin damages, with the type of damage depending on the wavelength. UVA radiation (320 - 400 nm) causes immediate pigment darkening which occurs within seconds and lasts for about 2 hours after exposure or, at doses above 8 J/cm^2, persistent pigment darkening which can last up to 24 hours. Both are consequences of redistribution and photooxidation of melanin.[30–32] However, the resulting tan does not

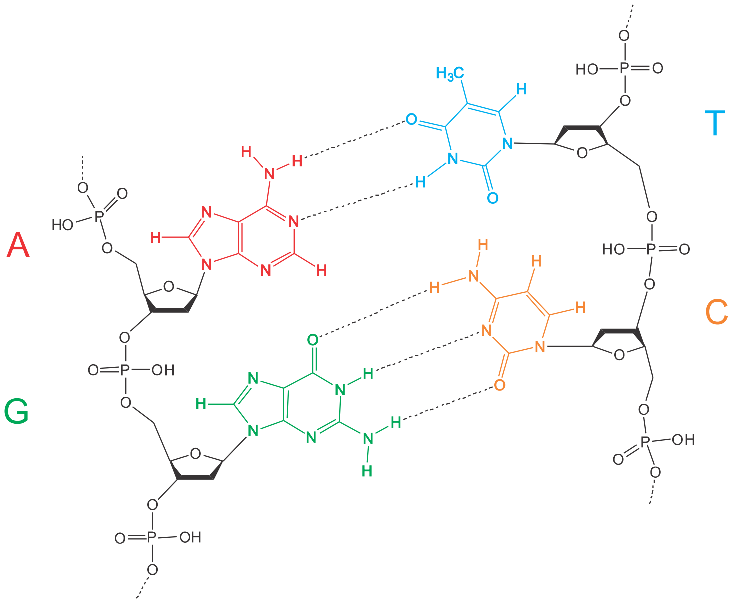

Figure 1.2: Schematic display of double stranded DNA with Watson-Crick base pairing. The two strands are connected via hydrogen bonds, formed between the Watson-Crick base pairs adenine (A) - thymine (T) and guanine (G) - cytosine (C), respectively.

lead to an enhanced protection against further UV induced damage, since no new melanin is produced.[33]
The effects of UVB radiation (290 - 320 nm) on the skin are of more severity. UVB rays are considered to be the main cause of sunburn.[33–35] It is also known to be responsible for formation of erythema, edema, thickening of epidermis and dermis, extracellular matrix degradation and dysregulation of the collagen metabolism, which may lead to wrinkles and loss of skin turgor and thus are also denominated as photoaging of the skin.[33;34;36] On the other hand, UVB radiation is needed for vitamin D synthesis.[34] Also, contrary to UVA radiation, UVB radiation induces increased tyrosinase activity and thereby formation of new melanin which results in delayed tanning (peaks at 72 hours after UV irradiation) and thus enhanced UV protection of the skin.[37] The most severe consequences of high UVB exposure are immunosuppression and photocarcinogenesis.[33;38]After absorption of the UV radiation by the desoxyribonuleic acid (DNA), photoproducts are formed which block DNA replication and transcription.[39]
DNA consists of two anti-parallel polymer strands of alternating sugar and phosphate groups. Attached to each sugar is one of the nucleobases cytosine (C), guanine (G), adenine (A) and thymine (T). According to the canonical Watson-Crick (WC) model, G and C as well as A and T form a base pair via three or two hydrogen bonds, respectively (see figure 1.2 for the structures).[40] Other hydrogen bond patterns may also occur, like the Hoogsteen or reverse Hoogsteen basepairs,[41] or the G-quadruplex motif found in the telomere region.[42;43]
The most frequent form of DNA UV-damage involves the dimerization of the pyrimidines T and C. This leads to the formation of cyclobutane pyrimidine dimers (CPD) and pyrimidine (6–4) pyrimidone photoproducts as the major DNA damage products.[44]CPDs can be formed between all pyrimidine pairs, however the formation trends are T-T > T-C > C-C, with the quantum yield of $\text{T-T}_{(\text{CPD})}$ being about three times higher than that of $\text{T-C}_{(\text{CPD})}$ and 10 times higher than that of $\text{C-C}_{(\text{CPD})}$.[45] The CPD is formed by a [2+2] cycloaddition via a singlet channel and appears within ∼1 ps after excitation.[46;47] The (6–4) photoproduct usually is found in significantly less amounts than the CPD, which may be due to the higher repair rate of the (6–4) photoproduct.[48–50] However, the ability

of those photoproducts to block DNA replication and transcription is much greater than that of the cyclobutane dimer.[51;52] Thus, the contribution of either of the dimerization products on cell mutagenesis is yet to be ascertained.
Besides pyrimidine dimerization, further processes like C to T mutation or proton transfer reactions occur upon UV irradiation.[53] The (6–4) photoproduct is known to undergo a light induced secondary photoreaction to form the so-called Dewar photoproduct.[54;55] UV light can also excite small molecules contained in the skin cells, such as riboflavin, tryptophane and porphyrin which can then activate cellular oxygen. The reactive oxygen species (ROS) obtained this way can cause oxidative base damage, e.g. formation of 8-oxoguanine.[44;56]
Quantum yields for these reactions are usually found to be less than 1 %, since highly efficient nonradiative decay pathways (via conical intersections)[57;58] enable the excited state nucleobases to relax back to the electronic ground state.[47;59]
The genetic code is contained in the sequence of the four nucleobases along the backbone and the arrangements of the hydrogen bonds between the nucleobases.[60] A change of these H-bonds, e.g. by the movement of a proton within a base or between two bases, will lead to changes of the genetic code and errors may occur during cell duplication. Accumulation of these code changes may be responsible for the occurrence of spontaneous mutations and subsequently for occurrence of tumors. Additionally, loss of useful genetic information induces aging.[60]
Formation of DNA photodimerization and photooxidization products is a field of high interest and a large variety of studies dealing with the details of those processes exists.[44;56;59;61–63] However, knowledge about proton transfer reactions is still limited. Although it has already been proposed in the 60s of the last century that light-induced proton transfer between DNA strands could induce mutations,[60] experimental evidence for H-transfer in DNA is still lacking.[59;61] Several studies provide evidence for the existence of charge-transfer states,[59;64;65] and calculations performed by several groups suggest that ultrafast decay to the electronic ground state is mediated by electron transfer from G to C followed by proton transfer in the same direction.[66;67] As Middleton *et al.* state in their recent extensive review article on DNA excited state dynamics "Time-resolved observation of the underlying proton motions is needed to confirm this explanation.".[59] The UV/Vis-absorption spectra of the neutral nucleobases and their corresponding ions and radicals differ considerably, therefore transient UV/Vis spectroscopy can be used to investigate proton transfer in solutions of the nucleobases. For the investigations presented in this work, guanosine was chosen as representative, since (i) it is difficult to probe H-transfer directly in DNA due to the complexity of the strands and (ii) G-G aggregates are known to be of biological relevance (e.g. in eukaryotic centromeres and telomeres).[68–72]

The aforementioned spectroscopic methods are not only suited for the investigation of photoreactions, but can also be applied to clarify photophysical processes. Of special interest are molecules which play a role in photosynthesis. Plants and bacteria which are capable of photosynthesis exhibit protein systems for this task, consisting of two different parts: antenna molecules (also called light-harvesting complexes, LHC), which efficiently absorb light of a broad wavelength range, and the photosynthetic reaction center, where the actual photochemistry takes place. The energy transfer from the antenna molecules to the reaction centre occurs via Förster resonance energy transfer (FRET)[73] and was in the focus of interest of many research groups.[74–78] In 1988 the Nobel prize in Chemistry

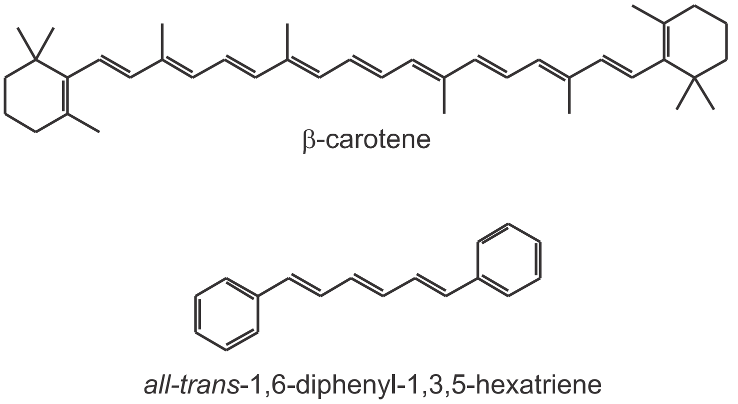

FIGURE 1.3: Chemical structures of the carotenoid β-carotene and the diphenylpolyene 1,6-diphenyl-1,3,5-hexatriene, which can serve as carotenoid model compound.

was awarded to Deisenhofer, Huber and Michel "for their determination of the three-dimensional structure of a photosynthetic reaction centre".[79]

Since then, investigations of numerous other photosynthetic reaction centres and light-harvesting complexes were performed with a variety of methods like X-Ray,[80] nonlinear spectroscopy,[81] NMR,[82] neutron and light scattering,[83] steady state[84] and transient spectroscopy[85;86] as well as quantum mechanical calculations.[76] It was shown, that light-harvesting complexes contain several chlorophyll (plants, algae and cyanobacteria) or bacteriochlorophyll (other phototrophic bacteria) moieties[87–89] as well as several carotenoids.[90–93] The latter not only serve as light collectors to enhance the energy available for photosynthesis, but also as photo-protectors.

Light is essential for virtually every life-form, but noxious when in excess (as described above). Besides the surplus energy which has to be effectively disposed, UV radiation bears another threat: the concentration of ROS is enhanced upon UV exposure of living tissue.[94;95] These oxygen centered free radicals (e.g. superoxide O_2^- or nitric oxide NO) are known to be involved in a multitude of cell disfunctions and mutations.[96;97] Most antioxidants act as radical scavengers and terminate radical chain reactions,[98] while carotenoids additionally are capable of quenching singlet oxygen, which also causes oxidative stress for proteins, lipids and DNA.[99]

Carotenoids are linear polyenes based on a tetraterpenoid structure often terminated by rings. Up to now, there are more than 700 different carotenoids identified, with β-carotene as the most renowned example.[98] Often used as model compounds are the *all-trans*-diphenylpolyenes ($[C_6H_5{-}(CH{=}CH)_n{-}C_6H_5]$) with n = 1 - 4: 1,2-diphenylethene (stilbene), 1,4-diphenyl-1,3-butadiene (DPB), 1,6-diphenyl-1,3,5-hexatriene (DPH) and 1,8-diphenyl-1,3,5,7-octatetraene (DPO). They differ from the carotenes as they do not feature any methyl groups and thus are no polyterpenes, but the photophysical properties are still very similar to those of their larger relatives.[100] As examples for these compounds, the structures of β-carotene and DPH are shown in figure 1.3.

Since first reported in 1935 by Hausser *et al.*[101–106] the photophysical behaviour of diphenylpolyenes was of constant interest and the exceptionally long fluorescence lifetime observed, the existence of a Stokes shift and the solvent dependence of emission and absorption raised many questions.[107] In 1972 Hudson and Kohler stated that the fluorescence can be ascribed to the S_1 state and the S_2 state,[108] which then led to many approaches to identify these two states. The evolution of theories explaining type and order of the excited singlet states of the diphenylpolyenes was recently subsumed by Catalán.[109;110]

In *trans*-stilbene (C_{2h}-symmetry), the lowest excited singlet state is the $1B_u$-state.[111] The state ordering of *all-trans*-DPB (C_{2h}) depends on its state of matter: in the gas phase, the

$2A_g$-state is lower in energy than the $1B_u$-state, while in the condensed phase molecule-solvent interactions preferentially stabilize the B_u state and lead to an inverted state order.[112] For *all-trans*-diphenylpolyenes with $n \geq 3$ (DPH and larger), the S_1 state is of A_g symmetry and the S_2 state of B_u symmetry.[113] Since the S_0 state also is an A_g state, direct transitions to the S_1-state are forbidden, but may occur due to intensity stealing from the S_2 state.

This order of states explains why an extraordinary emission lifetime can be observed. The kinetics of the processes involved, like internal conversion between S_1 state and S_2 state, as well as the emission rates from both of the states are yet to be determined. In this work, time dependent, laser-induced emission spectroscopy has been applied to investigate these photophysical processes, since it is obviously well suited for this task.

2. Theoretical Background

This chapter will only provide a brief introduction into the principles of photochemistry and photophysics of organic molecules with a focus on the processes studied in this work. The discussions in this chapter explicitly refer to the condensed phase, while they may not apply to molecules in the gas phase. For more detailed information the reader is recommended to consult the books by Calvert and Pitts,[114] Turro, Ramamurthy and Scaiano,[115] Demtröder,[116] Atkins and Friedman,[117] and Cramer.[118]

2.1. Photophysics

2.1.1. Electronic Excitation (UV/Vis)

Interactions between light and matter can be manifold. Irradiation of a molecule leads to absorption, if several requirements are met. Light in the ultraviolet or visual spectral range carries enough energy to allow electronic excitation of the absorbing molecule. The wavelength of the absorbed light is characteristic for each molecule and depends on the energy gap between the ground state and the excited states. The most important processes following electronic excitation can be depicted in a Jablonski diagram as shown in figure 2.1. In most organic molecules the ground state is a singlet state, the total spin of all electrons is zero. Upon excitation the electron does not change its spin, the excited state is also a singlet state. When an electronically excited state S_n other than the lowest electronic excited state (S_1) is populated, radiationless de-excitation (internal conversion, IC) takes place, with the redistributed energy being released as heat. The energy can also be emitted as nondirectional radiation (fluorescence, fl). The emission wavelengths are just as characteristic for each molecule as the absorption wavelengths, since they also depend on the S_n-S_0 energy gap. According to Kasha's rule,[119] in solutions fluorescence occurs from the S_1-state, since $S_n \rightarrow S_1$ IC usually is much faster than fluorescence. Therefore, the shape of the emission spectrum is independent on the excitation wavelength λ_{ex}. The emission intensity is influenced by λ_{ex}, since exciting a strong transition leads to a high population of the excited state which results in a high emission intensity.

Competing with $S_1 \rightarrow S_0$ IC and fluorescence is the intersystem crossing (ISC). Here, a spin conversion takes place and the triplet state T_n, which is nearest in energy to the S_1-state, is populated. ISC is rather slow in comparison with the aforementioned processes, since it is only weakly allowed due to spin-orbit coupling. If not the lowest triplet state (T_1) is excited, IC into the T_1-state takes place. From this T_1-state, de-excitation can occur via emission (phosphorescence, *ph*) or quenching by collision with solvent or ground-state molecules.

Two-photon absorptioncan be used to obtain the absorption spectrum of an excited state. If, for example, ISC occurs after UV-excitation, a second photon (UV/Vis) can be absorbed by the T_1-state molecule to populate a T_n-state. A method to obtain $T_1 \rightarrow T_n$ absorption spectra and triplet lifetimes is described in section 3.1.

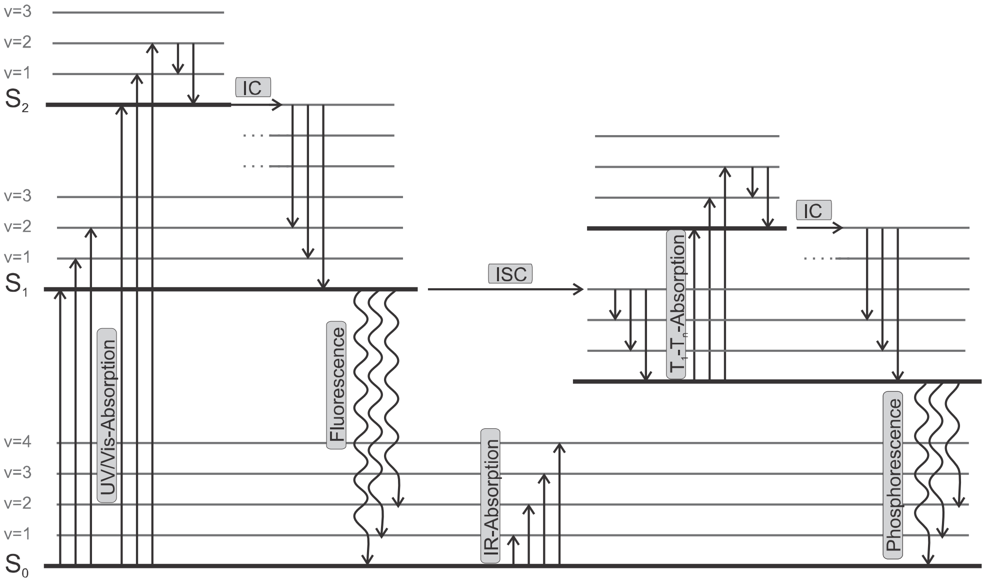

FIGURE 2.1.: Jablonski diagram with the fundamental interactions between electronic ground state and the lowest excited singlet and triplet states including their vibrational levels.

By UV/Vis-excitation either the vibronic ground state $S_{n(v=0)}$ of the electronically excited states or their higher vibrational levels $S_{n(v=m)}$ can be populated. After excitation of higher vibrational levels vibrational relaxation to the $S_{n(v=0)}$-state occurs. For n> 1, this process is followed by IC into a highly vibrationally excited state of an electronically excited state of lower energy. In figure 2.1 this is shown for $S_{2(v=0)} \rightarrow S_{1(v=6)}$. Since this happens very fast, further processes emanate from the zeroth vibrational level of the lowest electronically excited state $S_{1(v=0)}$. Exceptions are molecules where $S_1 \rightarrow S_0$ transitions are forbidden by symmetry (see chapter 6.1). Analogous, emission from $S_{1(v=0)}$ or $T_{1(v=0)}$ can occur to several vibrational levels of the ground state. The energy released by these transitions is always smaller than the energy required for excitation. Therefore, emission spectra typically are shifted red in respect to the absorption spectra (Stokes shift),[120] with an overlap in the spectral region corresponding to the $S_{1(v=0)} \leftrightarrow S_{0(v=0)}$ energy gap.

In solution, absorption and emission spectra feature no sharp peaks but rather broad bands. In most cases, the transitions to the different vibrational levels of one electronic state are close in energy and the corresponding absorption or emission bands overlap. Therefore one broad band with several maxima and/or shoulders results, as can be seen in the example spectra shown in figure 2.2. The spectral overlap between the two spectra is rather small for this molecule (375 nm - 400 nm), since the $S_{1(v=0)} \leftrightarrow S_{0(v=0)}$ transition is symmetry forbidden. The emission spectrum approximately mirrors the absorption spectrum. In this case the nuclear geometry is not altered strongly enough by electronic excitation to cause a distinct change in the spacing of the vibrational energy levels of emitting state and ground state.[121] As can be seen from equation 2.1 plotting a spectrum on the wavelength scale leads to a linear distortion in respect to the energy, while this is not the case on the wavenumber scale.

$$E = h\nu = \frac{hc}{\lambda} \tag{2.1}$$

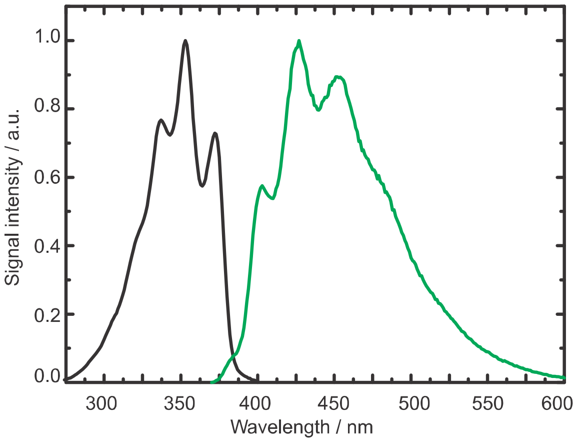

FIGURE 2.2: Normalised absorption and emission spectra of 1,6-diphenyl-1,3,5-hexatriene in cyclohexane on the wavelength scale.

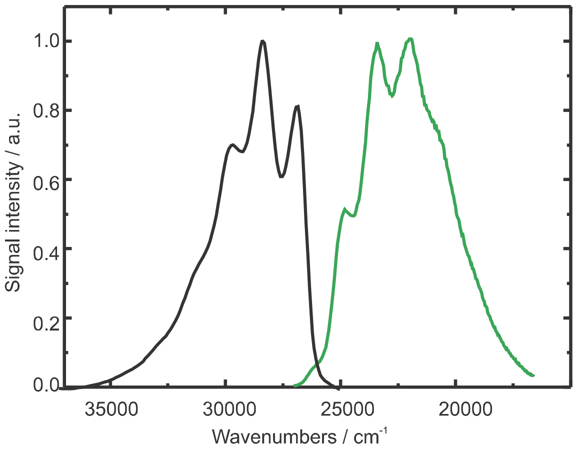

FIGURE 2.3: Normalised absorption and emission spectra of 1,6-diphenyl-1,3,5-hexatriene in cyclohexane on the wavenumber scale.

The spectra are detected with a constant wavelength resolution $\lambda + d\lambda$. The corresponding interval $\nu + d\nu$ decreases with decreasing energy. But since the intensity is proportional to the number of emitted photons, the overall integral of the intensity has to be the same on the wavenumber scale as it is on the wavelength scale. Thus, upon transformation to wavenumbers the intensity has to be corrected according to equation 2.2.

$$I_\nu(\nu) = I_\lambda(\lambda) \cdot \lambda^2 \tag{2.2}$$

The mirrored similarity between emission and absorption can be demonstrated more clearly by plotting on the wavenumber scale, as in figure 2.3. Nonetheless, UV/Vis absorption and emission is typically discussed in terms of the wavelength.

2.1.2. Vibrational Excitation (IR)

To excite higher vibrational levels of an electronic state, light of the infrared spectral range (IR) is required. The energy is transformed into movement of the nuclei, which oscillate around their equilibrium geometry r_0 with a characteristic frequency ν. In a first approximation, this can be described as an one-dimensional harmonic oscillation:

$$V(r) = \frac{1}{2}kr^2 \tag{2.3}$$

with the force constant k and the nuclei distance r. This description derives from Hooke's law ("Ut tensio, sic vis"), the classical correlation between force and displacement of a spring. The bonds between two atoms thus can be regarded as springs of different strengths. The harmonic oscillator features potential walls which continue up to infinity, with equidistant vibrational energy levels E_v, v being the vibrational quantum number.

$$E_v = (v + \frac{1}{2})h\nu \tag{2.4}$$

The model of the harmonic oscillator becomes inadequate when high vibrational quantum numbers or dissociation of the molecule are regarded, while the anharmonic oscillator model describes the vibrational behaviour of molecules more accurate. Here, the potential energy is expressed in terms of the Morse potential:

$$V(r) = hcD_e(1 - e^{-ar})^2 \text{ with } a = \sqrt{\frac{k}{2hcD_e}} \tag{2.5}$$

and D_e as the minimum depth of the potential curve. The vibrational levels E_v converge as the potential reaches the dissociation energy D_0:

$$E_v = (v + \frac{1}{2})h\nu - (v + \frac{1}{2})^2 h\nu x_e \tag{2.6}$$

with the anharmonicity constant x_e.
The frequency of a vibration is characteristic for the type of a chemical bond (single, double, triple) thus, light of different frequencies is needed to excite different types of bonds. To excite the stretching vibration of a C-C single bond, frequencies of ~1000 cm^{-1} are required, while a C=C double bond is excited with ~1640 cm^{-1} and a C≡C triple bond with ~2200 cm^{-1}.[122] Heteroatoms can increase or decrease the vibrational frequency, as a function of their mesomeric and/or inductive effect. Electron withdrawing atoms weaken the bond and thus minimize the vibrational frequency, while electron-releasing atoms have the opposite effect.
The frequency of a vibration is also influenced by the proximate environment of the corresponding nuclei. An aromatic system, amongst others, features stretching vibrations in the region of 1600 - 1500 cm^{-1}, which are well distinguishable from the C=C stretching vibrations of non-aromatic systems. Additionally, the ability of a molecule to form hydrogen bonds is of particular importance. The free O-H stretching vibration features a sharp band in the region of 3650 - 3590 cm^{-1}, while formation of a hydrogen bond leads to a broad and often very weak band which can reach down to 3200 cm^{-1}. It is: the stronger the hydrogen bond the weaker the O-H bond and the broader and lower in frequency the absorption band. Infrared spectroscopy can thus be employed to determine molecule (and aggregate) structures.
The intensity I of a transition from state i to state j is determined by the transition dipole moment μ:

$$I = P^2 = (\langle\psi_i|\,\mu\,|\psi_j\rangle)^2 \tag{2.7}$$

where ψ_i and ψ_j the wavefunctions of the two states and

$$\mu = -e\sum_i r_i + e\sum_j Z_j R_j = \mu_e + \mu_N \tag{2.8}$$

The probability P of a transition is high, when the wavefunctions of the two corresponding states overlap sufficiently. According to the Born-Oppenheimer principle the movement

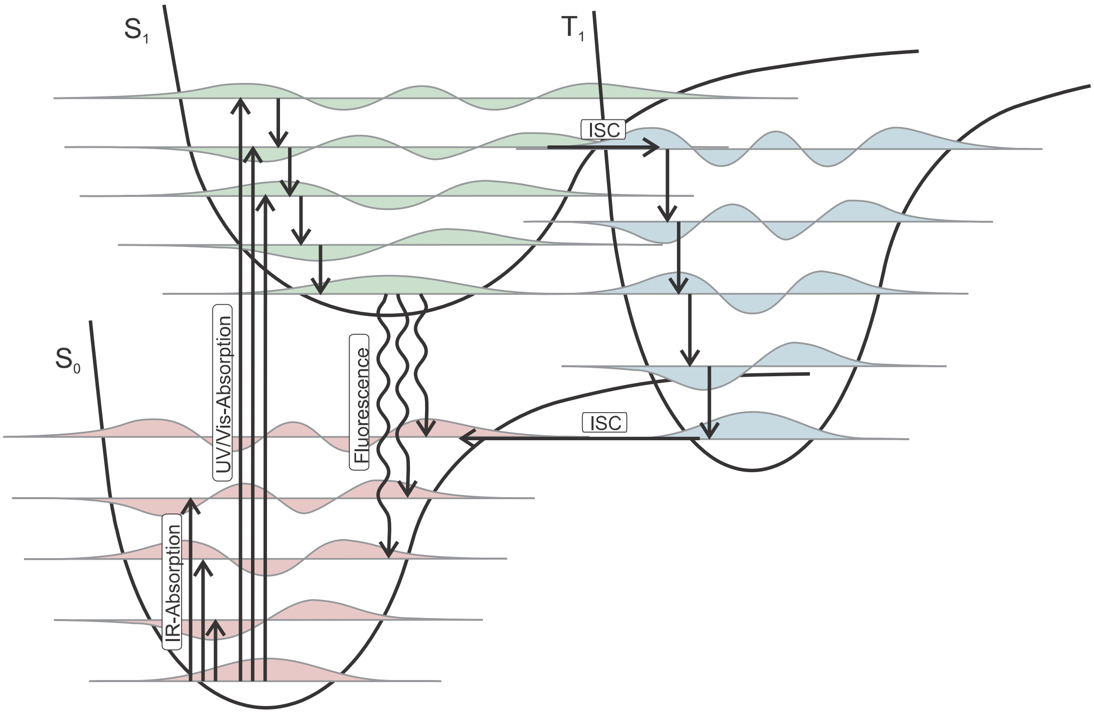

Figure 2.4.: Jablonski diagram with the fundamental interactions between electronic ground state and the lowest excited singlet and triplet states in consideration of the electronic wavefunctions.

of the nuclei, which is much slower than that of the electrons, can be neglected (due to the mass differences) and only the electronic wavefunctions have to be regarded.[123–125] After separation of the electronic and vibrational wavefunctions (see also chapter 3.6) the transition dipole moment for the transition between the ground state $|\epsilon\nu\rangle$ and the upper vibronic state $|\epsilon'\nu'\rangle$ becomes

$$\langle\epsilon'\nu'\,|\mu|\,\epsilon\nu\rangle = \mu_{\epsilon'\epsilon}\int\psi^*_{\nu'}(R)\psi_\nu(R)d\tau_N = \mu_{\epsilon'\epsilon}S(\nu',\nu) \tag{2.9}$$

with $S(\nu',\nu)$ as the overlap integral and $\mu_{\epsilon'\epsilon}$ as the pure electronic transition moment. That means, an electronic transition occurs in a stationary nuclear geometry and only after the electrons have reached their final configuration, the nuclei relax into the new adjusted geometry. Usually, the overlap is high for vibrational levels which are close in energy. Therefore, equilibration from a vibrationally excited state to the vibronic ground state is very fast ($k_{eq} \approx 10^{12}$ s^{-1}).[114;121] Including the electronic wavefunctions and the anharmonic oscillator model, the Jablonski diagram can be depicted as in figure 2.4.

2.2. Photochemistry

Photoreactions are those reactions which are initiated by irradiation of the sample. According to the first law of photochemistry (principle of photochemical activation) only light which is absorbed by a system can bring about a photochemical change. The second law of photochemistry (photoequivalence law), stated by Einstein in 1905, claims that every photon absorbed will cause a primary chemical or physical process. But upon usage of modern high intensity light sources (e.g. pulsed laser), multiphoton processes can occur. Here, several photons are needed to initiate a process. The most important physical processes which follow excitation with IR or UV/Vis light were covered in the chapters above. This chapter will deal with the photochemical processes, which are defined as processes which yield a photoproduct that is chemically different from the original reactant. Often, these primary processes induced by UV/Vis absorption are followed by secondary processes which are "normal" interactions of reactants, and thus do not require any absorption of light.

Photochemistry is sometimes claimed to be "green chemistry" since often no further reactants are needed and the activation energy has not to be provided by heat. In many cases the desired reaction cannot be accomplished thermally and thus extended synthesis routes are required, which could be replaced by one photochemical step. Thus costs of syntheses can be reduced by using photochemical processes. Control of photochemical reactions is rather simple, since they only go on as long as irradiation is sustained. This also means, that samples which can perform photoreactions should be protected from unwanted irradiation, e.g. by keeping them in brown glass bottles or vessels covered in tin foil and/or kept in the dark.

Photochemistry is excited state chemistry and differs in selection rules from ground state chemistry. Thus it offers access to reactions which are otherwise forbidden. These may be $\pi \rightarrow \pi^*$ transitions of alkenes, cycloadditions (including Paternò-Büchi-reactions) or Norrish-reactions. In the S_1-state the double binding character of C=C double bonds is lower which makes rotation around a double bond more easy and thus facilitates *cis/trans* isomerization.[126]

Although every photon which is absorbed induces a physical or chemical process, not all of the photons induce the desired or investigated process. The more times the desired process x occurs per photon absorbed the higher is the processes quantum yield ϕ.

$$\phi = \frac{n_x}{n_p} = \frac{\#\ of\ photochemical\ events}{\#\ of\ absorbed\ photons} \tag{2.10}$$

The sum of the quantum yields of all competing photophysical processes and for formation of all possible photoproducts may exceed unity, e.g. if reactions of the type A $\xrightarrow{h\nu}$ 2B occur. The quantum yield is wavelength independent, as long as the system has only one chromophore. This results from Kasha's rule, which applies for photochemical processes as well.

If the photoproduct features an isolated absorption band, the quantum yield can be obtained spectroscopically. When the energy absorbed by the sample during one laser pulse E_{abs} is known, ϕ can be calculated via equation 2.11 with c_r as product concentration, V_r as sample volume, N_A as Avogadro constant, h as Planck constant, c as light velocity, Z as number of laser pulses and λ as excitation wavelength.

$$\phi = \frac{c_r V_r N_A h c}{E_{abs} Z \lambda} \tag{2.11}$$

Otherwise, the product concentration has to be determined with other methods, e.g. analytically via gas chromatography (GCMS) or high-performance liquid chromatography (HPLC).

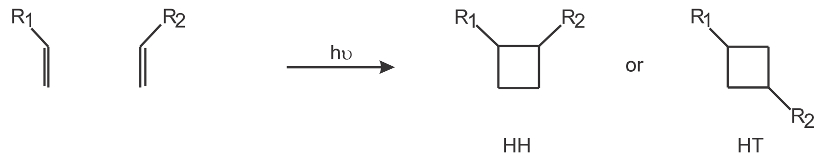

(A) Schematic drawing of a [2+2] cycloaddition. The regioselectivity, i.e. whether the head-to-head (HH) or the head-to-tail (HT) product is formed, depends on the substituents.

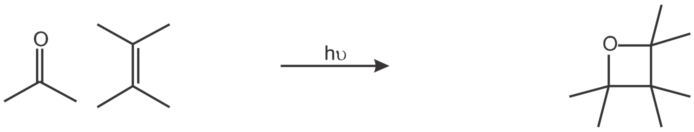

(B) The Paternò-Büchi reaction is a [2+2] cycloaddition of one carbonyl and one alkane group, which results in the formation of an oxetane.

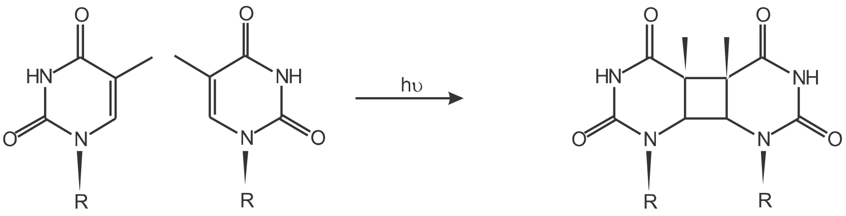

(C) The [2+2] cycloaddition of the alkene groups of two thymine moieties yields the CPD photoproduct.

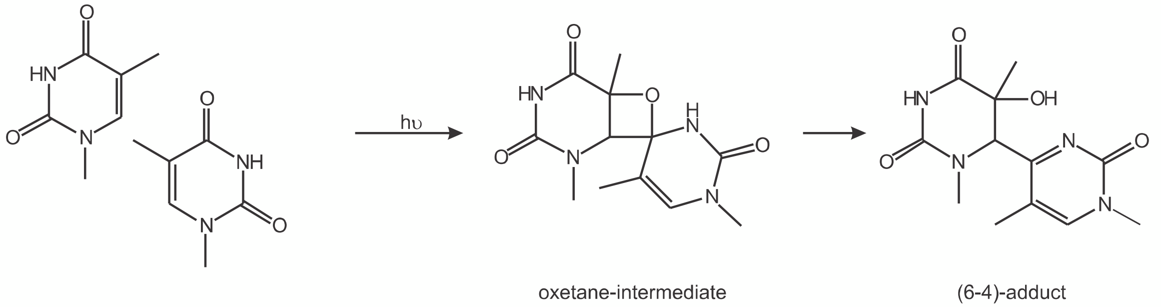

(D) The pyrimidine (6–4) pyrimidone photoproduct of thymine is formed via a Paternò-Büchi reaction. The isomerisation of the oxetane intermediate is a secondary reaction and requires no further irradiation.

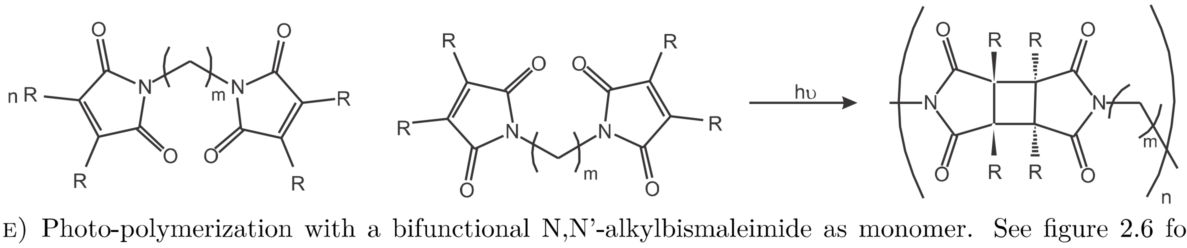

(E) Photo-polymerization with a bifunctional N,N'-alkylbismaleimide as monomer. See figure 2.6 for possible isomers.

FIGURE 2.5.: Examples for [2+2] cycloaddition reactions.

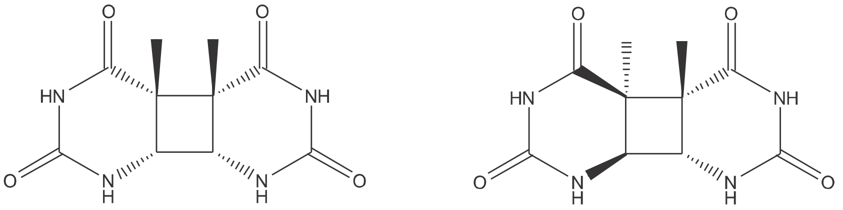

(A) *cis-syn* (B) *trans-syn*

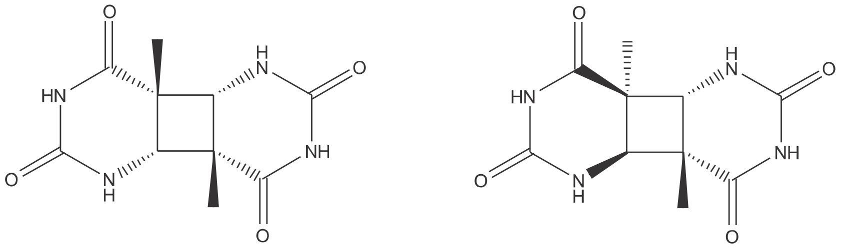

(C) *cis-anti* (D) *trans-anti*

Figure 2.6.: Possible diastereoisomers after [2+2] cycloaddition of thymine. The hydrogen atoms of the cyclobutane ring (not shown here) are oriented analogously as the respective methyl group originating from the same thymine moiety.

2.2.1. [2+2] Cycloadditions

According to the Woodward-Hoffmann rules (which brought the Nobel prize to Hoffmann in 1981)[127] pericyclic reactions are either thermally or photochemically allowed, but never both thermally and photochemically. To be more precise, cycloaddition reactions which feature 4n+2 π-electrons are allowed thermally, whereas those with 4n π-electrons are allowed photochemically. A well-arranged summary of the Woodward and Hoffmann selection rules and the suprafacial and antarafacial orbital interactions that are permitted or disallowed for cycloadditon reactions can be found in the review by Goodall and Hayes.[128] Concerted [2+2] cycloadditions (see figure 2.5a) are allowed after HOMO → LUMO excitation. The mechanism of the UV-light induced [2+2] cycloaddition reaction is described in detail in section 4.1 upon the dimerization of 3-hydroxypropyldimethylmaleimide. It was found, that after excitation of one maleimide moiety, ISC to the triplet state takes place, followed by electron transfer to ground state maleimide. The cation and anion radicals thus formed then combine to the cyclobutane dimer.[20]

Unsymmetrically substituted alkenes often yield a mixture of head-to-head (HH) and head-to-tail (HT) products. The ratio differs, depending on the substituents. While electron-donors favour the HT-isomer, electron-acceptors preferentially form the HH-isomer. If both types of substituents are present, the regiochemical control is usually dominated by the donor substituent and the HT-isomer will be the main product. Facial diastereoselectivity can be controlled by a stereogenic center vicinal to the double bond of the alkene and by sterically demanding substituents. Otherwise, a mixture of isomers will be obtained.[129]

As described in the introduction, the thymine cyclobutane-pyrimidine dimer (CPD) is the main photoproduct after UV irradiation of DNA (figure 2.5c). Of the possible configural isomers of the cyclobutane ring (see figure 2.6), the *cis-syn*-isomer is formed almost exclusively, due to the sterical control of the DNA double helix. When not restricted by the

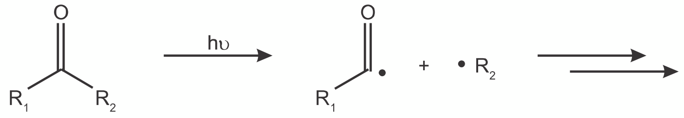

(A) Norrish type I.

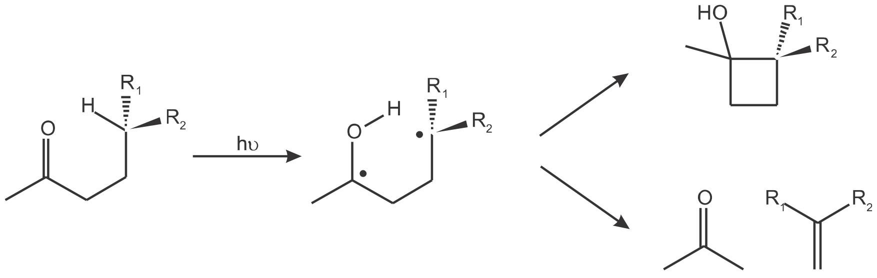

(B) Norrish type II.

FIGURE 2.7.: Norrish reactions can occur after irradiation of molecules containing carbonyl groups. (A) α-carbon bond cleavage results in formation of two radical fragments. (B) γ-hydrogen abstraction results in 1,4-biradical alcohol formation.

DNA double helix, e.g. in single-stranded DNA, denatured DNA or nucleobase monomers in solution, the ratio of the CPD diastereoisomers may differ.[130;131]
The pyrimidine (6–4) pyrimidone photoproduct is also formed by a [2+2] cycloaddition (see figure 2.5D). Here, the carbonyl group of one moiety undergoes a reaction with the alkene group of the other moiety and an oxetane is formed as intermediate product. This special case of cycloadditions (carbonyl + alkene ⟶ oxetane, figure 2.5B) is named "Paternò-Büchi reaction".[132;133] It is assumed, that the oxetane is formed via an intermediate 1,4-biradical, for which the carbonyl triplet state is a precursor. Thus, if the triplet state energy of the alkene compound is lower than that of the carbonyl compound, energy transfer is favoured and the oxetane formation is inhibited. The regioselectivity is controlled by the conformational preference in the most stable biradical.[129]
Since by [2+2] cycloaddition of two substituted alkanes up to four stereogenic centers can be formed in one single step, this reaction is very attractive for application in synthesis, especially in natural product syntheses. Here, this reaction often presents the answer for the challenge of stereoselective C–C bond formation in highly hindered environments.[134]
Recently, [2+2] cycloadditions also are increasingly utilized in polymer synthesis, since they provide access to linear, hyperbranched or cross-linked polymer architectures and can be used to create heterocyclic or strained multicyclic polymer backbones with high efficiency. An example for photopolymerization is shown in figure 2.5E, with a bifunctional maleimide as monomer which forms a multicyclic polymer backbone.[128]
Although formation of side products is a lesser threat upon performing photochemical reactions than upon thermal reactions, there is one reaction mechanism which should not stay unmentioned when describing [2+2] cycloadditions. Upon irradiation of a carbonyl group containing molecule, Norrish-reactions can take place, which especially is a problem when Paternò-Büchi reactions are performed. In the Norrish type I reaction cleavage of the α-carbon carbon bond takes place which results in formation of two radical fragments (figure 2.7A). These often highly reactive radicals can undergo a large variety of secondary reactions, so that in the end a mixture of several different products are obtained after

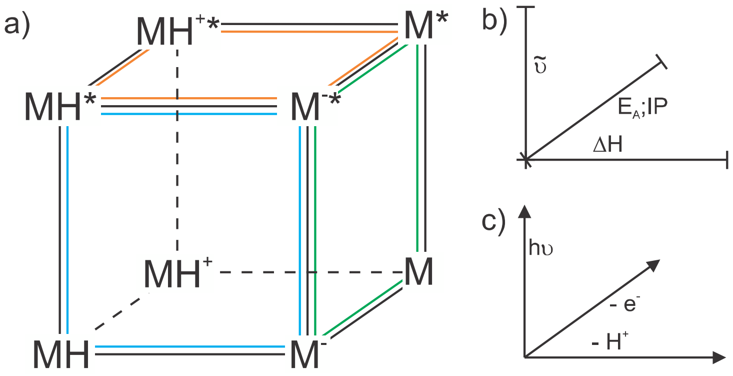

FIGURE 2.8: a) The Förster cycle. Vertices represent the chemical entities, edges represent the processes and the faces correspond to the thermodynamic cycles on which the Förster cycle is based. b) ΔH_0: standard enthalpy change in the acid-base reaction; E_A: electron affinity; IP: ionisation potential, $\tilde{\nu}$: excitation energy. c) Processes involved.

irradiation of the sample. Norrish type II reactions imply abstraction of a γ-hydrogen, by which a 1,4-biradical alcohol is formed (figure 2.7B). Recombination of the biradical leads to a four membered ring, where - in contrast to the Paternò-Büchi reaction - the oxygen atom is no part of the ring system, but is present as a tertiary alcohol. Additionally the biradical can fragment to an enol and an alkene.

Reactions like these can also cause photodegradation in polymers. This is not only a problem for the long-time stability of polymers in application, but also for spectroscopic studies of polymer or polymerisation properties, as described in section 4.2.

2.2.2. Excited state H-Transfer reactions

The electron density distribution is altered by electronic excitation and as a consequence the pK-values of the excited state and ground state molecule can differ considerably. The rate of H-transfer from the excited state can vary from the ground state value by more than 10 orders of magnitude. Generally, the $pK_a{}^*$ value of the energetically lowest triplet state lies between those of the ground state and the lowest excited singlet state.[135;136]

The excited state $pK_a{}^*$ can be determined via the Förster cycle, which links ground state thermodynamics with electronic transition energies (see figure 2.8). The Förster cycle is based on the following three thermodynamic cycles: (i) the protolytic Förster cycle, which combines excitation and proton transfer (figure 2.8, face pictured in blue, or opposing face), (ii) the Michaelis cycle, which combines proton transfer and electron transfer (face pictured in orange, or opposing face) and (iii) the electron transfer Förster cycle, which combines excitation and electron transfer (face pictured in green, or opposing face).[137]

With three values of one cycle being known, the last value can be easily calculated. For the protolytic Förster cycle, this can be done via equation 2.12, with the changes of enthalpy for the acid-base reaction in the excited state and in the ground state ΔH^* and ΔH, the Avogadro number N_A, the Planck constant h and the 0-0 ground-state-to-excited-state energy differences of the protonated and deprotonated molecule ν_{MH} and ν_{M^-}.[136;138]

$$\Delta H^* - \Delta H = N_A h(\nu_{MH} - \nu_{M^-}) \tag{2.12}$$

With several approximations[136] the $pK_a{}^*$ value can be estimated via equation 2.13, with the ideal gas constant R and the temperature T.

$$pK_a^* - pK_a = N_A h(\nu_{MH} - \nu_{M^-})/2.3RT \tag{2.13}$$

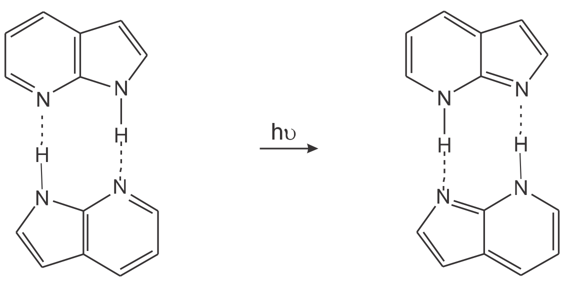

Figure 2.9: Photoinduced double proton transfer in the hydrogen bonded 7-azaindole dimer.

Alternatively, pK_a* can be obtained from time-resolved absorption spectroscopy measurements on the ps time scale, since a linear relationship exists between this value and the logarithm of the deprotonation rate constant. However, this is only applicable in systems where no other fast processes compete with excited state proton transfer (ESPT) and acid-base equilibration is reached during the excited state lifetime. If one of the involved species is fluorescent, time-resolved emission spectroscopy can be used for determination of the H-transfer rate constant.[138;139]

Molecules with higher excited state acidities (e.g. hydroxyaryls or aromatic amines), where hydrogen abstraction is enhanced upon irradiation, are also known as photoacids. Whether a molecule acts as photoacid or as photobase mainly depends on its substituents. Generally, electron donating substituents are stronger donors in the excited state and electron withdrawing substituents are stronger acceptors.

ESPT reactions usually occur on the femto- to nanosecond timescale. This indicates, that a very low barrier has to be overcome, or that the process is barrierless. Preferentially, the reaction path follows an existing hydrogen bond. A linear relation between the transfer barrier and the equilibrium H-bond length was found, whereas it seems to have only small influence on the reaction barrier whether e.g. oxygen or nitrogen atoms are connected via the H-bond.[140]

Obviously, proton transfer can only take place when a proper acceptor is present. This may be a substituent located in the same molecule (intramolecular proton transfer) or in another molecule (intermolecular proton transfer). The ESPT dynamics not only depend on the pK*-values but also on the number of acceptor molecules present within reach.[141]

ESPT has been extensively investigated in hydroxyaryls. After excitation to the S_1 state relaxation of the π electron cloud takes place, followed by intramolecular charge transfer from the hydroxy group to the aromatic ring system. Due to this redistribution of charges, the O-H bond is weakened and for proton transfer less energy is needed.[135] This can result in intramolecular proton transfer, when one of the carbon atoms of the aromatic ring, whose electronegativity has been increased by the electron migration, performs a nucleophilic attack on the hydroxy group proton whose bond has been weakened. This was also shown for aromatic molecules containing other electron donation substituents, like -OCH_3, -NH_2, or -$N(CH_3)_2$. In molecules with electron-withdrawing groups (e.g. -C≡N), the reverse effect has been found. That is, electron migration from the aromatic ring to the substituent takes place after excitation. The intramolecular proton transfer is assumed to proceed via a nuclear tunneling mechanism and the barrier to proton transfer is dictated by the proton tunneling distance and by solvent rearrangement and only to a lesser extend by the barrier height.[138;142;143]

Polar solvents (especially water) often act as proton acceptor, but proton transfer in hydrogen-bonded dimers also occurs frequently. As already mentioned, experimental evidence for H-transfer in DNA is still lacking, although the existence of hydrogen bonds between the nucleobases, along which H-transfer could occur, is undeniable. It has often been proposed, that photoinduced proton-transfer or photoinduced double proton-transfer along the hydrogen bonds in WC base pairs occurs regularly.[40;66;144;145]

In time-resolved studies of the hydrogen bonded 7-azaindole dimer (which is suitable to serve as simplified model for the WC base pairs, see figure 2.9 for stucture), emission was found to be originating from two components which decay within 1 ps and one component which rises with $\tau_r = 1.1$ ps and decays with $\tau_d = 3.2$ ns. The maximum emission wavelength of this component is shifted from those of the other two components by nearly 150 nm to the red. The first two components were assigned to the two energetically lowest excited singlet states of the 7-azaindole dimer and the third one to the tautomeric excited state formed by the proton-transfer reaction. Thus, the rise time of this component corresponds to the rate constant of the proton transfer in the hydrogen bonded 7-azaindole dimer. The authors of this study state, that the double proton transfer proceeds in a concerted way, since they found no evidence for a zwitterionic intermediate state.[146] However, evidence for this intermediate state, which rises within ~650 fs and decays within ~3 ps, was found in gas phase experiments.[147] Since then, an intense controversy has arisen on the question which of those two mechanisms is the correct one, which has not been resolved up to now, but arguments for the concerted mechanism became stronger in the last years.[66;148]

Of the WC base-pairs, GC has earned most interest in respect to H-transfer studies. Various quantum mechanical calculations predicted the charge transfer (CT) structure as a local minimum on the S_1 PE surface. The results support the prediction that initial charge separation between the nucleobases is followed by proton transfer from G to C. The most probable path is the one along the N-H$\cdots$N bond. It was found to be highly exothermic. Complete-active-space second-order perturbation theory (CASPT2) calculations show, that the potential energy (PE) profile of this path has an crossing with the PE function of the ground state which is assumed to provide an efficient channel for radiationless deactivation of the excited electronic state. This can explain the exceptionally short lifetime of the UV-absorbing state and thus the enhanced photostability of the WC base pair, in contrast to the non-WC base pairs or other base pairs such as GG.[66;67;149]

The electron transfer from G to C can also be described as hole transfer from C to G. In the DNA or in oligonucleotides, the charge transfer can proceed along several nucleobase moieties. G has the lowest ionization potential of the DNA bases and thus behaves as positive charge trap.[150;151]

It is assumed, that the mechanism of H-transfer in GG base pairs is analog to the one described above for GC. This proposed mechanism is shown in figure 2.10. PCM/CAM-B3LYP calculations in comparison with time-resolved absorption spectroscopy provide evidence, that proton-transfer along the N-H$\cdots$N bond takes place in the ^{3}CT-state (see chapter 5.1). Both, the ion pair (which is formed by the charge transfer process) and the radical pair (which is formed by the proton transfer following the charge transfer process) can separate along the hydrogen bonds in the large, ribbon-like G_n aggregates in nonpolar solutions.

The rate constant for charge recombination k_r depends on the probability of an isolated pair of point charges to become permanently separated and thus avoid recombination ($\Lambda(\infty)$) and the diffusion coefficient of one ion away from the other (D_{AB}), as shown in equation 2.14 where R_D is the Coulomb cage radius. The charge separation probability

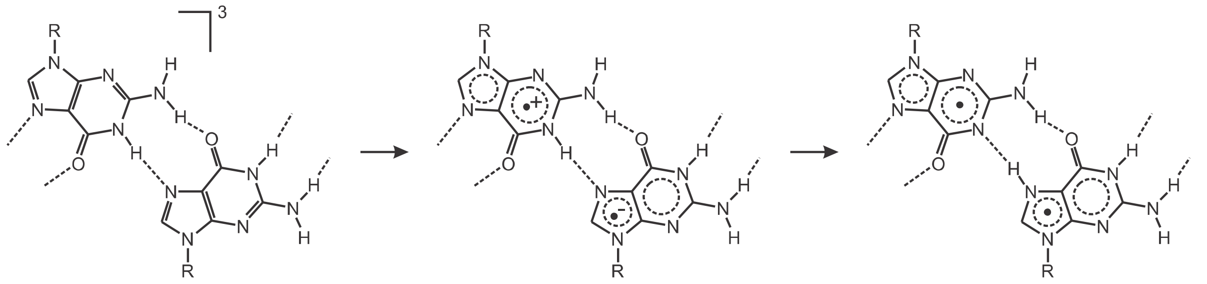

FIGURE 2.10.: Estimated mechanism of H-transfer in guanosine aggregates. One of the guanosine molecules is excited to the singlet state upon laser excitation, and subsequently ISC occurs. Electron transfer to the H-bonded counterpart guanosine takes place from the triplet state, leading to a $G\cdot^{+}G\cdot^{-}$ radical ion pair. The proton follows the electron, leading to a (G-H)·(G+H)· radical pair.

$\Lambda(\infty)$ is given by equation 2.15, where V_{r_0} is the potential energy of the ions, r_0 the initial distance between the ions, k the Boltzmann constant and T the absolute thermodynamic temperature.[139]

$$k_r = \left[R_D\Lambda(\infty)/2(\pi D_{AB})^{1/2}\right] t^{-3/2} \tag{2.14}$$

$$\Lambda(\infty) = exp(-V_{r_0}/kT) = exp(-R_D/r_0) \tag{2.15}$$

H-transfer in aggregates of trisilylated G and comparison to GC is described in detail in chapter 5.1.

3. Methods

In this chapter, the methods which were used for acquisition of the time-resolved absorption and emission properties of the systems studied in this work, are presented and the procedures carried into execution to interpret the acquired data are explained in detail. The experimental set-ups are described briefly, detailed information can be found in the corresponding specrometers' handbooks.

3.1. Transient UV/Vis-Absorption and Emission

Laser flash photolysis (also: pump-probe-spectroscopy) is a powerful method to investigate spectral properties of transient species, like triplet states, ions or radicals. It was introduced by Porter and Norrish in 1949.[152;153] The transient species is generated by irradiation ("pump" process) with the laser pulse. There are three major scenarios which can be set in motion by this irradiation. In most cases, $S_0 \rightarrow S_n$-absorption is the first process induced by the laser pulse, followed by fast IC into the vibronic ground state of the S_1-state. Only processes which are slower than the pulse width of the exciting laser pulse can be examined. The laser pulses used during this work are several nanoseconds long. The $S_n \rightarrow S_1$ IC occurs within picoseconds and therefore is too fast to be observable with our set-up. This implies, that only processes following the $S_n \rightarrow S_1$ IC can be studied.

If the laser wavelength is sufficient to exceed the ionisation potential (IP), the molecule can be ionized by the laser pulse. Even if the energy provided by one photon is not enough, ion formation can still be enabled by multi-photon absorption. To make the cation observable in our set-up, the electron has to be stabilized either by the solvent (e.g. water) or another molecule, to prevent fast recombination of cation and electron.

Another possible response of the system is the breaking of chemical bonds, which results in formation of radicals and/or (meta-)stable photoproducts. In this work only processes which follow excitation of the ground state molecule to the electronically excited singlet state molecule were examined.

After irradiating the sample after excitation ("probe" process), the absorption of the transient species A can be measured. Since only a small amount of the ground state molecules is excited, the absorption of the remaining S_0 molecules would dominate the measured signal. Therefore, the absorption of the non-irradiated sample instead of only the solvent is used as reference. This way, only changes of the absorption spectrum induced by the laser pulse are recorded. Depopulation of the ground state results in negative values for the absorption intensity in the region of ground state absorption ("bleaching"). It is

$$A = -log\left(1 - \frac{I_A - I_B}{I_0}\right) \tag{3.1}$$

with I_A as absorption after laser excitation, I_B as absorption without laser excitation and I_0 as intensity of the probe beam.

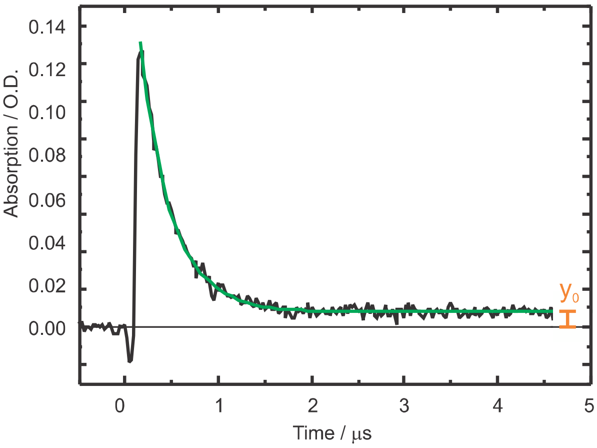

Figure 3.1: Kinetic trace of 1,6-diphenyl-1,3,5-hexatriene in cyclohexane at 417 nm after excitation with 355 nm (black) and monoexponential fit with $\tau = 3.4 \cdot 10^{-7}$ s ± $4.0 \cdot 10^{-9}$ s (green).

For each wavelength, the absorption is detected for several nanoseconds up to several microseconds. From the change of absorption intensity during this time, the rate constants for formation and depletion of the transient species can be calculated (see section 6.1). If photoreactions take place, information about the reaction kinetics is gained this way (see section 4.1).

As an example, the absorption of 1,6-diphenyl-1,3,5-hexatriene (DPH) during the first 5 µs after the laser pulse is shown in figure 3.1. Recording starts 1 µs before the laser pulse. Since no transient species is generated yet, the differential absorption is zero. The data points recorded before the pulse are thus used as reference, for instance to check if the ground state is repopulated completely or if photoproducts are formed which absorb in the same spectral region as the transient species. Directly after the laser pulse a small negative signal is detected, which results from scattered laser light and fluorescence emitted by the DPH. The absorption signal rises up to its maximum within a few nanoseconds and then decays monoexponentially. An exponential fit of the form

$$y(x) = Ae^{-kx} + y_0 \tag{3.2}$$

delivers the rate constant k and thus the lifetime τ of the absorbing species ($\tau = k^{-1}$, see also section 3.5). The signal does not recede to zero, which hints towards the formation of a photoproduct.

If more than one species show absorption in the same spectral region, the kinetic trace does show multi-exponential behaviour. In that case, a multicomponent fit function has to be applied to obtain the lifetimes of the different species:

$$y(x) = A_1e^{-k_1x} + A_2e^{-k_2x} + A_3e^{-k_3x} + ... + y_0 \tag{3.3}$$

This is repeated for several wavelengths, usually with $\lambda_{i+1} = \lambda_i + \Delta\lambda$ with $\Delta\lambda$ as the spectral resolution of the monochromator. By combining the absorption intensities at a distinct time after the laser pulse at different wavelengths, the absorption spectrum of the system at this time is obtained.

Once again, DPH is used as example. The spectra of a nitrogen purged DPH solution at different times after the laser pulse are shown in figure 3.2). The transient species absorbs between 380 nm and 430 nm, and probably even below 380 nm. The negative band in the region of 300 - 380 nm, which is assigned to the ground state bleaching may overlap the absorption of the transient species. It recovers with the same time constant as the absorption in the region of 380 - 430 nm is depleted. Therefore it is safe to assume,

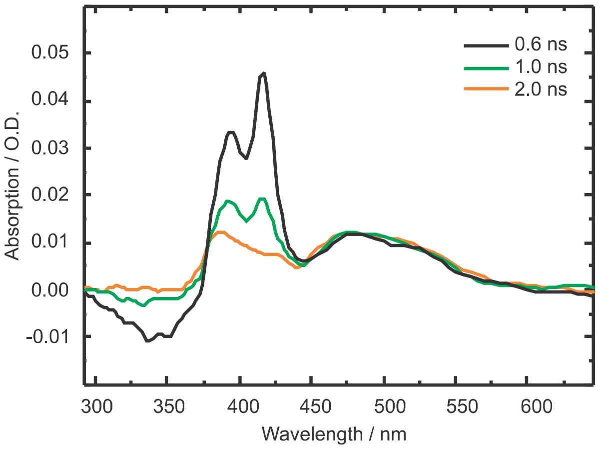

FIGURE 3.2: Absorption spectrum of DPH in cyclohexane at different times after excitation with 355 nm. Solution purged with N_2.

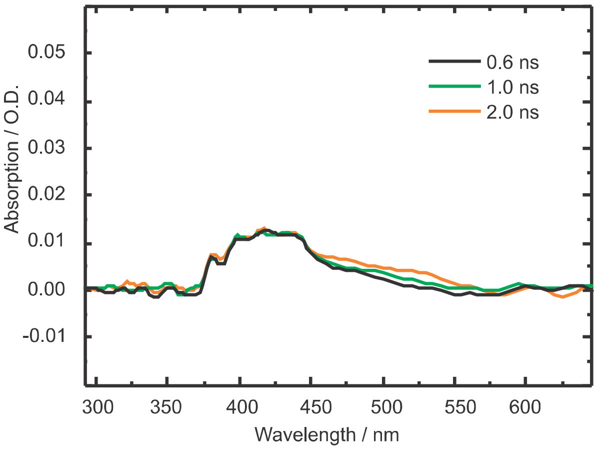

FIGURE 3.3: Absorption spectrum of DPH in cyclohexane at different times after excitation with 355 nm. Solution purged with O_2.

that a vast majority of the excited state molecules transform back into ground state molecules instead of performing a photoreaction which would result in a photoproduct. A second species absorbs light between 450 nm and 600 nm, with a lifetime so long, that it seems to be stationary in the time span shown here.

When the experiment is carried out under the same conditions except the purging gas being oxygen instead of nitrogen, the excited state absorption is considerably decreased (see figure 3.3). In this case, the oxygen molecules react with the excited state DPH molecules and thus depopulate the absorbing species. This is most likely a sign, that after excitation ISC into the triplet state DPH takes place, and that the absorption observed in the oxygen-free experiment was caused by triplet state DPH. Therefore not only the lifetime of the transient species can be measured by laser flash photolysis, but also hints about the nature of the species are obtained and reaction paths can be clarified.

As described above, excitation of the ground state molecule to the S_n state molecule is followed by fast IC into the S_1 state. Then, if the transition is allowed, fluorescence from the S_1 state can occur. Time-resolved detection of the fluorescence delivers information about the lifetime of the emitting state. Analogous to the transient absorption experiment, the emission at distinct wavelengths is detected for several nanoseconds. In simple cases, like 1-methylthymine in water, the S_1 state lifetime is obtained by a monoexponential fit of the kinetic trace, as shown in figure 3.4. The signal-to-noise ratio of the kinetic trace can be enhanced by integration over a larger spectral range of the emission. The kinetic trace shown in figure 3.4 was obtained by averaging the traces detected at 300 nm - 350 nm. The emission spectra of the transient species are obtained by combining

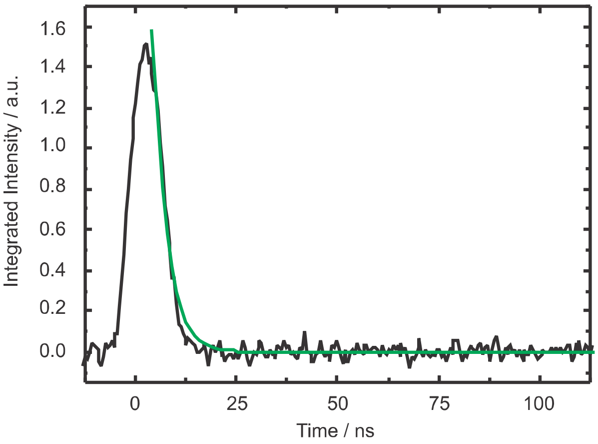

Figure 3.4: Fluorescence of 1-methylthymine in H_2O at 340 nm after excitation with 266 nm. Kinetic trace (black) and monoexponential fit with $\tau = 3.5 \cdot 10^{-9}$ s $\pm$ $8.6 \cdot 10^{-11}$ s (green).

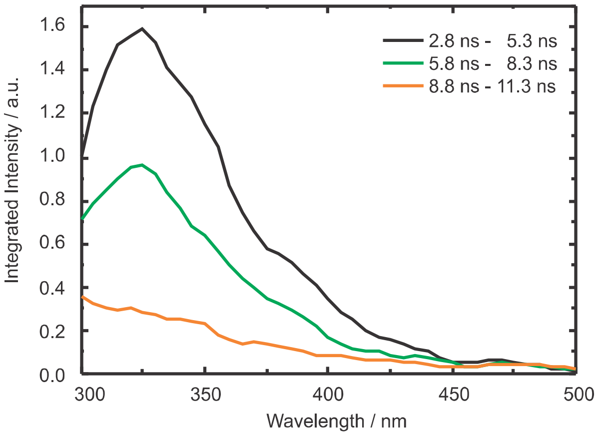

Figure 3.5: Fluorescence of 1-methylthymine in H_2O at 340 nm after excitation with 266 nm. Emission spectra at different times after excitation.

the intensities at each wavelength for a distict time after the laser pulse (see figure 3.5). Again, better signal-to-noise ratio can be achieved by integration, in this case over a part of or even the whole time range. The spectra shown in figure 3.5 were obtained by averaging over 2.5 ns (six data points), each.

A more complex case, with several excited states involved in the emission process, is described in detail in section 6.1.

3.2. Set-up for Transient UV/Vis Absorption and Emission Experiments

The set-ups of the spectrometer used for laser flash photolysis of solutions and films are schematically shown in figure 3.6 and 3.7, respectively. For absorption measurements, it features two light sources: a Nd:YAG laser (pump) and a xenon lamp (probe). For emission measurements no probe beam is required (see figure 3.8).

The laser (Spitlight 600, Innolas) originally generates 1064 nm pulses of 12 ns pulse width and can also be operated at wavelengths of 532 nm, 355 nm, 266 nm and 213 nm. By attaching an additional Pockels cell, the edges of the pulse are cut off and pulse widths down to 5 ns are enabled. This method to reduce the pulse width results in a decrease of laser intensity, e.g. at 266 nm, the power is reduced from 40 mJ to 15 mJ. The 150 W Xenon arc lamp can be operated in a pulsed mode as well as a continuous mode. Depending on the minimum wavelength needed, different lamps were employed: $\lambda_{\text{min}} =$

300 nm: Osram XBO; $\lambda_{\mathrm{min}} = 220$ nm: Hamamatsu 2274; $\lambda_{\mathrm{min}} = 185$ nm: Hamamatsu 2273. All lamps can be used to generate pulses of approximate 1.5 ms with a plateau of 400 µs. A more detailled description of laser and Xenon lamp as well as the photomultiplier (PEM) used for light detection (R928, Hamamatsu) and their specifications is provided elsewhere.[154]

The two beams are aligned in such a way that they cross in a near right angle in the sample. To avoid accumulation of reaction products, a flow-through cuvette can be used for experiments in solution. The reservoir can be purged with a gas (usually nitrogen or oxygen) during the whole experiment, to control the oxygen concentration in the sample and thus enable or suppress oxygen quenching. In the case of the sample being a film, the quartz window, on which the film is applied, is rotated during the experiment (see figure 4.1).[20] Thus, the beams constantly encounter a fresh region of the film. Control of oxygen concentration would only be possible by flushing the whole sample chamber.

The probe beam is dispersed in a monochromator, with variable entry- and exit-slits. By adjusting the slits, the spectral resolution of the monochromator can be controlled. In this work, the resolution was usually chosen to be between 2 nm and 2.5 nm. The spectral range available is limited on the high energy side by the xenon lamp, whose intensity is to weak below it's specific λ_{min}; and on the low energy side by the photomultiplier, which does not exhibit enough sensitivity for wavelengths above 750 nm.

3.3. Light-induced FTIR Difference Absorption

The principles of FTIR spectroscopy are described comprehensively by Herres and Gronholz.[155–157] Light-induced FTIR difference absorption spectroscopy can be used to determine the yield of photoreactions and to identify the photoproducts. The set-up shown in figure 3.9 was used to follow photoreactions by measuring the IR absorption of the sample after different irradiation times. Contrary to the transient UV/Vis absorption and emission experiments, not the time traces are collected for each wavelength, but an interferogram is collected after each of the different irradiation times, which then is computed to deliver the IR spectrum for this point of the reaction. With our set-up it takes about two minutes to obtain one interferogram, therefore it is not possible to investigate the actual reaction kinetics, but accumulation of reaction products and degradation of the educts can be pursued.

The difference absorption spectra for each irradiation time t are obtained from the single channel spectra before and after illumination:

$$\Delta A_t(\nu) = -lg\frac{I_t(\nu)}{I_0(\nu)} \tag{3.4}$$

This way, only changes in absorption appear in the spectrum: positive absorption bands are induced by the photoproducts, while negative absorption bands derive from educt absorption, which declines with the advance of the photoreaction. Absorption bands of the solvent or in the case of polymer films the polymer backbone do not contribute to the difference absorption spectrum as long as photodegradation does not take place. Otherwise they add to the negative signal.

In section 4.2.4 a detailed description of how to determine the yield of a photoreaction with the help of light-induced FTIR Difference Absorption is provided. Identification of photoproducts with this method is described in section 4.2.5.

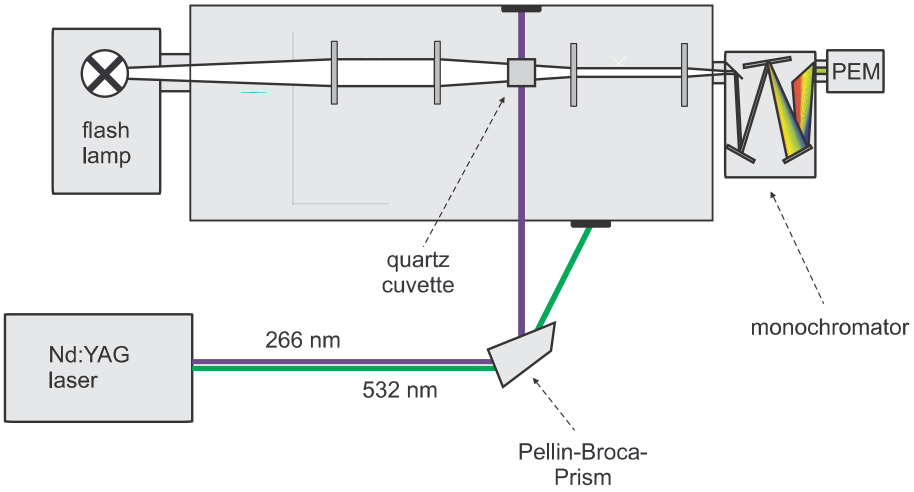

FIGURE 3.6.: Set-up of the spectrometer used for time dependent absorption spectroscopy in solution.

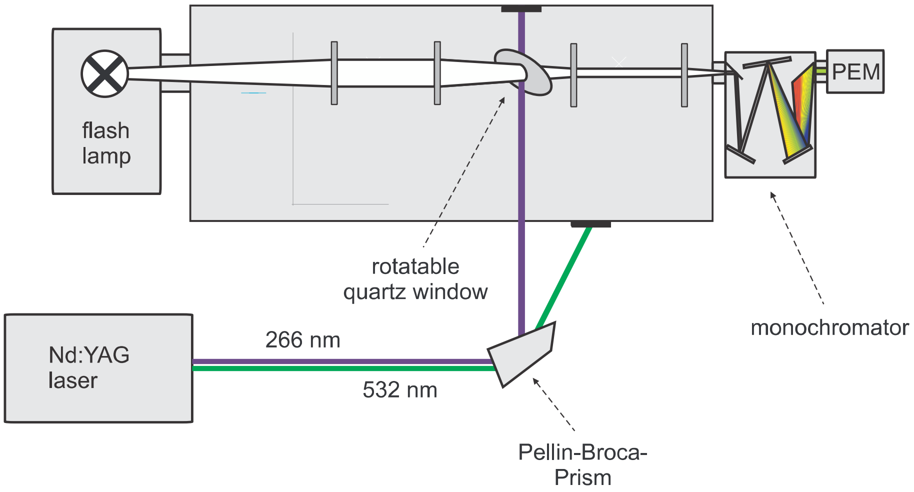

FIGURE 3.7.: Set-up of the spectrometer used for time dependent absorption spectroscopy in the film.

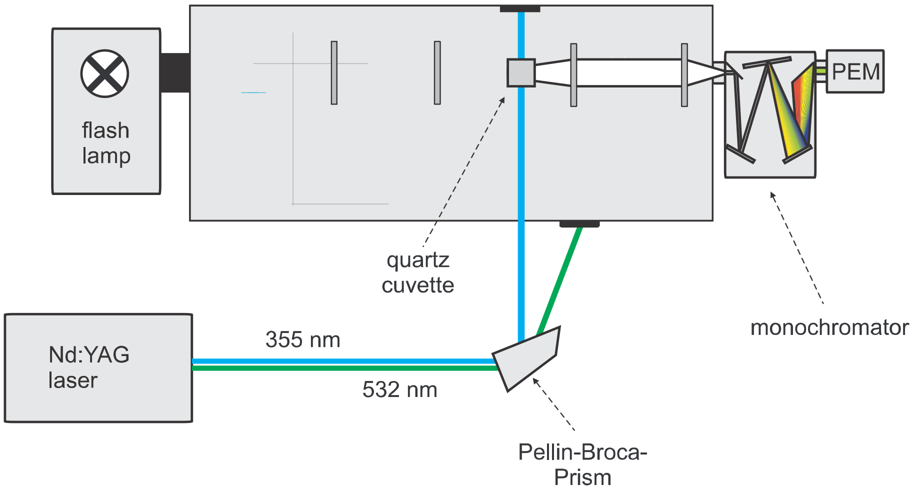

FIGURE 3.8.: Set-up for transient emission measurements in solution.

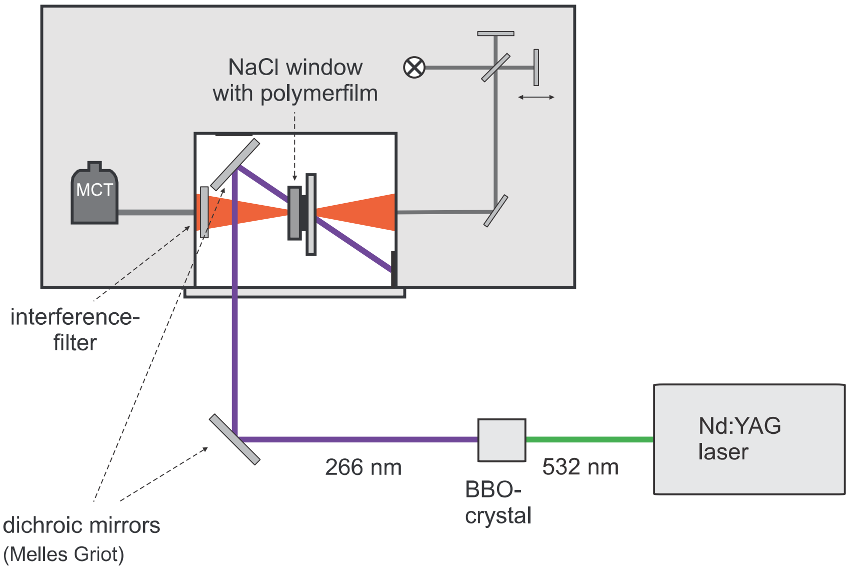

FIGURE 3.9.: Set-up for light-induced FTIR absorption measurements in a film.

3.4. Set-up for Light-induced FTIR Difference Absorption Experiments

The photoreaction is induced by 266 nm laser pulses with a pulse width of 10 ns and a repetition rate of 10 Hz (INDI, Spectra Physics). The fourth harmonic is generated by an external BBO crystal (BaB_2O_4). All samples investigated in this work with this method were films, applied onto NaCl windows via spin coating. The excitation energy had to be adjusted to 6 mJ/cm^2, to minimize photodamage of the samples. The laser beam is led into the evacuated (2.5 mbar) sample chamber of a standard FTIR spectrometer (Vertex 80V, Bruker) and adjusted such that irradiation beam and probe beam (diameter each: 8 mm) cross on the surface of the film. This way, the sample has not to be moved between irradiation and measurement. This is important since the beams do not illuminate the whole film, and it has to be ensured that the same region of the film is examined during the whole experiment. Scattered light is blocked by a broadband interference filter (Bruker, 4000 - 900 cm^{-1}) in front of the nitrogen cooled MCT-detector ($Hg_{0.8}Cd_{0.2}Te$).

3.5. Kinetic Simulations

The kinetic behavior of chemical reactions and processes depends on the concentration of the reactants, their state of matter and the presence of catalysts. It is affected by temperature and pressure and, in the case of reactions in solution, the solvent. To study the kinetics of a reaction, as many of these parameters as possible should be kept unchanged during each experiment, while the - controlled - change of one parameter between different experiments may be highly informative.

Most chemical processes are bimolecular and those reactions often follow a second order rate law. This is also true for photochemical reactions, where usually one excited state molecule reacts with one ground state molecule (see section 2.2). In contrast, photophysical processes (e.g. IC, ISC, emission) follow first order rate laws. Each photochemical reaction is preceded by a photochemical process (usually absorption), and the reaction

can be written as: $A + B \xrightarrow{h\nu} A^* + B \rightarrow C$, where the first step is of first order and the second step (in most cases) of second order. In photochemical reactions induced by laser pulses, the second step typically is the slower one and thus the rate determining step.
The reaction rate r of a first order reaction depends only on the initial state's concentration [A] and the reaction rate constant k:

$$r = -\frac{d[A]}{dt} = k \cdot [A] \tag{3.5}$$

By separation of variables and subsequent integration over the time, the time dependent concentration $[A]_t$ is obtained, where $[A]_0$ is the initial concentration:

$$[A]_t = [A]_0 \cdot e^{-kt} \tag{3.6}$$

In this rather simple case, the rate constant can be determined with time resolved spectroscopy if the state or species of interest is absorbing or emitting. According to the Lambert-Beer law, the concentration is correlated linearly with the absorption (or emission) intensity, and by performing an exponential fit of the observed kinetic trace, k can be directly obtained from the fit parameters. The lifetime τ of the state / species can then be calculated by:

$$\tau = k^{-1} \tag{3.7}$$

When several processes contribute to the decay (or rise) of an excited state, $[A]_t$ is affected by the reaction rates of all reactions by which this particular state is populated and/or depopulated:

$$[A]_t = [A]_0 \cdot e^{-(\Sigma k)t} \tag{3.8}$$

In this case, or when the spectral ranges of more than one species overlap in the observed wavelength region, the experimentally observed time traces may possibly show no single exponential behavior and the rate constants cannot be obtained from mono-exponential fits. To obtain the rate constants in such complicated systems, simulations with coupled differential equations may be required. These simulations can also be used to clarify mechanisms where not all processes involved are already known. Therefore, a possible mechanism has to be postulated and a set of rate constants has to be found which leads to the same kinetic trace as the observed time trace. Although with this method wrong mechanisms can be eliminated, the correct mechanism cannot be proven. A possible routine to solve such problems with MATHCAD can be found in Appendix A.
For a system with two emitting states, which are energetically close to each other (e.g. S_1 state and S_2 state), at least three processes have to be included in such a model. These are emission from both states (fl_1 and fl_2) and internal conversion from one state to the other (IC). The absorption process is not included in the model, the simulations start with the end of the exciting laser pulse. Such a system is schematically shown in figure 3.10a. In this work mainly condensed phase systems are discussed, and thus it is postulated for this model, that the vibrational relaxation (vr) is much faster than IC. Therefore, IC is the rate-determining one of those two steps and k_{vr} can be disregarded. In this model system $S_0 \rightarrow S_2$ excitation took place and the observed time-resolved emission is a superposition of S_1 state and S_1 state emission. The observed kinetic trace thus is represented by the simulated S_1+S_2 kinetic trace. The kinetic equations for this model are as follows:

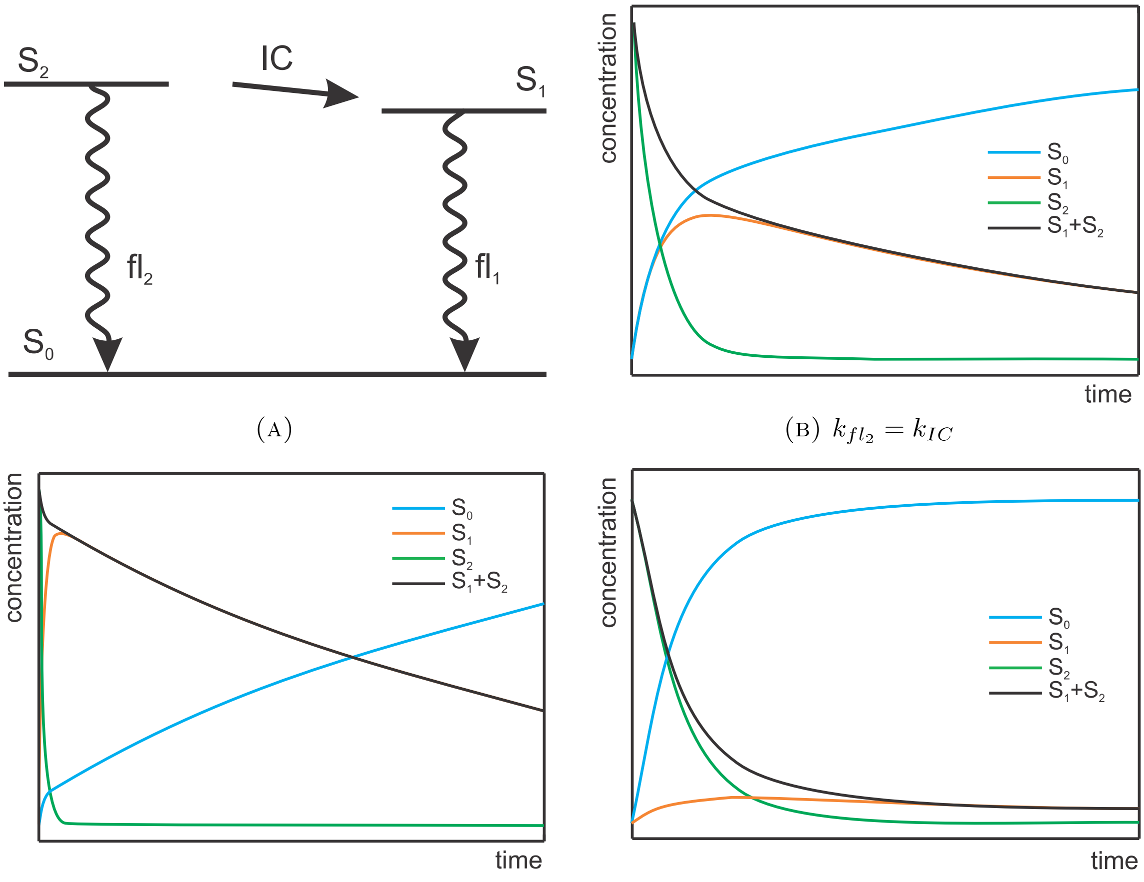

(A)

(B) $k_{fl_2} = k_{IC}$

(C) $k_{fl_2} < k_{IC}$

(D) $k_{fl_2} > k_{IC}$

FIGURE 3.10.: (A) Scheme of a model system with two emitting states. (B)-(D) Resulting kinetic traces of the involved states. In all three cases: $k_{fl_2} > k_{fl_1}$

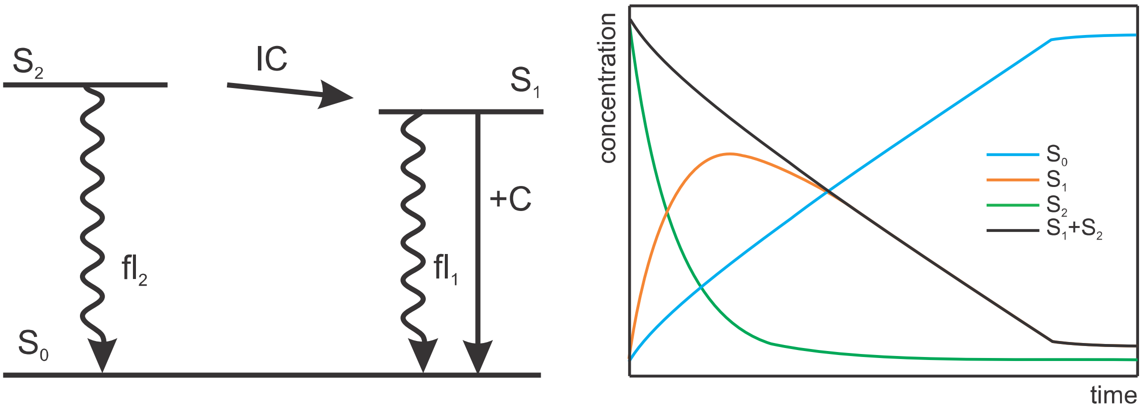

(A)

(B) $k_{fl_2} < k_{IC}, k_{fl_1} < k_C$

FIGURE 3.11.: (A) Scheme of a model system with two emitting states and one catalyzed deactivation process. (B) Resulting kinetic traces of the involved states.

$$\frac{d[S_2]}{dt} = -k_{fl_2}[S_2] - k_{IC}[S_2] \tag{3.9}$$

$$\frac{d[S_1]}{dt} = k_{IC}[S_2] - k_{fl_1}[S_1] \tag{3.10}$$

$$\frac{d[S_0]}{dt} = k_{fl_2}[S_2] + k_{fl_1}[S_1] \tag{3.11}$$

For illustrational reasons, $[S_0]_0$ is set to zero. Following the example of DPH emission, k_{fl_2} is defined to be faster than k_{fl_1}. The ratio $k_{fl_2} : k_{IC}$ has major impact on the kinetic traces. In all cases, the S_2 state is depopulated rather fast, but it has to be $k_{fl_2} \leq k_{IC}$ for the S_1 state to become populated fast enough to significantly contribute to the overall emission. The impact of S_1 state and S_2 state emission on the total emission thus is controlled by the rate constant ratio of the different parallel processes.

If the time trace can not be simulated with the postulated mechanism, implementation of further possible processes may lead to better results. As an example, for explanation of the untypical kinetic behavior of the emission observed in DPH (see chapter 6.1), an additional deactivation path of the S_1 state, which follows zero order kinetics, is required. Zero order reaction kinetics are found in processes where one partner is present in deficient proportion and is regenerated, like a catalyst ($A + C \longrightarrow B + C$ with $[A] >> [C]$). The reaction rate then only depends on $[C]$ (as long as it is significantly smaller that $[A]$) rather than on both concentrations and since $[C]$ is constant ($[C]_t = [C]_0$), the rate law can be written as:

$$-\frac{d[A]}{dt} = k[C]_0 \tag{3.12}$$

or in its integrated form:

$$[A]_t = -k[C]_0 t + [A]_0 \tag{3.13}$$

A model mechanism with such a catalyzed process as parallel process for S_1 state depopulation is shown in figure 3.11. The according kinetic equations for the involved states nominally are as follows:

$$\frac{d[S_2]}{dt} = -k_{fl_2}[S_2] - k_{IC}[S_2] \tag{3.14}$$

$$\frac{d[S_1]}{dt} = k_{IC}[S_2] - k_{fl_1}[S_1] - k_C[S_1][C] \tag{3.15}$$

$$\frac{d[S_0]}{dt} = k_{fl_2}[S_2] + k_{fl_1}[S_1] + k_C[S_1][C] \tag{3.16}$$

To account for the aforementioned proposition that the reaction is catalysed, a differentiation has to be used in the fit. As long as $[S_1] >> [C]$ is true, this path follows zero order rate law. When after a certain reaction progress $[S_1]$ has decreased and it is $[S_1] \approx [C]$, the reaction rate is of first order (it has always to be kept in mind that $[C] = const.$). The implementation of this differentiation in the MATHCAD fit routine is shown in Appendix A. The kinetic curves obtained from this simulation with $k_{fl_2} < k_{IC}$, $k_{fl_1} < k_C$ and $[C]_0 < [S_2]_0$ are shown in figure 3.11b. At first, the overall emission (S_1+S_2) is merely S_2 state fluorescence and thus shows slightly exponential behavior. With increasing S_1 concentration, the contribution of fl_1 to the overall emission increases and, since the catalyzed process dominates the S_1 state depopulation, the decay becomes linear.

When the shape of the simulated curve obtained from a model resembles the observed kinetic trace, the model is qualified to be implemented in the fit routine. In the routine used in this work (see Appendix A) each rate constant can be varied with different increments and over different ranges. For each combination of rate constants, the deviation of the simulated S_1+S_1 kinetic trace from the experimental trace is calculated. The combination with the smallest deviation is used as starting point for the next iteration. Finally a set of rate constants is obtained, with which the postulated mechanism delivers the same kinetic trace as was observed experimentally.

Under different experimental conditions, e.g. changed concentrations of the emitting molecule or the catalyst, significantly different kinetic traces can be observed. If the postulated mechanism describes the system accurately, simulations with the same rate constants but adapted initial concentrations suitably emulate all observed kinetic traces (see also chapter 6.1).

3.6. Quantum Mechanical Calculations

Quantum mechanical calculations are an indispensable aid for interpretation of spectroscopic experiments. Not only do they deliver information about the geometry of ground state and excited states molecules, but they also predict electronic and vibrational transitions. All calculations in this work were performed using the TURBOMOLE program package,[158–164] no molecule - solvent or molecule - molecule interactions were considered. *Ab initio* calculations are based on the Schrödinger equation,

$$\hat{H}\psi = E\psi \tag{3.17}$$

with the Hamilton operator $\hat{H}$, where $\hat{T}$ is the kinetic energy operator and $\hat{V}$ the potential energy operator:

$$\hat{H} = \hat{T} + \hat{V} \tag{3.18}$$

and the energy E (see equation 3.19). The derivation of the Schrödinger equation is covered in innumerous texbooks, such as those by Atkins[117], Jensen[165] and Kutzelnigg[166]. It can only be solved for one-electron systems, therefore to obtain the energies and wavefunctions of larger systems like organic molecules, certain simplifications have to be made. According to the Born-Oppenheimer approximation the movement of the atom nuclei can be regarded separate from the electron movement.[167] Due to the large mass difference and the momentum p of electrons and nuclei being of the same order of magnitude, the electron movement instantaneously follows a change of the nuclear configuration. Thus, the electronic Schrödinger equation $\hat{H}\psi_{(R,r)} = E_{(R)}\psi_{(R,r)}$ can be solved for each fixed set of nuclei locations R, with r as the electron coordinates. The energy of the electron system can be described as a functional of the electron probability density ρ.[168] While the wavefunction of an N-electron system depends on 3N cartesian coordinates, the electron density (which is the square of the wave function, integrated over N-1 electron coordinates) only depends on three cartesian coordinates. Utilisation of the density functional therefore reduces the costs of calculation by minimisation of the dimensionality.

The total energy of the electron system is composed of the kinetic energy of the electrons E_{kin}, the potential energy of the nucleus-nucleus and nucleus-electron interactions E_{pot}, the electron-electron Coulomb interaction E_{cou} and the exchange-correlation functional $E_{XC[\rho]}$:

$$E_\rho = E_{kin} + E_{pot} + E_{cou} + E_{XC[\rho]} \tag{3.19}$$

The form of the exchange-correlation functional is unknown, therefore approximated functionals are used.[169;170] By combination of Hartree-Fock (HF) energy, local spin density approximated (LSDA) and gradient approximated exchange and correlation functionals (GGA), hybrid functionals like the B3LYP functional (equation 3.20), which was used for all calculations within this work, are created.[171;172] The GGAs used in the B3LYP functional are the exchange GGA by Becke (B88, $E_{X[\rho]}^{GGA}$)[173] and the correlation GGA by Lee, Yang and Parr (LYP, $E_{C[\rho]}^{GGA}$)[174].

$$E_{XC[\rho]}^{B3LYP} = (1-a)E_{XC[\rho]}^{LSDA} + aE_X^{HF} + bE_{X[\rho]}^{GGA} + (1-c)E_{C[\rho]}^{LSDA} + cE_{C[\rho]}^{GGA} \tag{3.20}$$

The values of a, b and c vary between different calculation methods. In Turbomole V5.10, the B3LYP functional is implemented with $a = 0.2$, $b = 0.72$ and $c = 0.81$.

The LSDA functional contains the exchange-correlation energy per electron $\epsilon_{xc[\rho]}$, derived from the Dirac equations for a uniform electron gas.[175] These approximations lead to a slight overestimation of binding energies, but results obtained by DFT calculations with the B3LYP functional are nonetheless of good quality, particularly taking into account the low calculation costs.

As a matter of course, the quality of a calculation highly depends on the basis set used to represent the spinorbitals. An often used strategy to keep the basis set truncation error as well as the calculation costs low, Slater type orbitals (STO)[176] and Gaussian type orbitals (GTO)[177] are combined. While GTOs give poorer representations of the atomic orbitals (especially at the nucleus) they have the advantage that they are much easier to compute. Therefore it is a common approach to construct an contracted GTO set by performing an fit to a STO. In the minimal basis set one function is used for each of the systems orbitals, but usage of several functions for each orbital increases the calculations accuracy significantly. The triple-zeta split valence basis set (TZVP), which was applied in this work, uses one function for the core orbitals and three for each valence orbital.

All these calculations are performed for a fixed geometry of the nuclei. To find the equilibrium geometry of the molecule, i.e. that one with the lowest total energy, a Berny gradient optimization is performed, which utilizes the Hesse-matrix (second derivative of the energy with respect to the normal modes).[178] At the equilibrium geometry, the energy gradient is zero along all internal coordinates.

Once equilibrium geometry and energy of the molecule are known, a normal coordinate analysis delivers the vibrational frequencies, which aid in the interpretation of the molecule's IR spectrum. In a nonlinear molecule consisting of N atoms, there are $3N-6$ of those coordinates, which correspond to atom displacements without a change of the molecule's center of mass. If the geometry optimization ended in a transition state, at least one of the calculated frequencies is unreal. To obtain the minimum geometry, a new geometry optimization with the transition state geometry as starting point (optionally slightly distorted to force the system to leave the local minimum of the PES) and a more strict energy convergence criterion is a promising procedure.

The intensity of each vibration is calculated from the overlap of the wavefunctions, according to the Franck-Condon principle, see chapter 2.1 .

4. Photo-cross-linking of polymers with maleimide side chains

4.1. Photo-cross-linking of poly[ethene-*stat*-(methacrylic acid)] functionalised with maleimide side groups

NADINE SCHMELING*, KATHARINA HUNGER#, GERNOT ENGLER#, BENJAMIN BREITEN*, PATRICK RÖLLING*, ALEXANDER MIXA*, CLAUDIA STAUDT* AND KARL KLEINERMANNS#

* INSTITUTE OF ORGANIC AND MACROMOLECULAR CHEMISTRY, FUNCTIONAL MATERIALS, HEINRICH-HEINE UNIVERSITY DUESSELDORF, 40225 DUESSELDORF, GERMANY

INSTITUTE OF PHYSICAL CHEMISTRY, HEINRICH-HEINE UNIVERSITY DUESSELDORF, 40225 DUESSELDORF, GERMANY

Printed in *Polymer International*, 58(7):720-727, 2009.

4.1.1. Abstract

Background

Photo-cross-linkable polymers are well-known and commercially applied as photoresists. But so far they have not been applied as membrane materials for separation processes. They would offer certain advantages in membrane fabrication over conventional cross-linked polymer materials. Therefore, in this work, a poly[ethene-*stat*-(methacrylic acid)] (PEMAA) which is a potential membrane polymer for different separation problems was functionalised with photo-cross-linkable maleimide side groups.

Results

It has been shown that PEMAA can be used as basic polymer material and a conversion with 3-hydroxypropyldimethylmaleimide is possible in order to obtain a photo-cross-linkable polymer. Investigation of the cross-linking mechanism was performed using stationary infrared and UV-visible spectroscopy as well as nanosecond transient spectroscopy absorption measurements of a rotating film. Intense transient absorption of the maleimide-esterified PEMAA occurs at 250 nm in the film pointing to maleimide anion formation and cross-linking via an ionic dimerisation mechanism.

Conclusion

It is found that cross-linking reactions can be observed spectroscopically *in situ* using a maleimide functionalised PEMAA. Furthermore, experiments can be performed in the liquid phase (polymer in solution) as well as in the solid phase (polymer film) using a rotating polymer film sample. Maleimide anion formation and cross-linking via an ionic dimerisation mechanism can be investigated by variation of the polymer structure as well as the structure of the maleimide side groups.

4.1.2. Introduction

Cross-linkable polymers are of great interest for various applications, the best known being photoresists which are used for the fabrication of offset printing plates. Cross-linked materials are gaining attention as membranes used in separation processes for gaseous, vaporous and liquid mixtures, because they offer very high chemical resistance and good temperature stability, essential for long-term applications in the chemical industry.[179] For the preparation of cross-linked membranes, functionalised polymers are convenient and their separation characteristics in pervaporation[27;28;180–182] and gas separation[183–189] are much better than those of non-cross-linked commercially available membrane polymers.

In recent years carboxylic acid-containing polymers have attracted increasing interest as basic membrane materials because they can be easily cross-linked covalently or ionically by treatment with diols, diamines or aluminium acetyl acetonate.[27;28;180] Poly[ethene-*stat*-(methacrylic acid)]s (PEMAAs) are rubbery polymers produced by BASF. They are also functional polymers with carboxylic acid groups that can be used for preparing cross-linked membrane materials with exactly the same treatment as glassy copolyimides having carboxylic acid groups. In both cases, cross-linking of the polymer by esterification, for example with a diol, leads to partially or totally insoluble polymers which are promising candidates for a new generation of membrane material because they offer high resistance in aggressive solvents such as petrol or kerosene at temperatures greater than 150 °C.[190] However, cross-linking of polymers containing -COOH has the disadvantage that catalysts are necessary, e.g. *p*-toluenesulfonic acid is used in the case of esterification reactions with diols. After cross-linking, the catalyst is in the membrane and often causes problems in liquid separation because elution is observed which leads to an undesirable change of the membrane performance. Therefore new strategies have to be developed in order to circumvent these problems.

Photochemical cross-linking of membrane polymers has been investigated before,[191] but in the case of direct cross-linking of the polymer backbone the permeability loss is very large due to the increasing stiffness of the polymer network and the decrease of free volume in the polymer. Furthermore, control over the cross-linking reaction seems to be difficult. Therefore a new approach for the preparation of cross-linked membrane materials has been developed which allows control of the degree of cross-linking via functionalisation of polymers containing -COOH with UV-cross-linkable groups. Since no radical initiators are used, no unwanted changes of membrane performance are expected. Additionally bulky photo-cross-linkable groups are used which are supposed to increase the distance between the polymer chains so that loss in permeability due to cross-linking can be avoided.

In this approach, maleimide derivatives, which are well known to dimerise as monomers but also in polymeric compounds upon absorption of UV light in pericyclic reactions,[192] are used as photo-cross-linkable side groups. In order to obtain maleimide-functionalised copolymers of PEMAA, 3-hydroxypropyldimethylmaleimide was synthesised. The reaction mechanism was studied using stationary absorption measurements to determine the wavelength range where cross-linking takes place and using transient absorption spectroscopy to obtain information about transients (triplet species, ions, radicals) that occur in the course of dimerisation.

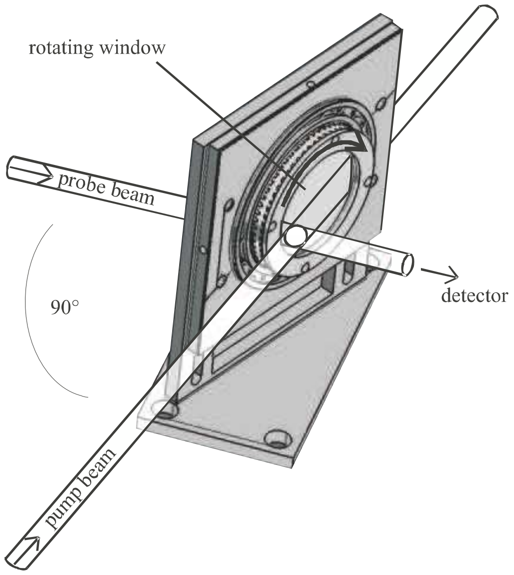

Figure 4.1: Sample holder for rotating window.

4.1.3. Experimental

Methods

The nanosecond transient absorption setup (Applied Photophysics) utilises the output from a frequency quadrupled (266 nm) pulsed Nd:YAG laser (Innolas) for maleimide photoexcitation. Liquid-phase samples were excited with 70 mJ pump energy at 15 ns laser pulse width and 1 Hz repetition rate. The pump beam of 1 cm diameter was directed into the sample (a standard 3.5 mL cuvette) at a right angle to the probe beam. The samples were purged with dry nitrogen to remove dissolved oxygen. For sensitive measurements of absorbance changes we used a high-intensity pulsed xenon lamp (150 W, 1.5 ms) as probe source. The central part of the probe pulse has a 400 µs flat plateau. Behind the sample the probe light was dispersed by a grating monochromator for wavelength selection. The output signal was detected by a photomultiplier (R928, 250-800 nm), digitised by an oscilloscope (Agilent Infinium) and transferred to a workstation (Iyonix). Typically 15 laser pulses were averaged to record a kinetic trace at a selected wavelength. Polymer film samples were formed by spin-coating a solution of 59 mg 3-hydroxypropyldimethylmaleimide esterified with PEMAA (esterification grade 6 %) in 10 mL of tetrahydrofuran (THF; spectroscopic grade) onto a quartz glass window (diameter: 40 mm, thickness: 4 mm). To measure transient spectra, the coated window was inserted into a sample holder, as shown in figure 4.1, in such a way that the overlapping pump and probe beams impinged on the film. The sample holder could be adjusted, to make sure that probe and pump beams overlap in the outer part of the film. The window was rotated by a motor using a driving belt. The rotation speed was adjusted to ensure that fresh film spots were exposed to the beams. The polymer film samples were excited using 15 mJ, 2 ns, 1 Hz as laser parameters.

Stationary absorption spectra were recorded with a Cary 100 (Varian) spectrophotometer. The films were irradiated with an Oriel 66011 Hg lamp, using a water-filled 2 cm wide cuvette as filter.

Infrared spectra were recorded with a Nicolet FT-IR.5SXB spectrometer. Solid samples

TABLE 4.1.: Physical properties of PEMAA (Fechtenkötter A, BASF Ludwigshafen, personal communication, 2004).

Composition[a] E (mol %)	Composition[a] MMA (mol %)	Composition E (wt %)	Composition MMA (wt %)	Titratable acid[b] (mmol/$g_{polymer}$)	Melting temperature (°C)	Recrystallisation temperature[c] (°C)
89.1	10.9	72.8	27.2	3.16	74	40-52

[a] E: ethene unit; MAA: methacrylic acid unit

[b] Measured by potentiometric titration according to DIN 53042)

[c] Measured by DSC)

TABLE 4.2.: Amount of oxalyl dichloride used for 16 g PEMAA which equates to 50.56 mmol acid units.

Oxalyl dichloride (g)	Conversion of acid groups (%)	Polymer yield (%)
3.09	48	92
0.49	8	95
0.37	6	94
0.25	4	93
0.12	2	92

were applied to a diamond crystal. The data obtained were Fourier transformed to give absorption spectra.
Geometry optimisations and harmonic frequency calculations at the B3LYP/TZVP level of theory were performed using the Turbomole program package.[158–161] Calculated harmonic vibrational frequencies were scaled by 0.961 (below 2000 cm^{-1}) and 0.941 (above 3000 cm^{-1}) in order to match the calculated and experimental C-H and C=O stretching vibrations of the 3-hydroxypropyldimethylmaleimide in solution.

Materials

PEMAA was kindly provided by BASF, Ludwigshafen. The structure of PEMAA is shown in figure 4.2A. Its physical properties are given in table 4.1. Solvents used for syntheses and membrane preparation were tetrachloromethane (analytical grade) purchased from Riedel de Haen, oxalyl dichloride (synthesis grade) from Merck, THF (analytical grade) from Prolabo and dimethylmaleic acid anhydride (98 %) from Aldrich.

Synthesis of 3-hydroxypropyldimethylmaleimide

In order to modify the PEMAA with photo-cross-linkable maleimide side groups and investigate their reactivity during photo-cross-linking in the solid state, 3-hydroxypropyldimethylmaleimide (structure shown in figure 4.2B) was prepared in one step[193] using a three-necked flask with dropping funnel and Dean-Stark apparatus. Dimethylmaleic acid (47.5 mmol) was dissolved in tetrachloromethane (300 mL). The solution was cooled

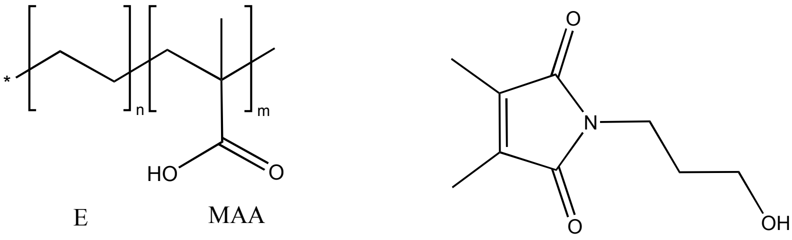

(A) (B)

Figure 4.2.: (A) Structure of PEMAA (E: ethene unit; MAA: methacrylic acid unit). (B) Structure of 3-hydroxypropyldimethylmaleimide.

to 0-5 °C and then 47.4 mmol 3-aminopropanol was slowly added dropwise to the solution. The reaction mixture was stirred for another hour at 5 °C, and then heated to reflux. Under vigorous stirring the reaction water was removed by azeotropic distillation. The reaction was deemed at an end after 8 h and the solvent was evaporated. The 3-hydroxypropyldimethylmaleimide was obtained as gold brown oil (yield 83 %). ^{1}H-NMR (500.13 MHz, $CDCl_3$): 1.76 (qui, 2H); 1.92 (s, CH_3); 2.7 (s, OH); 3.55 (t, 1H); 3.63 (t, 3H).

Synthesis of PEMAA functionalised with 3-hydroxypropyldimethylmaleimide

For functionalisation of the PEMAA, the polymer was activated in a first step with oxalyl dichloride. In a second step, the acid chloride groups on the polymer backbone were then converted with 3-hydroxypropyldimethylmaleimide (figure 4.2B) in order to yield the photo-cross-linkable polymer, as shown in figure 4.3.

The first reaction step as shown in figure 4.3 was carried out as follows. In a dry nitrogen-flushed three-necked flask with a reflux condenser and dropping funnel the polymer was dissolved in THF (10-15 wt%) completely by heating. Then the oxalyl dichloride was dissolved in THF and dropwise slowly during 45 min to the polymer solution. The reaction mixture was stirred for another 3 h at 64 °C and then cooled down to room temperature. The polymer acid chloride was concentrated with a rotary evaporator to 150 mL and the polymer residue was conserved in solution.

By varying the amount of oxalyl dichloride the number of activated groups on the polymer backbone can be controlled. Five different concentrations of oxalyl dichloride were investigated in the first step of the reaction. The amount of oxalyl dichloride and the yield obtained in the reaction are given in table 4.2.

Figure 4.4(1) shows the infrared attenuated total reflection (IR-ATR) spectrum of PEMAA. A broad signal in the region 3390 cm^{-1} - 2390 cm^{-1} (superposed on the sharp C-H vibrational bands of the CH_2 groups at 2918 cm^{-1} and 2848 cm^{-1}) can be seen, which is caused by the stretching vibration of the hydroxyl group. Further prominent bands are the C=O stretching vibration at 1695 cm^{-1} and the O-H bending vibration at 1257 cm^{-1}. Density functional theorie (DFT) calculations (B3LYP/TZVP) for 2,2-dimethylpropanoic acid, which was chosen as model system for the native PEMAA, give 3518 cm^{-1} for the O-H stretching vibration, 1730 cm^{-1} for the C=O stretching vibration and 1087 cm^{-1} for the O-H bending vibration (figure 4.4(2)). The absence of the 'free' O-H stretching vibration in the experimental spectrum and the broad band in the range 2390 - 3390 cm^{-1} point to strong hydrogen bonded OH groups. We therefore calculated the 2,2-

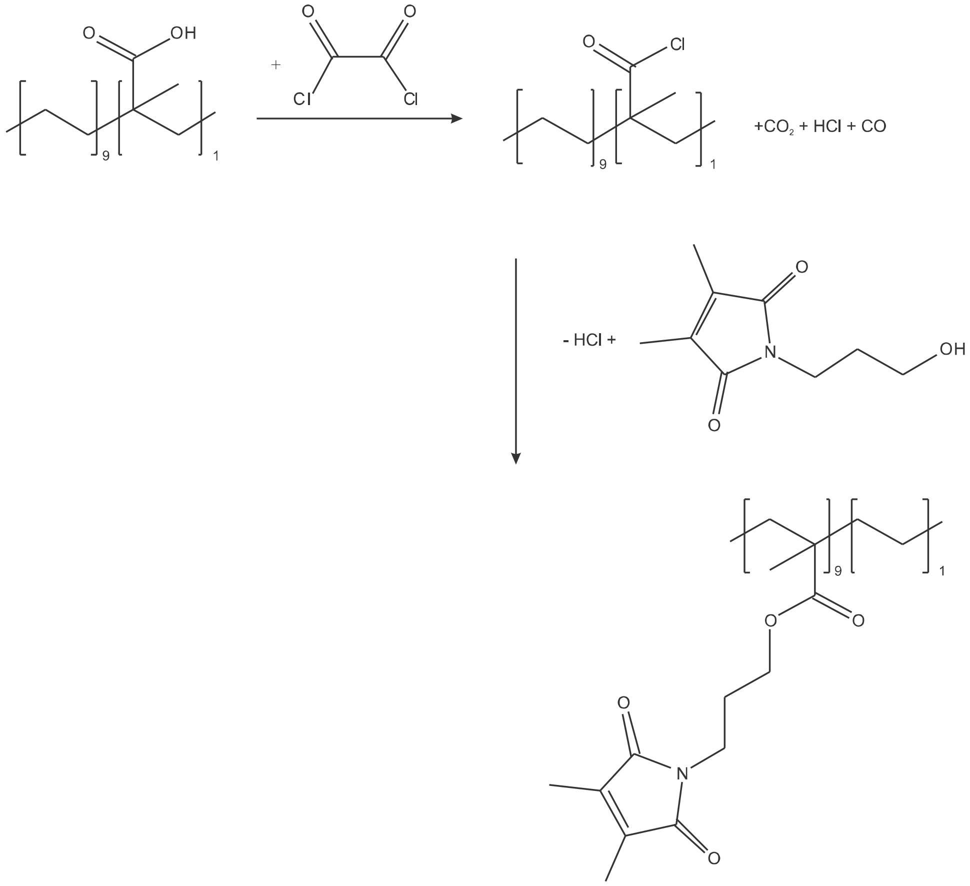

Figure 4.3.: Activation of PEMAA with oxalyl dichloride and conversion with 3-hydroxypropyldimethylmaleimide.

dimethylpropanoic acid dimer with hydrogen bonds between the carboxylic acid groups. Here the O-H stretching vibration appears at 2996 cm^{-1}, the C=O stretching vibration at 1671 cm^{-1} and the O-H bending vibration at 1276 cm^{-1} in much better agreement with experiment. Therefore it is likely that the carboxylic acid groups in PEMAA form hydrogen bonds between each other. The conversion of PEMAA to the acid chloride was followed via IR-ATR. In figure 4.5(1) the IR-ATR spectrum of the PEMAA acid chloride with a conversion yield of 48 % is shown in comparison with the spectrum of PEMAA starting material. The bands of the O-H stretching and bending vibration disappear after the conversion. The C=O stretching vibration is shifted from 1695 cm^{-1} in PEMAA to 1793 cm^{-1} in the acid chloride-modified polymer. These results are confirmed by DFT calculations of 2,2-dimethylpropanoic acid and 2,2-dimethylpropanoic acid chloride, which are shown in figure 4.5(2).

In the second step of the reaction shown in figure 4.3 the PEMAA-grafted acid chlorides were reacted with 3-hydroxypropyldimethylmaleimide as follows. The PEMAA acid chloride was slowly heated to a clear, colourless solution. Then an equivalent amount of 3-hydroxypropyldimethylmaleimide (calculated according to the amount of acid chloride groups on the polymer backbone) was dissolved in THF and added slowly dropwise to the polymer solution. The reaction mixture was stirred another for 3 h at room temperature. The solvents were then removed using a rotary evaporator at 60 °C and a vacuum of 77 mbar.

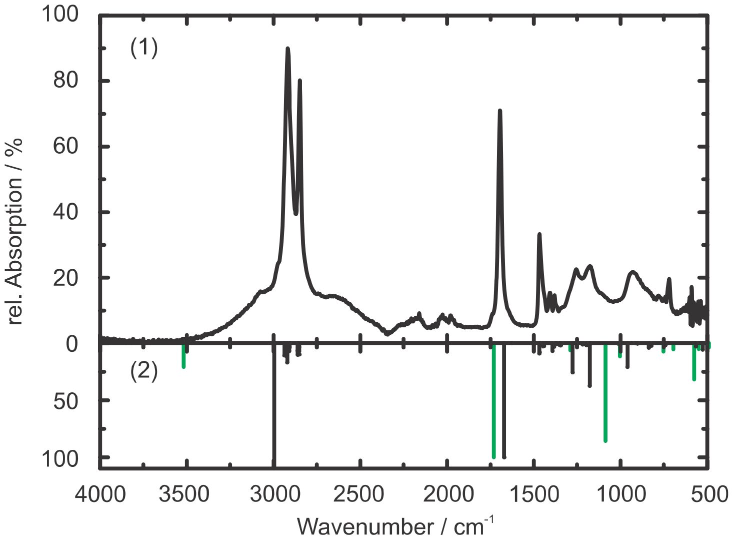

Figure 4.4: (1) IR-ATR spectrum of PEMAA. (2) Calculated IR spectra (DFT, TZVP) of the 2,2-dimethylpropanoic acid monomer as reference for the repeat unit of PEMAA (green lines) and hydrogen bonded dimer (black lines).

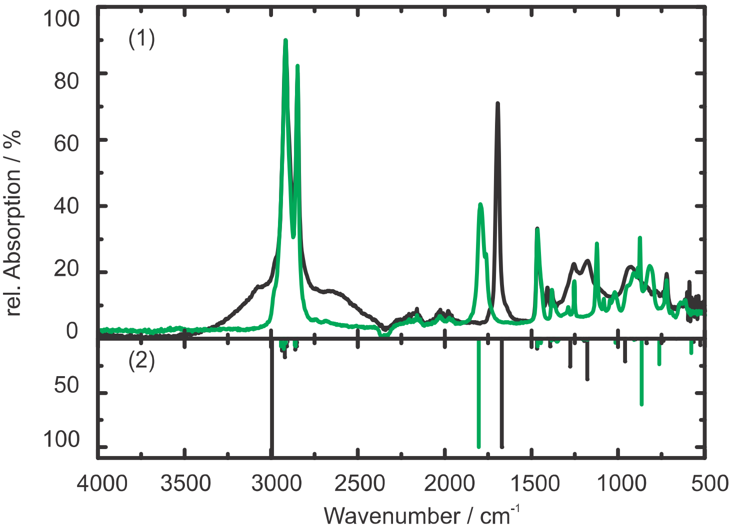

Figure 4.5: (1) IR-ATR spectrum of PEMAA (black curve) and PEMAA acid chloride with a conversion of 48 % (green curve). (2) Calculated IR bands (DFT, TZVP) of 2,2-dimethylpropanoic acid (black lines) 2,2-dimethylpropanoic acid chloride (green lines).

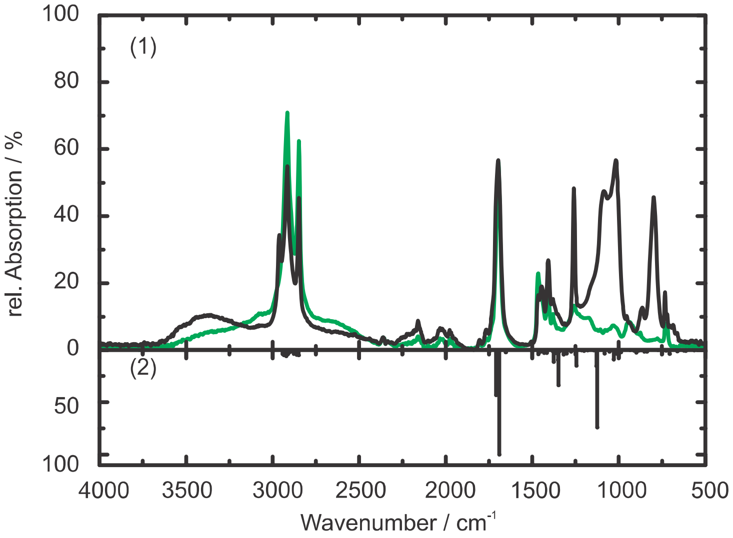

Figure 4.6: (1) IR-ATR spectrum of PEMAA esterified with 3-hydroxypropyldimethylmaleimide with a conversion rate of 2 % (green curve) and 48 % (black curve). (2) Calculated IR spectrum (DFT, TZVP) of isobutylesterpropyldimethylmaleimide.

4.1.4. Results and Discussion

PEMAA is a rubbery copolymer with a methacrylic acid content of 27.2 wt%. The melting point is 349 K. Although in previously published work a glass transition temperature (T_g) of 285 K was found (Fechtenkötter A, BASF Ludwigshafen, personal communication 2004), DSC measurements in the present work showed no T_g. PEMAA showed good film-forming properties and the films obtained were flexible. Films were obtained by coating a hot THF solution onto polyethylene foils. It has been shown that even covalently and ionically cross-linked film samples show superior mechanical properties.

While different compositions of PEMAA, e.g. with 38 wt% MAA, are available, investigations were exclusively made on a sample with 27.2 wt% MAA. The reason for this is that with higher degree of functionalisation the modified polymer tends to be insoluble so that membrane preparation was not possible. However, a 50 % esterification with 3-hydroxypropyldimethylmaleimide of PEMAA (27.2 wt% MAA) was performed in order to investigate T_g and melting point (T_m). It was observed that with increasing functionalisation, T_g decreases due to the softening effects of the maleimide groups on the polymer chains. In contrast, T_m increases with increasing functionalisation. Since the most important factor that controls T_m is the rigidity of the polymer backbone, T_m is dependent on the ease of rotation of the polymer backbone.[194] With increasing number of the ridged maleimide side groups on the polymer backbone decreases. Therefore an increasing T_m is observed with increasing number of functional groups.

It was also observed that the cross-linked PEMAA (6 % MMA modified with 3-hydroxypropyldimethylmaleimide) showed higher T_g compared to the non-cross-linked copolymer, but no melting point exists; a melting domain was observed. Similar effects have been found for cross-linked polymers that are infusible.[19]

Figure 4.6(1) shows the IR-ATR spectra of PEMAA esterified with 3-hydroxypropyldimethylmaleimide to different esterification degrees and the calculated spectrum of isobutylesterpropyldimethylmaleimide. The PEMAA with a degree of esterification of 2 % shows nearly the same IR-ATR spectrum as the starting PEMAA. At 48 % esterification, the broad OH band around 3000 cm^{-1} is smaller due to the smaller amount of unreacted carboxylic acid groups in the copolymer. Several additional bands appear in the fingerprint region. The bands at 1259 cm^{-1} and 804 cm^{-1} are caused by stretching and bending vibrations of the ester group. The broader feature in the region of 960 - 1200 cm^{-1} is formed by several vibrations of the maleimide ring. A broad band appears in the region 3070 - 3680 cm^{-1}. The calculated spectrum of isobutylesterpropyldimethylmaleimide shows no vibration with this frequency. In the IR-ATR spectrum of 3-hydroxypropyldimethylmaleimide, however, a similar band was observed. DFT calculations show an OH stretching vibration of this compound at 3597 cm^{-1}. Therefore it is assumed that some unreacted 3-hydroxypropyldimethylmaleimide is embedded in the polymer. For transient absorption measurements it is desirable to have polymers with high concentration of photo-cross-linkable groups. Unfortunately PEMAA with esterification degrees of 48 % and more does not dissolve in THF. Therefore for further mechanistic investigations of the photochemical cross-linking reaction we used PEMAA esterified with 6 %.

UV irradiation of the PEMAA copolymers functionalised with 3-hydroxypropyldimethylmaleimide was investigated in some detail. In order to appraise the potential application as membrane material, e.g. if cross-linking takes place without radical initiators, or if oxygen quenches the cross-linking, it is necessary to know more about the mechanistic details of the reaction, which is shown in figure 4.7.

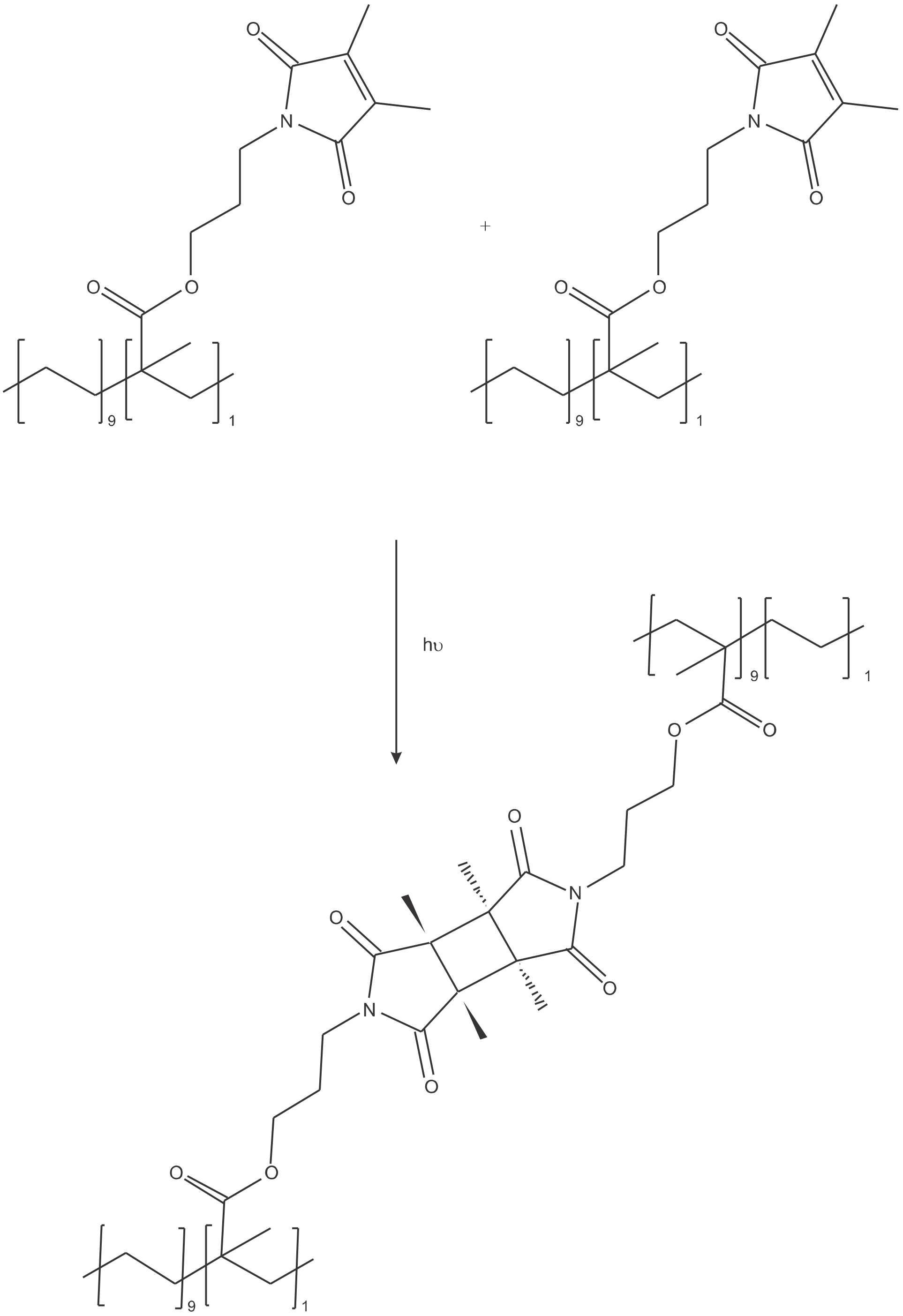

FIGURE 4.7.: Cross-linking reaction of PEMAA modified with 3-hydroxypropyldimethylmaleimide.

We first performed transient absorption measurements with maleimide-modified polymer samples in solution (50 mg dissolved in 10 mL of THF). It has been shown before[195] that *N*-alkylmaleimide shows a transient absorption maximum at around 340 nm in solution, which was assigned to triplet-triplet absorption. In figure 4.8 the time dependence of the absorption spectrum is shown for PEMAA esterified with 3-hydroxypropyldimethylmaleimide in solution.

To check if the absorption is caused by a triplet species, the time dependence of the

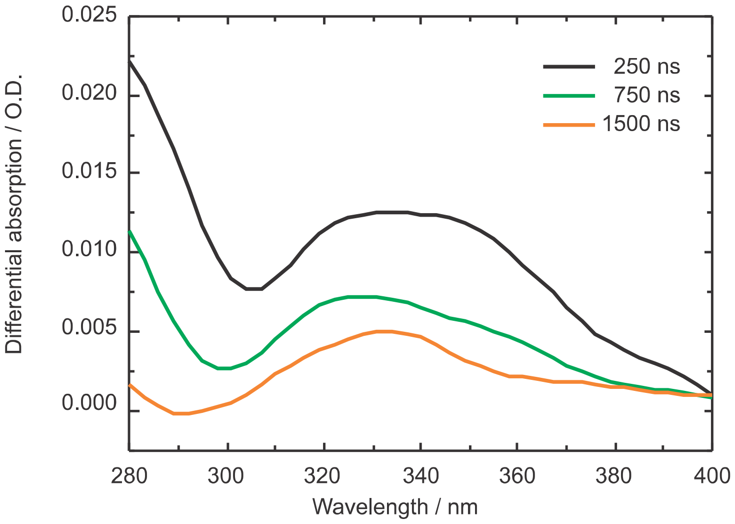

Figure 4.8: Transient absorption spectra of PEMAA esterified with 3-hydroxypropyldimethylmaleimide (esterification degree of 6 %) upon pulsed 266 nm excitation. Esterified PEMAA (50 mg) was dissolved in 10 mL of THF (spectroscopic grade) and flushed with nitrogen for 10 min. The spectra were obtained in THF solution at different times after irradiation with laser light.

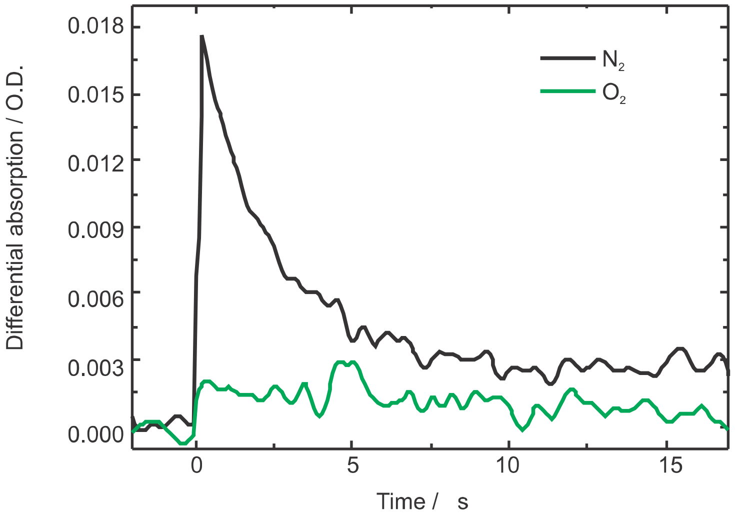

Figure 4.9: Kinetic curve of PEMAA with 3-hydroxypropyldimethylmaleimide (esterified 6 %) in THF (spectroscopic grade) at 340 nm. For the sample flushed with nitrogen for 10 min, the decay time was determined to be 2.58 ± 0.23 µs. For the sample flushed with oxygen for 10 min, no absorption was observed.

340 nm absorption was investigated with addition of oxygen or nitrogen. The results are shown in figure 4.9. The decay time of the sample flushed with nitrogen is determined to be 2.58 ± 0.23 µs. Under saturation with oxygen the absorption at 340 nm was completely quenched. An even higher absorption can be seen at 280 to 290 nm, but the maximum of the band lies beyond our measuring range. The absorption at 280 nm disappears with the same rate as the absorption at 250 nm. The microsecond lifetime in the presence of nitrogen as well as the quenching of absorption in the presence of oxygen leads to the conclusion that a maleimide triplet state is excited upon UV irradiation of maleimide-functionalised PEMAA in solution. In a second step we investigated films of maleimide-modified PEMAA. Again 3-hydroxypropyldimethylmaleimide was used to esterify the polymer. The stationary absorption spectrum of the film displayed in figure 4.10(1) shows an absorption band at 230 nm which can also be observed with pure maleimide. This absorption disappears after 20 min of irradiation with a mercury lamp and does not recover after the irradiation has been stopped. Therefore it can be assumed that photochemical cross-linking has occurred and that no monomer with typical absorption at 230 nm has remained. The cross-linked product was no longer soluble in THF. The spectrum of PEMAA without maleimide shows no absorption at 230 nm (figure 4.10(2))

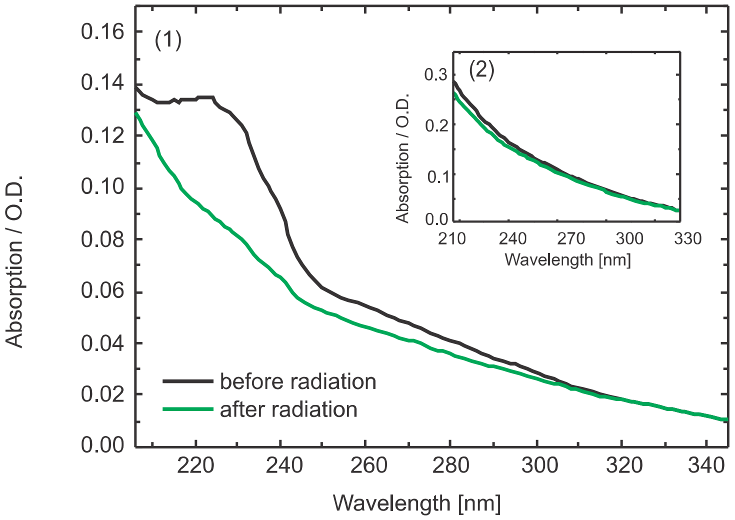

Figure 4.10: Absorption spectra of PEMAA films. (1) PEMAA with 3-hydroxypropyldimethylmaleimide (esterified 6 %). (2) PEMAA without maleimide. The spectra were obtained before and 20 min after irradiation using a mercury lamp.

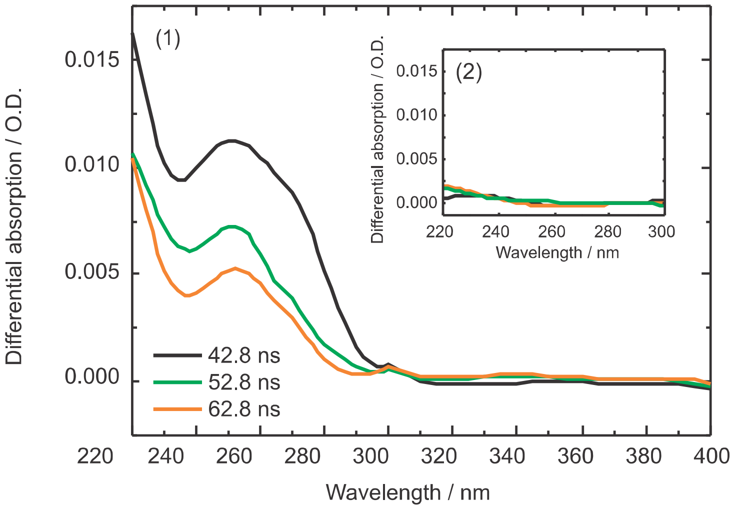

Figure 4.11: Transient absorption spectra of PEMAA films upon excitation at 266 nm. The spectra were obtained at different times after irradiation with laser light. Absorption between 264 nm and 268 nm is dominated by scattered light and therefore the measured absorption in this range is omitted from the spectral average over five data points (8 nm). (1) PEMAA with 3-hydroxypropyldimethylmaleimide (esterified 6 %). (2) PEMAA without maleimide.

and does not change after irradiation. Since there is no cross-linker present, photoreaction can not occur.

Film formation from oxygen-saturated solution and intense flushing with oxygen during irradiation did not change the photoreaction rate. Hence either product formation does not occur via the triplet state (which is quenched by oxygen as discussed above) or dimerisation of triplet maleimide is faster than oxygen diffusion in the film.

Additionally experiments were performed using maleimide in acetonitril in order to observe changes in spectral characteristics. Slight changes in absorption maxima were found for the maleimide (maximum at 216 nm) compared to 3-hydroxypropyldimethylmaleimide (230 nm). After irradiation of the maleimide, a product band at 195 nm appears. The nanosecond transient absorption spectra of a film of PEMAA esterified with 3-hydroxypropyldimethylmaleimide (6 %) are shown in figure 4.11(1). Time-dependent absorption at 250 nm is clearly discernible. The spectra of the film of PEMAA without maleimide (figure 4.11(2)) show no absorption between 220 and 500 nm. Von Sonntag and Knolle[195] observed transient absorption at 250 nm upon excitation of maleimide in *tert*-butanol

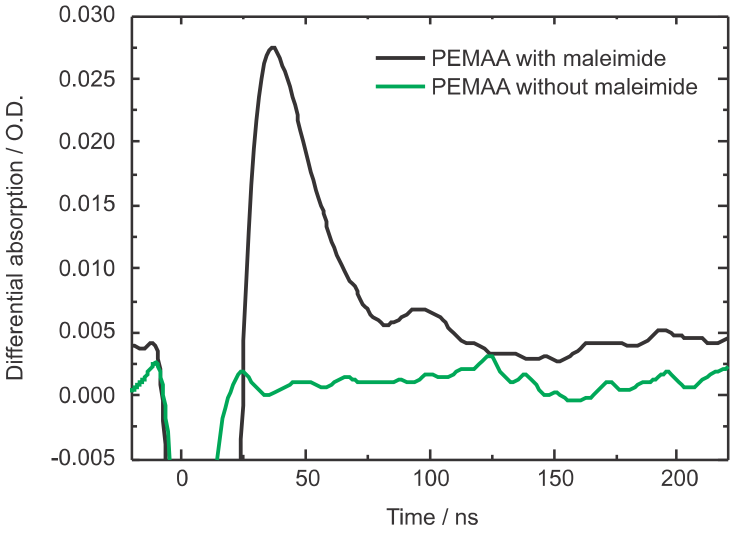

Figure 4.12: Kinetic curves of PEMAA films at 250 nm. For PEMAA with 3-hydroxypropyl-dimethylmaleimide (esterified 6 %), the decay time was determined to be 18.05 ± 0.36 ns. For PEMAA without maleimide, no absorption was observed.

solution in the presence of several thiourea reducing agents or maleimide itself as reducer. They assumed the formation of the maleimide radical anion by electron transfer via the maleimide triplet state.[196]
Time dependence of the absorption at 250 nm for PEMAA with and without maleimide esterification is shown in figure 4.12. In both kinetic curves negative absorption caused by scattered light can be seen which is greater for the film with maleimide. In accordance with figure 4.11, no change of absorption at 250 nm is observed in the film without maleimide. The absorption at 250 nm decays within 18.05 ± 0.36 ns (single exponential fit). Due to the very similar absorption wavelengths compared to the electron donor experiment in solution,[195] we assign the absorption at 250 nm in the film to the radical anion. No triplet absorption at 340 nm is discernible in figure 4.11 despite the triplet state being clearly excited in solution using the same precursor solution as for film preparation. Further measurements on maleimide showed the formation of different products after irradiation with oxygen and nitrogen. With oxygen, product absorption at 380 nm was found; with nitrogen, product absorption at 263 and 195 nm were found. However, the products were not identified. Due to the fact that with oxygen an additional product is observed, it is probable that oxygen reacts with triplet maleimide and thereby singlet oxygen is formed. The singlet oxygen then reacts with the maleimide and the product at 380 nm appears.
Based on these results we propose the photo-cross-linking mechanism shown in figure 4.13. Maleimide is excited to the triplet state and transfers an electron to maleimide in the singlet ground state. The cation and anion radicals thus formed can combine to the maleimide cyclobutane dimer.
During the course of these reactions spin reversal takes place. We assume that $k_1 >> k_2, k_{-1}$ because we have no indication of significant build-up of triplet population during photo-cross-linking (no absorption at 340 nm). Instead, considerable anion population builds up. We very tentatively assign the anion disappearance rate 1/18 ns to the dimerisation rate k_2. This assumption is only valid if electron loss via back reaction k_{-1} and/or ion recombination to hot ground-state monomers is slow compared to k_2. Otherwise 1/18 ns is just the sum of these rate constants. The fact that polymer cross-linking cannot be quenched by oxygen probably shows that dimerisation occurs faster than oxygen diffusion in the film so that oxygen cannot quench the maleimide triplet linkers. We

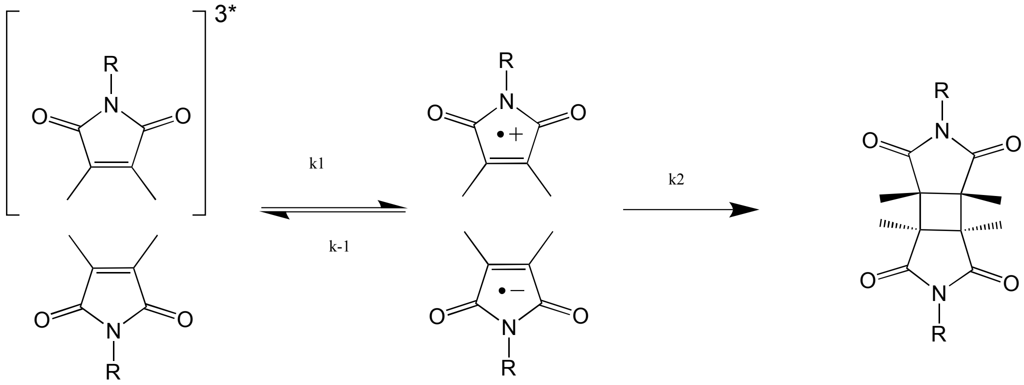

Figure 4.13.: Proposed mechanism for photo-cross-linking of PEMAA with maleimide.

cannot exclude, however, at this stage of investigation that dimerisation occurs from the singlet state and is sufficiently fast in the film to quench intersystem crossing and triplet formation. The strong anion absorption, in our experiment anyway, points to an anionic reaction mechanism for maleimide photo-cross-linking.

4.1.5. Conclusions

With the functionalisation of PEMAA with a maleimide derivative it has been shown that *in situ* cross-linking can be investigated in the liquid phase as well as in the solid phase using nanosecond transient absorption measurements. Results point to maleimide anion formation and an ionic dimerisation mechanism. Further work will be directed to investigate more quantitatively the efficiency and mechanism of maleimide photo-cross-linking. We will search for the transient absorption of the maleimide cation in solution and in the film and try to reduce contributions of scattered light to the anion absorption to more fully map out the appearance and disappearance rates of the transients. We will also try to look for product absorption signatures. Synthesis of maleimide derivatives having different structures, e.g. longer carbon chains that provide higher mobility and also phenyl substituents with different absorption maxima, will be investigated. Furthermore different polymer structures with the same maleimide side groups will be prepared and the mechanism of cross-linking investigated.

4.1.6. Acknowledgments

The authors would like to thank BASF for providing the basic polymers. This research was supported by the German Reseach Foundation SFB 663 (project A4 and B5).

4.1.7. Contributions

Title: Photo-cross-linking of poly[ethene-*stat*-(methacrylic acid)] functionalised with maleimide side groups.

Authors: Nadine Schmeling, Katharina Hunger, Gernot Engler, Benjamin Breiten, Patrick Rölling, Alexander Mixa, Claudia Staudt and Karl Kleinermanns.

Published in: Polymer International (Impact Factor: 1.902)

For this publication, all UV/Vis absorption experiments, stationary and time resolved, were performed by me. The device which enabled execution of experiments in the film, was developed by Gernot Engler. All synthesis was done by Nadine Schmeling. In close collaboration with Karl Kleinermanns I did the interpretation of the obtained spectra and kinetic information, and thus developed the mechanism of the investigated reaction. Finally, I wrote the major part of the article.

4.2. Characterization of Maleimide Dimers in Photo-Cross-Linked Copolyimide Films

KATHARINA HUNGER#, LAURA BUSCHHAUS#, NADINE SCHMELING*, CLAUDIA STAUDT*, ANNA PFEIFER# AND KARL KLEINERMANNS#

* INSTITUTE OF ORGANIC AND MACROMOLECULAR CHEMISTRY, FUNCTIONAL MATERIALS, HEINRICH-HEINE UNIVERSITY DUESSELDORF, 40225 DUESSELDORF, GERMANY

INSTITUTE OF PHYSICAL CHEMISTRY, HEINRICH-HEINE UNIVERSITY DUESSELDORF, 40225 DUESSELDORF, GERMANY

Printed in *Physical Chemistry Chemical Physics*, 14(13):4538-4547, 2012.

4.2.1. Abstract

Copolyimide membranes are established materials for the separation of gaseous and liquid mixtures. Cross-linking of the polymer strands improves the physical and chemical stability. The photo-cross-linking of a 6FDA-ODA/6FDA-DABA 4:1 copolyimide membrane containing maleimide side groups as linker was investigated by FTIR spectroscopy. IR absorption spectra of the copolyimide backbone, 3-hydroxypropyldimethylmaleimide and the copolyimide functionalized with 3-hydroxypropyldimethylmaleimide were measured before and after different irradiation times and compared to each other. For band assignment a normal mode analysis was performed. The backbone of the polymer and the maleimide linker can be well distinguished due to their different spectral band positions. Only the films containing a maleimide moiety perform a photoreaction, the polymer backbone does not interfere. Based on the difference spectra and the results of the DFT calculations it was shown that the *trans*- and the *cis*-cycloadduct as well as the previously suggested 2-2'-adduct without a cyclobutane ring are formed upon UV irradiation. Evidence for an oxetane-like photoproduct was not found. Different time constants for the increase of the product bands were observed. The cycloadduct accumulates with a shorter time constant (τ = 2 to 5 min) than the 2-2'-adduct (τ = 75 min). The yield of the photo-cross-linking reaction was determined by spectral deconvolution and kinetic fitting of several marker bands. For the copolyimide synthesized in this work, a maximum value of 6 % was reached. The stiffness of the copolyimide backbone inhibits further photo-cross-linking.

4.2.2. Introduction

In recent decades polymers gained importance for membrane-based separation processes especially for gaseous and liquid mixtures[2] since the costs for purification of industrially relevant chemicals as benzene is drastically lower compared to high energy consumptive conventional separation processes, e.g. extractive distillation. The theory of membrane-based separation of aromatics/aliphatics using pervaporation is described in detail elsewhere.[29] Polyimides are well suited as membrane materials due to their stability over a wide temperature range and resistance against most organic solvents. However, several drawbacks are occurring in applications, where severe conditions of pressure or aggressive components in the mixture are present. In these cases, e.g. CO_2-induced plasticization, physical ageing and strong swelling effects appear.[197] As a result, a dramatic loss in the separation performance is observed. The lack of stability for polymeric membrane materials can be avoided if cross-links in the polymer backbone are implemented.[29;198] Different approaches are possible for obtaining cross-linked materials. If suitable functional groups, e.g. benzophenone, are present in the polymer backbone, cross-linking can be performed by UV irradiation via a radical reaction.[199] However, in this case the packing density of the polymer is reduced drastically which is undesirable. Another approach is to start with polymers having a specific number of functional groups, e.g. hydroxyl, amino, carboxyl groups, *etc.*, on the polymer backbone, which can be used for further polymer-analogous reactions. These polymers can be cross-linked either covalently[184;190] or ionically[200]. Since polyimides e.g. Upilex (UBE), P84 (Evonik) and Kapton (Du Pont) copolyimides have been established as advanced membrane material on the market, a lot of research activities were performed to reach cross-linked copolyimides with a high stability and outstanding separation properties. As basic materials functional copolyimides are used and cross-linking has been performed chemically as well as ionically.[29;197;201–203]

A different approach is the cross-linking by light. In a first approach polyimides were cross-linked by UV irradiation using benzophenone as linker.[204–206] One of the major advantages of photo-cross-linking is that the reaction does not need a catalyst. The problem of washing out reaction residues during the separation process does not occur. The procedure of cross-linking is easy to perform with a UV lamp and up-scaling for the production of large membrane areas is possible. First approaches for photo-cross-linking of polymer films have been done using maleimide side groups as photo-linker.[192;207–211] It is known that maleimide performs a [2+2] cycloaddition upon irradiation with UV light.[212] Seiffert *et al.* found evidence for a second dimerization product in aqueous solutions.[213] The structure of this asymmetric product was confirmed by X-Ray analysis.[214] In contrast to the cycloaddition reaction, a cyclobutane ring is not generated.

A covalent bond between the carbons in position 2 and 2' (see figure 4.19) in both maleimide rings is formed instead. On account of this structure the second photoproduct is called 2-2'-adduct. Maleimide functionalized polymers are commonly used as negative photoresists.[215] First investigations of the light-induced cross-linking in polymer films for production of pervaporation membranes used poly[ethane-*stat*-[methacrylic acid)] functionalized with maleimide side groups.[20] It was found that UV irradiation leads to the formation of the maleimide triplet state. An electron transfer from a triplet maleimide to an adjacent ground state moiety follows. The radical anion and radical cation then recombine to form the cycloadduct.[20] The kinetic investigation in the nanosecond to microsecond time range was performed by UV/Vis transient absorption spectroscopy. In the investigated sample maleimide was the only chromophore absorbing in the UV.

In this work we combined the photo-cross-linking using maleimide side groups with an established class of membrane materials. The following monomers were used: 4,4'-hexafluoroisopropylidene diphthalic anhydride (6FDA) and 4,4'-diaminodiphenyl ether (ODA). In order to obtain a copolyimide with functional groups, the monomer ODA and 3,5-diamino benzoic acid (DABA) was used in the polymerization reaction in a ratio of 4:1. Thereby a copolyimide with carboxyl groups was produced with a statistical distribution of the functional groups. The repeating units of 6FDA-ODA to 6FDA-DABA were adjusted to 4:1. The carboxylic acid groups of the DABA subunits were functionalized with 3-hydroxypropyldimethylmaleimide as photo-cross-linker. The distance between two maleimide moieties has a distinct influence on the degree of cross-linking. The amount of cross-links between the polymer chains affects stability and permeability of the membrane material and is therefore an important property. Controlling the degree of cross-linking is highly desired since it is very important that membrane materials can be manufactured reproducibly. In the case of photo-cross-linking, the cross-linking yield can be adjusted by the duration and intensity of UV irradiation. Generally it can be examined by the determination of gel fractions,[216] weight ratios,[217] rheology,[213;218] swelling properties,[219] or spectroscopy.[192;203;207;210;213;220]

A major advantage of spectroscopic methods is that the sample can be investigated noninvasively and in real time. Furthermore, it provides structural information of the sample. Transient absorption spectroscopy in the UV/Vis region is not applicable with this copolyimide due to the fact that absorption from the maleimide cross-linker and from the phthalimide moiety of the polymer backbone cannot be distinguished. Fourier transform infrared (FTIR) spectroscopy provides structural information and is well suited to follow chemical reactions. FTIR difference spectroscopy can be applied for the detection of photoproducts with minor yields. By using this technique only bands arising from vibrations which change during the monitored reaction appear in the spectrum. Vibrations that were not altered are not present. By this means small changes can be isolated from the strong background absorption in the IR. The sensitivity allows for monitoring changes of the initial IR absorption of 0.1 %. In this study, we established a noninvasive method for a quantitative analysis of the degree of cross-linking in a maleimide functionalized copolyimide membrane.

4.2.3. Materials and Methods

Synthesis and sample preparation

Polyimides were synthesized according to Sroog *et al.*[24] In this work the following monomers were used for the formation of a copolyimide: 6FDA (4,4'-hexafluoroisopropylidene diphthalic anhydride), ODA (4,4'-diaminodiphenyl ether), DABA (3,5 diamino benzoic acid) in DMAc (dimethyl acetamide) as solvent. The polyaddition was performed in a 500 mL flask with a reflux condenser and a septum under nitrogen atmosphere. First the diamines 0.5607 g (2.8 mmol) ODA and 0.1065 g (0.7 mmol) DABA were dissolved in 2.91 mL of DMAc at room temperature. After complete dissolvation of the diamines, 1.5549 g (3.5 mmol) 6FDA and 3.5 mL DMAc were added to the mixture which was then stirred for 24 hours. Afterwards 5.85 mL DMAc was added to the highly viscous solution. For performing the imidization, a mixture of 1.072 g (10.5 mmol) acetic anhydride and 1.062 g (10.5 mmol) triethylamine was added and the solution stirred for 30 minutes at 120 °C. After cooling down to room temperature the solution was poured into a 1:1 mixture of water/ethanol for precipitation. The formed fibres were washed several times with ethanol and sheared with a polymer mill to a yellow powder. The powder was dried at room temperature over night and then dried further in vacuum at 150 °C and 89 mbar for 24 hours. The yield was 1.7 g (0.57 mmol, relative yield 81 %). The stoichiometric ratio between ODA and DABA in the copolyimide was determined *via* ^{1}H and ^{13}C NMR spectra recorded in tetrahydrofurane (d$_8$). The obtained ratio of ODA:DABA was 4:1. The functionalization of the synthesized polymer was performed

by the activation of the carboxylic acid groups *via* acid chloride formation and esterification with 3-hydroxypropyldimethylmaleimide in tetrahydrofurane. This is described in detail with poly[ethene-*stat*-(methacrylic acid)] as copolymer.[20] The esterification was performed with the synthesized copolyimide at room temperature.
For the FTIR measurements the polymer dissolved in tetrahydrofurane was spread on a NaCl window (International Crystal Laboratories, Garfield, USA) by spin coating and dried at room temperature overnight. The film thickness was determined with a micrometre calliper to be 15 µm. Films made from the copolyimide without the esterification step and of 3-hydroxypropyldimethylmaleimide were prepared analogously.

FTIR spectroscopy

We performed FTIR spectroscopy using a Vertex 80V spectrometer (Bruker, Ettlingen, Germany) with a MCT detector. All samples were measured in transmission mode in vacuum (2.5 mbar) and at room temperature. 2048 scans in the forward-backward mode were averaged for each spectrum with a spectral resolution of 2 $\mathrm{cm^{-1}}$. A broadband interference filter (Bruker, 4000 - 900 $\mathrm{cm^{-1}}$) in front of the detector was used which efficiently blocked stray light. The photo-cross-linking was induced by the fourth harmonic of a Nd:YAG laser (INDI, Spectra Physics, Darmstadt, Germany) at 266 nm with a pulse width of 10 ns and a repetition rate of 10 Hz. The excitation energy was adjusted to 6 $\mathrm{mJ/cm^2}$. Light-induced FTIR difference spectra were obtained by calculating the negative common logarithm of the ratio of the single channel spectra before and after illumination. These light-minus-dark IR difference spectra were recorded at several positions on the same film and reproduced with different films.

DFT calculations

Geometry optimizations and harmonic frequency calculations were performed at the B3LYP / TZVP level of theory using the Turbomole program package.[158–161] Calculated harmonic vibrational frequencies were scaled by 0.971 in order to match the experimental C=O stretching vibrations of the 3-hydroxypropyldimethylmaleimide modified copolyimide.

4.2.4. Results

The three following samples were investigated with FTIR spectroscopy and compared: 6FDA-ODA/6FDA-DABA 4:1 copolyimide functionalized with 3-hydroxypropyldimethylmaleimide as cross-linker (*copolyimide with MI*), 6FDA-ODA/6FDA-DABA 4:1 copolyimide without the maleimide linker (*copolyimide without MI*) and 3-hydroxypropyldimethylmaleimide without the polymer (*MIOH*) (figure 4.14).

Absorbance spectra

The IR absorbance spectrum of the copolyimide with MI (figure 4.15) shows multiple bands in the region of 1800 - 1000 $\mathrm{cm^{-1}}$. For band assignment, spectra of the MIOH film and the copolyimide without MI were measured under the same conditions in vacuum. In order to correct for the different thicknesses of the films the spectra were scaled to marker bands. For the polymer backbone these were absorptions at 1502 and 1244 $\mathrm{cm^{-1}}$

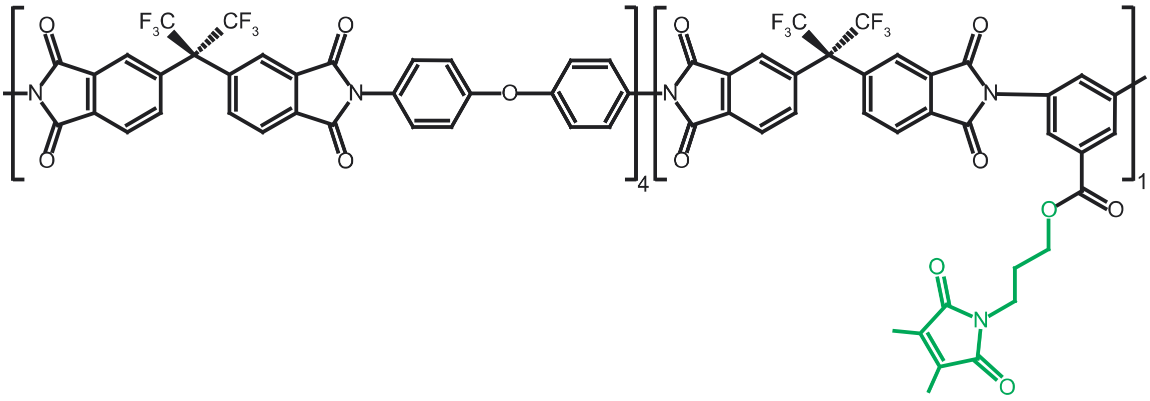

Figure 4.14.: Chemical structure of 6FDA-ODA/6FDA-DABA 4:1 copolyimide functionalized with 3-hydroxypropyldimethylmaleimide. Depicted in green is the maleimide side group.

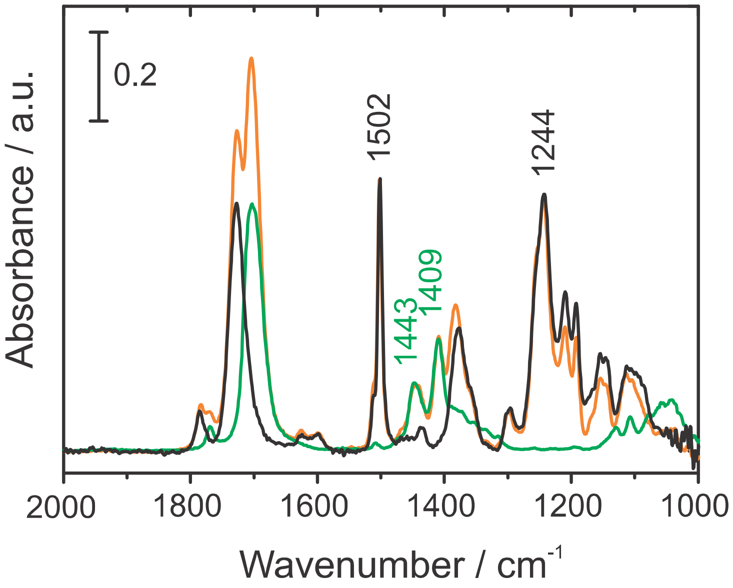

Figure 4.15: FTIR absorbance spectra of 3-hydroxypropyldimethylmaleimide (green), 6FDA-ODA/6FDA-DABA 4:1 copolyimide (black) and the copolyimide with 3-hydroxypropyldimethylmaleimide (orange). All samples were prepared as films.

and for the maleimide at 1443 and 1409 cm^{-1}.[2] The sum of the spectrum of the copolyimide without MI and the spectrum of MIOH reproduces the absorbance spectrum of the copolyimide with MI very well. The comparison of the absorbance spectra shows that the backbone of the polymer and the maleimide linker can be well distinguished due to their different spectral band positions.

In order to assign the band pattern of the polymer, a normal mode analysis was performed (figure 4.16). Since the whole copolyimide unity is very large, only subunits were calculated to save calculation time. As model compounds 3-hydroxypropyldimethylmaleimide (MIOH), *N*-methyl phthalimide (PHI), benzoic acid propylester (BAPE), diphenyl ether (DPE) and 2,2-bis-trifluoromethyl propane (TFMP) were used (figure 4.17).

The most interesting bands in terms of photo-cross-linking arise from carbonyl stretching vibrations in the region between 1800 and 1700 cm^{-1}. An overview of the assigned bands is given in table 4.3. The MIOH and the PHI subunits comprise two carbonyl groups each. The calculations reveal also two carbonyl normal modes for both molecules. The normal mode at higher wavenumbers represents the vibration of the carbonyl groups in phase. Approximately 50 cm^{-1} red shifted a vibration is calculated in which the two

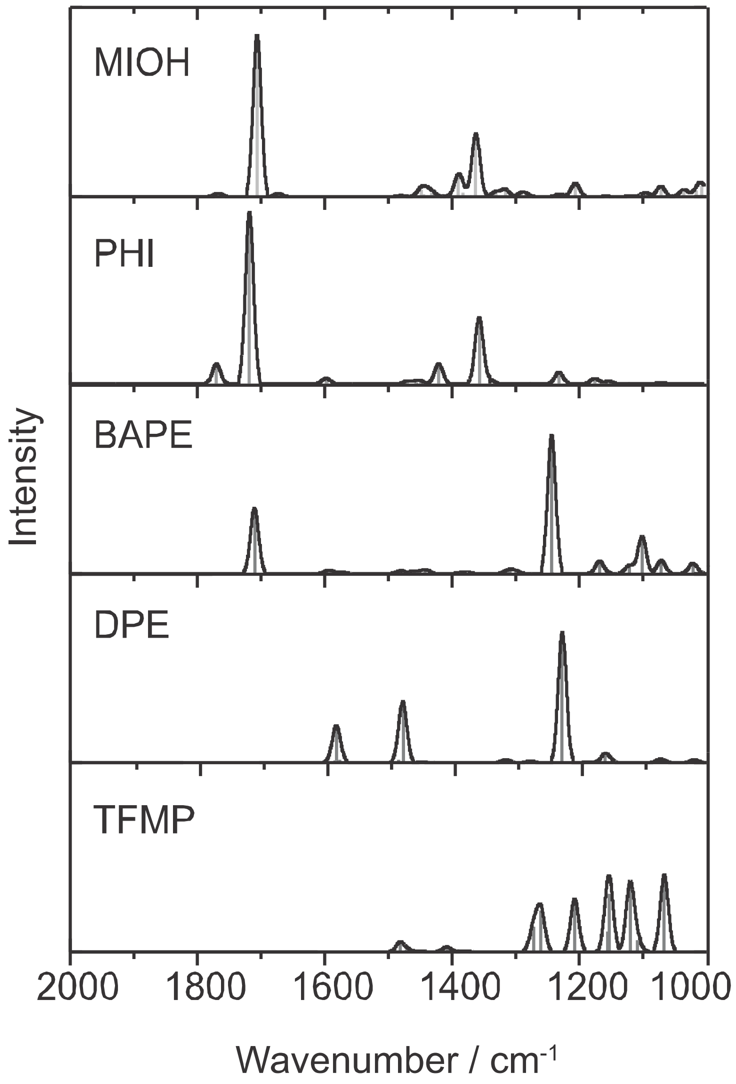

Figure 4.16: Calculated IR bands (grey) and spectra with line broadening (Gaussian function, $\omega = 15\ \mathrm{cm}^{-1}$, black).

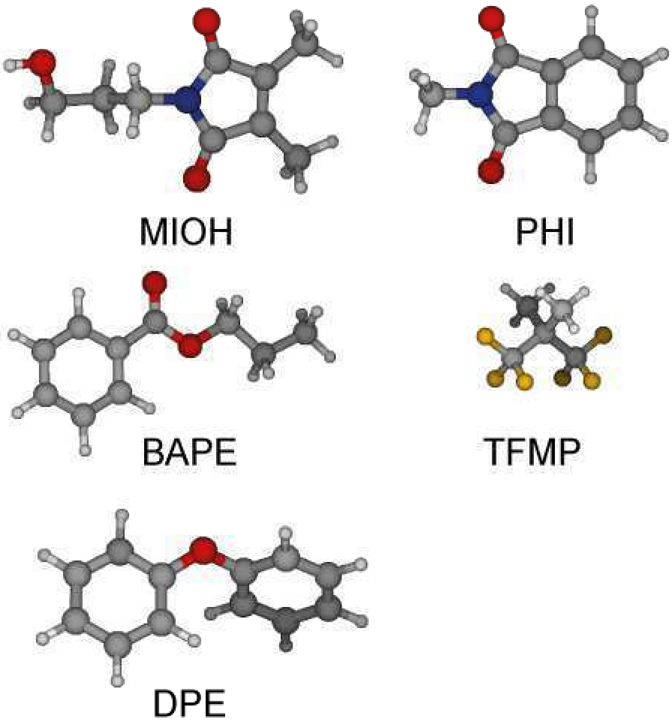

Figure 4.17: Chemical structures of the calculated subunits of the copolyimide polymer: 3-hydroxypropyldimethylmaleimide (MIOH), *N*-methyl phthalimide (PHI), benzoic acid propylester (BAPE), 2,2 bistrifluoromethyl propane (TFMP) and diphenyl ether (DPE). White: hydrogen, grey: carbon, red: oxygen, yellow: fluorine, blue: nitrogen.

Table 4.3.: Vibrational bands of the copolyimide with MI.

spectral position experiment (cm^{-1})	spectral position calculation (cm^{-1})	vibrational assignment
1784	1771.3	PHI, C=O symmetric stretch
1770	1768.5	MIOH, C=O symmetric stretch
1727	1719.1	PHI, C=O antisymmetric stretch
1707	1711.2	BAPE, C=O stretch (ester)
1704	1706.9	MIOH, C=O antisymmetric stretch
1625	1597.6	PHI, C=C stretch, ring
1600	1587.5	DPE, C=C stretch, ring
1502	1476.3	DPE, C=C stretch, C-H bend, ring
1443	1389.0	MIOH, C-N stretch, chain
1409	1361.2	MIOH, C-N stretch, ring
1382	1356.2	PHI, C-N stretch
1298	1270.0	TFMP, C-F stretch
1244	1241.7	BAPE, C-O stretch
1210	1224.0	DPE, C-O-C antisymmetric stretch
1192	1205.4	TFMP, CF3 stretch
1154	1150.5	TFMP, CF3 stretch
1114	1117.7	TFMP, CF3 stretch

carbonyl groups move with opposite phase. The change of the net dipole moment of the opposite phase vibration exceeds the change during the symmetric in phase vibration. Hence, the extinction coefficient of the opposite phase C=O stretching vibration is much more intense than the combination with two in phase C=O stretching elongations. This is the case in the MIOH as well in the PHI subunit. In the carbonyl stretching region of the calculated spectra, the PHI bands are red shifted by 3 to 12 cm^{-1} compared to the MIOH bands. This is consistent with the experimental data where similar red shifts of 14 to 24 cm^{-1} were observed. In the absorbance spectrum of the 3-hydroxypropyldimethylmaleimide film, the bands at 1770 and 1704 cm^{-1} were assigned to the in phase and opposite phase carbonyl stretching combinations of MIOH (figure 4.15, dark grey curve). The corresponding C=O bands of the phthalimide moiety in the polymer backbone can be identified in the spectrum of the copolyimide without MI film at 1784 and 1727 cm^{-1} (figure 4.15, black curve). The carbonyl vibration of the ester group in the BAPE subunit shows up at 1711 cm^{-1} in the calculation and at 1707 cm^{-1} in the experiment. Due to the small difference in their band positions, the PHI, BAPE and MIOH carbonyl stretching bands overlap in the absorbance spectrum of the copolyimide with MI film (figure 4.15, light grey curve).

In the lower wavenumber region the band assignment becomes more complex because the vibrations are not isolated anymore. The intense absorption band at 1502 cm^{-1} (figure 4.15) from the polymer backbone can be explained by a vibration with contributions of the carbon atoms in the phenyl rings and a bending of C-H in the diphenyl ether group. At 1443 and 1409 cm^{-1} the maleimide subunit has prominent absorption bands. The

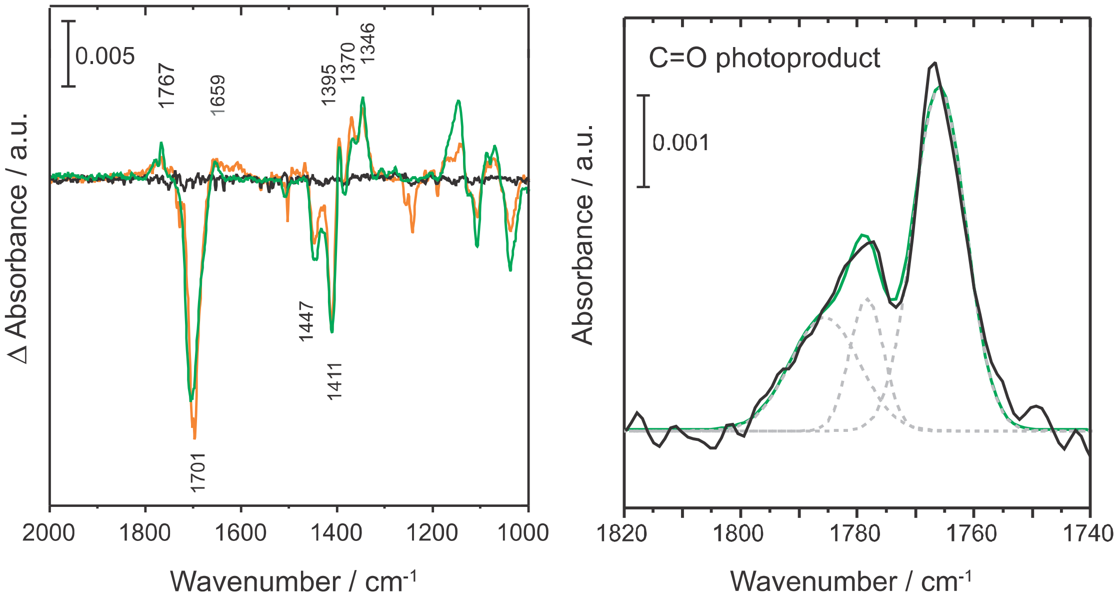

(A) (B)

Figure 4.18.: (A) Laser-induced FTIR difference spectra of 3-hydroxypropyldimethylmaleimide (green), 6FDA–ODA/6FDA–DABA 4:1 copolyimide (black) and the copolyimide with 3-hydroxypropyldimethylmaleimide (orange). (B) Difference spectrum of 3-hydroxypropyldimethylmaleimide (black) in the carbonyl region. The positive feature can be reproduced by the sum of three Gauss curves (green).

calculation reveals stretching vibrations of the C-N bond of the propyl chain and of the C-N bonds in the ring at 1389 and 1361 cm^{-1}, respectively. These vibrations were assigned to absorption bands in the spectrum of the 3-hydroxypropyldimethylmaleimide film. Below 1400 cm^{-1} bending and torsion vibrations of the trifluoromethane groups in the copolyimide backbone dominate the spectrum.

Photo-cross-linking

All three films were illuminated by a pulsed laser. Behind the 15 μm thick films the laser energy was determined to be 0.6 mJ cm^{-2}, i.e. 10 % of the initial laser energy. Therefore it is safe to assume that the area of excitation extends over the whole thickness of the film, but is not completely homogeneous. In the maleimide containing films, the irradiation is expected to induce the cross-linking of the maleimide side chains. The copolyimide without MI is used as reference. The light-induced difference spectrum of the copolyimide with MI resembles the spectrum of the film with only 3-hydroxypropyldimethylmaleimide present (figure 4.18a). This provides evidence that only the maleimide moiety takes part in the photoreaction. The spectrum of the copolyimide without MI does not exhibit any light-induced difference bands. Without the maleimide cross-linker a photoreaction does not occur. The positions of the negative peaks correspond to absorbance bands of the maleimide in the dark which are reduced upon irradiation.

The most prominent band at 1701 cm^{-1} results from the opposite phase combination of the carbonyl stretching vibration in the maleimide monomer. A negative band in the region of the weaker in phase stretching combination was not observed. The bands at 1447 and 1411 cm^{-1} were assigned to C-N stretching vibrations of maleimide. In the absorbance

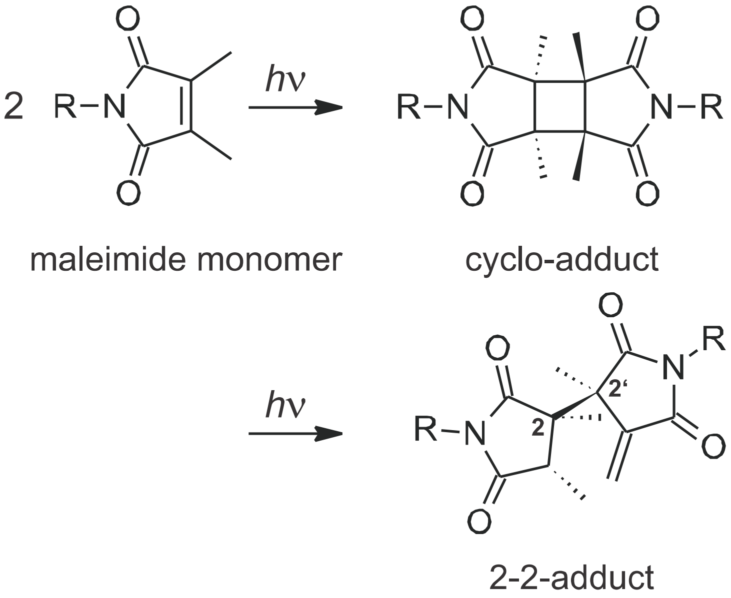

Figure 4.19: Scheme of the dimerization of dimethyl maleimide under UV light to the cycloadduct and the 2-2'-adduct.[214]

spectrum of the polymer maleimide bands overlap with bands from the copolyimide. As a consequence, the band maxima are shifted. Copolyimide bands do not contribute to the light-induced difference spectrum. Therefore the band positions of the negative peaks represent the unshifted positions of the maleimide monomer. Positive bands show those vibrations of the maleimide photoproduct, which exhibit different frequencies than the educts. Maleimide is known to form dimers *via* a [2+2] cycloaddition (figure 4.19).
Therefore, the positive band pattern should contain bands from this cycloadduct. It can be expected that the stretching vibration of the C=C double bond in the maleimide monomer vanishes upon formation of the cyclobutane ring.
Unfortunately, this vibration absorbs very weakly in the IR. However, a positive feature was detected in the region of the in phase stretching vibration of the carbonyl groups at 1767 cm^{-1}. The difference spectrum of the copolyimide with MI shows the same pattern as the difference spectrum of MIOH alone. Due to a better signal-to-noise ratio the positive band of the MIOH sample was further analyzed. A detailed view of this spectral region (figure 4.18b) shows two bands at 1777 and 1767 cm^{-1}. A sum of three Gaussian functions was needed to reproduce the band pattern. This hints at a contribution of three different carbonyl vibrations upon illumination. At lower wavenumbers a broad absorption with a maximum at 1659 cm^{-1} appears. In this region the unlinked film does not absorb. The most prominent photoproduct bands show up at 1395, 1370 and 1346 cm^{-1}. For a better assignment of the difference bands, the IR spectra of the cycloadduct in *cis*- and *trans*-configuration were simulated by DFT calculations (figure 4.23). Additionally, a third possible dimer structure, the 2-2'-adduct,[214] was calculated (figure 4.19). In order to compare the calculated spectra with the measured light-minus-dark difference spectra, difference spectra were simulated by subtraction of the maleimide monomer (MIOH) absorbance spectrum calculated with doubled intensity from the calculated adduct spectrum. By this means, the number of oscillating carbonyls was kept constant during the simulated reaction. The intensities were not normalized but used with their calculated oscillator strengths. Thus, changes of the extinction coefficient of altered vibrations are taken into account. The resulting simulated difference spectra show similar band patterns (figure 4.20). The only significant difference is the additional band at 1652 cm^{-1} from the stretching vibration of the terminal C=C double bond in the

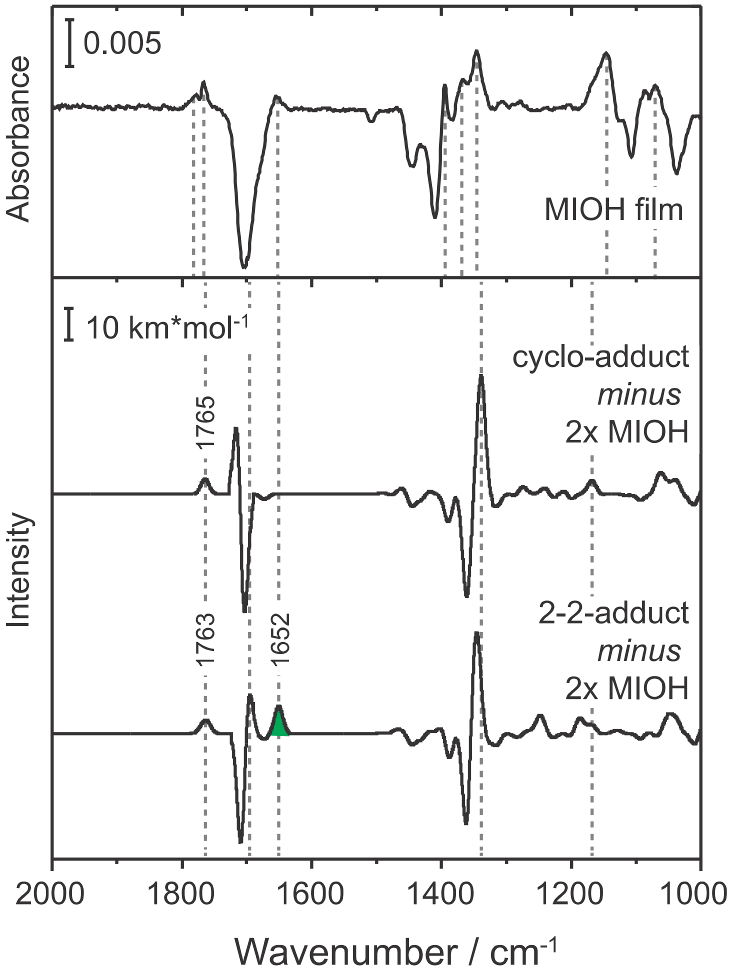

Figure 4.20: Laser-induced FTIR difference spectra of 3-hydroxypropyldimethylmaleimide (upper trace), the calculated difference spectrum of the cycloadduct minus two times the calculated absorbance spectrum of 3-hydroxypropyldimethylmaleimide (middle trace) and the calculated difference spectrum of the 2-2'-adduct minus two times the calculated absorbance spectrum of 3-hydroxypropyldimethylmaleimide (lower trace). The marker band of the 2-2'-adduct at 1652 cm^{-1} is highlighted in green.

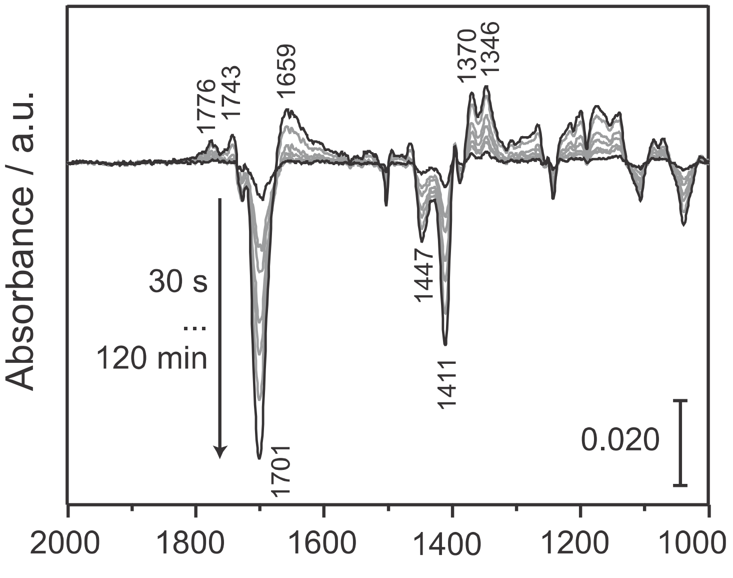

Figure 4.21: Laser-induced FTIR difference spectra of 6FDA–ODA /6FDA–DABA 4:1 copolyimide functionalized with 3-hydroxypropyldimethylmaleimide after different illumination times. The first spectrum (30 s) is marked in black. The following spectra after 2, 4, 10, 20 and 60 min are depicted in grey and the last spectrum (120 min) of illumination is again marked in black. With longer UV illumination the difference bands become more intense.

2-2'-adduct. Therefore, this band serves as marker band for this adduct species. The calculated difference spectrum of the cycloadduct does not show a band in this spectral region. In the measured difference spectrum of the MIOH film and in the spectrum of the copolyimide with MI a band at 1659 cm^{-1} is present. This fact points to a contribution of the 2-2'-adduct to the cross-linked dimers after UV-illumination. Additional evidence for more than one photoproduct is provided by the positive carbonyl band with at least two contributions. Each of the two different photoadducts exhibits a band from the carbonyl symmetric stretching combination that differs by 2 cm^{-1}. The measured band pattern can be explained by a mixture of both adducts. The same situation appears in the area of the C-N stretching vibrations. In both adducts they are shifted to lower wavenumbers and display one intense band. The measured difference spectrum shows at least three prominent positive bands in this region. The comparison of the measured and calculated difference spectra lead to the conclusion that the cycloadduct and the 2-2'-adduct are formed in the film of 6FDA-ODA/6FDA-DABA 4:1 copolyimide functionalized with 3-hydroxypropyldimethylmaleimide under UV illumination.

Degree of cross-linking

The photo-cross-linking of the copolyimide film *via* the maleimide side chains was monitored at different illumination times from 30 s to 120 min (figure 4.21). The longer the sample was irradiated, the more intense the difference bands became. Saturation could only be observed for the positive bands. The negative band intensities increase with further illumination while the positive bands did not change any more after 120 min illumination. During the photoreaction most vibrations of the maleimide monomer are shifted upon dimerization due to the structural change. It is expected that the monomer bands decrease roughly to the same extent as the dimer bands appear. If the negative bands continue to increase and the positive bands do not change their intensity, a disappearance of the sample vibrations due to photodamage is likely. After 120 min of laser irradiation the copolyimide film showed brown spots. This implies that we did not only observe the photo-induced cross-linking but also a degradation process of the polymer backbone.

The kinetics of the difference bands were analyzed by exponential fitting (figure 4.22). For the negative bands a biexponential fit ($\tau_1 = 5$ min and $\tau_1 > 120$ min) was necessary. The slower process with $\tau_2 > 120$ min is assigned to photodamage and the faster process with $\tau_1 = 5$ min to the decrease of the concentration of monomeric maleimide due to the cross-linking. With a similar early time constant $\tau_1 = 3$ min the increase of the photoproduct bands below 1600 cm^{-1} can be fitted. A second time constant for product formation was determined to $\tau_2 = 40$ min. The product bands above 1600 cm^{-1}, where the carbonyl and C=C double bond stretching vibrations absorb, could well be described by a monoexponential curve with $\tau = 75$ min. The different behavior of the positive bands under prolonged irradiation hints at a secondary photochemical pathway or to contributions of several photoproducts with different rate constants for their formation. The band at 1659 cm^{-1}, which is a marker band for the 2-2'-adduct, can be reproduced by a monoexponential curve with $\tau = 75$ min. This leads to the conclusion that this adduct species plays a role at longer irradiation times. For a more precise analysis, the photoreaction should be followed by a pump-probe experiment in real time.

For analysis of the yield of cross-linking the amount of maleimide moieties which perform the photoreaction in the copolyimide film is determined. Thereby it is assumed that only

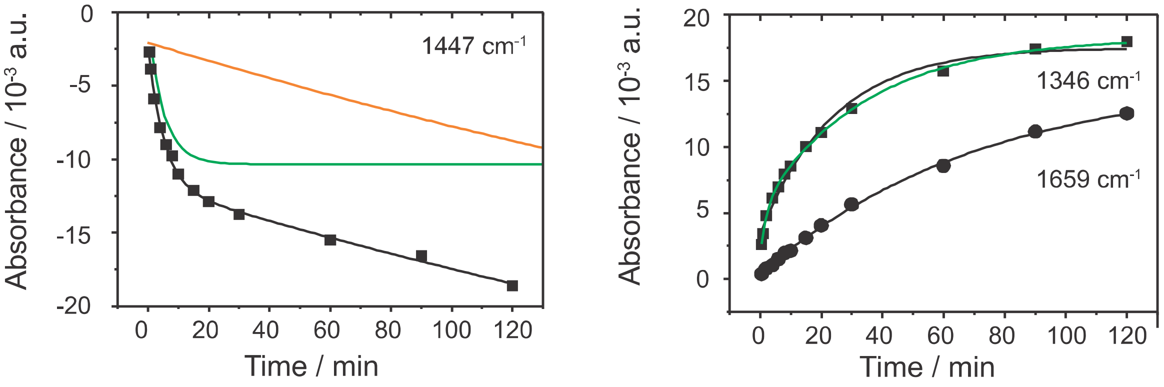

(a)

(b)

Figure 4.22.: (a) Kinetic trace of the negative band at 1447 cm^{-1} that represents a C–N stretching vibration of the maleimide monomer (black squares). The biexponential fit with $\tau_1 = 5$ min and $\tau_2 > 120$ min is shown in black. The colored curves illustrate exponential functions with $\tau = 5$ min (green) and $\tau\ 2 > 120$ min (orange). The former was used to evaluate the amount of maleimide that undergoes the photoreaction and was not photodegraded. (b) Kinetic traces of the positive bands at 1659 and 1346 cm^{-1} which originate from the vibration of the terminal C=C stretching of the 2-2'-adduct and a C–N vibration from the cycloadduct, respectively. The monoexponential fits are shown in black and the biexponential fit is drawn in green.

maleimide side chains that react with $\tau_1 = 5$ min contribute to adduct formation. In order to avoid contributions from overlapping product bands, the region between 1450 and 1400 cm^{-1} is used for the quantitative analysis. The photoadduct bands are red shifted by more than 40 cm^{-1} compared to the monomer bands in this spectral range. Monoexponential curves with the time constant $\tau_1 = 5$ min and the amplitude A_1 derived from the biexponential fit of the negative bands at 1447 cm^{-1} and 1411 cm^{-1} have a maximum difference absorbance of $\Delta A = 0.010$ and $\Delta A = 0.018$, respectively (figure 4.22a). The initial absorption A is derived from the absorbance spectrum of the copolyimide with MI, which was deconvoluted by fitting Gauss curves (see S1). At 1447 cm^{-1} and 1411 cm^{-1} the contribution to the absorption is $A = 0.16$ and $A = 0.28$. The relative cross-link yield $\Delta A/A$ is thus determined to be 6.4 % for both bands. The major part of the maleimide side chains therefore did not cross-link.

4.2.5. Discussion

Carbonyl stretching vibrations

The light-induced difference spectrum of the MIOH film as well as the spectrum of the copolyimide with MI shows a strong negative band at 1701 cm^{-1} and 1699 cm^{-1}, respectively, which corresponds to the C=O stretching vibration in the maleimide ring with opposite phase of the C=O elongations. Obviously, this band is altered upon UV illumination. Since the C=O double bond is not destroyed upon photoreaction, its stretching vibration is expected to be present among the positive bands.

A corresponding positive band is however not observed in the characteristic carbonyl region. There are three possible explanations. First, the bond strength is significantly weaker in the photoadduct so that the vibration is red shifted by more than 300 cm^{-1}.

In the region below 1400 cm^{-1} different positive bands appear. In contrast, the calculations reveal a blue shift in the cycloadduct of 5 cm^{-1} and a red shift in the 2-2'-adduct of 2 cm^{-1}. Therefore, a dramatic shift to other wavenumber regions is not likely. The second scenario is based on a negative band at the same spectral position that compensates the existent positive band from the asymmetric carbonyl stretching vibration.
From the comparison of the copolyimide with MI and the MIOH film it is evident that only the maleimide moiety reacts under UV irradiation. In the MIOH absorbance spectrum only two bands, the in phase and opposite phase carbonyl stretching vibration, are present in the spectral region of interest. Therefore, further contributions to the negative difference bands are not likely. A negative band that compensates the positive band from the opposite phase carbonyl vibration is not expected.
A third possibility is a significant decrease in the extinction coefficient. The inversion center of the *trans*-cycloadduct leads to a smaller net change of the dipole moment during the normal mode vibration. In this scenario it is expected that the maleimide before the photoreaction takes place absorbs stronger than the cycloadduct and as a result the difference spectrum contains only a negative contribution. The calculated absorbance spectra show however similar intensities of the asymmetric carbonyl stretching band in MIOH, the cycloadduct and the 2-2'-adduct (figure 4.24). The intensity refers to the unit km $\cdot$ mol^{-1}. In the investigated sample volume 2 mol monomeric maleimide formed 1 mol adduct species. To account for this, the calculated MIOH absorbance spectra were scaled by a factor of 2 in the difference spectrum simulation. In these simulations a positive band is still visible though with smaller intensity. If the spectral shifts would be smaller than in the calculation, the positive part of the difference band would vanish. Therefore, the decrease of the extinction coefficient for the asymmetric stretch vibration might be the reason for the absence of a positive band in the difference spectrum. The assumption that the negative maleimide band at 1701 cm^{-1} is compensated by contributions of the photoproducts to the light-induced difference spectrum impedes the quantitative analysis. Therefore, the most prominent band is not applicable to determine the yield of cross-linking.
A negative band for the weaker absorbing in phase carbonyl stretching vibration of the maleimide was not detected. Either its intensity is too small to appear in the spectrum or it is compensated by a positive band arising from a photoproduct. The possibility that this band does not change frequency or intensity at all in the photoproduct is not likely because the opposite phase vibration shifts considerably.

Three photoproducts

It is well known that the cycloadduct is formed during the photoreaction.[212] Depending on the orientation of the maleimide moieties in the non-cross-linked film, not only the *trans*-configuration but also the *cis*-configuration can be formed. According to the calculations in the *cis*-cycloadduct the ring system is drilled which leads to a C_2 symmetry, while the *trans*-conformer shows higher symmetry (C_{2h}). The two configurations cannot be distinguished easily by infrared spectroscopy, since there are no prominent marker bands (figure 4.23). In the cycloadduct, four combinations of the carbonyl stretching vibrations are possible (figure 4.25).
(I) all four C=O bonds stretch in phase,
(II) the two C=O bonds of one ring stretch in phase, while the oscillation between the two rings shows opposite phase,

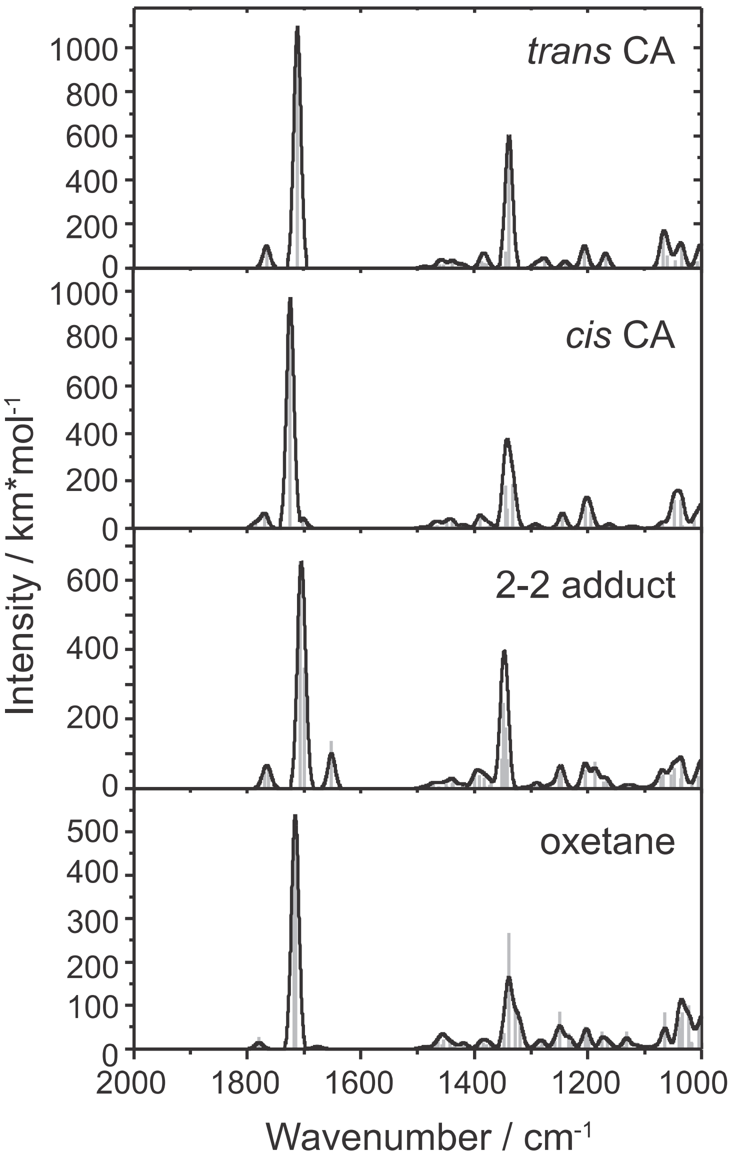

Figure 4.23: Calculated IR bands (grey lines) and calculated absorbance spectra with line broadening (Gaussian function, $\omega = 15$ cm^{-1}, black curves) of the photoproducts *cis*-cycloadduct, *trans*-cycloadduct, 2-2'-adduct and oxetane.

(III) the two C=O bonds of one ring stretch in opposite phase, whereas the two rings vibrate in phase,
(IV) the two C=O bonds in one ring stretch in opposite phase, between the two rings the vibration is in opposite phase. Therefore the two C=O diagonal to each other move in phase. Due to the high symmetry of the *trans*-configuration only combinations II and III result in a net change of the dipole moment and therefore absorb IR light. The calculated IR spectrum of the *trans*-adduct shows only two carbonyl bands. In the *cis*-configuration all four combinations contribute to the absorption spectrum.

In the MIOH film the band pattern in the higher frequency C=O stretching region of the formed photoproduct shows three contributions that were verified by fitted Gauss curves centered at 1786, 1778 and 1766 cm^{-1} (figure 4.18b). The 2-2'-adduct was detected in solutions of polymers containing maleimid moieties before.[213;214] In our experiments the presence of the 2-2'-adduct was proved by the marker band from the terminal C=C double bond. Therefore it is evident that it also contributes to the absorption pattern around 1770 cm^{-1}. The calculation predicts one band in this spectral region of interest. If the *trans*-cycloadduct and the 2-2'-adduct are formed in the copolyimide environment,

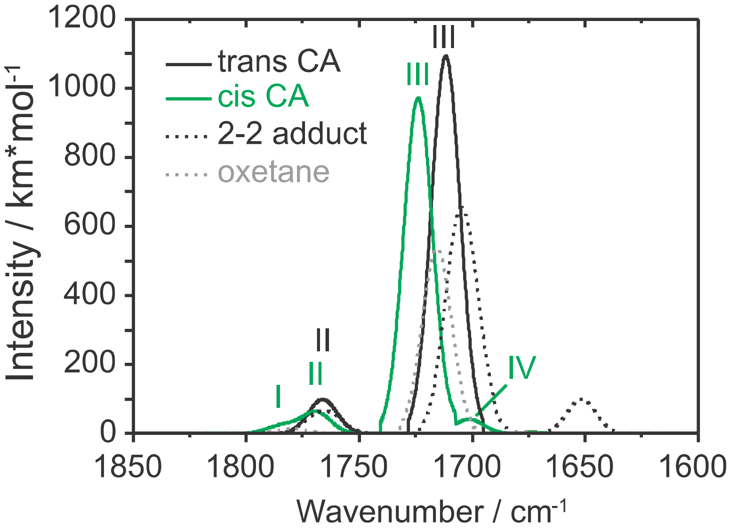

FIGURE 4.24: Details of the carbonyl region of the calculated IR spectra of all four photoproducts. The absorption bands of the *trans*- and the *cis*-cycloadduct are labeled with the combinations of the vibrations according to figure 4.25.

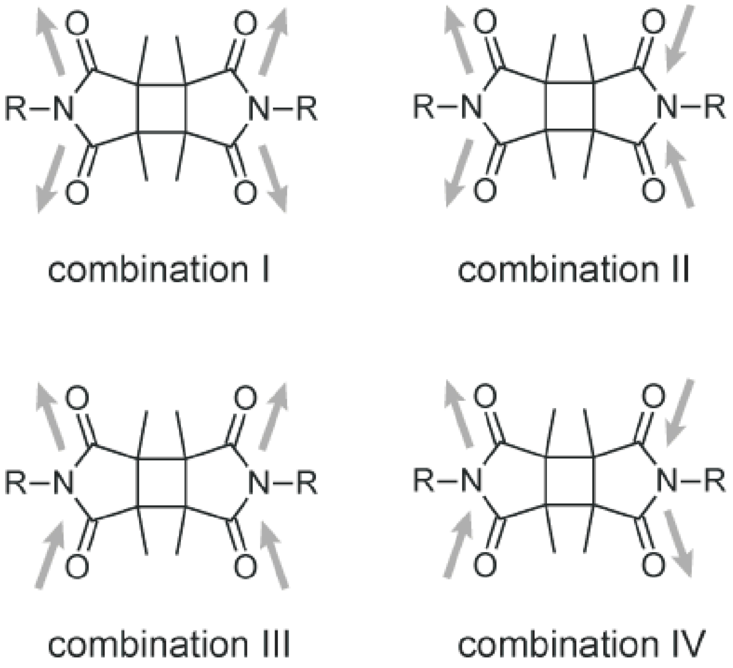

FIGURE 4.25: Scheme of all four possible coupling combinations of the carbonyl stretching vibration combinations between 1600 and 1800 cm^{-1} in the cycloadduct.

only two bands would contribute to the positive difference band pattern. The calculated spectral difference is less than 1 cm^{-1}.

Presumably, only one band would be visible in the measured spectrum. This is not sufficient to explain the band shape. A third contribution at higher wavenumbers is needed. Band I of the *cis*-adduct is calculated to 1786 cm^{-1}. The existence of both cycloadducts in the film could explain the spectral band pattern. One contribution from the *trans*-adduct (band II) heterodyned with two contributions from the *cis*-adduct (band I and II) could reproduce the positive band shape around 1770 cm^{-1}. Therefore, the shoulder at 1786 cm^{-1} in the measured absorption spectrum might be assigned to the all-in-phase carbonyl stretching combination of the *cis*-adduct. A combination of the *cis*-adduct and the 2-2'-adduct would additionally explain the measured band pattern.

Two maleimide moieties can also undergo a reaction according to Paternò and Büchi, resulting in an oxetane-like photoproduct.[133] The energies of all four possible photoadducts were determined by DFT calculations. Among these photoproducts the *trans*-cycloadduct is the most stable one, followed by the 2-2'-adduct (+8.76 kJ/mol) and the *cis*-cycloadduct (+17.23 kJ/mol). The oxetane product has much higher energy (+123.93 kJ/mol) and will therefore not be considered in the further discussion. It cannot be excluded that further photoproducts absorbing at the same spectral position are formed. Since the *trans*-cycloadduct is the most favorable adduct in energy, it is assumed that it contributes to the positive bands in the difference spectrum. Based on the light-induced difference spectra and the results of the DFT calculations it is assumed that the *trans*- and the *cis*-cycloadduct as well as the 2-2'-adduct are formed after UV irradiation of maleimide bound to copolyimide.

The photo-cross-linking of the copolyimide polymer *via* the maleimide side chains was followed in the minute time range. In contrast, the kinetics of the photoaddition of two maleimides is much faster and the elementary processes cannot be investigated with FTIR difference spectroscopy. Only the accumulation of the photoproduct was observed. This provides information on the yield of the cross-linking whereas the detailed photoreaction pathway could not be investigated. However, different time constants for the increase of the product bands were observed. Prominent bands in the C-N stretching region appear with $\tau = 2$ to 5 min. The band at 1653 cm^{-1} assigned to the 2-2'-adduct marker band increases with $\tau = 75$ min. This indicates that the 2-2'-adduct is formed with a lower yield than the cycloadduct. It is possible that the 2-2'-adduct is formed directly from the maleimide monomers. Additionally, the cycloadduct can serve as reactant for a rearrangement to the 2-2'-adduct. Both adduct species, the 2-2'-adduct and the cycloadduct (*cis* and *trans*), absorb at 266 nm better than the monomeric maleimide.[214] Therefore, further photoreactions should be considered. To obtain further insights on the reaction mechanism of the cycloadduct and 2-2'-adduct formation a time resolved experiment in the nano- and microsecond time range is required. This will be realized by step-scan FTIR spectroscopy in further investigations.

Determination of the cross-linking yield

For quantification of the cross-linking yield we established a method to determine the amount of maleimide moieties which perform the photoreaction in the copolyimide film. With regard to the application as pervaporation membranes, this value is of greater importance than the amount of polymer chains which were cross-linked.[213;216] By our approach intramolecular reactions, which also affect the separation properties, are additionally taken into account. It is a common method to determine the cross-linking yield by analyzing a single prominent band.[192;207;213;220] But since multiple competing processes have to be considered, like photodegradation and the spectral overlap of the absorption of products and reactants, this may not be sufficient. Therefore, we performed our analysis on several bands and additionally applied Gauss deconvolution to correct for the spectral overlap. The amount of cross-linked maleimide moieties reaches a maximum value of 6.4 %, determined by analysis of the bands at 1447 and 1411 cm^{-1}, where no overlap with product bands occurs. The possibility that negative bands might be compensated to some extent by photoproduct bands could not be excluded in the case of the carbonyl bands. In this case the negative maleimide bands would have an increased difference absorption that is compensated by adduct bands. As a result the cross-linking yield would exceed the 5 % determined from analysis at the carbonyl bands.

Further irradiation does not lead to a further increase of the cross-linking. In the film, the polymer chains are not as flexible as in solution. Additionally diffusion is inhibited.

As a consequence not every excited maleimide side chain has a second maleimide in the vicinity to perform the photoaddition. A rearrangement is impeded by the high stiffness of the 6FDA-ODA/6FDA-DABA 4:1 backbone due to π-π-interactions of the aromatic systems in the copolyimide chains, in contrast to other photo-cross-linkable polymers like polyurethane-acrylate or polymethacrylate, where higher cross-linking yields were reported.[192] In these polymers the backbone is much more flexible. In principle, a low cross-linking yield is not disadvantageous for pervaporation membranes, since a high cross-linking degree mostly leads to a decrease in flow rates or poor mechanical stability, which makes the material inapplicable for the aspired application.

4.2.6. Conclusions and Outlook

UV-irradiation of 6FDA-ODA/6FDA-DABA 4:1 copolyimide films functionalized with 3-hydroxypropyldimethylmaleimide results in cross-linking of the polymer strands. We have shown with FT-IR difference spectroscopy that different photoreactions occur, which lead to at least three photoproducts, the *trans*- and *cis*-cycloadducts as well as the 2-2'-adduct. The degree of photo-cross-linking was defined as the amount of maleimide moieties which perform the photo-cross-linking reaction. A method to extract this information from the time-dependant changes of product and reactant absorption bands was established. The photo-cross-linking yield of 6 % is restricted by the stiffness of the polymer backbone, which inhibits the photoreaction due to a spatial separation of the cross-linker side chains. To obtain further insights on the formation mechanism of the cycloadduct and the 2-2'-adduct a time resolved experiment in the nano- and microsecond time range is required. This will be realized by step-scan FTIR spectroscopy in further investigations. In separation experiments the performance of the 6FDA-ODA/6FDA-DABA 4:1 cross-linked with photo-induced maleimide dimerization will be investigated concerning the affinity towards several solvent mixtures and the selectivity.

4.2.7. Acknowledgment

Financial support for this study from the German Research Foundation (Project KL 531/29-1) is gratefully acknowledged.

4.2.8. Supplementary Information

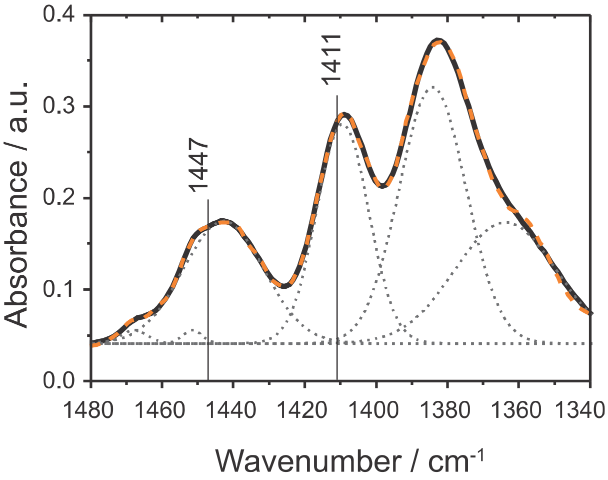

Figure 4.26.: Deconvolution of the absorbance spectrum of the copolyimide with MI by five Gauss curves. The sum of the five Gauss curves is depicted in orange, the experimental absorbance spectrum in black.

4.2.9. Contributions

Title: Characterization of Maleimide Dimers in Photo-Cross-Linked Copolyimide Films.

Authors: Katharina Hunger, Laura Buschhaus, Nadine Schmeling, Claudia Staudt, Anna Pfeifer and Karl Kleinermanns.

Published in: Physical Chemistry Chemical Physics (Impact Factor: 3.573)

This paper is a result of very effective teamwork. All synthesis was performed by N. Schmeling, the FTIR experiments by Laura Buschhaus and the quantum mechanical calculations by me. Discussion and interpretation of the obtained results was done in equal share by L. Buschhaus, Anna Pfeifer and me. I did the major survey of literature already published in this field, the writing was mainly done by A. Pfeifer.

4.3. Investigation of cross-linked and additive containing polymer materials for membranes with improved performance in pervaporation and gas separation

KATHARINA HUNGER#, NADINE SCHMELING*, HAROLD B. TANH JEAZET‡, CHRISTOPH JANIAK‡, CLAUDIA STAUDT† AND KARL KLEINERMANNS#

INSTITUTE OF PHYSICAL CHEMISTRY, HEINRICH-HEINE UNIVERSITY DUESSELDORF, 40225 DUESSELDORF, GERMANY

* INSTITUTE OF ORGANIC AND MACROMOLECULAR CHEMISTRY, FUNCTIONAL MATERIALS, HEINRICH-HEINE UNIVERSITY DUESSELDORF, 40225 DUESSELDORF, GERMANY

‡ INSTITUTE OF INORGANIC CHEMISTRY, HEINRICH-HEINE UNIVERSITY DUESSELDORF, 40225 DUESSELDORF, GERMANY

† BASF SE, ADVANCED MATERIALS AND SYSTEMS RESEARCH, CARL-BOSCH STR., 67056 LUDWIGSHAFEN

Printed in *Membranes*, Special Issue "Membrane Processes and Energy", 2(4):727-763, 2012.

4.3.1. Abstract

Pervaporation and gas separation performances of polymer membranes can be improved by crosslinking or addition of metal-organic frameworks (MOFs). Crosslinked copolyimide membranes show higher plasticization resistance and no significant loss in selectivity compared to non-crosslinked membranes when exposed to mixtures of CO_2/CH_4 or toluene/cyclohexane. Covalently crosslinked membranes reveal better separation performances than ionically crosslinked systems. Covalent interlacing with 3-hydroxypropyldimethylmaleimide as photocrosslinker can be investigated in situ in solution as well as in films, using transient UV/Vis and FTIR spectroscopy. The photocrosslinking yield can be determined from the FTIR-spectra. It is restricted by the stiffness of the copolyimide backbone, which inhibits the photoreaction due to spatial separation of the crosslinker side chains. Mixed-matrix membranes (MMMs) with MOFs as additives (fillers) have increased permeabilities and often also selectivities compared to the pure polymer. Incorporation of MOFs into polysulfone and Matrimid® polymers for MMMs gives defect-free membranes with performances similar to the best polymer membranes for gas mixtures, such as O_2/N_2, H_2/CH_4, CO_2/CH_4, H_2/CO_2, CH_4/N_2 and CO_2/N_2 (preferentially permeating gas is named first). The MOF porosity, its particle size and content in the MMM are factors to influence the permeability and the separation performance of the membranes.

4.3.2. Introduction

Membranes processes are very important in our every day´s life but also in industry, e.g. for water and waste water treatment, in medical applications or separation of petrochemicals. Classical separation methods used for purification of chemical products, notably distillation, extraction and crystallization are energy and cost intensive. Over 50% of the energy costs in the chemical industry are used for the separation of gaseous or liquid mixtures.[221] With membrane technology, the costs for difficult separations e.g. of azeotropic mixtures can be reduced significantly.[222] Membranes with pore sizes of more than 2 nm made out of ceramics, zeolithes, glass, metal or polymers are frequently used in practice.[223–225] Here, separation is based on size exclusion and thus these membranes are suited for separation of components with sufficient size difference, e.g. in dialysis, waste water treatment and functional clothing. For other applications, especially for separation of components with comparable sizes or the separation of ions from water, solution-diffusion membranes are used.[226]

The solution diffusion mechanism is based on the principle that the mixture component with higher solubility and higher diffusion rate permeates preferentially through the membrane, independent on the component sizes.[12;227] Solution-diffusion membranes feature free volume sites which cannot be occupied by polymer chains due to restricted motion and packing density of the polymer chains. The components are transported through the membrane by successive movement between the transient free volume gaps close to the feed side to those close to the permeate side due to thermal motion of segments of the polymer chains.[29]

The pervaporation process, which is used for the separation of liquid mixtures is schematically shown in figure 4.27. The liquid mixture (feed) whose components shall be separated is led over the membrane. Before permeation a phase transition from the liquid phase to the vapour phase is induced by thermal heating. The component which permeates preferentially is concentrated in the permeate, whereas the detained component is enriched in the retentate. Which component is preferentially permeating is dependent on the solubility of the components in the polymer matrix and the diffusion rate of the components through the membrane. The driving force for permeation is given by the difference of chemical potentials of the components on feed and permeate side respectively, depending on pressure, temperature and concentration difference.[227–229] In gas separation, the feed as well as retentate and permeate are gaseous and no phase transition occurs.

The separation characteristics of a membrane are classified in terms of permeability P and selectivity α. The permeability is a measure of productivity of the membrane while the selectivity describes its quality (mole fraction of preferentially permeating component in the permeate).[29] There are different types of materials which are suitable for membrane applications. Inorganic membranes like ceramic membranes of metal oxides (γ-Al_2O_3, ZrO_2, TiO_2 or $ZrTiO_4$), perovskites or zeolites, porous carbon membranes, metal membranes or porous glass membranes[231] have exceptionally high permeability and selectivity together with thermal and chemical stabilities. However, manufacturing procedures are more complicated (e.g. require support treatment, zeolite crystallization, thermal programming for pyrolysis and a controlled inert gas atmosphere in terms of flow, pressure and composition) and there is a lower reproducibility for membrane properties associated with high cost and low mechanical stability. This makes the production of inorganic membranes more difficult than for polymer membranes.[231–233]

Therefore, most of the commercial solution-diffusion membrane units contain polymeric

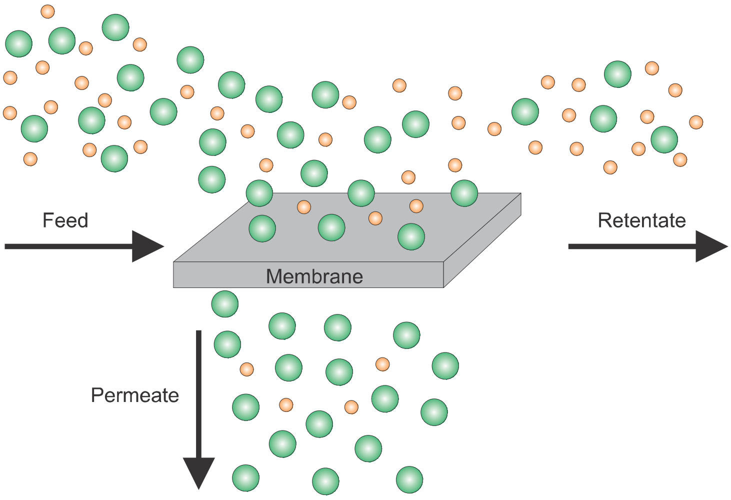

Figure 4.27: Principles of pervaporation. The liquid feed mixture flows along the membrane and the feed components diffuse into and through the membrane at different rates. The liquid retentate is depleted and the vaporous permeate enriched in the preferentially permeating component.[230]

materials,[234–237] which can be divided into rubbery and glassy polymers. While glassy polymers show very attractive separation characteristics, rubbery polymers show comparably low selectivity with high permeability for common gas pairs such as O_2/N_2, H_2/CH_4, CO_2/CH_4, etc.[238;239] Of the glassy polymers, polyimides have been found to be very promising as membrane materials because they not only have better separation characteristics than the commonly used ones (e.g., polycarbonates) but also offer good thermal and chemical resistance and are easy to process.[29] Additionally they can be easily functionalized and therefore customized for any given separation problem. Solution-diffusion membranes already find application in removal of CO_2 from natural gas, dehydration of organic solvents, desalination, removal of polar low molecular weight components in equilibrium reactions, oxygen or nitrogen enrichment from air as well as in vapour recovery systems and several more.[240–243]

Of those applications, natural gas treatment is of the highest industrial interest.[244] Currently, less than 5 % of the plants processing natural gas employ membrane technology, which is mainly used for removal of carbon dioxide.[245] As mentioned above, processing costs can be reduced significantly by substitution or extension of the commonly used amine absorption plants[246] by membrane separation processes. Natural gas is composed of mainly methane (75-90 %) and some higher. Unfortunately, a significant number of natural gas resources cannot be exploited due to the high amount of CO_2 (up to 30 %) and other undesirable impurities (water, nitrogen, hydrogen sulfide, etc.) contained in the mixture, since they lead to corrosion of the pipelines.[241] The specifications for natural gas delivery to the U.S. national pipeline grid[247] demand carbon dioxide contents of less than 2 %. First polymeric membranes for removal of CO_2 from natural gas consisted of cellulose acetate.[242] Cellulose acetate membranes have a CO_2/CH_4 selectivity of about 12-15 under normal operating conditions, which is not sufficient for industrial application.[241] Today, more and more polyimides are used as membrane material instead of cellulose derivatives, since the separation properties are better (selectivities of 20-25).[29;241] However, the low durability of unmodified polyimide membranes poses a problem, which can be overcome by crosslinking.[29;187]

Besides natural gas treatment, separation of aromatics and aliphatics is a promising field for application of solution-diffusion membrane technology. In Europe, the benzene percentage in motor fuel is limited to 1 vol% by law.[5] Reduction of the benzene content of reformates is usually done by extraction with usage of a tetraethylene glycol/water mixture as the extracting solvent. Here, the separation factor for the aromatics is between 2 and 3.[9] By implementing pervaporation membranes, the cost-intensive extracting unit can be replaced. The pervaporation properties of many different polymers were studied in respect to an application as membrane material for aromatics/aliphatics separation, *i.e.* polyimides, polyphosphonates, acetyl cellulose, benzoylated chitosan or polyurethane-silica hybrid membranes. The benzene/cyclohexane selectivity obtained with those polymers as membrane material typically lies between 5 and 20, with a normalized flux of 5-10 kg µm m^{-2} h^{-1}.[248–250] It is important that the membrane material is stable and that the separation characteristics will not change drastically in dependency on the concentration of aromatics in the reformate. Although all of those polymers show promising pervaporation characteristics, the stability often recedes at high aromatic concentrations and elevated feed temperatures. Again, crosslinking of the polymer can lead to an increased durability of the membrane.[9] As was shown for methyl methacrylate/methacrylic acid copolymer membranes ionically crosslinked with metal ions, the separation factor and normalized flux are not smaller than those of the non-crosslinked polymers.[180]

The separation of olefin/paraffin mixtures is rather difficult because of the small differences in physical properties. Currently, such separations are carried out by low temperature distillation, which is rather cost intensive. Although membrane based hybrid processes would be less cost intensive they are not applied, since the separation factors of the membrane materials currently commercially available (e.g., silicone rubber, polysulfone, cellulose acetate, 1,2-polybutadiene or polyethylene) are too low.[251;252] Very attractive separation characteristics can be achieved with polyimides as membrane materials[179;253–256] but these materials are very sensitive to plasticization. To obtain membrane materials suitable for olefin/paraffin separation on industrial scales, the problem of plasticization has to be resolved, first. Some strategies for increase of membrane durability are presented in this review.

Gas separation membranes used in industrial applications are usually integrated as hollow fibers or flat sheets packaged as spiral-wound modules.[245] They are composed of a thin nonporous gas-selective layer (typically less than 0.5 µm[241]) deposited onto a highly porous carrier layer.[227;229;257] The carrier material increases the mechanical stability of the membrane, without influencing the separation characteristics.[235] A promising advance is the usage of composite membranes, in which different materials are used for the two different layers. This way, materials for both layers can be optimized separately and the high-cost polymer materials necessary for good separation properties can be applied more economically, since they are only needed for the very thin selective layer.[245]

A membrane material is well suited for separation, when permeability and selectivity both are high. By modification of the polymer, these parameters can be increased. Unfortunately, improvement of the permeability often is gained in conjunction with a loss of selectivity, or the other way around.[235;238;258] For several polycarbonates, poly(ether sulfone)s and polyimides the solubility selectivities for O_2/N_2 and CO_2/CH_4 were found to be very similar, independent on the polymer structure, while the selectivities varied significantly.[229;259] That implies, that diffusion selectivity D_x/D_y is of higher importance in gas separation than solubility selectivity S_x/S_y, according to equation 4.1.[235]

$$\alpha = \frac{S_x}{S_y}\frac{D_x}{D_y} \tag{4.1}$$

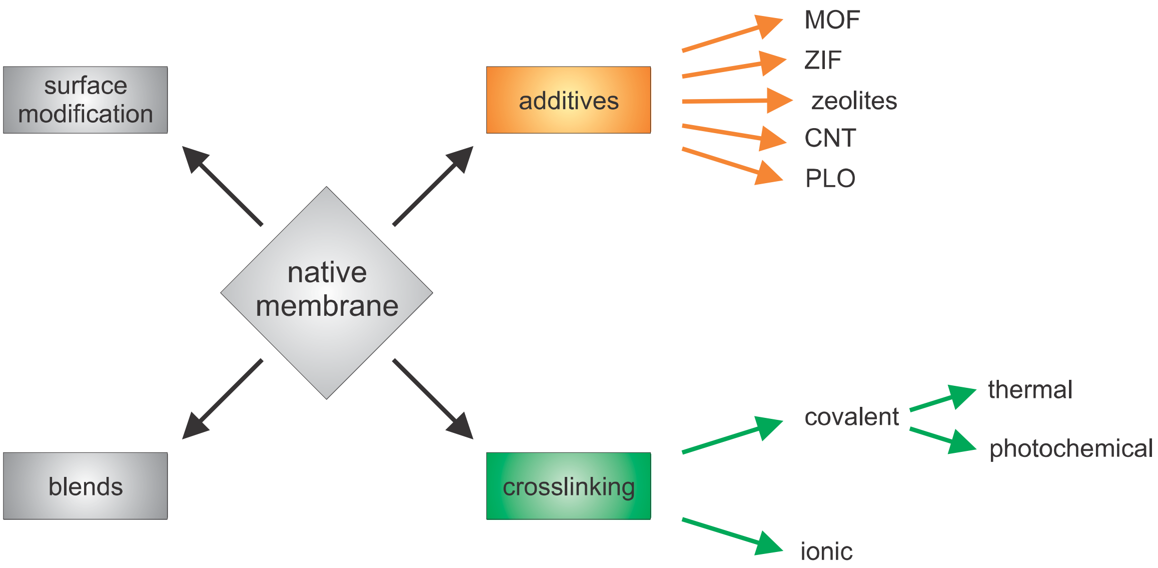

Figure 4.28.: Different approaches to improve polymeric membrane materials (MOF = metal organic frameworks; ZIF = zeolitic imidazolate frameworks; CNT = carbon nanotubes; PLO = porous layer oxides).

Therefore, to optimize both permeability and selectivity, a narrower free volume distribution in combination with a higher chain stiffness should be attempted.[260]
The most common approaches for membrane modification are shown in figure 4.28. Usually at least two polymers are blended together, to take advantage of the different properties of those components. For example, it was found that monomers having bulky substituents, e.g. the 6FDA dianhydride which contains -CF_3 groups (see figure 4.35 for structure), restrict chain mobility and simultaneously chain packing, and lead to significantly improved selectivity as well as permeability.[259;261] Today, most copolymers consist of alternating bulky and flexible monomer units are used and by now a variety of monomers is available.[235] Although permeability and selectivity are the main criteria for classification of the separation characteristics of a membrane, other properties of the material have to be considered as well, as already mentioned above. The membranes are required to be thin but nonetheless stable, and they are desired to be low in cost. Additionally to mechanical stability, the chemical resistance against the feed mixture is of great importance. Membrane fouling, that is adsorption of impurities on the membrane surface or into the membrane, can lead to significant decreases in permeability of the membrane. By surface modification, e.g. grafting adequate monomers on the surface or plasma treatment, the surface roughness, hydrophilicity and charge can be adjusted to the particular feed mixture and thus prevent or confine fouling.[262]
Native, i.e. unmodified, polymeric membranes often show strong plasticization effects when exposed to high partial pressures of CO_2,[186;263] hydrocarbons[264;265] or ethylene oxide.[266] This leads to an increase in intermolecular distance and molecular motion of the polymer chains due to a decrease of inter- and/or intramolecular attractive forces. Consequently, the permeability for all feed components increases whereas the selectivity decreases. Strong plasticization can even lead to a partial dissolution of the membrane.[9] The hydrocarbons present in natural gas can reduce the selectivity by 30 %-50 %.[186;267] The effect is larger for rubbery polymers than for glassy polymers, which implies that plasticization is a problem especially for polyimides. This can be confined by implementing either

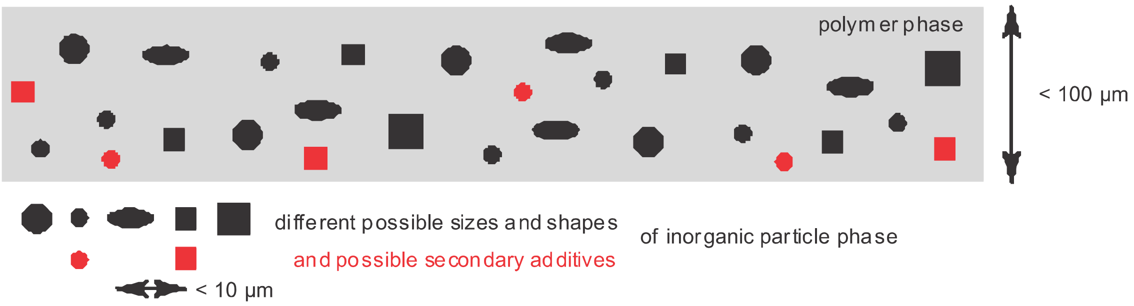

Figure 4.29.: Schematic representation of a mixed-matrix membrane indicating the different possible sizes, shapes and components for the inorganic filler materials (e.g. MOFs, ZIFs, nanotubes).

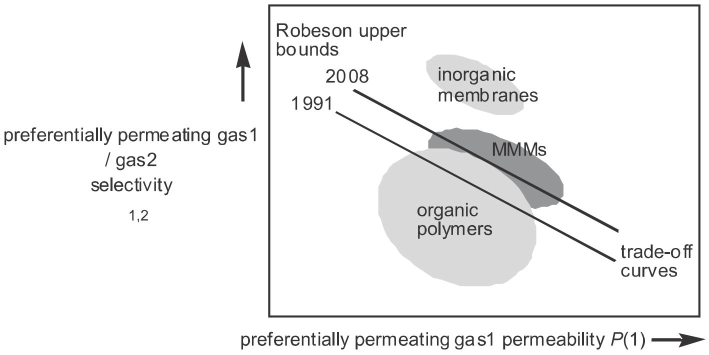

Figure 4.30: Schematic presentation of the trade-off between permeability and selectivity with the 1991 and 2008 Robeson upper bounds.[238;239] In most cases the technologically attractive region lies around or above the Robeson upper bound.

covalent or ionic crosslinks of the polymer backbone. In both cases the plasticization resistance[187;265;266;268] as well as the separation efficiency can be improved[28;269–271] compared to the non-crosslinked polymer for pervaporation[180;185] and gas separation.[199;206;272;273] Another approach to increase the separation characteristics of a membrane is the implementation of additives. Mixed-matrix membranes (MMMs) are constructed from an inorganic material in the form of discrete micro- or nanoparticles incorporated into a polymeric matrix as the continuous phase (see figure 4.29). The utilization of two materials with different flux and selectivity opens the possibility to improve a gas separation membrane by allowing the synergistic combination of polymers with their easy processability and the superior gas separation performance of inorganic materials. A strong improvement of permeability could be expected, if porous inorganic additives, e.g., zeolites, metal organic frameworks (MOFs)[274–280], carbon nanotubes (CNTs)[264;281–288] or porous layered oxides (PLOs)[289–295] with a pore diameter larger than the kinetic diameter of one gas component but smaller than the other one could be applied to the organic polymer. This would be economically very attractive for large scale applications if the selectivity does not change. First MMMs were studied in the 1980s and are more and more investigated in recent years.[296–300] MMMs receive attention as a possibility to enhance the properties of pure polymer membranes.[301] Separation properties with MMMs can be well above the Robeson upper bond (see figure 4.30),[238;239] which is a plot of permeability versus selectivity for most industrial relevant gas mixtures. Porous inorganic fillers can overcome the tradeoff between selectivity and permeability which is typical for continuous (pure) polymer membranes. Carbon nanotubes (CNTs) have been potentially suggested for their application in molecular separation by considering their hollow channels. In fact, simulations and detailed predictions demonstrated that the diffusivities of light gases in-

side the pores of CNTs are highly rapid compared to other porous materials[281]. According to this potential application, the use of CNT/polymer nanocomposites in membrane based separation processes is growing rapidly and considerable efforts were undertaken for the development in last decade[264;282–287] CNT particles are added as fillers to create preferential permeation pathways and thereby improve the separation performance in terms of the gas permeability[264;288]. The processability of polymeric membranes is combined with the higher permeability of nanotubes in order to achieve a synergistic separation performance that surpasses that of conventional polymeric and inorganic membranes.
To increase the gas permeability and also enhance the selectivity behavior of polymer membranes, addition of nanoporous fillers have been intensively investigated.[297;300;302–305] However, zeolites particle face the problem of formation of aggregates creating defects, especially if the polymer matrix is consisting of a glassy polymer.[306] Several attempts of modifying the surface of the zeolites to chemically bond them to the polymer chains and avoid macrovoid formation have been made, which often led to a considerable decrease of the gas permeability due to the rigidification of the polymer chains near the zeolite surface.[307;308] Also modification of the zeolite surface by using amino functionalized siloxan to induce the formation of hydrogen bonds has been used.[309]
Furthermore, interest has risen in sheet-shaped porous layer oxides (PLOs) with TiO_2,[296] SiO_2[310–313] and $Na_4Ti_2Si_8O_{22}\cdot"4H_2O$[294;295] as fillers which are also called flakes or nanosheets if one of the dimensions is in the nanometer range. The aforementioned materials in lamellar form have been used as inorganic fillers in mixed-matrix membranes.[294;295] Such sheet-shaped or lamellar fillers have a high aspect ratio, which allows casting of thin mixed-matrix membranes. The selectivity of the membrane can be improved by size exclusion due to their microporous structure. Such filler materials are subdivided into selective and non-selective fillers depending on the permeability of the feed components through these materials. Also, such sheet-shaped fillers can be incorporated into MMMs in random or distinct parallel orientation. It was previously shown that the orientation of non-permeable inorganic sheets in different polymers has a great influence on the permeability.[289;290] Similar improvement of the separation characteristics can be achieved with smaller amounts of oriented fillers as with higher loads of non-oriented filler. Predictions of the permeation properties of mixed-matrix membranes with sheet-shaped inorganic fillers like porous layered oxides have been made for oriented non-selective sheets[291] as well for selective flakes.[292] Another approach to oriented sheet membranes dealt with fully inorganic MCM-22/silica nanocomposite membranes.[293]

4.3.3. Crosslinking

Crosslinking of polymer membranes can be achieved by different approaches, depending on the functional groups of the polymer and the desired separation properties of the membrane. The aim is to increase the durability of the membrane by circumvention of plasticization without causing losses in selectivity and permeability. Ideally, the separation characteristics of the membrane, especially the selectivity, are enhanced by implementation of crosslinks.
Often there is a variety of approaches to induce crosslinking of a polymer. For instance, a detailed review of different crosslinking methods for poly(vinyl alcohol) (PVA) membranes is provided by Bolto *et al.*.[314] PVA membranes show high stability in highly acidic or alkaline environments.[315] They are often chosen for dehydration procedures, where

swelling due to adsorption of water presents a problem.
By performing several freeze-thaw cycles, crystalline regions are formed that act as crosslinks.[316] With increasing crystallinity the swelling is reduced. Although the physical crosslinks are not as strong or as stable as chemical ones, membranes modified this way last several months without a change of separation properties.[314;317] Reduction of plasticization of PVA can also be achieved by heat treatment at temperatures up to 160 °C, but the permeability is decreased as well. This, too, is explained by a change in crystallinity rather than the introduction of covalent crosslinks.[318;319]
Treatment of PVA with strongly oxidizing radical producers (e.g. $K_2S_2O_8$) leads to formation of polymer radicals, which form crosslinks by radical coupling. This has also been shown to reduce the solubility of the polymer.[320] By varying the amount of persulfate the crosslinking degree can be regulated.[321]

Ionic Crosslinking

Crosslinking of copolyimides can be achieved by different ways, since they can be easily functionalized and thus modified.[322] Copolyimides containing carboxyl groups can be ionically crosslinked by thermal reaction of the dissolved polymer with a stoichiometric amount of aluminium(III)-acetylacetonate or zircon(IV)-acetylacetonate (figure 4.31). The metal ions form a complex with three (Al^{3+}) or four (Zr^{4+}) deprotonated carboxyl groups in a heterogeneous distribution of regions with ionic and non-ionic domains. Therefore the membrane exhibits polymer regions which are sensitive to plasticization in the presence of strong plasticizers such as CO_2.[29;187] The acetylacetonate evaporates during the crosslinking reaction, but not necessarily to completeness. The remaining anions can cause problems in separation due to elution which leads to an undesirable change of the membrane performance and contamination of the retentate. In addition, the strong solvation by CO_2 is able to weaken the ionic interactions in the ionic regions.

Thermal Crosslinking

In order to separate mixtures which contain high amounts of strong plasticizers, the membrane is better crosslinked covalently[187;322] (figure 4.31). Covalent crosslinking can be achieved by thermal reaction of the dissolved polymer with the crosslinking agent (e.g. diols or CNTs).[323] It was shown that covalent binding of fullerenes to poly(2,6-dimethyl-1,4-phenylene oxide) leads to improved separation characteristics for gas separation in respect to the native membrane, while implementation of dispersed fullerenes leads to worse separation characteristics, due to formation of fullerene agglomerates.[324]

Other studies, using dispersed CNTs instead of fullerenes, present more promising results.[325;326] However, the long term stability of those membranes has not been investigated and it is assumed that a CNT-loss due to membrane swelling occurs. This can be prevented by binding the CNTs covalently to the polymer. Copolyimides crosslinked with CNTs are for example well suited for the removal of sulfur containing aromatics from fuel. Sorption capacity tests showed that the covalent incorporation of hydroxyl-functionalized CNTs does not affect the solution selectivity of the copolyimide,[323] while the mechanical stability of the membranes is enhanced.[327]
Non-crosslinked PVA membranes contain hydroxyl groups, which can form hydrogen bonds with water. By crosslinking of PVA with formaldehyde, the chemical stability of the membrane material can be significantly increased but the amount of free hydroxyl

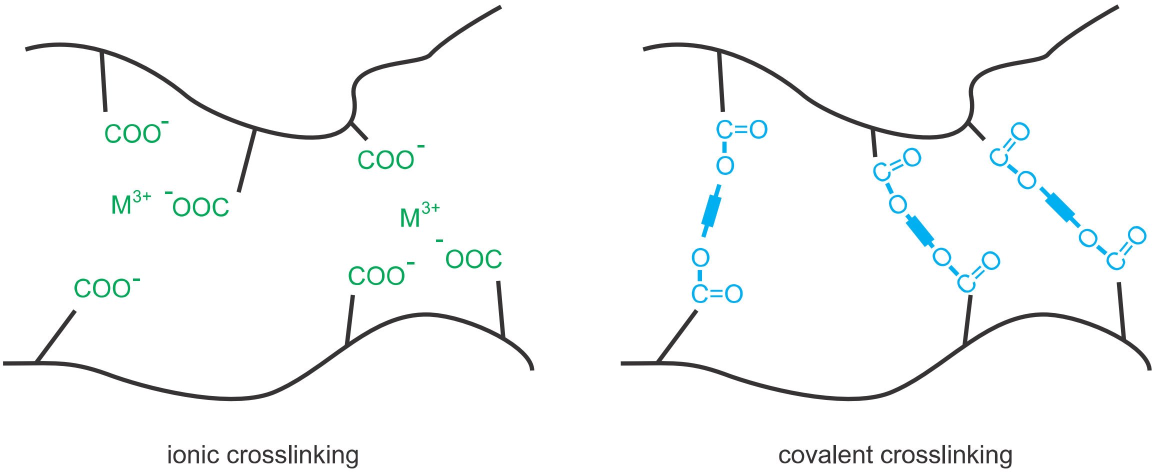

Figure 4.31.: Possible crosslinking methods in polymers containing carboxyl groups. In ionic crosslinked polymers the metal ions form a complex with several deprotonated carboxyl groups. Covalent crosslinking can be achieved thermally or photochemically.

groups is reduced, which results in reduced sorption rate of water vapour in the PVA membrane.[328] However, crosslinking with formaldehyde demands application of sulphuric acid catalysts, which is assumed to result in negatively charged membranes.[329;330]
PVA membranes are also used in reverse osmosis. It was found that upon crosslinking with different dicarboxylic acids with increasing number of carbon atoms in the crosslinker the water flux increased, while the salt rejection was decreased, due to the increased flexibility of the crosslinks.[331] Covalent crosslinking of PVA with maleic anhydride leads to lower water fluxes but higher separation factors than found for non-crosslinked PVA in the dehydration of benzene.[328] In another study, PVA crosslinked with maleic anhydride showed not only an higher separation factor (dehydration of 2-propanol and 1-butanol) but also a higher water flux.[332] Although the same crosslinker was used in both studies, the effect of crosslinking on the separation characteristics is different. This leads to the conclusion that mechanistic studies of crosslinking reactions are of great importance, since they provide vital information for the control of polymer crosslinking.
For these reactions, catalysts are necessary, which remain in the membrane after the crosslinking reaction and thus can lead to the same disadvantages as the anions in ionic crosslinking. One strategy to obtain covalent crosslinks without the usage of catalysts was presented by Evonik. Here, the polyimide is formed by polycondensation of a tetracarboxylic acid anhydride and an aromatic diisocyanate and then treated with a diamine solution. The crosslinking reaction takes place at moderate temperatures (preferentially 20-50 °C) without addition of further reactants.[333]

Photocrosslinking

Another promising strategy to circumvent these problems is to achieve the covalent crosslinking by a photochemical reaction, since in this case no catalyst is needed.[192;207–211]
The photochemical reaction has to be efficient without usage of sensitizers, since sensitizers would again cause the problems in separation mentioned before. First approaches based on direct crosslinking of the polymer backbone had to deal with very large permeability losses due to the increased stiffness of the polymer network and decreased free

volume of the polymer.[191;248;334] By functionalisation of polymer carboxyl groups with flexible molecules (e.g. ethylene glycol or propanediol), this disadvantage can be overcome.[186;188;264;335] Depending on stiffness and length of the crosslinker, the permeability loss of the membrane can be minimized.[197] Thus, functionalization of the polymer carboxyl groups with flexible molecules capable of dimerisation upon UV irradiation (e.g. maleimide derivatives) is a promising strategy to obtain membranes with a high plasticization resistance and excellent separation characteristics.[192;336;337] A detailed summary of polymer materials and photo-crosslinkers suitable for gas separation and pervaporation was recently provided by He et al..[338]

Photo-crosslinking of a polyimide with benzophenone as crosslinking unit was performed by Kang et al..[339] They found that the O_2 permeability decreased and the O_2 over N_2 selectivity increased with increasing irradiation time. The same results were obtained for H_2/CH_4 separation.[206] Here, the selectivity increased by the factor of 50 after 30 min of irradiation, with a decrease in H_2 permeability by the factor of 5. With increasing irradiation time, the larger crosslinking degrees were obtained, which caused further increases in gas permselectivity and decreases in gas permeability. Thus, by varying the irradiation time, the separation characteristics can be tuned.

Since most of the UV light was absorbed by the benzophenone, the irradiation intensity became smaller with increasing penetration depth. Thus an inhomogeneous distribution of crosslinks was obtained.[199;340] This results in lower crosslinking degrees than achievable with thermal activation and thus improvements in separation selectivity with only modest reduction in fast gas flux are obtained. In contrast, thermal activation of the same system results in larger improvements in chemical resistance, thermal stability and gas selectivity but also a more significant reduction of gas flux, as was shown for a copolyimide with crosslinkable ethynyl-terminated monomers.[341]

Benzophenone forms radicals upon irradiation, which may lead to undesirable side reactions.[204] Thus molecules like maleimide, which are capable of forming crosslinks via [2+2]-cycloaddition present an interesting alternative for application in gas separation or pervaporation membranes.[192;336;337] Unfortunately, up to now, no detailed study of the separation characteristics of membranes crosslinked with maleimide is available.

Mechanistic studies of Photocrosslinking

Mechanistic studies of photo-crosslinking reactions can be performed using UV/Vis absorption spectroscopy. This was done for polymer membranes containing maleimide moieties as crosslinker.[20] Maleimides undergo dimerization by [2+2]-photocycloaddition (figure 4.32).[192;212;342] Due to the high photoactivity of the maleimides no sensitizers are needed for this reaction. Thiomaleimides absorb better and at longer wavelengths than maleimide and thus perform photodimerization with increased efficiency.[343] However, the separation properties of membranes which are crosslinked with thiomaleimides remain to be further investigated.

Copolyimides feature intense absorption in the same spectral region (210-250 nm) as maleimide. Therefore, the reaction mechanism is better studied with a polymer backbone which does not absorb UV-light. Here, poly[ethene-stat-(methacrylic acid)] (PEMAA) represents a good alternative, because the separation properties of crosslinked PEMAA membranes are comparable to those of glassy copolyimides having carboxylic acid groups. In either case, crosslinking of the polymer material results in decreased swelling without significant loss of selectivity.[28]

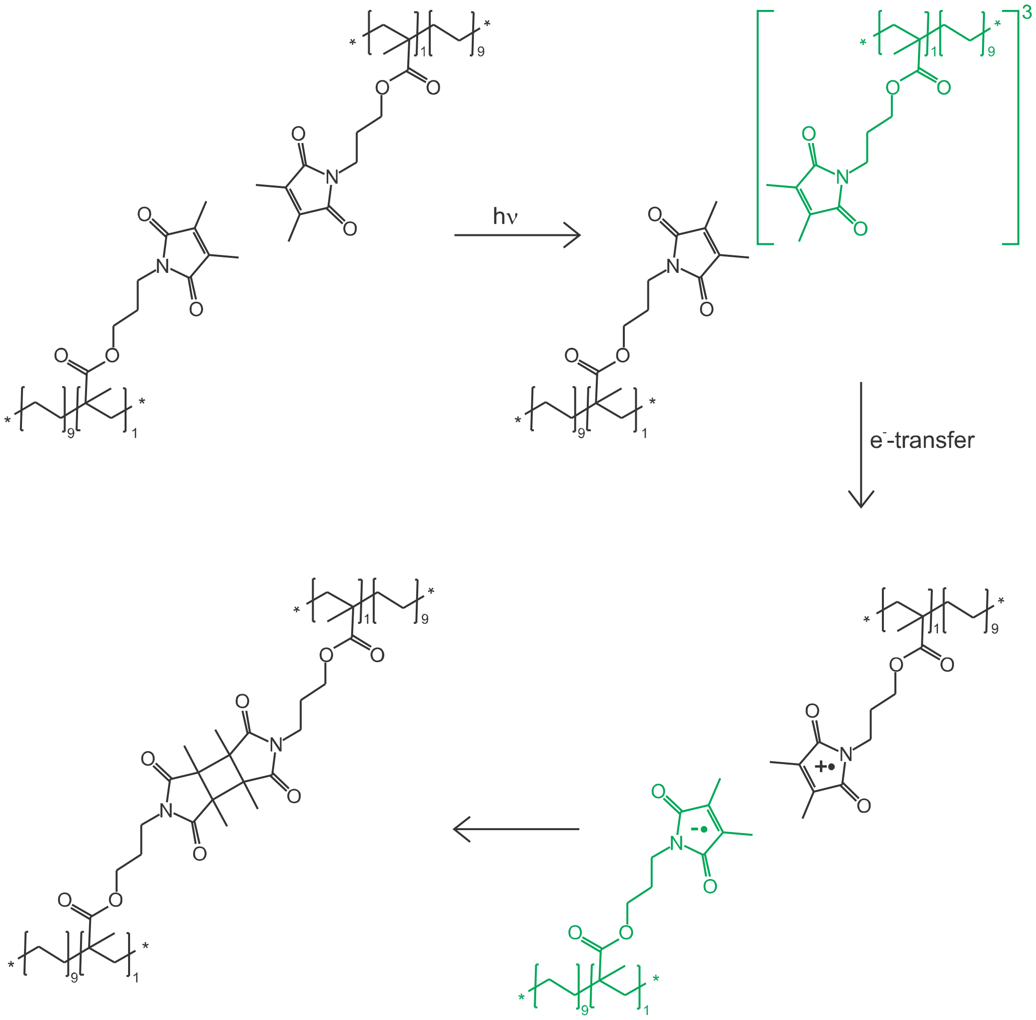

FIGURE 4.32.: Mechanism for photocrosslinking of PEMAA modified with 3-hydroxypropyldimethylmaleimide. Upon excitation to the bright singlet state some population is transferred to the triplet state by intersystem crossing. Electron transfer leads to quenching of the triplet population and allows spectroscopic identification of the maleimide anion. Photocrosslinking occurs by recombination of the ions to the dimer. Our spectroscopic results do not exclude a parallel reaction path via direct cross linking of favourably oriented maleimides in the excited singlet state, see text. Transient species which were detected spectroscopically (triplet state, radical anion) are marked in green.

It is known that crosslinking of a polymer influences the glass transition temperature, T_g.[19] The glass transition temperature depends highly on the polymer chain mobility. Crosslinkers which enlarge the packing density of the polymer limit the mobility of the polymer chains, which results in higher T_g. Crosslinkers which function as spacer between the polymer chains or have a high flexibility increase the polymer chain mobility and thus induce a decrease of T_g.[344] PEMAA with 6 % MI shows a higher glass transition temperature (58 °C) compared to the non-crosslinked copolymer (48 °C).[20] Thus, by functionalization of the PEMAA with maleimide the polymer chain mobility is reduced. Analogous observations have also been made for covalently crosslinked glassy copolyimides, like 6FDA-4MPD/6FDA-DABA 4:1 (see figure 4.35 for structure).[345]
The stationary UV/Vis absorption spectrum of PEMAA films esterified with 3-hydroxy-

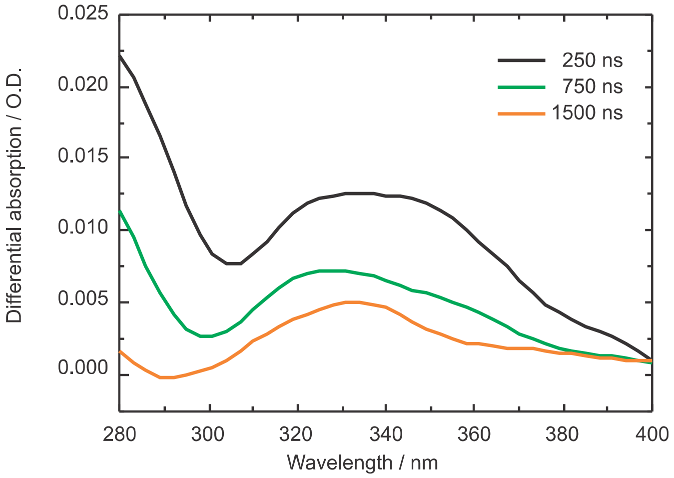

Figure 4.33: Transient absorption spectra of PEMAA esterified with 3-hydroxypropyldimethylmaleimide (esterification degree of 6 %) in THF upon excitation at 266 nm. The spectra were obtained at different time delays to the laser pulse. The broad absorption at 340 nm is due to triplet-triplet excitation in maleimide [107].

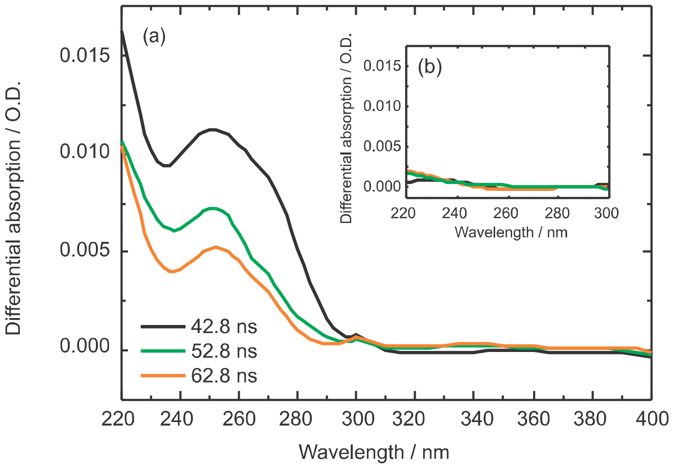

Figure 4.34: Transient absorption spectra of PEMAA films upon excitation at 266 nm. The spectra were obtained at different time delays to the excitation laser pulse. Absorption between 264 nm and 268 nm is dominated by scattered light and therefore the measured absorption in this range is omitted from the spectral average (five data points: 8 nm). (a) PEMAA with 3-hydroxypropyldimethylmaleimide (esterified 6 %). (b) PEMAA without maleimide.

propyldimethylmaleimide (MI) shows an absorption band at 230 nm just as maleimide solutions do.[346] This absorption disappears completely after 20 minutes of irradiation with a mercury lamp and does not recover after the irradiation has been stopped, which indicates that photochemical crosslinking occurs efficiently and irreversible.[20]

Microsecond transient UV/Vis absorption investigations of maleimide modified PEMAA in tetrahydrofuran (THF) provide evidence that, after excitation with a 266 nm laser pulse, intersystem crossing takes place and the triplet state is populated (see figure 4.33). The broad absorption band at around 340 nm is effectively quenched by oxygen. The decay time of the triplet state in solution was determined to be 2.58 ± 0.23 µs, see also Schmeling et. al..[20]

In films prepared from the same solution no triplet absorption is observed anymore. Nonetheless, nanosecond transient absorption spectra of the maleimide modified PEMAA films feature an absorption band with a maximum at 250 nm (see figure 4.34). Films which do not contain the maleimide side group show no absorption in this spectral region. This band was observed in pulse radiolysis experiments as well and was assigned to the maleimide radical anion.[195;196] The maleimide radical anion lifetime in the PEMAA film is determined to be 18.05 ± 0.36 ns. Our time resolution, limited to ~15 ns, does not allow to exclude a parallel singlet reaction path via direct (concerted) cross linking

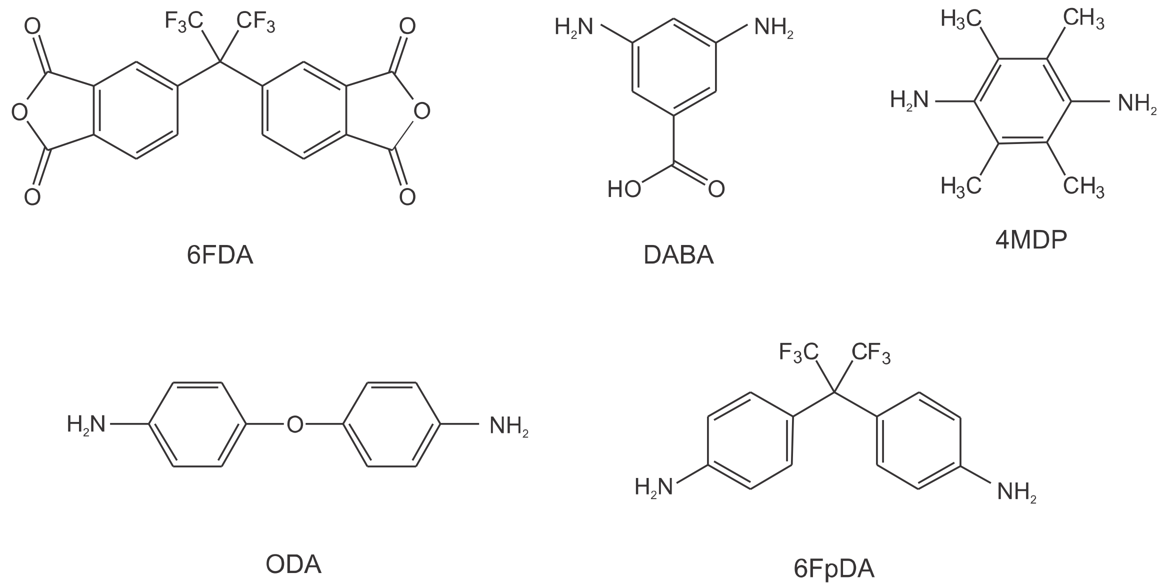

Figure 4.35.: Chemical structures of the copolyimid components discussed in this review. 6FDA: 4,4'-(hexafluoroisopropylidene)diphthalic anhydride; DABA: 3,5-diaminobenzoic acid; ODA: 4-(4-aminophenoxy) benzenamine; MPD: 2,3,5,6-tetramethylbenzene-1,4-diamine; 6FpDA: 4,4'-hexafluoroisopropylidene dianiline

of favourably oriented maleimides in the excited singlet state. In the film, crosslinking is not quenched by oxygen which indicates that dimerisation occurs faster than oxygen diffusion.

In the PEMAA membranes described above only 6 % of all carboxylic acid groups were esterified with MI. Upon irradiation the maleimide absorption band vanishes completely, which means that nearly all maleimide groups have formed crosslinks. At higher esterification degrees PEMAA becomes insoluble and production of films is not possible.

As mentioned before, UV/Vis absorption spectroscopy is not suitable to investigate photocrosslinking of copolyimide membranes with maleimide as crosslinking unit. However, this can be achieved by FTIR difference spectroscopy, a method by which only bands arising from vibrations which change during the monitored reaction appear in the spectrum. Band positions of negative peaks represent the unshifted positions of the disappearing educts, positive bands can be assigned to those vibrations of the photoproducts, which exhibit different frequencies than the educts. The strong absorption of the polymer backbone is not subject to changes caused by the photoreaction[347] and is thus not visible in the FTIR difference spectra. This method is non-invasively and can be performed in real time which is a great advantage over other established methods as the determination of gel fractions,[216] weight ratios,[217] swelling properties,[219] or rheology.[213;218] Additionally, structural information about the membrane and the photoproducts can be obtained.

An extensive FTIR difference absorption study was performed on 6FDA-ODA/6FDA-DABA 4:1 films functionalized with MI. The structures of the different monomers used for the synthesis of the copolyimides investigated are shown in figure 4.35. The structure of the 6FDA-ODA/6FDA-DABA 4:1 polymer is shown in figure 4.36a. Although it was intended to obtain complete functionalization, that is each DABA moiety carries a maleimide moiety (theoretical functionalization degree: 100 %), it cannot be excluded, that free carboxyl groups remain in the polymer.

Comparison between films of (i) 6FDA-ODA/6FDA-DABA 4:1, (ii) 6FDA-ODA/6FDA-DABA 4:1 with MI and (iii) MI shows, that appreciable photochemistry only occurs in the presence of the crosslinker (see figure 4.36b). The difference spectrum of the copolyimide without maleimide moiety does not exhibit any light-induced difference bands. The difference spectra of MI containing films feature a positive band in the region of 1800 - 1750 cm^{-1} which is shown in detail in figure 4.36c. It derives from a superposition of three bands which cannot be generated by the main photoproduct, the trans-cycloadduct, alone. According to DFT calculations the cis-cycloadduct (see figure 4.36c for the structure) cannot be distinguished easily by infrared spectroscopy from the trans-cycloadduct, since there are no prominent marker bands. However, due to its drilled ring system, an additional carbonyl vibration shows significant IR activity and thus contributes to the absorption spectrum.[347]

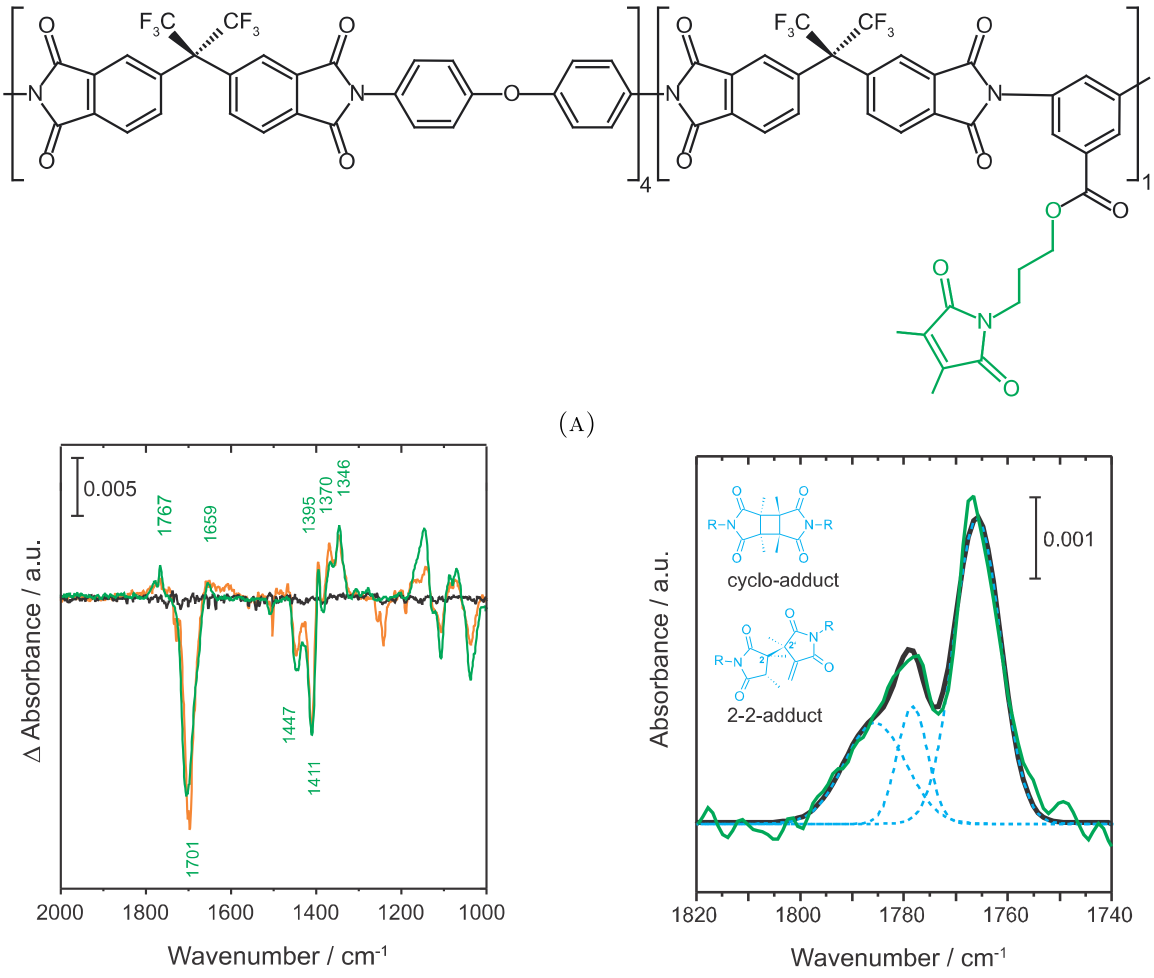

(a)

(b)

(c)

Figure 4.36.: (a) Chemical structure of 6FDA-ODA/6FDA-DABA 4:1 copolyimide functionalized with 3-hydroxypropyldimetylmaleimide. Depicted in green is the maleimide side group. (b) Laser-induced FTIR difference spectra of 3-hydroxypropyldimethylmaleimide (green), 6FDA-ODA/6FDA-DABA 4:1 copolyimide (black) and the copolyimide with 3-hydroxypropyldimethylmaleimide (green). (c) Difference spectrum of 3-hydroxypropyldimethylmaleimide (green) in the carbonyl region. The positive feature can be reproduced by the sum of three Gauss curves (blue).

Formation of a third photoproduct, the 2-2'-product (see figure 4.36c for the structure), is assumed due to the appearance of a positive absorption band at 1659 cm^{-1}, which corresponds to the terminal C=C double bond stretching vibration. This photoproduct was also detected in solutions of different N-alkyl-3,4-dimethylmaleimides[214] and polyacrylamide hydrogels functionalized with dimethyl-maleimide.[213] No evidence was found for the formation of an oxetane-like photoproduct, which would result from a Paternò-Büchi-reaction.[133]

The time constants for photoproduct accumulation upon irradiation with laser pulses with 266 nm and 6 mJ cm^{-2} are in the range of several minutes. Prominent bands assigned to the cycloadduct appear with $\tau = 2$ to 5 min while the 2-2'-adduct marker band increases with $\tau = 75$ min. This indicates that the 2-2'-adduct is formed with a lower yield than the cycloadduct. Both adduct species absorb at 266 nm better than the monomeric maleimide,[214] therefore it is not unlikely that the 2-2'-adduct is not only formed directly from the maleimide monomers but also by rearrangement of the cycloadduct. Photodegradation of the polymer backbone competes with photocrosslinking. Biexponential fits of the negative difference absorption bandswith time constants $\tau = 5$ min and $\tau > 120$ min were obtained. The slower process is assigned to photodamage of the polymer backbone and the faster process to photocrosslinking.

Photocrosslinking yield

The separation characteristics of a crosslinked membrane are strongly influenced by the number of crosslinks in the membrane. This value is of greater significance for pervaporation membranes than the amount of polymer chains which were crosslinked.[213;216] When using a photocrosslinker, the crosslinking yield can be controlled by duration and intensity of the irradiation.

The yield can be determined with the help of FTIR difference absorption spectroscopy, by calculating the ratio of difference absorbance ΔA to initial absorption A. Since multiple processes compete and many absorption bands are generated by superposition of product and reactant absorption, determination of the crosslinking yield by analyzing a single prominent band may not be sufficient.[192;207;213;219] An analysis of several bands, after Gauss deconvolution to correct for the spectral overlap, is more likely to deliver significant results.

For a 6FDA-ODA/6FDA-DABA 4:1 copolymer with MI it is assumed that only maleimide side chains that react within $\tau = 5$ min contribute to product formation. In order to avoid falsification due to overlapping product bands, the quantitative analysis is restricted to the region between 1450 and 1400 cm^{-1} where products do not absorb significantly. After subtraction of the contribution due to photodegradation, the difference absorbances of the negative bands at $\nu_1 = 1447$ cm^{-1} and $\nu_2 = 1411$ cm^{-1} are calculated to be $A_1 = 0.010$ and $A_2 = 0.018$. The initial absorptions A_i, derived from the absorbance spectrum of the copolyimide with MI, are $A_1 = 0.16$ and $A_2 = 0.28$. With these values, a crosslinking yield $\Delta A/A$ of 6.4 % is calculated for both bands.

For polyurethane-acrylate crosslinked with maleimide, crosslinking yields of 50 % are reported,[348] while with polymethacrylate as polymer backbone crosslinking yields are even higher (up to 90 %).[192] These high values are obtained when the polymer backbone is of high flexibility. The stiffness of the 6FDA-ODA/6FDA-DABA 4:1 polymer backbone prevents close vicinity of the excited maleimide moieties to a second maleimide during the lifetime of the radical anion as necessary for crosslinking. This effect is higher in films than in solution. The low crosslinking yield is not necessary a disadvantage. High crosslinking yields lead to low flow rates and can cause the membrane to be brittle, which makes the material inapplicable for separation. Thus, it is desirable to fabricate membranes with a crosslinking yield high enough to prevent plasticization but not too high so that the obtained flow rates are still high enough to qualify for industrial applications.

4.3.4. Pervaporation and Gas Separation studies of Crosslinked Membranes

Copolyimides show excellent separation characteristics for different gaseous and liquid mixtures. Here, aromatic/aliphatic separation and the removal of carbon dioxide from natural gas with high CO_2 content are discussed in detail. The crosslinking yield of the PEMAA membranes with MI discussed above was too low to prevent plasticization efficiently. The membranes of 6FDA-ODA/6FDA-DABA 4:1 with MI were very brittle and thus not suited for pervaporation experiments. However, sorption capacity measurements of the photocrosslinked 6FDA-ODA/6FDA-DABA 4:1 membrane show decreased swelling degrees and increased sorption selectivities in respect to the native membrane material.[17]
The best results for covalently crosslinked membranes in pervaporation performance studies were obtained with 6FDA-4MPD/6FDA-DABA 4:1 crosslinked by thermal reaction of the polymer backbone with 1,4-butanediol.[17]

Aromatic/Aliphatic Separation

It has been shown that crosslinked membranes can be conditioned, that means treated with high aromatic feed mixtures prior to use. This leads to a more open structure and results in a higher flux also in long term experiments without a significant loss in selectivity, whereas non-crosslinked copolymides swell very strongly or even partially dissolve at high aromatic concentrations.[9]
For comparison of covalently, ionically and non-crosslinked 6FDA-4MPD/6FDA-DABA 4:1 membranes, pervaporation experiments using a toluene/cyclohexane mixture were performed. The ionically crosslinked membrane was prepared from the basic polymer material by addition of zircon(IV)-acetylacetonate (theoretical functionalization degree: 10 %). The covalently crosslinked membrane was prepared from the basic polymer material by addition of 1,4-butanediol in a six-fold excess over the amount of carboxylic acid groups and with toluenesulfonic acid as catalyst at 150 °C (theoretical functionalization degree: 100 %).
The results obtained show that the selectivity is slightly higher for covalently crosslinked membranes with respect to the non-crosslinked ones and lower for ionically crosslinked membranes (see figure 4.37). The flux is significantly lowered by covalent crosslinking and even more so by ionic crosslinking. This effect increases with increasing aromatic feed concentrations. Whereas usually the feed concentration for the aromatics in the reformate stream ranges between 40 % and 50 %, much higher concentrations occur occasionally.[29]
It is obvious that in both cases of crosslinking, ionically as well as covalently, the flux is reduced compared to the non crosslinked membrane material. However the strong increase of flux with increasing aromatic content in feed is suggesting swelling of the membrane. Comparing the performance of the crosslinked membrane materials it can be seen from

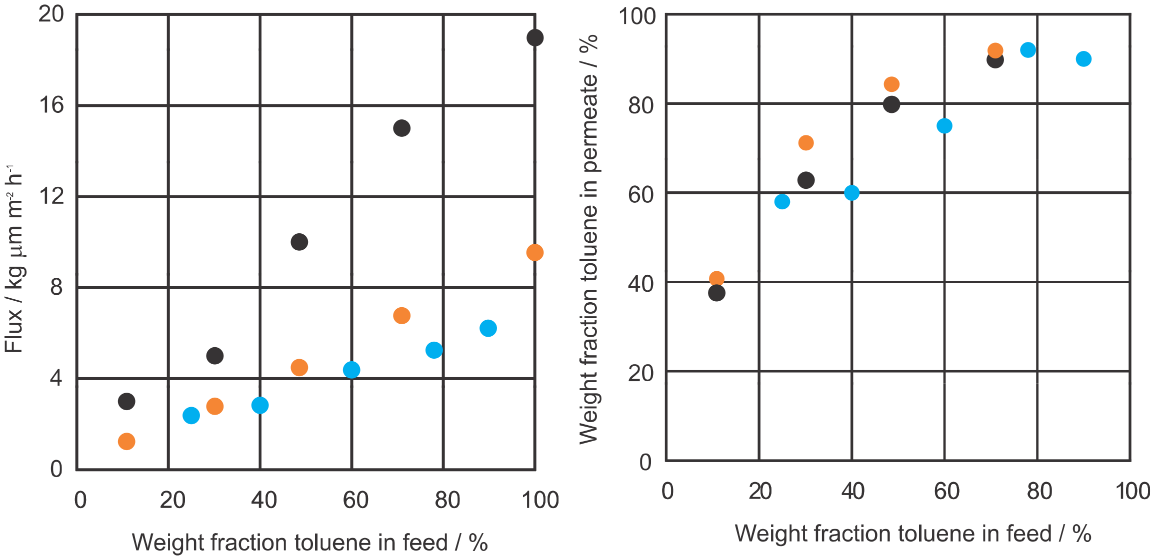

Figure 4.37.: Pervaporation results for conditioned 6FDA-4MPD/6FDA-DABA 4:1 copolyimide membranes, crosslinked with 1,4-butanediol (orange) and crosslinked with zircon(IV)-acetylacetonate (blue) and non-crosslinked (black) using a toluene/cyclohexane mixture at 60 °C. Permeate pressure was kept between 20 and 25 bar.[29]

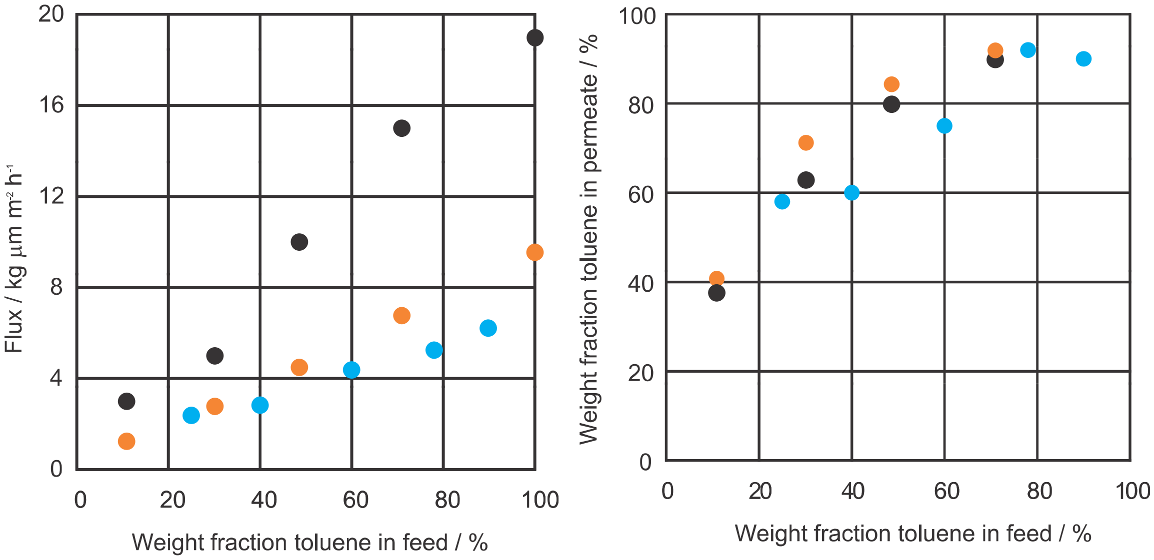

Figure 4.38.: CO_2/CH_4 separation characteristics for the 6FDA-6FpDA/6FDA-4MPD/6FDA-DABA 3:1:1 copolyimide ionically crosslinked with aluminium(III)-acetylacetonate (blue) and covalently crosslinked with ethylene glycol (orange) at 35°C using a 50:50 CO_2/CH_4 feed gas mixture.[29]

figure 4.37 that the fluxes of both membrane types do not vary significantly. However, although the selectivity of ionically and covalently crosslinked membranes are comparable at high-range aromatic concentrations, covalently crosslinked membranes should be favored for this kind of separation since a better long term performance is expected.

Natural Gas Treatment

Plasticization is also a problem for separation of CO_2 from natural gas. For non-crosslinked copolyimides it generally occurs at 10 - 20 bar partial CO_2 pressure in the feed. Crosslinked copolyimides not only offer plasticization resistance up to much higher CO_2 pressures but also have a better chemical resistance.

The non-crosslinked copolyimide 6FDA-4MPD and ionically crosslinked 6FDA-4MPD/ 6FDA-DABA 4:1 start plasticizing at a CO_2 pressure of approximately 15 bar whereas the covalently crosslinked 6FDA-4MPD/6FDA-DABA 4:1 membrane is resistant to plasticization up to CO_2 pressures of more than 30 bar.[29] These results are in good agreement with those found for other copolyimides.[187] With both crosslinked membranes the permeability is decreased whereas the selectivity is not changed significantly compared to the non-crosslinked systems.

By substitution of 75 % of the 4MPD by 6FpDA the selectivity can be increased up to commercially attractive values. 6FpDA contains bulky -CF_3 groups which cause restricted rotation around the main polymer chain and also provide a higher free volume. The permeability of the covalently crosslinked 6FDA-6FpDA/6FDA-4MPD/6FDA-DABA 3:1:1 membranes is nearly constant for CO_2 partial pressures of 5 to 50 bar, whereas the ionically crosslinked membranes plasticize approximately at 20 bar (figure 4.39). With covalent crosslinking, the selectivity is approximately 20 % higher than with ionic crosslinking. In both cases, a decrease in selectivity was found with increasing feed pressure.

Most importantly, the crosslinked membranes show good CO_2/CH_4 selectivity even above CO_2 partial pressures of 40 bar, and thus qualify for commercial applications since the separation factors are much higher than those of the cellulose derivatives in current use.[349]

4.3.5. Metal-organic frameworks in Mixed Matrix Membranes

Metal-organic frameworks (MOFs) are of increasing interest as porous filler in mixed-matrix membranes (see figure 4.29). MOFs offer various advantages over zeolites or other porous inorganic additives[350–354]: The organic ligands as an inherent part of MOFs allow them to interact well with the polymer material and its functionalities. This way, the formation of gaps between the "inorganic" filler and the organic polymer phase, which would cause losses in selectivity, can be avoided. Also the MOF surface properties can be easily tuned by functionalization with various organic molecules if necessary. Moreover, MOFs also have higher pore volumes and lower density than zeolites, and therefore their effect on the membrane properties can be more pronounced for a given mass loading. For MMMs a perfect interaction between the two components is highly important in order to achieve optimized separation properties of the hybrid material.

Incorporation of the MOF 4,4'-bipyridine-hexafluorosilicate-copper(II) (Cu-BPY-HFS) (see figure 4.39a) into a dense Matrimid® 5218 membrane increased the gas permeabilities and selectivities for pure gases (from single gas experiments) and gas mixtures of CH_4/N_2 but decreased the ideal CO_2/CH_4 and H_2/CH_4 selectivities.[355]

Cu-BTC MOF (see figure 4.39b) as additive in an asymmetric membrane of Matrimid® 9725 or of 3:1 Matrimid®/polysulfone Utrason S 6010 N blend showed a higher CO_2 permeance compared to the unfilled membrane in mixed gas permeation experiments.[356;357] The binary gas mixtures CO_2/CH_4 and CO_2/N_2 were studied for CO_2 concentrations from 10 vol% to 75 vol%. The permeance of the preferential permeating gas CO_2 and, hence, the CO_2 selectivity increased with the filler loading. Noteworthy, the CO_2/CH_4 selectiv-

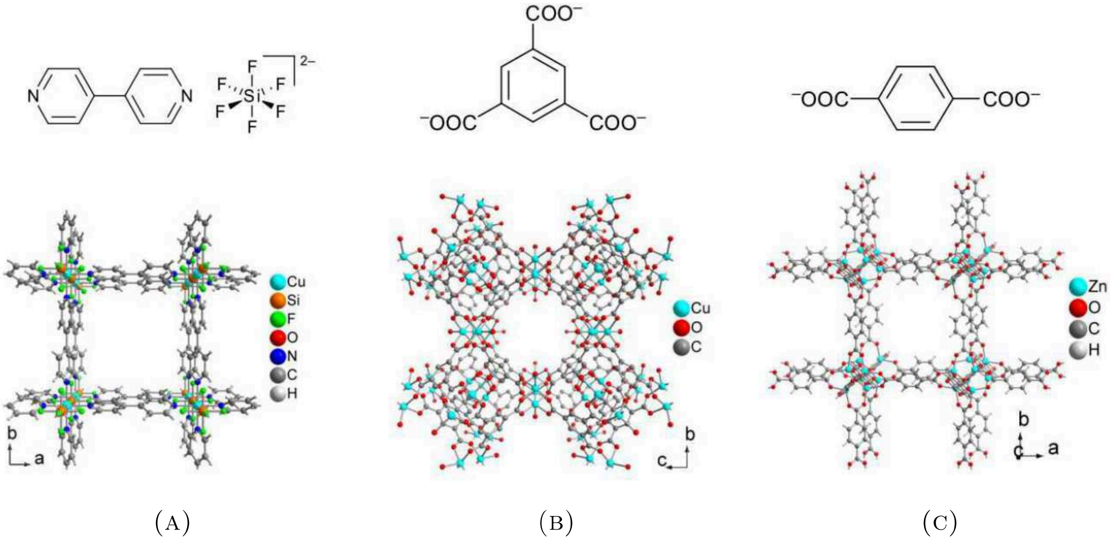

Figure 4.39.: Linkers and sections of the packing diagrams of (a) Cu-BPY-HFS, [Cu(μ-SiF_6)(μ-4,4'-bipy)$_2$] (BPY = 4,4'-bipyridine, HFS = hexafluorosilicate), (b) Cu-BTC, [$Cu_3(BTC)_2(H_2O)_3$] (BTC = benzene-1,3,5-tricarboxylate) and (c) MOF-5 (IRMOF-1), [$Zn_4O(BDC)_3$] (BDC = benzene-1,4-dicarboxylate, terephthalate)

ity α_{CO_2/CH_4} dropped linearly when the CO_2 content increased from 10 to 75 vol%. The slope of this selectivity drop did not depend on the [$Cu_3(BTC)_2$] additive content.[356;357] This could be due to plasticization phenomena with higher CO_2.

Cu-BTC with polyimide (PI) prepared from 4,4-oxydianiline (ODA) and pyromellitic dianhydride (PMDA) was successfully spun into MMM hollow fibers by a dry/wet-spinning method. H_2 permeance and selectivity of H_2 with respect to N_2, CO_2, O_2, and CH_4 increased with increased Cu-BTC loading. At 6 wt% Cu-BTC, the permeance of H_2 was higher by 45 %, and its ideal selectivity from other gases was up by a factor of 2-3 compared to pure PI.[358]

Cu-BTC (see figure 4.39b) or ZIF-8 MOF (see figure 4.40a) and the zeolite silicalite-1 (S1C) were combined in a polysulfone Udel® P-3500 MMM[359] for the separation of CO_2/N_2, CO_2/CH_4, O_2/N_2, and H_2/CH_4 mixtures. For some of these gas mixtures, the combined-filler MMM showed a synergetic enhancement in selective gas transport when compared either to the pure polymer or to the MMM with only one filler type. All fillers, at the same loading of 16 wt%, increase the CO_2 permeability when compared to that of the bare polymer in the two CO_2-containing mixtures. However, the maximum separation selectivities for CO_2/CH_4 and CO_2/N_2 mixtures ($\alpha_{CO_2/CH_4} = 22.4$ with P = 8.9 barrer for CO_2, and $\alpha_{CO_2/N_2} = 38.0$ with P = 8.4 barrer for CO_{22}) were only achieved when Cu-BTC was combined with S1C in a PSF MMM.[359]

When the same Cu-BTC / ZIF-8 / S1C single- or double-additive MMMs were applied to O_2/N_2 and H_2/CH_4 separations, for which mechanism is based mainly on diffusion and not on adsorption differences, the combination of Cu-BTC and S1C significantly enhanced the selectivities of O_2 or H_2, respectively. This may be due to an improved diffusion through zeolite crystals from the synergy with Cu-BTC.[359]

MOF-5 as nanocrystals showed a strong affinity to the polymer matrix of Matrimid® 5218. In MOF-5, six carboxylate groups coordinate to the six edges of the tetrahedral

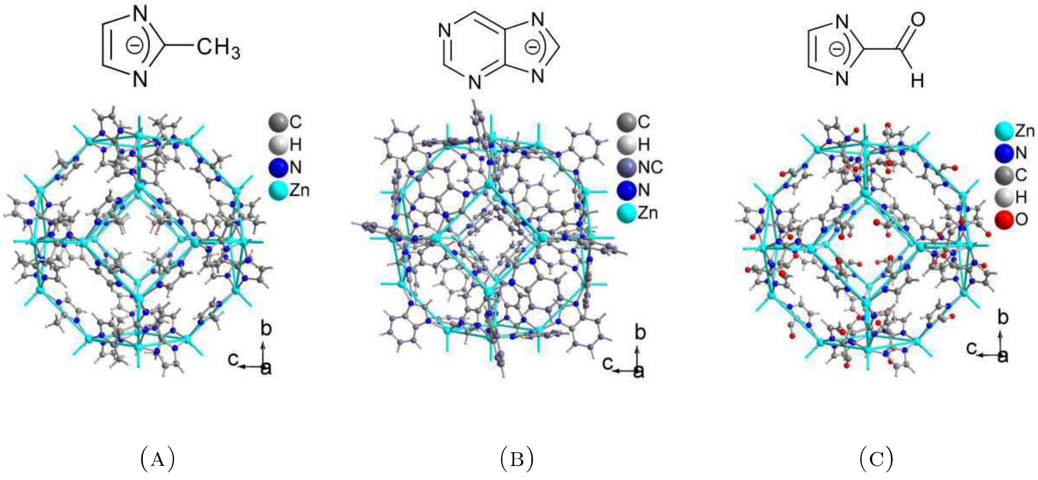

(A) (B) (C)

Figure 4.40.: Linkers and sections of the packing diagrams emphasizing the cuboctahedral β-sodalite cage which is depicted by blue topological lines connecting the Zn atoms of (A) ZIF-8, [Zn(2-methylimidazolate)$_2$], (B) ZIF-20, [Zn(purinate)$_2$] and (C) ZIF-90, [Zn(2-carboxyaldehyde imidazolate)$_2$].

Zn_4O unit in octahedral geometry and the terephthalate linker then form the edges of a cube in the primitive cubic network (see figure 4.39C).

Single gas permeabilities of H_2, CO_2, O_2, N_2 and CH_4 doubled approximately with MOF-5 loadings of 30 wt% from those of the pure polymer. This increase was ascribed to the MOF-5 porosity. Tests with binary CH_4-containing gas mixtures for the MMM with 30 % MOF-5 in the polyimide revealed an increase in selectivity for CH_4. The larger solubility of CO_2 and N_2 in the polymer matrix was seen as the reason to favor enhanced CH_4 transport.[360]

Zeolitic imidazolate framework-8 (ZIF-8) with Matrimid® 5218 MMMs was prepared with loadings up to 80 % (w/w), which are much higher than the typical loadings achieved with selected zeolite materials.[361] In ZIF-8, the 2-methylimidazolate ligands connect individual zinc atoms and form the edges of a cuboctahedral β-cage in a sodalite network (see figure 4.40A). The ZIF-8/Matrimid® MMMs permeabilities were tested for H_2, CO_2, O_2, N_2, CH_4, C_3H_8, and gas mixtures of H_2/CO_2 and CO_2/CH_4 and increased as the ZIF-8 loading increased to 40 % (w/w). This increase in permeability suggested that the addition of ZIF-8 nanoparticles to Matrimid® increases the distance between polymer chains creating higher free volume in the polymer matrix. For the majority of gas pairs (O_2/N_2, CH_4/N_2, H_2/O_2, H_2/CO_2, H_2/N_2), there was no significant change in the ideal selectivity until 40 wt% ZIF-8 loading. However, at higher loadings of 50 wt% and 60 wt%, the permeability decreased for all gases, and the selectivities increased. Ideal selectivities of gas pairs containing gases of different size, such as H_2/O_2, H_2/CO_2, H_2/CH_4, CO_2/CH_4, CO_2/C_3H_8, and H_2/C_3H_8, showed improvement with the 50 wt% ZIF-8 loading through a shift from polymer-driven to ZIF-8-controlled gas transport process. ZIF-8 can selectively transport smaller gas molecules, such as H_2 and CO_2.[361]

An asymmetric MMM of Matrimid® 9725 and ZIF-8 (or MIL-53(Al), see below) exhibited a higher CO_2 permeance than the unfilled membrane in mixed gas permeation experiments.[357] MOF fillers with 10 wt%, 20 wt% and 30 wt% were loaded in Matrimid®.

Binary gas mixtures CO_2/CH_4 and CO_2/N_2 with CO_2 concentrations from 10 vol% to 75 vol% were investigated and the results compared to Cu-BTC/Matrimid®[356] or MIL-53(Al).[357] The permeance of the preferentially permeating gas CO_2 increased with the filler loading in the binary mixtures in all three cases but the CO_2 selectivity only increased slightly in the case of Cu-BTC or MIL-53(Al) and remained almost constant for ZIF-8. The CO_2/CH_4 selectivity α_{CO_2/CH_4} showed a constant drop when the CO_2 content increased from 10 to 75 vol% for all three additives. The selectivity drop was independent of the filler content. Increase in CO_2 permeance was assigned to the extra pore network of the MOF fillers. Scanning electron microscopy cross-section images showed the MOF filler well distributed and embedded in the polymer matrix even for the 30 wt% loaded membranes.[356;357]

MMMs made of poly-(1,4-phenylene ether-ether-sulfone) (PPEES) and ZIF-8 with filler loadings of 10 wt%, 20 wt% and 30 wt% were employed in CO_2 diffusion studies using pulsed field gradient (PFG) NMR techniques.[362] The self-diffusion coefficient increased from $2.1 \cdot 10^{-8}$ cm^2 s^{-1} for the pristine PPEES membrane to $9.3 \cdot 10^{-8}$ cm^2 s^{-1} for the 30 wt% ZIF-8/PPEES-MMM. ZIF-8 provides Langmuir adsorption sites for CO_2 molecules, thus, the gas adsorption in the MMM increases with the filler content. ZIF-8 contributes greatly to gas permeation by increasing the gas solubility in the composite membranes.[362]

Combining both ZIF-8 and silicalite-1 in polysulfone Udel® P-3500 (ZIF-8/S1C-PSF MMM) did not improve the separation results from either S1C-PSF or ZIF-8-PSF MMMs in the case of CO_2/CH_4 and CO_2/N_2 gas mixtures. Probably the relatively large silicalite-1 crystals could not be intercalated between small ZIF-8 particles. ZIF-8 alone produced the highest increase of CO_2 permeability, which can be attributed to its textural properties and its small particle size, albeit giving poorly dispersed aggregates.[359] For O_2/N_2 and H2/CH_4 gas separation a ZIF-8-PSF MMM produced the best selectivity-permeability results compared to a Cu-BTC- or S1C-PSF MMM. This may be due to an increase in free volume (as suggested for ZIF-8-polyimide MMMs)[361] together with an efficient molecular separation effect (based on diffusion differences) because of the small pore aperture window of ZIF-8 (3.4 Å, 0.34 nm) compared to Cu-BTC (6 Å, 0.6 nm) and S1C (5.5 Å, 0.55 nm).[359]

Different sonication powers were applied on ZIF-8 nanoparticles for the preparation of ZIF-8/Matrimid® nanocomposite membranes with the aim of investigating the effect of typical membrane processing conditions on the structure, the interfacial morphology and the gas separation performance. It was shown that ultrasonication generates significant changes in the shape, size distribution, and structure of ZIF-8 particles suspended in an organic solvent during membrane processing. Although there are significant changes in the particle morphology, there are only minor losses in crystallinity and microporosity as proven from powder X-ray diffraction, synchrotron X-ray pair distribution function analysis and nitrogen physisorption. Dynamic light scattering and electron microscopy show that ZIF-8 nanoparticles undergo substantial Ostwald ripening when subjected to high intensity ultrasonication. Composite films prepared with both direct (high-intensity) and indirect (low-intensity) sonication show good adhesion between the polymer and ZIF-8 phases. However, films prepared using indirect sonication exhibit drastic agglomeration of nanoparticles while direct sonication produced ripened nanoparticles with variable dispersion. The ripened particles give lower pore volumes and lower surface areas compared to the as-synthesized material. ZIF-8/Matrimid® composite membranes prepared from the two different sonication methods show significant differences in microstructure. Permeation measurements in membranes fabricated with high-intensity sonication show strong enhancement in permeability of CO_2 and increased CO_2/CH_4 selectivity, in agreement with the Maxwell model. In contrast, composite membranes prepared with low-intensity sonication are found to be defective.[363]

Small and less agglomerated ZIF-20 with 8 wt% in a polysulfone Udel® P-3500 mixed matrix membrane gave a better separation of an equimolar O_2/N_2 mixture than the pure polymer. As in ZIF-8 the imidazolate moiety in the purinate ligands connects individual zinc atoms and forms the edges of a cuboctahedral β-cage but in a zeolite-A network (see figure 4.40b). The increase in O_2/N_2 selectivity from 4.7 (± 0.4) to 6.7 (± 0.5) in the MMM could be justified by the small difference in kinetic size between O_2 (kinetic diameter $d_k = 0.343$ nm) and N_2 ($d_k = 0.368$ nm).[364]

Submicrometer-sized particles of ZIF-90 (see figure 4.40b, sodalite network again as in ZIF-8) were used to fabricate nanocomposite membranes with three different polyimides [Ultem® 1000, Matrimid® 5218, and 6FDA-DAM (6FDA: 2,2-bis(3,4-carboxyphenyl) hexafluoro-propane dianhydride, DAM: diaminomesitylene)].[354] Scanning electron microscopy revealed an excellent adhesion of ZIF-90 crystals with the polyimides with no interfacial voids and well dispersed MOF crystals. Ultem® and Matrimid® MMMs showed significantly enhanced CO_2 permeability without any loss of CO_2/CH_4 selectivity.

ZIF-90 with the highly permeable polymer 6FDA-DAM showed significant enhancements in both CO_2 permeability and CO_2/CH_4 selectivity. Membranes containing smaller particles showed slightly better results. The performance of ZIF-90/6FDA-DAM MMM exceeded the polymer upper bound for polymeric membrane performance from 1991,[238] and reaches the technologically attractive region (see figure 4.30).[354]

The CO_2/CH_4 binary mixture gas-permeation properties of pure 6FDA-DAM and 15 wt% ZIF-90/6FDA-DAM membranes revealed an enhanced gas-separation performance of the MMM. The CO_2/CH_4 mixed-gas selectivity of the ZIF-90 MMM was higher than the ideal selectivity measured by single-component gas permeation, presumably because of selective sorption and diffusion of CO_2 in the ZIF-90 crystals.[354] Also, a ZIF-90/6FDA-DAM membrane showed an ideal CO_2/N_2 selectivity of 22 compared to 14 for pure 6FDA-DAM indicating the possibility for separation of CO_2 from flue gases.[354]

The MOF $Mn(HCOO)_2$, where each formiate ligand bridges between three manganese atoms (see figure 4.41a), has very small channels of ~2 Å diameter only, and hence, as PSF-MMM showed high adsorption affinity for H_2 only. Higher loadings reduced the gas solubility, but increased the permeability, indicating defective membranes with interfacial voids.[365]

An asymmetric membrane from MIL-53(Al) (or Cu-BTC or ZIF-8, see above) and Matrimid® 9725 showed a higher CO_2 permeance than the unfilled membrane in mixed gas permeation experiments.[357] The framework of MIL-53(Al) is a flexible, 'breathing'-type network, that is, it can assume different shapes and porosities depending on guest presence or absence. The BDC ligand bridges between four Al atoms. The hydroxo-bridging takes place along the metal chains in the b direction (see figure 4.41b).

The permeance of the preferentially permeating CO_2 in the binary gas mixtures CO_2/CH_4 and CO_2/N_2 with CO_2 concentrations from 10 vol% to 75 vol% increased with the filler loading for all three MOFs but the CO_2 selectivity slightly increased only in the case of Cu-BTC or MIL-53(Al) and remained almost constant for ZIF-8. Under the same conditions the CO_2 permeability remained invariant with the type of MOF for the CO_2/N_2

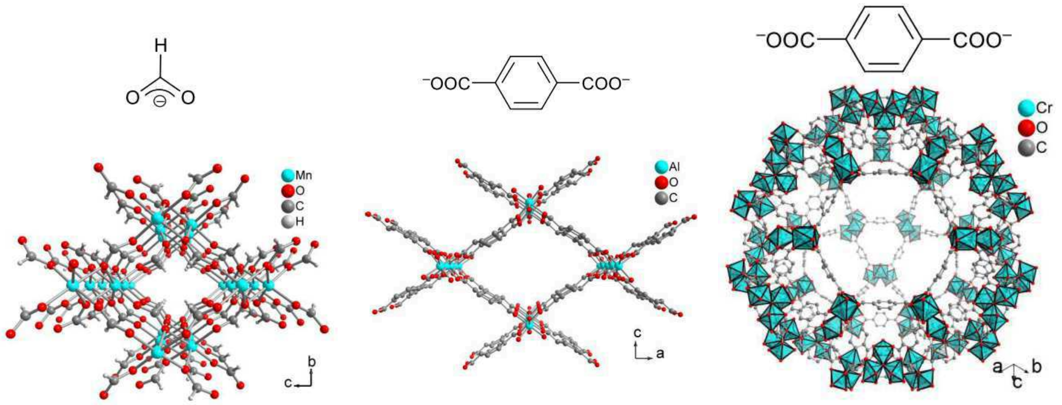

(a) (b) (c)

Figure 4.41.: Linkers and sections of the packing diagrams of (a) $Mn(HCOO)_2$, (b) MIL-53(Al), [Al(BDC)(μ-OH)] (BDC = benzene-1,4-dicarboxylate, terephthalate) and (c) MIL-101, $[Cr_3(O)(BDC)_3(F,OH)(H_2O)_2]$.

gas mixture. The CO_2/CH_4 selectivity α_{CO_2/CH_4} dropped linearly when the CO_2 content increased from 10 to 75 vol% for all three MOFs. The decrease in selectivity was essentially independent of the MOF filler content.[356;357]

A variant of MIL-53(Al), namely compound NH_2-MIL-53(Al) with the 2-aminobenzene-1,4-dicarboxylate linker (NH_2-BDC) but the same structure as MIL-53(Al) was used to fabricate nanocomposite membranes with PSF Udel® P-3500. The homogeneously distributed NH_2-MIL-53(Al) particles showed excellent adhesion with the polysulfone without any additional compatibilization. In contrast to most reported membranes, CO_2/CH_4 separation selectivity of NH_2-MIL-53(Al)/PSF-MMM increased with pressure due to the flexibility of the NH_2-MIL-53(Al) filler.[359]

Mixed-matrix membranes with the water-stable MOF MIL-101 in polysulfone Ultrason S 6100 N exhibited a remarkable four-fold increase (compared to pure PSF) in the permeability of O_2 to technically needed values above 6 barrer and a simultaneous high selectivity for O_2 over N_2 of 5-6. The largest cage in this network with MTN zeolite topology is shown here with an inner diameter of 34 Åand pore aperture windows up to 16 Å. The benzene-1,4-dicarboxylate ligands bridge between trinuclear Cr_3O building units (see figure 4.41c). The MIL-101 particles showed very good adhesion with polysulfone and long term stability.[366]

Single gas experiments of MIL-101/PSF membranes with CO_2, CH_4 and N_2 at different MOF loadings showed increases in gas permeabilities with increasing MIL-101 weight percentage in PSF (see figure 4.42). CO_2 is the preferentially permeating gas with permeability increases from about 5 to over 35 barrer from pure PSF to 20 wt% MIL-101/PSF. The increase for CO_2 also raises the ideal selectivities for CO_2/CH_4 and CO_2/N_2 from about 20 to 25.[367]

The CO_2 permeability is rather invariant to the thickness of the membrane (see figure 4.43) while the CH_4 and N_2 permeabilities decrease when the membrane becomes thicker for the same MIL-101 loading. Hence, the ideal CO_2/CH_4 and CO_2/N_2 selectivities strongly increase with the membrane thickness, in particular for CO_2/CH_4 (see figure 4.43c).[367]

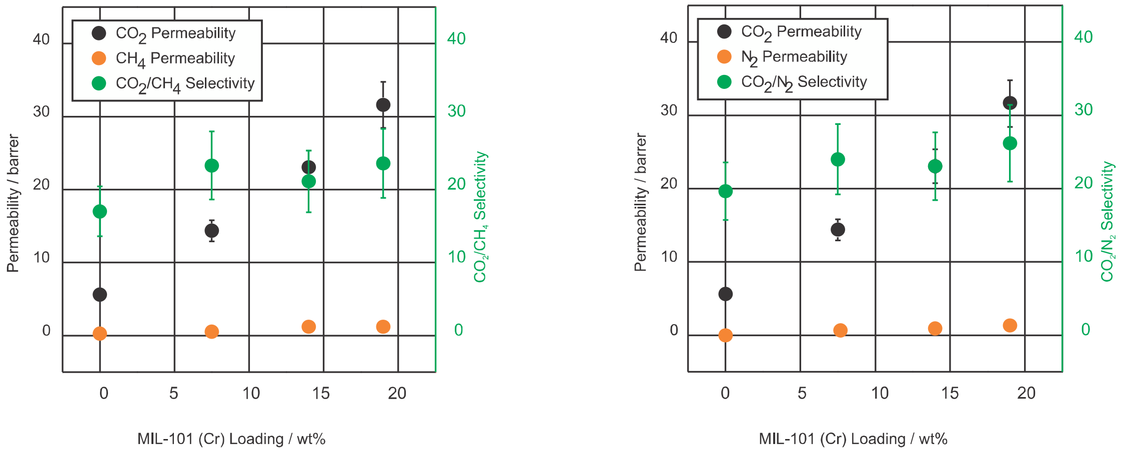

(A) (B)

FIGURE 4.42.: Single-gas CO_2, CH_4 and N_2 permeabilities and ideal (A) CO_2/CH_4 and (B) CO_2/N_2 selectivities of pure PSF and MIL-101/PSF membranes with different MIL wt% loadings (averaged values for different membrane thicknesses).

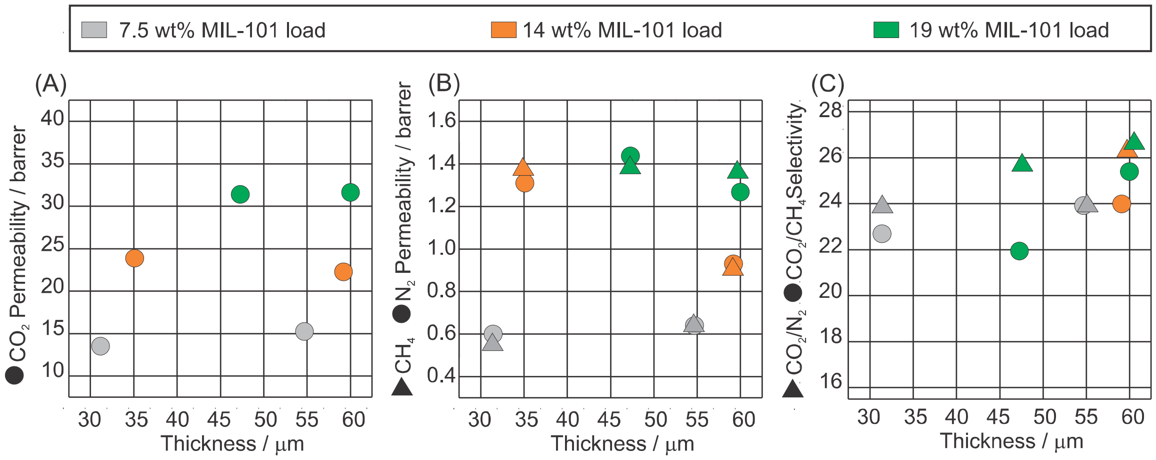

FIGURE 4.43.: (A) Single-gas CO_2, (B) CH_4 and N_2 permeabilities and (C) ideal CO_2/CH_4 and (C) CO_2/N_2 selectivities for MIL-101/PSF membranes at different MIL wt% loadings and membrane thicknesses.

4.3.6. Conclusion

Covalent crosslinking with maleimide derivatives as crosslinking unit can be investigated *in situ* in the liquid phase as well as in the solid phase using nanosecond transient UV/Vis absorption and FTIR measurements. Results point to maleimide anion formation via the triplet state and ionic dimerisation to the cycloadduct as main reaction path upon UV irradiation. Additionally, the 2-2'-adduct is formed either from the educt or in a consecutive reaction from the cycloadduct. For 6FDA-ODA/6FDA-DABA 4:1 with MI the photocrosslinking yield was determined to be ~6 %. The yield is restricted by the stiffness of the polymer backbone, which inhibits the photoreaction due to permanent spatial separation of the crosslinker side chains.

It has been shown for the separation of high-pressure mixtures of CO_2/CH_4 as well as for toluene/cyclohexane mixtures that the photocrosslinked copolyimide membranes are much more plasticization resistant than noncrosslinked copolyimide membranes. Generally covalent crosslinking results in much higher plasticization resistance and better selectivity than ionic crosslinking.

Mixed matrix membranes with metal-organic frameworks as additives (fillers) exhibit enhanced permeabilities and possibly also selectivities when compared to the underlying pure polymer. Matrimid® and polysulfone are popular polymer matrices for MOF fillers. MOF particle adhesion to these organic polymers does not represent a problem. Permeability increases can be traced to MOF porosity. Crucial permeability-selectivity factors worth further investigations are, *inter alia*, filler content, filler (nano)size and dispersion, gas-binding functional groups in filler (e.g. amines for CO_2), water-stability of MOF-filler[368–371] as well as mixed-gases with different volume fractions instead of single gases. Addition of MOFs to polymers in MMMs easily yields performances similar to the best polymeric membranes and selectivities 10 times higher than those reported to date for any pure MOF membrane for the respective separation. In the end MOF-polymer MMMs allow for an easier synthesis and handability compared to pure MOF membranes.[372–376]

4.3.7. Acknowledgments

The authors thank the German Research Foundation (KL 531/29-1) and the Anton-Betz-Stiftung (CJ) for their support.

4.3.8. Contributions

Title: Investigation of cross-linked and additive containing polymer materials for membranes with improved performance in pervaporation and gas separation.

Authors: Katharina Hunger, Nadine Schmeling, Harold B. Tanh Jeazet, Christoph Janiak, Claudia Staudt and Karl Kleinermanns.

Published in: Membranes (Impact Factor: 4.314)

In this review article, the findings presented in the two articles "Photo-cross-linking of poly[ethene-*stat*-(methacrylic acid)] functionalised with maleimide side groups" and "Characterization of Maleimide Dimers in Photo-Cross-Linked Copolyimide Films" are brought into context with other studies performed on polymeric membrane materials. The personal contributions to these results are described above. The presented separation and pervaporation experiments were performed by N. Schmeling and other members of the Staudt group. The first part of this review, which covers the effect of crosslinking on the separation characteristics of membranes, as well as the extensive introduction was completely written by me. The survey of literature required for this review was also my responsibility. The second part, which covers additive containing polymer membranes, was written by Christoph Janiak and Harold B. Tanh Jeazet.

5. Guanosine hydrogen transfer

5.1. UV light induced hydrogen transfer in guanosine-guanosine aggregates

Katharina Hunger*, Laura Buschhaus*, Lars Biemann*, Michaela Braun*, Sergey Kovalenko#, Roberto Improta†, Karl Kleinermanns*

* Department of Physical Chemistry, Heinrich-Heine-University, 40225 Düsseldorf, Germany

\# Department of Chemistry, Humboldt University, 12489 Berlin, Germany

† Istituto Biostrutture e Bioimmagini-CNR, 80134 Napoli, Italy

Accepted by *Chemistry - A European Journal*, 2013.

5.1.1. Abstract

Aggregates of a lipophilic Guanine (G) derivative have been studied in n-hexane by femtosecond-to-microsecond UV/VIS broad-band transient absorption, stationary infrared resp. UV/Vis spectroscopy and by quantum chemical calculations. We report the first time-resolved spectroscopic detection of hydrogen transfer in GG aggregates, which leads to (G-H)· radicals via G^+G^- charge transfer followed by proton transfer. These radicals show a characteristic electronic spectrum in the range 300-550 nm. The calculated superimposed spectrum of the species resulting from $NH \cdots N$ proton transfer agrees best with the experimental spectrum.

5.1.2. Introduction

Beside Watson-Crick (WC) base pairs in DNA, less common homodimers like GG play an important role in replication and transcription, especially in tRNA.[68;69] Sequences with G repeats exist in eukaryotic centromeres and telomeres which form hairpins at the end of linear chromosomes via GG H-bonding.[70;71] Their end acts as primer for the synthesis of the complementary DNA strand. Gradual loss of G from telomers is probably important in aging. In addition superstructures of DNA triplexes and quadruplexes are formed by GG base pairs and play a role in specific recognition mechanisms.[72] DNA damage and mutagenesis by formation of rare tautomers via hydrogen transfer along the GG and GC WC H-bonds has long been assumed to be induced by UV-light, however it is difficult to probe these processes directly by spectroscopy due to the complexity of DNA strands and collective modes of the DNA backbone.[60;61;144] In the absence of the backbone, IR-UV hole-burning spectra provide evidence for electron-driven interbase proton-transfer in WC base pairs.[149] Ab initio calculations show that this path is barrierless in WC but not in non-canonical base pairs.[67]

Here we report hydrogen transfer in GG aggregates by using nucleosides with bulky non-polar groups which sterically enforce specific hydrogen bonded G·G ribbon aggregation motifs and prevent stacking. The derivatized nucleoside is highly solvable in aprotic and

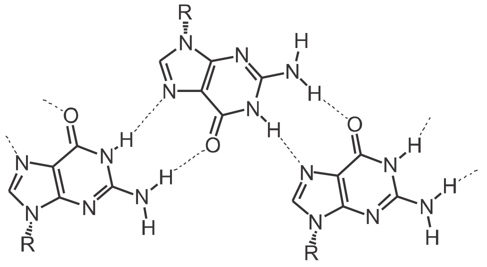

Figure 5.1: Structure of the Ribbon I motif in GG aggregates, formed by reverse Hoogsteen hydrogen bonds.

nonpolar solvents like n-hexane, where the formation of H-bonded aggregates is strongly favoured, whereas solvated monomers and probably also stacked complexes are generated in polar protic solvents like water. NMR investigations point to extended G ribbons as prevailing structures in concentrated solutions of derivatized guanine in chloroform and hydrocarbon solvents with two different H-bond arrangements.[377] Ribbon I is built by reverse Hoogsteen hydrogen bonding (figure 5.1), a motif which is also found in vivo in triple-helical DNA structures.

The biological functions of this structure are yet to be surveyed. However, it has been ascribed to play a role as molecular switch to modulate gene expression, in chromatin organization and DNA repair.[378;379] Recently, ribbon structures formed by G in self-assembly have gained much interest in material science. The highly ordered structures can be brought on solid surfaces by evaporation. In this form they can find application in electronic and optical devices, due to their optical and photoconductive properties.[377;380]

In this paper we follow the dynamics of the guanosine ribbons from the Franck-Condon (FC) region of the optical transition pumped at 266 and 284 nm to the formation of the (G-H)· radical.

5.1.3. Results and Discussion

Figure 5.2 shows the stationary infrared spectra of 0.8 mM 2',3',5'-O-tris (tert-butyl-dimethylsilyl) guanosine (displayed in figure 5.11, see supplementary information SI) (henceforth called G) in n-hexane as solvent. The IR spectral features in figure 5.2 point out, that only aggregate bands of guanosine are present in n-hexane whereas monomer and aggregate bands show up in the spectrum in figure 5.3 taken in $CDCl_3$. Below 3400 cm^{-1} are the stretch vibrations of the hydrogen bonded NH groups. At 3487 cm^{-1} in n-hexane and 3490 cm^{-1} in $CDCl_3$ the stretching vibration of the free NH (NH_f) in the hydrogen bonded NH_2-groups shows up. The NH stretch vibrations of the amine group of monomeric G (3410 cm^{-1} and 3516 cm^{-1} in $CDCl_3$) are not discernible anymore in n-hexane pointing to nearly complete GG aggregation under these conditions. figure 5.3 shows that 0.8 mM G in $CDCl_3$ as solvent lead to less aggregation with the monomer bands clearly visible. See also Biemann et al.[381] with similar results for C.

Our proposal of the prevailing GG ribbon structure with HNH···O=C and NH···N double hydrogen bonds as depicted in figure 5.1 (ribbon I in Ref.[377]) is based on the observed IR spectra and DFT calcuations, see figure 5.13. Our IR data clearly show that beside the ribbon I motif we have a minor quantity of ribbon II motifs with HNH···N and NH···O=C interactions in our solution of G in n-hexane (see figure 5.12 for structure of ribbon II). PCM/CAM-B3LYP calculations in solution on the trimer (see figure 5.4a)

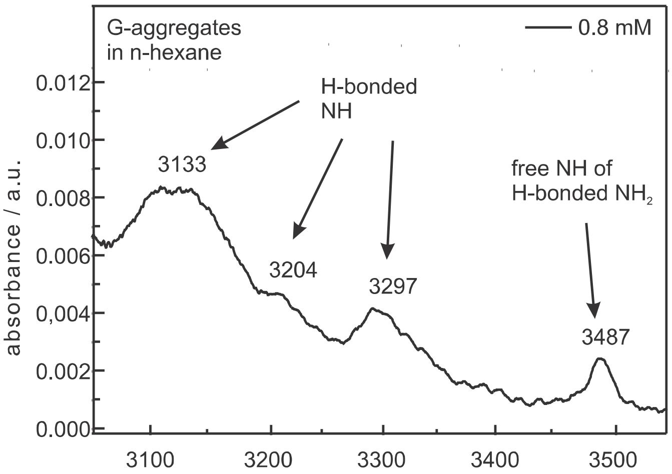

FIGURE 5.2: FT-IR measurements of 0.8 mM trisylilated guanosine in dry n-hexane.

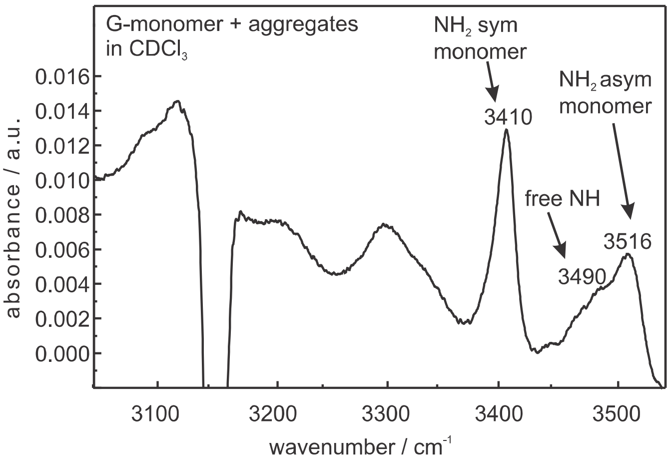

FIGURE 5.3: IR spectrum of 0.8 mM trisilylated guanosine in $CDCl_3$. No bands from water impurities could be detected in the IR experiments.

indicate that Ribbon I is more stable than Ribbon II by 0.16 eV (6-31G(d)) and 0.20 eV (6-311+G(2d,2p)), in agreement with the experimental indications.

The experimental absorption and fluorescence spectra of G in the UV/Vis spectral range are displayed in figure 5.5a for comparison with the calculated spectra in figure 5.5b. A description of the lowest energy singlet and triplet states is reported in Tab.5.1 and 5.2, respectively. There are three excited states in the trimer that are reminiscent of the lowest energy excited state of the monomer which is a bright HOMO-LUMO $\pi\pi^*$ transition (usually labelled as L_a).[382] Cartesian coordinates of the Ribbon I trimer and the L_a state of ribbon I trimer are reported in Tab.5.3 and 5.4. Analogously, there are three excited states similar to the HOMO-LUMO+1 transition of the monomer (usually labelled as L_b). The three $n\pi^*$ transitions are destabilized with respect to what is found in the monomer in non-polar solutions due to the presence of intermolecular hydrogen bonds. Their energy is more similar to that predicted in water, i.e. ~0.7 eV less stable than L_a-like transitions.[382]

Finally, we find several Charge Transfer (CT) transitions. The most stable CT transition (G2→G3, according to the atom labelling reported in figure 5.4a) is higher in energy by ~0.6 eV than the lowest energy transition at the Linear Response (LR)PCM/CAM-B3LYP level. TD-DFT calculations using standard functionals overestimate the stability of CT transitions, but this deficiency can be averted by the use of Long Range corrected functionals at the CAM-B3LYP level, which indeed provides fairly reliable estimate of CT transition energies.[383–386] Just to make an example, concerning intra-strand CT tran-

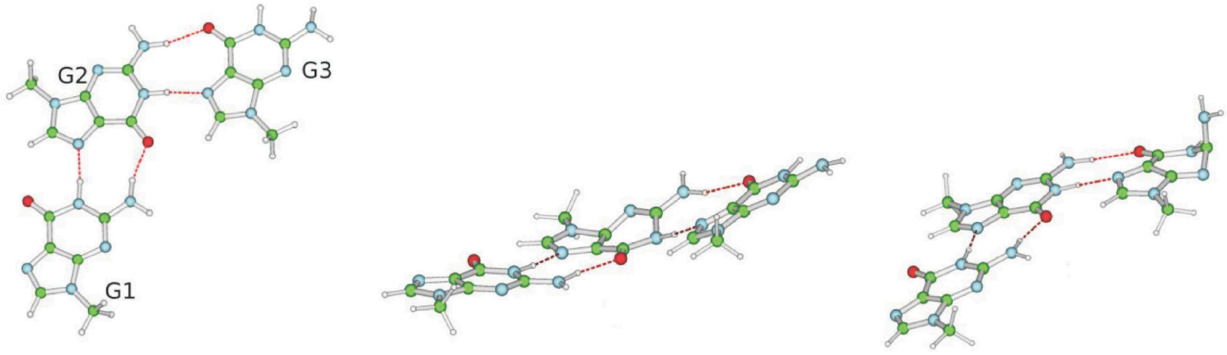

(a) (b) (c)

Figure 5.4.: (a) Schematic drawing of the L_a excited state minimum localized on G2. (b) Schematic drawing of the L_a excited state minimum localized on G2. (c) Schematic drawing of a representative structure of the crossing region between the L_a excited state localized on G3 and S_0.

sitions, CAM-B3LYP predictions are within 0.2 eV of those obtained at the CC2 level,[387] and a similar accuracy has been found for cytosine-guanine and adenine-thymine interstrand CT states.[383–386] In particular, CAM-B3LYP provides a description of the proton-coupled electron transfer in GC[383] and AT[386] pairs, extremely close to that obtained at the CASPT2 and at the CC2 levels.

On the other hand LR-PCM/TD-DFT calculations are known to underestimate solvent stabilization of CT excited states, and it would be necessary to resort to State Specific (SS) PCM methods.[388;389] SS-PCM/CAM-B3LYP/6-31G(d) calculations indeed predict that the G2→G3 CT transition is 0.45 eV lower in energy than the S_1 L_a-like excited state at the FC point. This value has to be considered with some caution: the CT transition energy is expected to be rather sensitive to the value of the radii used to build the PCM cavity, a parameter not investigated in detail for non-polar solvents. Furthermore in low-dielectric solvents transition energies could be sensitive to properties not considered in standard PCM treatments, such as the solvent polarizability.[390] Though CAM-B3LYP[391] is not biased by the deficiencies of 'standard' density functionals in the treatment of long range CT transitions, some overestimation cannot be excluded.

On the other hand, a G→G CT transition is not expected to be much less stable than a G→C CT transition, since the electron affinity of C is not significantly larger than that of G (∼0.2 eV,[392]). The G→C CT transition is known to be close in energy to the lowest excited electronic states in the gas phase, constituting the main excited state deactivation channel.[66] It is thus reasonable that the G2→G3 CT transition falls in the proximity of S_1 L_a-like excited states. The computed vertical excitation energies to the lowest energy triplets are collected in Tab.5.2. The nine lowest energy triplets can be described as three π-π^* triplets localized on the different G monomers, significantly more stable than the corresponding singlet excited states. The energy of the triplet G2→G3 CT is instead similar to that of its singlet counterpart, and it should therefore fall in the proximity of the spectroscopic singlet states.

Geometry optimizations of the three L_a-like states for 'external' G residues (G1 and G3) provide a picture very similar to that obtained for the isolated G monomer.[382] The system reaches a flat plateau (L_a-pla, mainly responsible for the monomer emission) and then a barrierless motion, involving mainly the out-of-plane motion of the NH_2 sub-

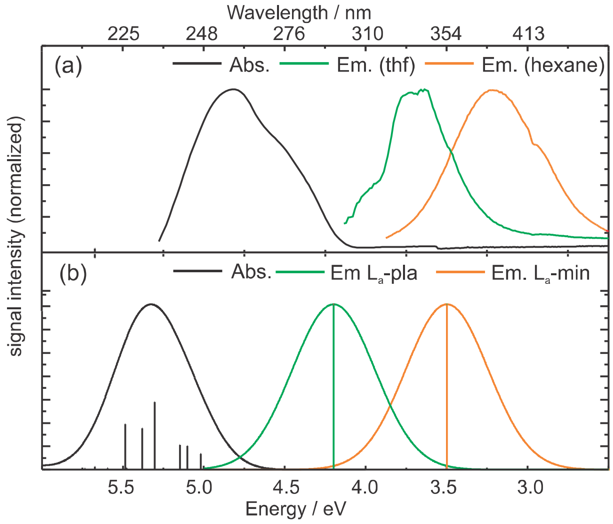

FIGURE 5.5: (a) Absorption and stationary fluorescence spectra of G in hexane and tetrahydrofurane (THF). Fluorescence bands with maxima at 390 nm in hexane compared to 330 nm in THF can be attributed to a higher degree of aggregation in non-polar hexane compared to the polar and H-bond solvent THF. (b) Computed absorption spectrum of Ribbon I in n-hexane, (LR-PCM/ TD-CAM-B3LYP/ 6-31+G(d,p) // PCM/ CAM-B3LYP/ 6-31G(d)), black. Computed emission spectra (SS-PCM/ TD-CAM-B3LYP/ 6-31+G(d,p) // PCM/ CAM-B3LYP/ 6-31G(d)), orange: L$_a$-min, green: L$_a$-pla. The curves are obtained by convoluting the stick spectra with a phenomenological Gaussian with HWHM=0.3 eV.

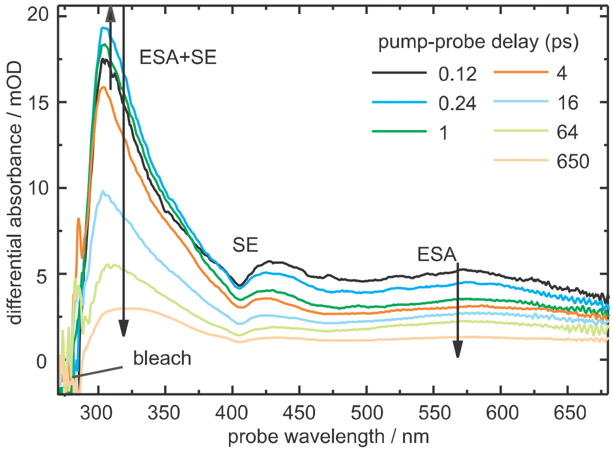

FIGURE 5.6: Femtosecond transient absorption spectra of trisylilated 6 mM G in n-hexane upon excitation at 284 nm.

stituent, leads to a crossing region with the ground electronic state (see figure 5.4a), and therefore to excited state deactivation. For the inner G2 residue, after the planar plateau the system decays to a real minimum of the PES (L$_a$-min), characterized by partial pyramidalization at the N3, C2 and C4 atoms. This minimum is stabilized by the hydrogen bonds with the G3 molecule which hinders the out-of-plane motion of the C2-NH$_2$ group. SS-PCM/CAM-B3LYP/6-31+G(d,p) calculations predict that the emission energy from the planar plateau is ∼4.2 eV, whereas emission from L$_a$-min appears at ∼3.5 eV, as shown in figure 5.5b. The computed absorption maximum (∼5.30 eV, PCM/PCM-B3LYP/6-31+G(d,p) calculations) is blue-shifted by ∼0.5 eV with respect to the experimental one (∼260 nm resp. 4:77 eV). We can thus associate emission from L$_a$-pla to the peak at 330 nm (∼3.75 eV) registered in THF, where the formation of hydrogen bonded aggregates is not as favoured as in hexane, and emission from L$_a$-min to the peak (∼390 nm, 3.20 eV) found in hexane.
Figure 5.6 shows the fs transient absorption spectra of 6 mM G in n-hexane, i.e. at concentrations where GG aggregation is complete. At early times the signal at about 300 nm

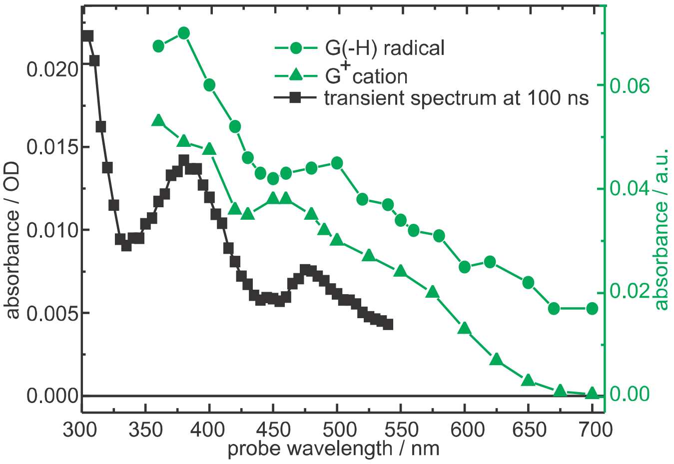

FIGURE 5.7: Spectrum of the neutral guanosine radical and of the G cation in water obtained by pulse radiolysis by Kobayashi et al.[393] (green) in comparison with the transient absorption spectrum measured by us (black).

first increases ($\tau_1 = 0.1$ - 0.2 ps) and then decays with similar time constants as the signal in the range 400-700 nm, namely $\tau_2 = 4$ ps, $\tau_3 = 40$ ps. The evolution is qualitatively similar to the behaviour of GMP in water at pH 7.[383] The time component τ_1 corresponds to fast molecular rearrangement when fluorescence in a flat local minimum of the excited state close to the Franck-Condon region (320 nm) decays and emission at about 400 nm appears. This red-shifted emission arises from a deeper S_1 potential minimum at lower energies and decays with τ_2 due to internal conversion into the electronic ground state S_0. The excited state minima discussed above are discernible as stimulated emission (negative absorption) contributions at ~320 and ~400 nm to the transient signal in figure 5.6 and as stationary fluorescence maximum at ~390 nm in figure 5.5a.
Beside these fast transients significant spectral contributions persist up to 650 ps ($\tau_4 >$ 650 ps) which is the largest pump-probe delay used in our fs experiments. The "late" spectrum shows an intensity minimum at about 410 nm followed by a signal increase up to around 310 nm. Below 310 nm the spectrum is obscured by the bleaching contribution (negative absorption) so that the true maximum of the band in the blue part of the spectrum cannot be determined. Above 410 nm the spectral intensity increases up to about 450 nm followed by a flat curve progressing up to 680 nm.
For elucidation of this temporally enduring spectral contribution we measured the transient spectrum at later times in our nanosecond pump-probe spectrometer. Figure 5.7 shows the spectral course at 100 ns delay and figure 5.14 exhibits persistence of this spectrum up to about 1.4 μs. The monoexponential lifetimes (figure 5.16) are slightly higher at wavelengths below 425 nm ($\tau = 291 \pm 26$ ns) than above ($\tau = 197 \pm 32$ ns). We observe these spectra only from solutions of protected G in n-hexane which are kept in the dark for 1-2 days. In fresh solutions no spectrum could be observed.
Figure 5.15 demonstrates complete quenching of the "late" transient spectrum by flushing the solution with oxygen. Since triplet species can be efficiently quenched by O_2, we assume that triplet states act as precursors for the transient spectrum observed on the ns time scale. We very tentatively assign the transient spectrum persisting up to 650 ps in the fs-experiment to triplet state absorption. For comparison, figure 5.7 shows the spectra of the G^+ radical cation and the neutral deprotonated G radical (G-H)· in water.[393] The transient spectrum at 100 ns is in good agreement with the electronic spectrum of the (G-H)· radical. The spectral course however is not specific enough to exclude contributions from the G radical cation or other species like ^{3}GG.
For comparison of the measured transient spectra with calculations we have explored the

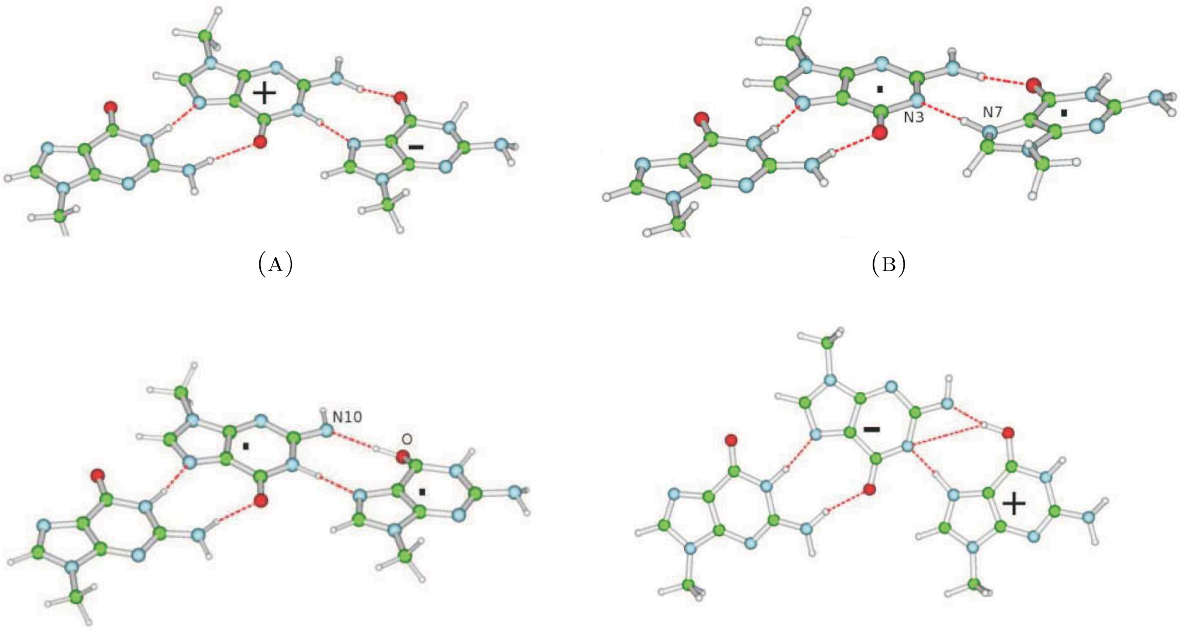

(A) (B)

(C) (D)

FIGURE 5.8.: Schematic drawing of the species which could be involved in the deactivation path of the G2G3 CT state.

reactivity of the G2→G3 singlet CT (^{1}GG$_{\mathrm{CT}}$) state. LR-PCM/CAM-B3LYP geometry optimizations predict that three exoergonic barrierless decay paths are possible, as depicted in figure 5.8 and figure 5.17. A proton transfer from N3-H of G2 cation to N7 of G3 anion can occur, leading to the formation of a (G-H)·/(G+H)· diradical species (path b in figure 5.8). The proton transfer reaction can involve an amino proton of G2 and the oxygen atom of G3 (path c in figure 5.8), leading to the (G-NH)·/(GOH)· diradical. A double proton transfer reaction is also possible (path d in figure 5.8), leading to the formation of the G enol form. From the thermodynamic point of view, path b is energetically favoured over path c and d by 0.21 eV and 0.42 eV, respectively (LR-PCM/CAM-B3LYP/6-31G(d) calculations). Interestingly, the three minima resulting from the proton transfer reactions are close in energy to the electronic ground state (S_1/S_0 energy gap in the range 1.4-0.6 eV), suggesting that these processes could act as deactivation paths for the GG excited states, in analogy with the findings for GC dimers in the gas phase.[66;394] Geometry optimization of the G2→G3 triplet CT (^{3}GG$_{\mathrm{CT}}$) provides the same conclusions. Three exoergonic barrierless paths are possible, involving proton transfer(s) and leading to stable triplet minima. The minimum resulting from path b is the favoured one, followed by path c (+0.18 eV) and path d (+0.33 eV), according to PCM/CAM-B3LYP/6-311+G(2d,2p)//PCM/CAM-B3LYP/6-31G(d) calculations. Interestingly, the minimum of the most stable ^{3}GG$_{\mathrm{CT}}$ state, which is formed in path b as precursor of the (G-H)·/(G+H)· diradical species, is the most stable triplet minimum. It is slightly more stable (0.01 eV) than the minimum of the $^3\pi\pi^*$ state localized on G2.

We have computed the absorption spectra of the different radical species at the LR-PCM/TD-CAM-B3LYP/6-31+G(d,p) level, optimized in n-hexane at the CAM-B3LYP/6-31G(d) level, together with that of the G^+ radical cation and G^- radical anion, which

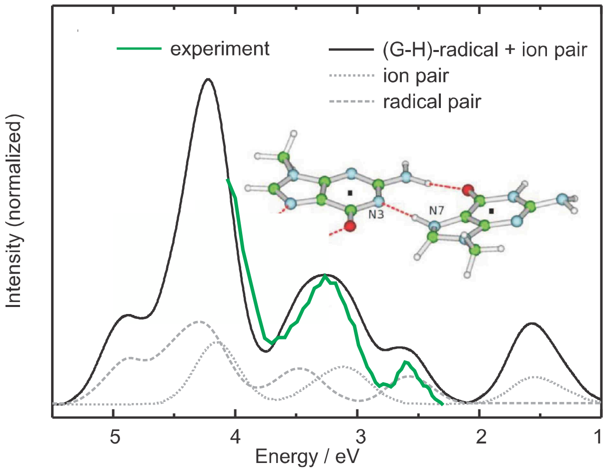

Figure 5.9: Comparison between experimental and calculated transient spectrum. The calculated spectrum (convolution with HWHM=0.2 eV) of G(N-H)G(N+H) was shifted to the blue by 0.3 eV and normalized to obtain an overlap with the experimental spectrum at 3.3 eV. The calculated spectrum of the ion pair was adjusted with the same parameters. The best agreement with the experimental spectrum is obtained with a 2:3 superposition of the calculated G(N-H) G(N+H)- and ion pair spectra.

would be the product of GG CT transfer if proton transfer reactions are slowed down by dynamical solvation effects, as in the GC dimer in $CHCl_3$,[383] (figure 5.17). It seems that path b agrees best with the experimental 100 ns spectrum, however, we cannot exclude a contribution of path a to our transient spectra.

Of the triplet-triplet absorption spectra computed for the three minima resulting from the GG CT deactivation paths and the optimized triplet radical ion pair (figure 5.18), path b shows the best resemblance with the experimental 100 ns spectrum (figure 5.19). Any superposition of path b and c results in less agreement than path b alone. By combination of the spectrum of the species obtained after proton transfer via path b with that of the radical ion pair present before H-transfer (path a), a very good agreement with the experimental spectrum is obtained, taking into account all the possible limitations of our theoretical treatment. The normalized 2:3 superposition (2 times path b + 3 times path a) is shown in figure 5.9.

At first glance, the observed transient lifetimes seem too long for radicals or radical ions in a solvent like hexane with a low dielectricity constant of 1.8. However, G aggregates are known to be photoconductive, hence G^+G^- charge separation via hole transfer is possible in large aggregates.[395;396] Due to the spatial separation, charge recombination is inhibited and as a result long lifetimes are observed. Thus we suggest that the late transient spectrum originates from the separated G radical ions as well as from the (G-H)· and (G+H)· radicals. This assumption is strengthened by the two different lifetimes observed. The absorption in the wavelength region of 335 - 425 nm is dominated by the radicals with $\tau_{rad} = 300$ ns and in the wavelength region of 425 - 540 nm by the radical ions with $\tau_{ion} = 200$ ns. The fact, that the 100 ns spectrum only is observed in solutions which were kept in the dark for 1-2 days, leads to the assumption that more extended networks of hydrogen bonded G are formed upon aging. These extended networks based on motifs as depicted in figure 5.1 are necessary for separation of the radical ions and thus prevent fast recombination. In fresh solutions, where extended networks are not yet formed, recombination of the radical ion pair occurs on a time scale faster than our ns-resolution.

It is known, what happens during aging in guanosine solutions in lipophilic solvents: In chloroform, ribbon I (which was found to be the solid state structure) is predominant directly after dissolution. Within several days the structure changes to ribbon II (which is thermodynamically more stable in chloroform). The rate of transformation is increased in the presence of water.[377] In hexadecane, ribbon I was observed exclusively, with no structural transition to ribbon II.[380] Our IR spectra show that ribbon I is the predomi-

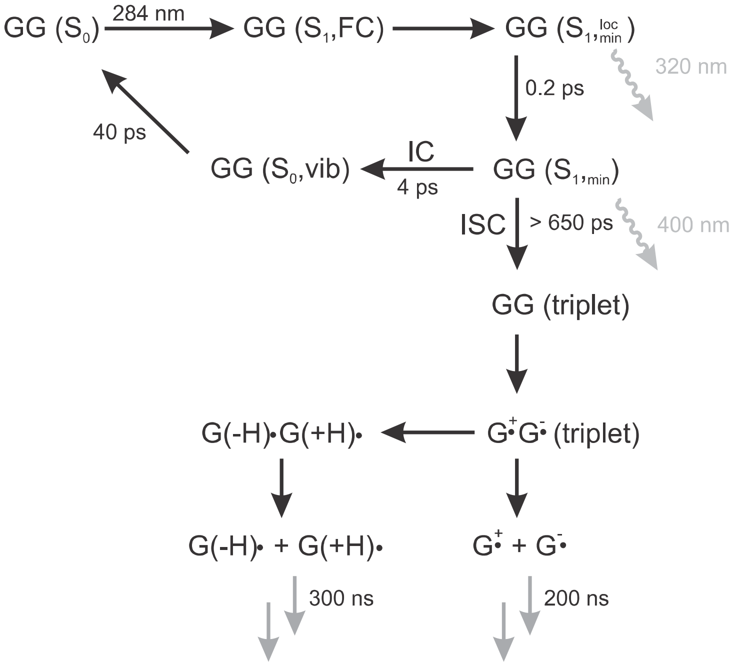

Figure 5.10: Proposed mechanism for H-transfer in GG aggregates. For detailed desription, see text.

nant structure in our solution of G in n-hexane, with a minor fraction of ribbon II (see figure 5.2). Since we observe no changes in the IR spectra of fresh and aged solutions, we conclude that no structural transition occurs. However, growth of the aggregates does not lead to changes in the IR spectrum. The extended aggregates have the same binding motifs as the shorter ones, thus the network size cannot be distinguished by IR spectroscopy. The observed time for generation of extended networks is consistent with the reorganisation times of several days observed in the studies on guanosine derivatives mentioned above.[377;380]

A possible scheme for our findings is depicted in figure 5.10. After relaxation of the initially excited S_1 state of the GG aggregates and ISC to an energetically nearby triplet $\pi\pi^*$- or $n\pi^*$- state the system internally converts to a triplet charge transfer (^{3}CT) state (transfer of HOMO electron density of one G moiety to the LUMO of its H-bonded counterpart) leading to a G^+G^- radical ion pair. Shortly after the electron follows the proton along the $NH\cdots N$ or $NH\cdots O{=}C$ pathways leading to the (G-H)·/(G+H)· radical pair which subsequently dissociates, reacts back or possibly converts to other products like the G enol form. Our calculations suggest that, among these possible paths, path b with $NH\cdots N$ proton transfer is the more likely. The G^+G^- radical ion pair can also be separated by hole transfer, whereby proton transfer is inhibited.

Further work will be directed towards detection of the (G-H)· radical in G repeats of centromeres and telomeres and superstructures of DNA triplexes and quadruplexes where stacking occurs and thus enables exciplex formation as a competing deactivation channel.

5.1.4. Materials and Methods

The guanosine derivative was synthesized according to Sheu and Ogilvie[397;398]. For detailed information, see figure 5.11.

Stationary absorption spectra were recorded with a Shimadzu UV-3101 spectrophotometer. Stationary emission was measured with a Spex Fluorolog 212 upon excitation at 267 nm. The spectra were corrected for the instrument response.

FTIR spectra were performed using a Nicolet 5700 spectrometer (Thermo Scientific) with a MCT detector. All samples were measured in transmission mode at room temperature. The sample chamber was flushed with dry, CO_2 free air during the measurements. 32 scans in the forward backward mode were averaged for each spectrum with a spectral resolution of 2 cm^{-1}. A cell with CaF_2 windows and a 3 mm spacer was used (International Crystal Laboratories). All the measurements were performed at ambient temperature (21 °C).

In the femtosecond transient absorption setup the Ti:Sa amplifier (Femtolasers) provides basic 30 fs pulses of 500 µJ at 800 nm with a 140 Hz repetition rate. The beam is split in two parts. 420 µJ are used to pump an optical parametric amplifier (TOPAS, Light Conversion) which delivers 50 fs, 5 µJ pump pulses at 284 nm. The remaining 80 µJ are converted into second harmonic 400 nm, 15 µJ pulses in a 0.2 mm BBO crystal. The probe supercontinuum is generated by focusing the 400 nm pulses into a 1 mm CaF_2 plate. The probe light is spectrally altered with a dye solution flowing in a 0.3 mm cell and then split for the signal and reference. The signal beam is imaged onto the sample flow cell to a spot size of 100 µm. The sample has typically an absorbance A = 0.7 over a 0.3 mm thickness. The signal and reference light is dispersed with homemade grating spectrographs and finally registered by photodiode arrays with 512 pixels (S39901-512Q, Hamamatsu) covering the spectral range 270-690 nm.

The nanosecond transient absorption setup (Applied Photophysics) utilises the output from a frequency quadrupled (266 nm) pulsed Nd:YAG laser (Innolas) for guanosine photoexcitation. The solutions (0.8 mM G in n-hexane) were excited with 70 mJ pump energy at 15 ns laser pulse width and 1 Hz repetition rate. The pump beam of 1 cm diameter is directed into the sample at right angle to the probe beam. A 0.4 mL cuvette with 1 cm length in the pump beam direction and 1 mm length in the probe beam direction was used. The samples were purged with dry nitrogen to remove dissolved oxygen from the solutions. For sensitive measurements of absorbance changes we use a high intensity pulsed xenon lamp (150 W, 1.5 ms) as probe source. Behind the sample the probe light is dispersed by a grating monochromator for wavelength selection. The output signal is detected by a photomultiplier (R928, 250-800 nm), digitized by an oscilloscope (Agilent Infinium) and transferred to a workstation (Iyonix). Typically 20 laser pulses are averaged to record a kinetic trace at a selected wavelength. The displayed spectra are averaged over five measured spectra.

Geometry optimizations were performed in aqueous solution at CAM-B3LYP[391] or the TD-CAM-B3LYP levels, by using 6-31G(d) basis set[399] and including bulk solvent effects by the polarizable continuum model (PCM).[390] Excited state geometry optimizations in solution have been performed by using the 'standard' LR (linear-response) implementation of PCM/TD-DFT, for which analytical gradients are available.[400;401] All the calculations were performed by the Gaussian09 Program.

5.1.5. Acknowledgements

The Düsseldorf group thanks the Deutsche Forschungsgemeinschaft (Kl 531/29-1) for financial support. R.I. thanks MIUR (PRIN 2008 and FIRB Futuro in Ricerca 2008) for financial support.

5.1.6. Supplementary Information

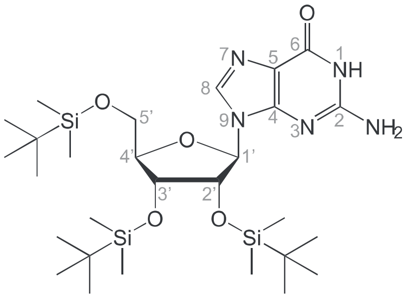

FIGURE 5.11.: Silylated guanosine: 2',3',5'-O-Tris(tertbutyldimethylsilyl)guanosine used in the experiment.

For preparation of 2´,3´,5´-O-tris(tert-butyldimethylsilyl)guanosine, 2.025 g guanosine (SIGMA, 98 %), 4.817 g imidazole and 4.255 g TBDMSCl (tert-butyldimethylsilylchloride) were solved under nitrogen in 30 ml dry DMF (dimethylformamide). The solution was stirred for 24 h at room temperature. Afterwards 20 ml water and 20 ml ethyl acetate were added. The aqueous phase was washed three times with 20 ml ethyl acetate and the joined organic phases were dried over $MgSO_4$. After filtration the solution was reduced under vacuum to yellow oil. The product was precipitated as a white solid by addition of 20 ml water and dried under vacuum. The sample was characterized by NMR spectroscopy and mass spectrometry.
^{1}H-NMR (500 MHz, DMSO-d_6): δ = -0.18 (s, 6H, $Si(CH_3)_2$), -0.01 (s, 6H, $Si(CH_3)_2$), 0.00 (s, 6H, $Si(CH_3)_2$), 0.81 (2s, 27H, $SiC(CH_3)_3$), 3.60 - 3.77 (m, 2H, 5´-H), 3.85 (m, 1H, 4´-H), 4.07 (m, 1H, 2´-H), 4.49 (m, 1H, 3´-H), 6.36 (s, 1H, 1´-H), 6.91 (s, 2H, NH_2), 7.79 (s, 1H, 1-H), 10.52 (s, 1H, NH) ppm.
^{13}C-NMR (125 MHz, DMSO-d_6): δ = -5.14, -5.10, -5.09, -4.44, -4.40,-4.30 ($Si(CH_3)_2$), 17.93, 18.17, 18.39 ($SiC(CH_3)$), 25.83, 26.10, 26.21 ($SiC(CH_3)_3$), 63.34 (5´-C), 73.30 (3´-C), 75.58 (2´-C), 85.39 (1´-C), 86.11 (4´-C), 116.69 (2-C), 135.47 (1-C), 151.98 (5-C), 154.25 (4-C), 157.09 (3-C) ppm.
ESI: m/z : 626 [M]+, 649 (+Na+), 511 ($-Si(CH_3)_2C(CH_3)_3$).

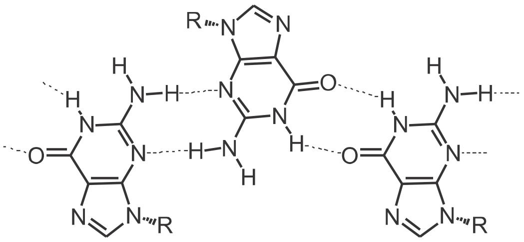

FIGURE 5.12.: Structure of the Ribbon II motif in GG aggregates.

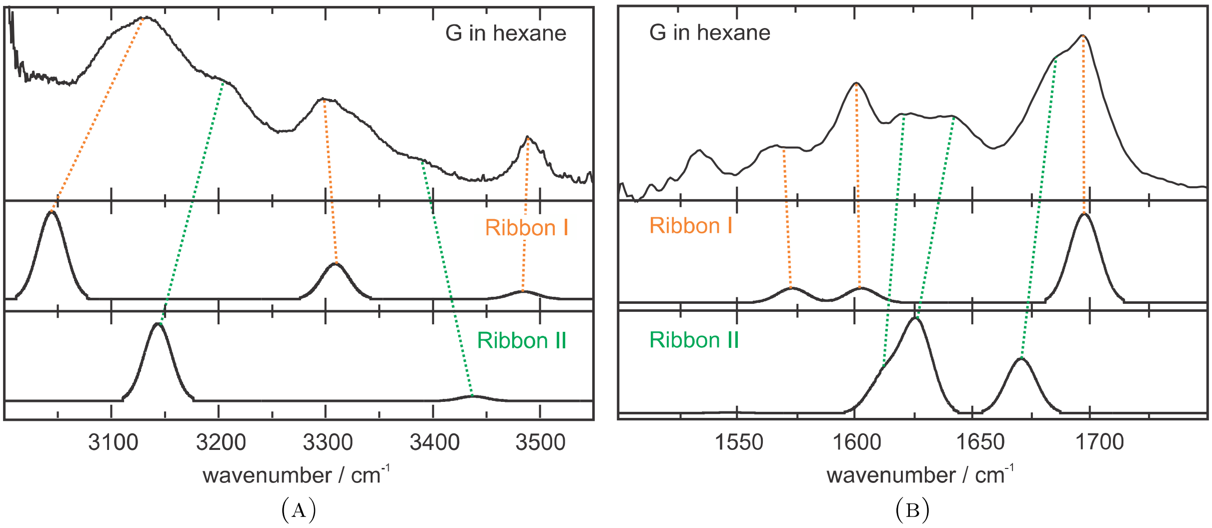

(A)

(B)

Figure 5.13.: Comparison of the experimental spectrum of G aggregates in n-hexane with the calculated spectra of the ribbon I and ribbon II structural motifs (DFT-B3LYP/ TZVP).

In ribbon I the fHNH···O=C stretch vibration (3487 cm^{-1}) fits very well with the experiment (3487 cm^{-1}). According to the calculations the free NH stretch vibration in the fHNH···N hydrogen bonds containing dimer absorbs at a much lower frequency of 3438 cm^{-1} in ribbon II. However, no IR absorption is observed in this spectral region. Furthermore, the H-bonded HNH···O=C stretch vibration in ribbon I (3308 cm^{-1}) is found in the experiment (3297cm^{-1}). In this spectral area no absorption band is expected in ribbon II. Therefore we hypothesize ribbon I[377] to be the prevalent structure for our G in n-hexane. This is in agreement with NMR and IR investigations from Giorgi et al.[377] for guanosines with different bulky substituents as obtained in crystals, in a dry film and in hydrocarbon solvents. We have a high contribution of ribbon I motif and minor contribution of ribbon II motif in our hexane solution. All IR frequencies are scaled to the free NH stretch vibration of H bonded NH2 in ribbon I at ~3487 cm^{-1} (factor: 0.94).

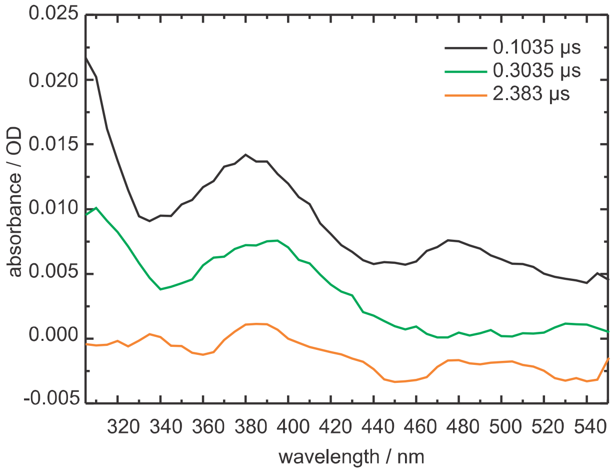

FIGURE 5.14: Transient absorption spectra of a 0.8 mM solution of guanosine in n-hexane at different pump-probe delays after laser excitation at 266 nm. The solution was deaerated with N_2. The measurements were performed in a 1 mm cuvette. The spectra could only be observed in n-hexane solutions older than two days. The decay times were fitted monoexponentially and vary between 200 ns and 300 ns (figure 5.17c).

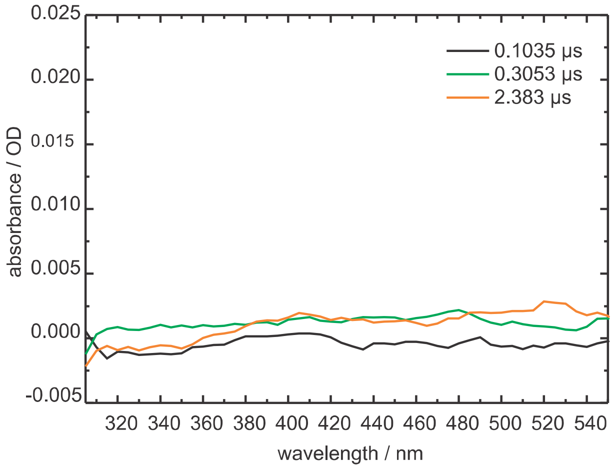

FIGURE 5.15: Transient absorption spectra of a 0.8 mM solution of guanosine in n-hexane at different times after laser excitation. The solution was flushed with O_2. The measurements were performed in a 1 mm cuvette. The absorption bands observed in the N_2-flushed solution (figure 5.17a) are quenched by oxygen. Therefore it is assumed that the triplet state (or a long-lived singlet state with a lifetime longer than the diffusion time of O_2) is a precursor for the formation of the radical.

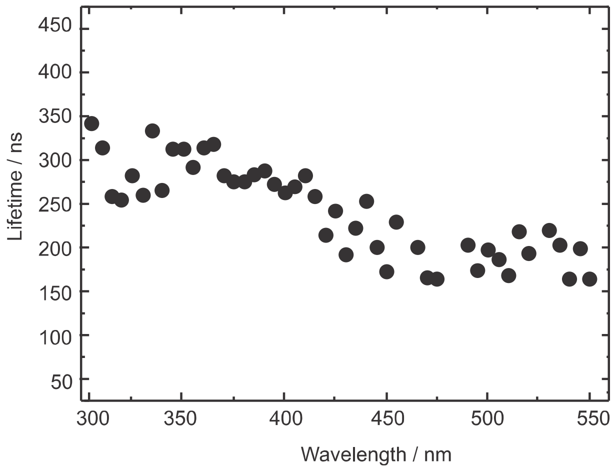

FIGURE 5.16: Excited state lifetimes of a 0.8 mM solution of guanosine in n-hexane at different wavelengths. The kinetic curves were fitted monoexponentially. The lifetimes vary between 291 ± 26 ns below and 197 ± 32 ns above 425 nm.

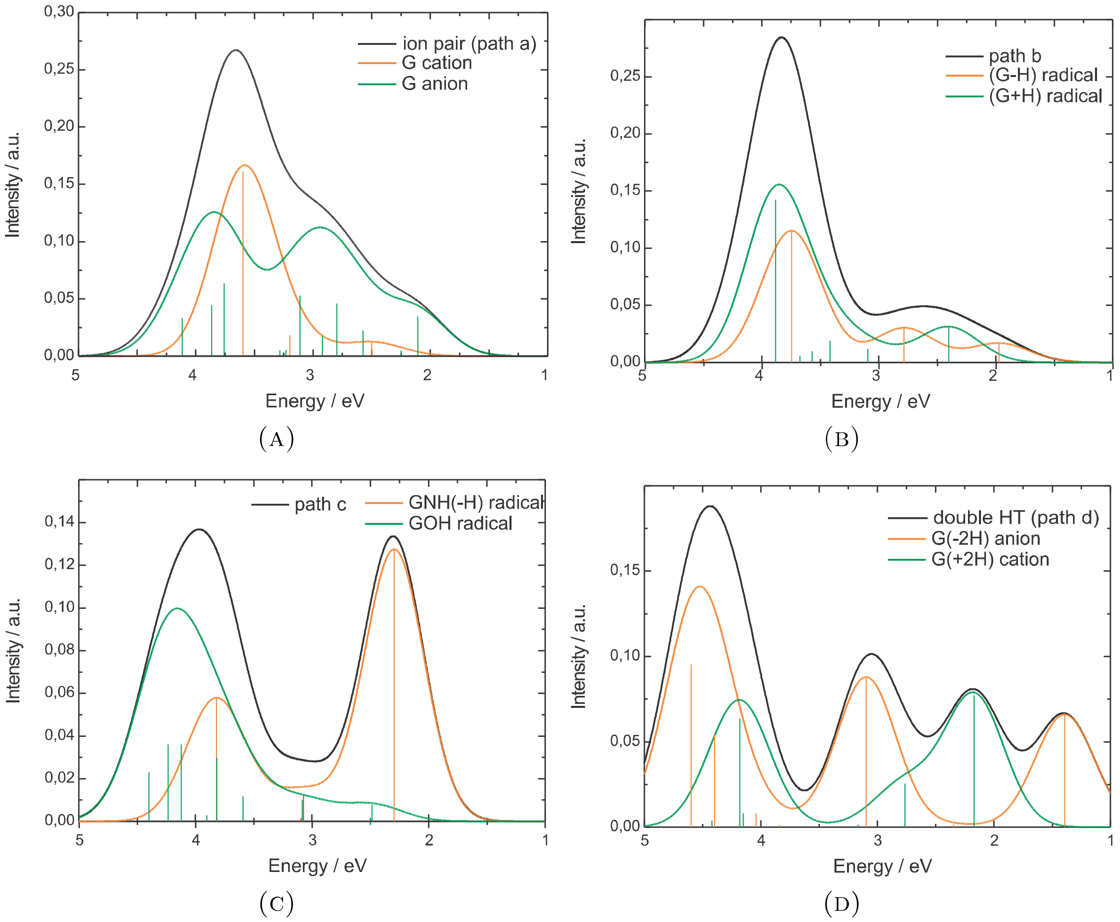

FIGURE 5.17.: Computed absorption spectra of the species involved in the possible deactivation paths of G2→G3 CT state. (A) Spectra of the G^+ cation and G^- anion; (B) spectra of the species resulting from a proton transfer from N3-H of G2 cation to N9 of G3. c) Spectra of the species resulting from a proton transfer from NH_2 group of G2 cation to O atom of G3. (D) Spectra resulting from the double G2→G3 proton transfer. The curves are obtained by convoluting the stick spectra with a phenomenological Gaussian with HWHM=0.3 eV. Black curves are the spectra resulting from the sum of the spectra of the radical/ion species involved in each path.

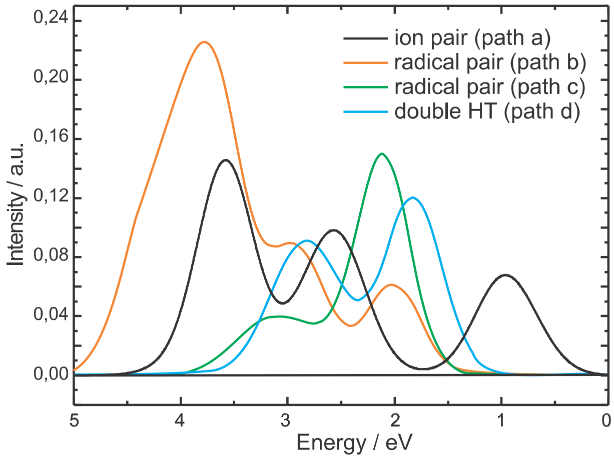

Figure 5.18: Computed absorption spectra of the triplet species involved in the possible deactivation paths of G2→G3 3CT state. Black: spectrum of the G^+ cation and G^- anion; red: spectrum of the species resulting from a proton transfer from N3-H of G2 to N9 of G3 (path b); green: spectrum of the species resulting from a proton transfer from NH_2 of G2 cation to O of G3 (path c); blue: spectrum resulting from the double G2→G3 proton transfer (path d). The curves are obtained by convoluting the stick spectra with a phenomenological Gaussian with HWHM=0.3 eV.

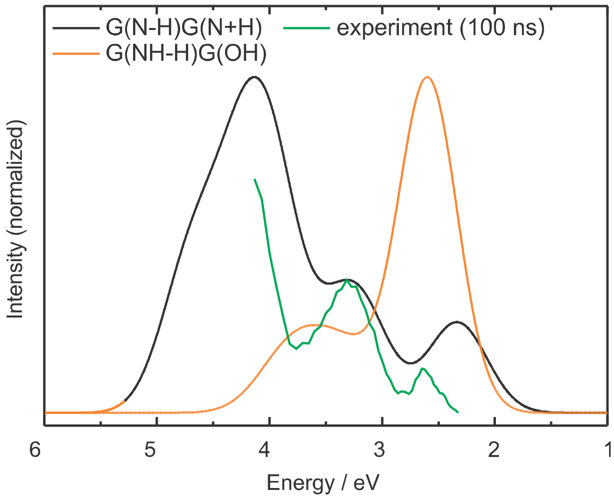

Figure 5.19: Comparison between experimental and calculated transient spectra. The calculated spectrum of G(N-H) G(N+H) was shifted to the blue by 0.3 eV and normalized to obtain an overlap with the experimental spectrum at 3.3 eV. The calculated spectrum of G(NH-H) G(OH) was adjusted with the same parameters. The spectrum of G(N-H) G(N+H) (path b) agrees better with the experimental 100 ns spectrum than that of G(NH-H) G(OH) (path c). Superposition of both spectra does not lead to a better agreement with the measured spectrum.

TABLE 5.1.: Vertical excitation energies of lowest energy singlet excited states computed for Ribbon I model by using LR-PCM/TD-CAM-B3LYP calculations on PCM/CAM-B3LYP/6-31G(d) minimum. Oscillator strengths are given in parentheses. See figure 5.11 for the guanine labelling.

States	6-31G(d)	6-31+G(d,p)	6-311+G(2d,2p)
$\pi\pi^*$ L_a G2	5.17(0.15)	5.02(0.13)	4.94(0.09)
$\pi\pi^*$ L_a G3	5.23(0.20)	5.10(0.20)	5.02(0.18)
$\pi\pi^*$ L_a G1	5.28(0.16)	5.15(0.21)	5.07(0.23)
$\pi\pi^*$ L_b G2	5.62(0.65)	5.38(0.36)	5.32(0.36)
$\pi\pi^*$ L_b G1	5.64(0.37)	5.30(0.58)	5.24(0.58)
$\pi\pi^*$ L_b G3	5.68(0.26)	5.49(0.39)	5.41(0.40)
$n\pi^*$ G1	5.66(0.00)	5.65(0.00)	5.61(0.00)
$n\pi^*$ G3	5.89(0.00)	5.85(0.00)	5.85(0.00)
$n\pi^*$ G2	5.90(0.00)	5.88(0.00)	5.86(0.00)
CT G2→G3	5.78(0.03)	5.67(0.03)	5.60(0.03)
CT G1→G3	5.89(0.00)	5.84(0.00)	5.77(0.00)
CT G1→G2	5.92(0.00)	5.89(0.00)	5.80(0.00)

TABLE 5.2.: Vertical excitation energies of lowest energy triplet excited states computed for Ribbon I model by using LR-PCM/TD-CAM-B3LYP calculations on PCM/CAM-B3LYP/6-31G(d) minimum. See figure 5.11 for the guanine labelling.

States	6-31G(d)	6-31+G(d,p)	6-311+G(2d,2p)
$\pi\pi^*$ G2	3.77	3.72	3.65
$\pi\pi^*$ G3	3.83	3.78	3.71
$\pi\pi^*$ G1	3.89	3.84	3.76
$\pi\pi^*$ G1	4.04	4.01	3.98
$\pi\pi^*$ G3	4.07	4.04	4.01
$\pi\pi^*$ G2	4.12	4.09	4.06
$\pi\pi^*$ G1	4.99	4.93	4.87
$\pi\pi^*$ G2	5.00	4.96	4.90
$\pi\pi^*$ G3	5.00	4.97	4.91
$n\pi^*$ G1	5.19	-	-
$n\pi^*$ G1	5.43	-	-
$n\pi^*$ G3	5.49	-	-
CT G2→G3	5.76	-	-

Table 5.3.: Cartesian coordinates of the Ribbon 1 trimer minimum as optimized at the PCM/CAM-B3LYP/6-31G(d) level in hexane.

Atomic number	X	Y	Z	Atomic number	X	Y	Z
7	-4.054432	-0.097836	0.116743	6	-5.342899	0.467752	0.057621
6	-6.340274	-0.561731	-0.015487	6	-5.917936	-1.883993	-0.023397
7	-4.662979	-2.382296	0.031857	6	-3.753828	-1.428974	0.104804
7	-7.060498	-2.631196	-0.103289	6	-8.103116	-1.728925	-0.138718
7	-7.716987	-0.487031	-0.089031	6	-7.133757	-4.074736	-0.137358
8	-5.476160	1.686310	0.072313	7	-2.446305	-1.760361	0.198295
1	-1.681881	-1.089837	0.110474	1	-2.232869	-2.737236	0.076137
1	-3.284801	0.593290	0.148402	1	-9.128561	-2.069783	-0.202597
1	-6.717293	-4.502648	0.777811	1	-6.574813	-4.465045	-0.991037
1	-8.179823	-4.371271	-0.227782	6	0.283306	0.959447	-0.003951
6	-0.691486	1.995584	0.042482	6	-0.271169	3.314960	0.012039
7	0.988719	3.789465	-0.052090	6	1.888240	2.823941	-0.091587
7	1.573428	1.489330	-0.069726	7	-1.418051	4.063054	0.060447
6	-2.463118	3.171115	0.115932	7	-2.063445	1.930907	0.108523
6	-1.493464	5.509934	0.049713	7	3.196340	3.135346	-0.169960
8	0.109574	-0.264897	0.005667	1	-3.500020	3.477965	0.155610
1	-1.059421	5.906035	-0.870813	1	-0.950876	5.923110	0.902540
1	-2.541189	5.805315	0.110869	1	2.331722	0.785800	-0.094280
1	3.954073	2.455190	-0.137626	1	3.428991	4.115081	-0.139913
8	5.719014	1.563334	-0.107810	6	5.864983	0.346199	-0.070531
6	4.882940	-0.685202	-0.051415	7	3.513099	-0.601354	-0.069454
7	7.159577	-0.209699	-0.030105	6	7.454548	-1.551246	0.022925
1	7.907989	0.472370	0.008577	7	8.772703	-1.880651	0.107958
1	8.968819	-2.864626	-0.009659	1	9.466449	-1.252427	-0.270347
7	6.546587	-2.491899	0.039544	6	5.283892	-2.007239	0.011212
7	4.129702	-2.740767	0.030399	6	3.096658	-1.836505	-0.018922
1	2.055081	-2.128723	-0.012703	6	4.032716	-4.188382	0.098997
1	5.045537	-4.589941	0.100979	1	3.521732	-4.493313	1.014505
1	3.492110	-4.574358	-0.767456				

Table 5.4.: Cartesian coordinates of the L_a-minimum in Ribbon 1 trimer minimum as optimized at the PCM/TD-CAM-B3LYP/6-31G(d) level in hexane.

Atomic number	X	Y	Z	Atomic number	X	Y	Z
6	-0.273098	1.070345	0.699966	6	0.699642	2.085392	0.582168
6	0.284182	3.481678	0.428107	7	-0.913685	3.739939	-0.133283
6	-1.833559	2.783909	0.060088	7	-1.602233	1.616821	0.759955
7	1.479921	4.128795	0.026280	6	2.453940	3.198465	0.041185
7	2.027398	1.979336	0.330263	6	1.612650	5.543807	-0.224314
7	-3.071497	3.000838	-0.405218	8	-0.116838	-0.165376	0.781079
1	1.402273	6.114685	0.685789	1	0.906634	5.848700	-1.000872
1	2.629252	5.754608	-0.558530	1	-2.325407	0.887827	0.677048
1	3.493245	3.412329	-0.180283	1	-3.867788	2.375720	-0.257222
1	-3.228051	3.863895	-0.904816	7	3.939884	-0.111588	0.113838
6	5.193946	0.419970	-0.240451	6	6.166709	-0.626998	-0.362322
6	5.755780	-1.933210	-0.132375	7	4.533090	-2.399957	0.202957
6	3.646106	-1.429349	0.318775	7	6.870360	-2.703356	-0.317892
6	7.886492	-1.829818	-0.645266	7	7.508852	-0.584939	-0.683073
6	6.944575	-4.140488	-0.178429	8	5.322703	1.629919	-0.397450
7	2.376935	-1.720856	0.674332	1	1.609282	-1.045449	0.671112
1	2.153398	-2.699742	0.752533	1	3.192163	0.594136	0.220357
1	8.886676	-2.192927	-0.844252	1	6.219715	-4.623533	-0.837432
1	6.734042	-4.439643	0.851382	1	7.949432	-4.468606	-0.448477
8	-5.624721	1.559016	-0.331436	6	-5.761008	0.340410	-0.264274
6	-4.797804	-0.661526	0.042118	7	-3.465824	-0.540076	0.348549
7	-7.014209	-0.246712	-0.524552	6	-7.287492	-1.594299	-0.502798
1	-7.736627	0.407085	-0.803278	7	-8.558068	-1.959490	-0.831569
1	-8.768885	-2.933083	-0.662502	1	-9.316224	-1.318006	-0.648981
7	-6.394817	-2.510781	-0.233281	6	-5.170106	-1.993426	0.018789
7	-4.036304	-2.695721	0.316907	6	-3.043117	-1.763684	0.503582
1	-2.023306	-2.030045	0.747743	6	-3.920840	-4.139410	0.408045
1	-4.168063	-4.599594	-0.550504	1	-2.894128	-4.389636	0.674886
1	-4.597402	-4.523573	1.173697				

5.1.7. Contributions

Title: UV light induced hydrogen transfer in guanine-guanine aggregates.

Authors: Katharina Hunger, Laura Buschhaus, Lars Biemann, Michaela Braun, Sergey Kovalenko, Roberto Improta and Karl Kleinermanns.

Accepted by: Chemistry - A European Journal (Impact Factor: 5.925)

The time resolved UV/Vis spectra on the nanosecond time scale and the stationary emission spectra were measured under my supervision by L. Buschhaus in the scope of her Diploma thesis. The ps transient absorption spectra were measured by Sergey Kovalenko and the stationary IR spectra by Lars Biemann. The calculated IR frequencies were obtained by Michaela Braun, all further quantum mechanical calculations were performed by Roberto Improta. The conjunction and interpretation of all these results was done by K. Kleinermanns with my assistance.

6. Long-lived emission of DPH

6.1. Intense long-lived fluorescence of 1,6-diphenyl-1,3,5-hexatriene: Emission from the S_1-state competes with formation of O_2 contact charge transfer complex

KATHARINA HUNGER AND KARL KLEINERMANNS

INSTITUTE OF PHYSICAL CHEMISTRY, HEINRICH-HEINE UNIVERSITY DUESSELDORF, 40225 DUESSELDORF, GERMANY

Accepted by *Open Journal of Physical Chemistry.*

6.1.1. Abstract

The fluorescence kinetics of 1,6-diphenyl-1,3,5-hexatriene (DPH) dissolved in cyclohexane was investigated as a function of temperature, concentration and 355 nm excitation pulse energy. At concentrations above 2.5 μM and excitation energies above 1 mJ a long-lived, very intense emission, which appears within less than 5 ns and lasts up to 70 ns, is observed. During the first 50 ns the decay does not follow an exponential but rather a linear behaviour. In oxygen saturated solutions the long-lived emission is suppressed and solely short-lived fluorescence with $\tau < 5$ ns can be detected. A kinetic simulation was performed, based on a model whereupon the long-lived emission originates from the S_1-state and competes with the formation of DPH - O_2 contact charge-transfer complexes and intersystem crossing which both quench the fluorescence. Our investigations show that even the small amount of oxygen dissolved in nitrogen saturated solutions has a distinct influence on the fluorescence kinetics of DPH.

6.1.2. Introduction

Carotenes constitute an important molecular class for photosynthesis. They are part of the light-harvesting complex, where they absorb visible light and transfer the energy to the reaction center of the photosystem. All-trans-α,ω-diphenylpolyenes (also referred to as minicarotenes) are well established as model compounds for the bigger carotenoids such as β-carotene or lutein. The latter absorb light and transfer the energy to the chlorophyll unit of the pigment.[402] Another function is protection of the photosynthetic apparatus against damage by highly reactive singlet oxygen.[403] The photophysical properties of these molecules are complex and not fully understood.

Because of its strong emission 1,6-diphenyl-1,3,5-hexatriene (DPH) is used as a fluorescence probe in biological membrane systems.[404] It is known, that the measured fluorescence lifetime is longer than that calculated using the Stickler-Berg[405] relationship and that the lifetime varies with the solvent.[406;407] Hudson and Kohler found evidence that the lowest excited singlet state in diphenyloctatetraene is the ^1A_g-state with the ^1B_u-state lying slightly above and applied this ordering of states to other polyenes as well.[108;407;408] Alford and Palmer stated that DPH emission occurs from both states.[409] In the gas phase fluorescence lifetimes up to 90 ns are reported and assigned to S_1-(^1A_g) state emission

with intensity borrowing from the S_2-(^1B_u) state.[410]
Combined density functional theory/multi reference configuration interaction DFT/MRCI calculations of the low-lying singlet and triplet states of mini-β-carotenes showed that the sequence of states depends on conjugation length and nuclear geometry.[411] According to the DFT/MRCI calculations for DPH the lowest excited singlet state upon vertical excitation is the ^1B_u-state, while it switches order with the ^1A_g-state during geometry relaxation.[412] Equilibration of the states takes place within less than a picosecond,[112] due to the conical intersection between the S_1 and S_2 potential energy hypersurfaces.[412]
Emission from the S_1-state is symmetry forbidden, but it can occur via mixing with the S_2-state, due to the small S_1-S_2 energy gap.[113;413] Unlike the S_1-state, the energy of the S_2-state is influenced by the solvent, which leads to a solvent dependent S_1-S_2 energy gap and, because of the state mixing, to a solvent dependent S1 radiative rate.[408]
Saltiel et al. presented evidence showing that the fluorescence spectrum of DPH not only consists of the combined S_1/S_2-emission, but also of emission from the *s-cis* conformers of DPH.[414–418] Catalán confirmed the influence of *s-cis* conformers on the emission spectra also for other minicarotenes by calculations.[109;419] A detailed resolution of the emission spectra was accomplished by Turek et al.[420]
We observe DPH emission with an exceptionally long lifetime which decays non-exponentially under special experimental conditions. The long lifetime may be due to the emission originating from a forbidden transition. But to understand the unusual temporal behaviour, additional influences have to be considered. In this work we studied the temporal fluorescence behaviour under different conditions like various DPH and O_2 concentrations and different temperatures and excitation laser pulse energies to identify the various competing processes like formation of DPH - O_2 contact charge-transfer (CCT) complexes, whose interplay leads to the linear decay of the long-lived emission.

6.1.3. Materials and Methods

1,6-Diphenyl-1,3,5-hexatriene (98 %, Aldrich) and cyclohexane (99+ %, Acros Organics) were used without further purification. The nanosecond transient fluorescence setup (Applied Photophysics) utilizes the output from a frequency tripled (355 nm) pulsed Nd:YAG laser (Innolas) for photoexcitation. DPH samples were excited with 0.01 - 5 mJ pump energy at 5 ns laser pulse width and 1 or 10 Hz repetition rate. The short laser pulse is created by cutting out the maximum of the 12 ns pulse with a pockels cell. The pump beam of 1 cm diameter is directed into the sample (a flow-through 3.5 mL cuvette) perpendicular to the fluorescence sampling direction. If not stated otherwise, the solution reservoir was purged with nitrogen during the experiment to remove dissolved oxygen from the solutions. The same setup was used to saturate the solutions with oxygen. The samples were purged at least for 20 minutes before the start of the first measurement. The fluorescence light is dispersed behind the sample with a grating monochromator (Applied Photophysics) for wavelength selection. The output signal is detected by a photomultiplier (R928, Hamamatsu) and digitized by an oscilloscope (Agilent Infinium). Typically 16 laser pulses are averaged to record a kinetic trace at a selected wavelength. Stationary absorption spectra were recorded with a Cary 50 (Varian) spectrometer.
The simulations of the kinetic curves were performed with Mathcad 2001 (MathSoft, Inc.) by solving the coupled nonlinear partial differential equations by numerical integration.

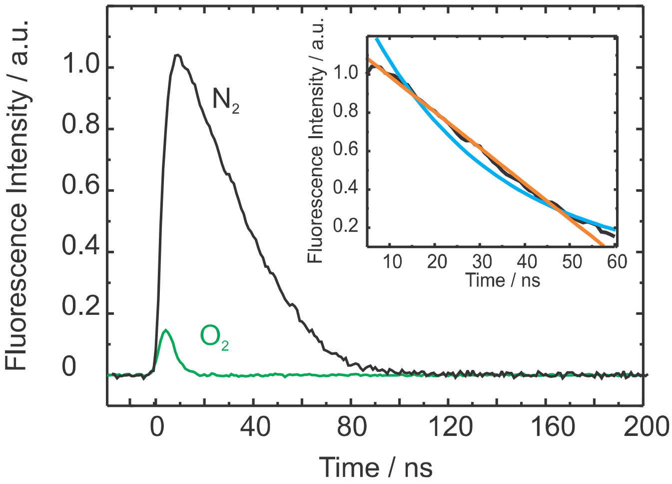

Figure 6.1: Kinetic curves of DPH ($8.0 \cdot 10^{-6}$ M) at 427 nm upon excitation at 355 nm with 1 mJ pulse energy. The sample flushed with nitrogen shows long-lived fluorescence. In the presence of oxygen intensity and lifetime of the fluorescence are decreased significantly. The decay of the nitrogen flushed sample can be seen on a larger scale in the inset with monoexponential (blue) and linear (orange) fits.

6.1.4. Results and Discussion

1,6-Diphenyl-1,3,5-hexatriene in cyclohexane shows strong absorption in the region of 300 - 380 nm. The excitation wavelength of our transient fluorescence measurements (355 nm) is near to the absorption maximum of DPH at 353 nm. The emission is very intense and can be detected in solutions with DPH concentrations below 10^{-10} mol/L (spectra not shown here). After excitation, the fluorescence kinetics can be investigated in our setup. figure 6.1 shows the fluorescence decay of an $8.0 \cdot 10^{-6}$ M DPH solution flushed with nitrogen. The fluorescence intensity reaches its maximum within the 5 ns laser pulse and subsequently decreases linearly until 50 ns after the laser pulse, where the decay becomes monoexponential. As can be seen in the inset, a monoexponential fit does not describe the observed fluorescence decay as well as a linear fit. Linear decay kinetics is characteristic for zero order reactions which are typical for systems saturated by the reactants (no concentration change) or for processes where the minority partner is regenerated like a catalyst. The rate constant k obtained according to the rate law $[DPH]_t = -kt + [DPH]$ is $1.85 \cdot 10^{-7}$ M·s^{-1}.

If the same sample is flushed with oxygen, fluorescence intensity and lifetime decrease dramatically (see figure 6.1). Under these conditions the fluorescence decay is best described monoexponentially, with a decay time of $\tau = 4.59$ ns ± 0.11 ns, which corresponds to the laser pulse width. Thus, the observed decay time does represent an upper limit for the emission lifetime. The dispersed emission spectra after laser excitation of both the nitrogen and oxygen flushed samples agree with the stationary emission spectrum, except for the distortion in the region around 470 nm, where $S_1 \rightarrow S_n$ absorption takes place.[421;422] If the oxygen flushed sample is flushed again with nitrogen, the long-lived fluorescence reappears. The decrease of fluorescence lifetime and intensity is thus not caused by oxygen induced chemical degradation of DPH but by a reversible physical process.

Both intensity and lifetime of the long-lived fluorescence increase with increasing concentration, see figure 6.2. At concentrations below 1 μM the fluorescence decays exponentially. Above 1 μM the decay shows the aforementioned linear behaviour. Therefore the fluorescence lifetimes shown in figure 6.2 were obtained by monoexponential ([DPH] < 1 μM) and linear ([DPH] > 1 μM) fits of the kinetic traces. Upon excitation with 0.3 mJ pulse energy the lifetime reaches a plateau at 37 ns and does not increase further with increasing concentration. At concentrations below 1 μM the number of DPH molecules within the excitation volume is smaller than the number of photons irradiating the sample

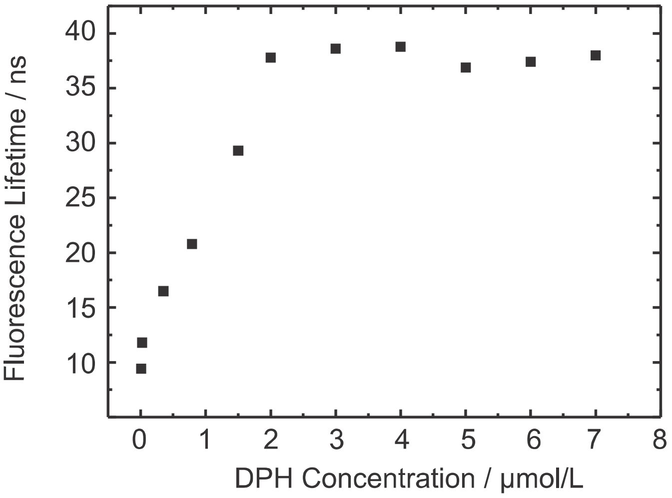

Figure 6.2: Fluorescence lifetime of DPH in cyclohexane at 427 nm upon excitation at 355 nm with 0.3 mJ pulse energy as a function of DPH concentration. The kinetic curves were fitted monoexponentially at concentrations below 1 µM (τ given in ns) and linear above 1 µM (τ given in ns·M^{-1}).

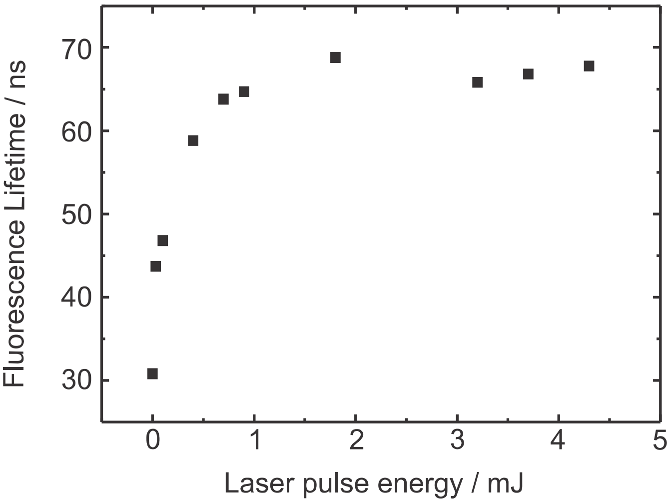

Figure 6.3: Dependence of fluorescence lifetime of DPH in cyclohexane ($8.0 \cdot 10^{-6}$ M) at 427 nm upon pumping at 355 nm on excitation laser pulse energy. For calculation of the lifetime the kinetic curves were fitted linear (τ given in ns·M^{-1}).

($N_{photon} \approx 5.4 \cdot 10^{14}$). The saturation plateau at ≈ 1.8 µM DPH at 0.3 mJ pulse energy can thus be explained by nearly complete photon absorption if the number of molecules exceeds the number of photons sufficiently.

A further increase of fluorescence lifetime can be reached by an increase of laser pulse energy. The effect of pulse energy on the fluorescence lifetime of an $8.0 \cdot 10^{-6}$ M DPH solution is shown in figure 6.3 between 0.01 mJ and 4 mJ. In the region of laser pulse energies below 1 mJ ($N_{photon} < 1.8 \cdot 10^{15}$) the lifetime increases with increasing laser pulse energy, since the number of photons is smaller than the number of molecules ($N_{molecule} \approx 2.4 \cdot 10^{15}$). Above 1 mJ once again a plateau is reached (at 68 ns for the $8.0 \cdot 10^{-6}$ M DPH solution). Our results thus show that fluorescence intensity and lifetime depend on the concentration of excited molecules.

The observed concentration dependence points to aggregate formation as possible cause of the long-lived fluorescence. It is well known that larger carotenoids are capable of forming aggregates easily. The emission of the aggregates is generally blue-shifted with respect to the emission of the monomer.[423] Increase of temperature leads to aggregate dissociation and a corresponding red-shift of the emission.[424] To check if the long-lived emission originates from DPH aggregates, the emission spectra of DPH were measured at different solution temperatures, spanning the complete range between melting point and boiling point of cyclohexane. The spectra at 8 °C and 75 °C are shown in figure 6.4.

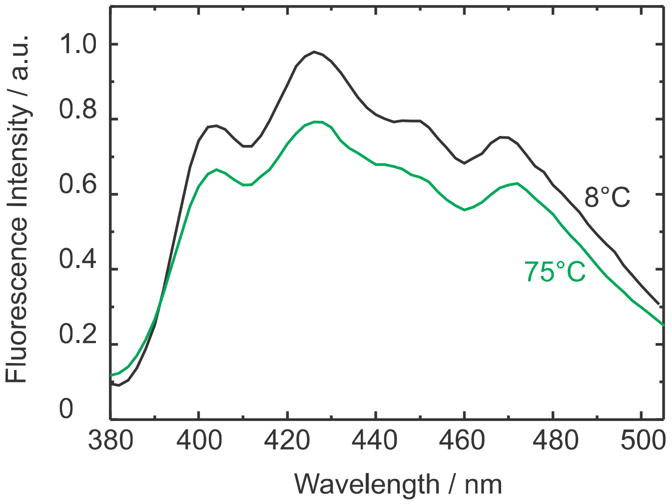

FIGURE 6.4: Emission spectra of DPH in cyclohexane ($8.0 \cdot 10^{-6}$ M) upon excitation at 355 nm with 1 mJ pulse energy at 8 °C and 75 °C. The spectra were obtained by integrating the emission during the first 30 ns after the laser pulse.

While the shape of the kinetic traces stays unchanged (see figure 6.8), it is evident that an increase of temperature leads to a decrease of fluorescence intensity. This behaviour is reversible, i.e. decreasing the temperature leads to recovery of the intensity. However, no spectral changes could be observed. Therefore we assume that DPH does not form aggregates in cyclohexane to an appreciable extent in the concentration range of our studies. We attribute the change of intensity to an increased molecular diffusion rate at higher temperatures and therefore increased collisional quenching of the fluorescence.
The correct mechanism for generation of the long-lived fluorescence has to take the following experimental findings into account: (i) fluorescence lifetimes up to 70 ns, see figure 6.1; (ii) zero order decay of fluorescence intensity at short times followed by exponential decay, see figure 6.2; (iii) significant population of the DPH triplet state, because we observed intense triplet-triplet absorption (spectra not shown here, since they are well known[112;415;425–427]); (iv) fluorescence lifetime depends on concentration of electronically excited DPH, see Figs.6.2 and 6.3; (v) fluorescence intensity decreases with increasing temperature, see figure 6.4; (vi) fluorescence is quenched by higher oxygen concentrations, see figure 6.1.

Different mechanisms can be discussed to explain these effects. It is known, that triplet-triplet annihilation (TTA) generates excited singlet state population with an increased fluorescence lifetime. But TTA is diffusion controlled and therefore, at the concentrations studied in this work, too slow to explain the < 5 ns fluorescence risetime observed in our experiments.[428] Further on the triplet ground state of DPH is very low in energy, so that the energy available by triplet-triplet annihilation is insufficient to populate the lowest excited singlet state.[415;429] Additionally, the quantum yield for intersystem crossing (ISC) of DPH is very small (i.e. 0.02 in benzene and ethanol[430]). Nevertheless the triplet state has to be included in any model explaining the long-lived fluorescence since ISC is a competing pathway for depopulation of excited singlet states.

Ionisation, followed by electron-cation recombination to electronically excited singlet states, could also cause long fluorescence lifetimes in principle. By the recombination process, the emitting singlet state becomes populated during a certain time period, which extends the emission time. To ionize DPH (ionisation potential: 7.27 eV[431]) upon excitation with 355 nm (3.49 eV) a multiphoton process is required. The lifetime should be longer in polar solvents but very short in nonpolar solvents, since electrons are not stabilized in nonpolar solvents and recombine immediately. All experiments presented here were

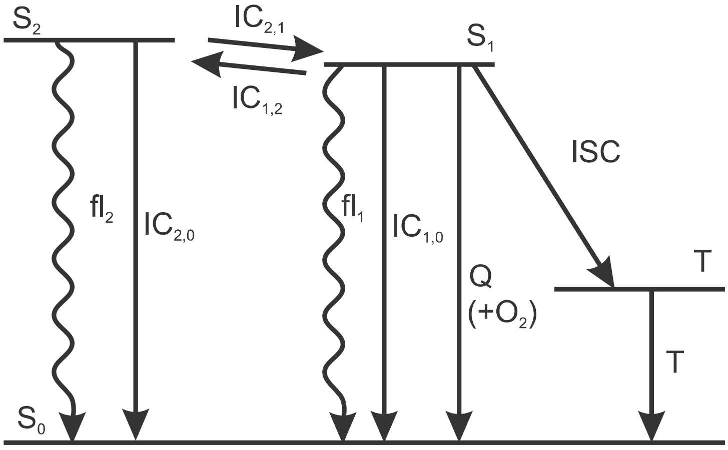

Figure 6.5.: Proposed mechanism for emergence of long-lived fluorescence. Photoisomerization processes are not shown for clarity reasons.

performed in cyclohexane, an nonpolar solvent. We did observe long-lived fluorescence in other solvents as well, but no correlation between polarity of the solvent and fluorescence lifetime was discernible from our experiments. Therefore, ionisation/recombination is not considered to be important for the emergence of long-lived DPH fluorescence.

We instead propose the mechanism displayed in figure 6.5 to explain the intense long-lived DPH fluorescence. The corresponding kinetic equations, which are used to simulate the observed kinetic traces, are as follows:

$$\frac{d\left[S_0\right]}{dt} = k_{fl_1}\left[S_1\right] + k_{fl_2}\left[S_2\right] + k_Q\left[S_1\right]\left[O_2\right] + k_{IC_{2,0}}\left[S_2\right] + k_{IC_{1,0}}\left[S_1\right] + k_T\left[T\right] \tag{6.1}$$

$$\frac{d\left[S_1\right]}{dt} = -k_{fl_1}\left[S_1\right] - k_Q\left[S_1\right]\left[O_2\right] + k_{IC_{2,1}}\left[S_2\right] - k_{IC_{1,2}}\left[S_1\right] - k_{IC_{1,0}}\left[S_1\right] - k_{ISC}\left[S_1\right] \tag{6.2}$$

$$\frac{d\left[S_2\right]}{dt} = -k_{fl_2}\left[S_2\right] - k_{IC_{2,1}}\left[S_2\right] + k_{IC_{1,2}}\left[S_1\right] \tag{6.3}$$

$$\frac{d\left[T\right]}{dt} = k_{ISC}\left[S_1\right] - k_T\left[T\right] \tag{6.4}$$

After excitation of DPH into the S_2-state a cascade of processes follows. Internal conversion into the S_1-state ($IC_{2,1}$) as well as the S_0-state ($IC_{2,0}$) occurs fast and competes with (short-lived) fluorescence (fl_2) from the S_2-state. The lifetime of the S_1-state is affected by internal conversion into the ground state ($IC_{1,0}$), reverse internal conversion into the S_2-state ($IC_{1,2}$) and intersystem crossing into the triplet state (ISC). Additionally CCT complex formation with oxygen takes place. Other O_2-induced processes may occur as competing processes, e.g. singulet oxygen formation[432] or photoisomerization.[417] These processes, with the CCT complex formation as main reaction are described as oxygen quenching, (Q). In the simulation non-radiative, non-oxygen induced processes which depopulate the S_1-state are indistinguishable from each other, as long as the emerging state or species has no influence on the S_1-state. This includes $IC_{1,0}$ and ISC as well as other possible processes, like isomerization (iso, not shown in figure 6.5). Therefore it is appropriate to use a combined rate constant k_{dep} for S_1-state depopulation.

$$k_{dep} = k_{IC_{1,0}} + k_{ISC} + k_{iso} + ... \tag{6.5}$$

TABLE 6.1.: Concentration of the contact complex [O_2-M] in cyclohexane and in a DPH/cyclohexane solution ($8.0 \cdot 10^{-6}$ M), calculated from deconvoluted UV/Vis absorption and the extinction coefficients published by Brownrigg and Kenny[433].

sample	purging gas	[O_2-M] mol/L
cyclohexane	O_2	- $^{a)}$
cyclohexane	unpurged	$2.1 \cdot 10^{-3}$
cyclohexane	N_2	$2.4 \cdot 10^{-4}$
DPH + cyclohexane	O_2	- $^{a)}$
DPH + cyclohexane	unpurged	- $^{a)}$
DPH + cyclohexane	N_2	$2.5 \cdot 10^{-4}$

$a)$ Complex absorption too large to determine complex concentration.

$IC_{1,2}$ is not included, since here the S_2-state is repopulated and subsequently $IC_{2,1}$ takes place, which means that the S_1-state population is influenced by the state emerging from this process. Emission from the S_1-state to the electronic ground state (fl_1) is symmetry forbidden and should be weak, but can be promoted by intensity borrowing via S_1-S_2-state mixing. The triplet state is depopulated within several microseconds (T).[415]

In the following we substantiate our model. Kohler and Spiglanin observed a DPH fluorescence lifetime of 90.7 ns in the gas phase and assigned this to emission from the S_1-state which borrows intensity from the nearby S_2-state.[410] We follow this assignment and ascribe the long-lived fluorescence observed in our experiments to emission from the S_1-state.

The zero order fluorescence decay of deoxygenated DPH solutions necessitates a quencher of constant concentration. The most obvious candidate is oxygen which at high concentrations quenches the long-lived fluorescence of DPH completely. Although the solutions were purged with nitrogen continuously during the experiments to avoid quenching, a small amount of oxygen remains in the solution.[433] It is well known, that molecular oxygen forms contact complexes with hydrocarbons,[433–435] whether they are unsaturated, like DPH, or saturated, like cyclohexane (CH), from which absorption to the contact charge-transfer complex ($M^{\cdot +}O_2^{\cdot -}$) can take place. Strong O_2/CH CCT complex absorption occurs in the region around 210 nm.[433] A deconvolution of the broad absorption band was carried out for unpurged cyclohexane as well as for nitrogen and oxygen saturated cyclohexane and the O_2-CH contact complex concentrations were determined (see table 6.1) using the extinction coefficients published by Brownrigg and Kenny[433] (for a detailed description see section 6.1.7). The same analysis was carried out for a solution of DPH in cyclohexane. By saturating the unpurged solutions with nitrogen, the contact complex concentration is reduced by at least an order of magnitude, but the amount of remaining oxygen is still considerable ([O_2-CH] = 0.2 mM). We assume that oxygen bound in the O_2-CH complex does not contribute to quenching of the DPH fluorescence in contrast to free oxygen which is in equilibrium with the O_2-CH contact complex:

$$O_2 + CH \overset{K}{\rightleftharpoons} [O_2 - CH] \tag{6.6}$$

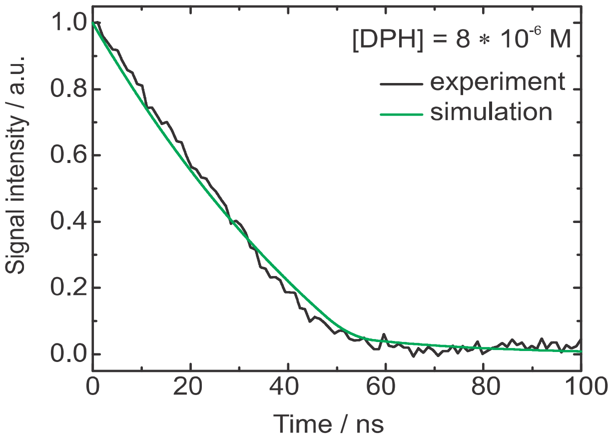

FIGURE 6.6: Time dependent fluorescence of DPH in cyclohexane at 427 nm upon excitation with 1 mJ pulse energy, flushed with N_2. The green curves show the sum of concentrations of S_1 and S_2-state DPH obtained from the simulations. [DPH] $= 8.0 \cdot 10^{-6}$ M.

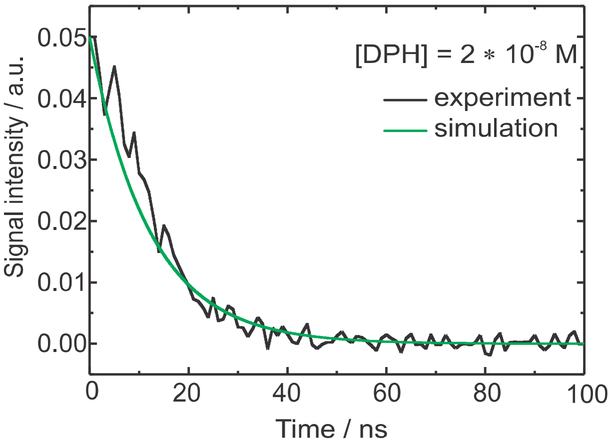

FIGURE 6.7: Time dependent fluorescence of DPH in cyclohexane at 427 nm upon excitation with 1 mJ pulse energy, flushed with N_2. The green curves show the sum of concentrations of S_1 and S_2-state DPH obtained from the simulations. [DPH] $= 2.0 \cdot 10^{-8}$ M.

To include the oxygen quenching into the simulation it is thus necessary to estimate the amount of free oxygen contained in the solution. It is safe to assume that the equilibrium is strongly located on the side of the contact complex.[436–438] For some hydrocarbons the value of the equilibrium constant K is known to be larger than 1000 M^{-1}. In our case this would imply a free oxygen concentration on the order of $3 \cdot 10^{-8}$ M. This is not sufficient to effectively quench the triplet state, but formation of contact complexes between oxygen and excited DPH molecules can occur and thereby depopulate the S_1-state. Ultimately, the complexes will break apart under formation of ground or triplet state DPH and free O_2.[434;435] The O_2-CH complex serves as oxygen reservoir, the concentration of free oxygen $[O_2]$ therefore can be regarded as constant. Directly after the laser pulse the O_2 concentration is distinctly smaller than the concentration of S_1-state DPH so that the reaction rate depends on constant $[O_2]$ and nearly constant $[S_1]$ which serves as excess reservoir. This results in zero order reaction kinetics. Later on, when $[S_1]$ and $[O_2]$ are in the same order of magnitude, the reaction rate depends on the declining S_1 concentration and the constant $[O_2]$ and the quenching of S_1-DPH becomes a first order reaction. With these assumptions made, the kinetic trace of the DPH fluorescence was simulated by fitting the rate constants to the experimental kinetic trace of the $8.0 \cdot 10^{-6}$ M DPH solution, excited with 1 mJ pulse energy. The value for k_T was set to $5.0 \cdot 10^4$ s^{-1}, according to the triplet state lifetimes known from literature[415;425;439;440] and $[O_2]$ to 0.03 µM according to the estimations described in section 6.1.7.

The fluorescence signal detected in the experiments is composed of contributions from the S_1-state and the S_2-state. For comparison to the emission intensity detected during

TABLE 6.2.: Rate constants derived from the simulation of the time dependent fluorescence of DPH in cyclohexane ($8.0 \cdot 10^{-6}$ M) upon excitation with 1 mJ pulse energy. The solutions are flushed with N_2, leading to a free oxygen concentration of $[O_2] = 0.03$ µM.

process		rate constant / s^{-1}	time constant / s
fl_2	S_2-state fluorescence	$< 8.0 \cdot 10^{8}$	$> 1.3 \cdot 10^{-9}$
fl_1	S_1-state fluorescence	$1.1 \cdot 10^{5}$	$9.4 \cdot 10^{-6}$
Q	oxygen quenching	$1.7 \cdot 10^{9}$	$5.9 \cdot 10^{-10}$
$IC_{2,1}$	internal conversion ($S_2 \rightarrow S_1$)	$7.3 \cdot 10^{11}$	$1.4 \cdot 10^{-12}$
$IC_{1,2}$	internal conversion ($S_1 \rightarrow S_2$)	$4.1 \cdot 10^{8}$	$2.4 \cdot 10^{-9}$
$IC_{2,0}$	internal conversion ($S_2 \rightarrow S_0$)	$< 1.0 \cdot 10^{10}$	$> 1.0 \cdot 10^{-10}$
dep	radiationless depopulation processes ($IC_{1,0}$, ISC, *iso*, ...)	$< 2.8 \cdot 10^{5}$	$> 3.6 \cdot 10^{-6}$

the first 100 ns after the laser pulse, the time-dependent evolution of the combined S_1+S_2 population derived from the simulation is depicted in figure 6.6 (signal intensity simulation: grey curves). The resulting set of rate constants is displayed in table 6.2 together with the time constants derived thereof. The slope of the experimental data is emulated considerably better than by a simple monoexponential fit (see inset of figure 6.1). Since the concentration of free oxygen could only be estimated, it is advisable to discuss the value of $[O_2]k_Q$ rather than k_Q alone.

Apparently the long emission lifetime detected in our experiments derives from the S_1 fluorescence, while fluorescence from the S_2-state with its lifetime of 1.3 ns (table 6.2) cannot be held responsible. The value for k_{fl_2} obtained in our simulation corresponds well with the Einstein probability of spontaneous emission ($A_{21} = 7.98 \cdot 10^{8}$ s^{-1}), which can be calculated via equation 6.7 with the oscillator strength $f_{21} = 2.16$, determined by Ye et al.:[114;441]

$$A_{21} = \frac{8\omega^2\pi^2e^2}{m_e c}\frac{g_1}{g_2}f_{21} \tag{6.7}$$

Increasing the value for k_{fl_2} to the theoretical rate constant determined by Turek et al.[420] ($k_{fl_2} = 2.2 \cdot 10^{9}$ s^{-1}) also leads to satisfying results with the root-mean-square deviation of the simulation slightly increasing from 0.005 to 0.006.

Simulations with $k_{fl_2} < 7.98 \cdot 10^{8}$ s^{-1} (even with $k_{fl_2} = 0$) describe our experimental data equally well. However, exclusion of S_2-state emission influences the simulation during the first picoseconds. Without S_2-state emission, an increase of emission intensity should be observed within the first 5 ps. This rise should not be observable if emission from the S_2-state occurs, since S_2-state emission would superimpose the S_1-state emission. Since this is far beyond our experimental time resolution, we can make no substantiated statement whether S_2-state emission occurs in DPH or not.

In simulations with larger k_{fl_2} or smaller $k_{IC_{2,1}}$ combined with smaller k_{fl_2} emission now occurs from the S_2-state with a long lifetime but the decay is strictly exponential rather than showing the described linear behaviour during the first 50 ns. The linearity can only be obtained by including the O_2 quenching as competing process to S_1 fluorescence.

The simulation starting value for $k_{IC_{2,1}}$ was set to $1.6 \cdot 10^{12}$ s^{-1}, which is the value corresponding to the S_2-state lifetimes obtained by Hirata et al,[426] but a better agreement with our experimental data was obtained with $k_{IC_{2,1}} = 7.3 \cdot 10^{11}$ s^{-1}. Decreasing $k_{IC_{2,0}}$ to values below $1.0 \cdot 10^{10}$ s^{-1} has no effect on the simulation at all, while higher values for this rate lead to insufficient simulations. Therefore $1.0 \cdot 10^{10}$ s^{-1} is only an upper bound for $k_{IC_{2,0}}$.

It was found that the fluorescence intensity increases with increasing temperature, while the shape of the kinetic trace stayed unchanged. The emission intensity strongly depends on the S_2-state concentration. At higher temperatures, depopulation of the S_2-state by collisional quenching increases. Since this process competes with $IC_{2,1}$, the S_1-state is populated less at higher than at lower temperatures. This results in a decrease of emission intensity. Apparently, collisional quenching plays a minor role in S_1-state depopulation.

With an adjusted initial $[S_2]$ the same rate constants can also be used to describe the fluorescence of DPH solutions at much lower concentrations, as is shown in figure 6.7 for $[\mathrm{DPH}] = 2.0 \cdot 10^{-8}$ M. In this case $[S_1]$ is already smaller than $[O_2]$ directly after the laser pulse. The fluorescence decay is therefore exponential, in the experiment as well as in the simulation. The emission in oxygen saturated solutions resembles the shape of the laser pulse with its lifetime of 5 ns, see figure 6.1. In oxygen saturated solutions $[O_2]$ is much higher than the initial concentration of excited state DPH. This leads to a very fast O_2-quenching of the S_1-state, in our simulations, which results in a fluorescence decay within 1 ns. Due to our 5 ns laser pulse it is not possible in our setup to measure the correct fluorescence lifetime of the oxygen saturated sample. Anyway the model sufficiently explains all experimental findings described above.

6.1.5. Conclusion

At high pulse energies of the excitation laser the singlet emission of 1,6-diphenyl-1,3,5-hexatriene can occur via two different pathways. On the one hand, after excitation to the S_2-state, emission occurs directly from the pumped state. On the other hand, IC into the S_1-state takes place. The fluorescence from the S_1-state features long lifetimes since it is symmetry forbidden and can only occur by intensity borrowing via state mixing with the S_2-state. The S_1-state is depopulated by several processes like reverse IC, ISC and fluorescence. Most important competing process is the formation of DPH-O_2-CCT complexes, which at low oxygen concentrations considerably influences the kinetic trace of the long-lived fluorescence and quenches the long-lived fluorescence considerably at high oxygen concentrations.

6.1.6. Acknowledgments

The authors thank the Deutsche Forschungsgemeinschaft (KL 531/29-1) for financial support and Prof. Weinkauf for valuable discussions.

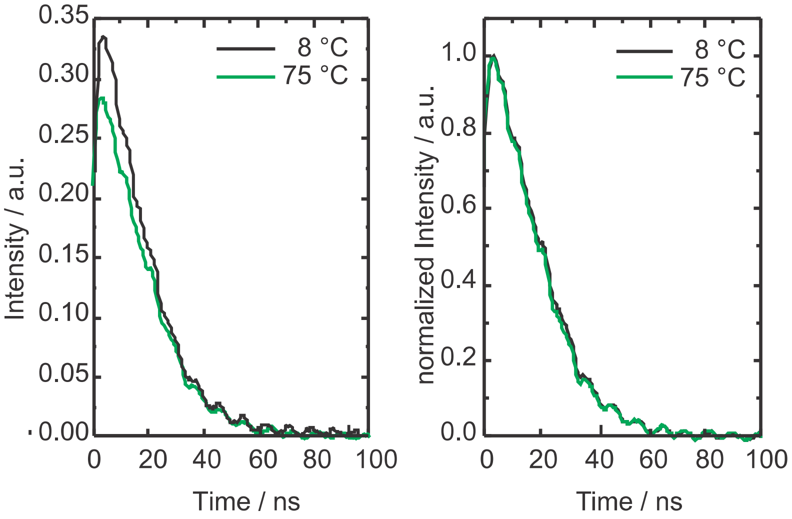

FIGURE 6.8: Kinetic curves of DPH ($8.0 \cdot 10^{-6}$ M in cyclohexane flushed with nitrogen) at 25 °C and 75 °C upon excitation at 355 nm with 1 mJ pulse energy.

6.1.7. Supplementary Information

Kinetic Traces at different Temperatures

The emission intensity decreases with increasing temperature, while the shape of the kinetic curves does not depend on the temperature, see figure 6.8.

Determination of Oxygen Concentration

The intense curves with maxima < 190 nm depend on O_2 concentration and can thus be described to absorption of O_2-M CCT complexes. In pure cyclohexane, neither purged with nitrogen or oxygen, the CCT absorption band can be emulated by one Gaussian curve with $\lambda_{max} = 186$ nm and three distinctly smaller Gaussian curves with maxima at 199 nm, 194 nm and 218 nm. Unfortunately, it is not possible to investigate absorption bands below 190 nm with our UV/Vis spectrometer; hence $\lambda_{max} = 186$ nm is merely a guess. The sample was purged with nitrogen for 15 minutes and an absorption spectrum was measured every minute. Only the intensity of the Gaussian curve with $\lambda_{max} =$ 186 nm had to be adjusted to emulate the spectra, while all other contributing curves remained unchanged. Therefore we assign this band to the O_2-cyclohexane CCT complex absorption. The other bands are due to cyclohexane absorption and will be disregarded when calculating the contact complex concentration. Obviously the oscillator strengths of the CCT complex bands are much higher than those of uncomplexed cyclohexane in the displayed spectral range.

After seven minutes the sample was saturated with nitrogen and no changes could be observed in the absorption spectra any more. The measured CCT-absorption of the sample purged with oxygen for 15 minutes at 210 nm lies well beyond 1 O.D. where the Lambert-Beer law is not valid any more. For this sample no concentration could be determined. The concentration was calculated using the CCT extinction coefficients determined by Brownrigg and Kenny in the region of the red flank of the 186 nm band: $\epsilon_{210nm} = 250\ \mathrm{L} \cdot \mathrm{mol}^{-1} \cdot \mathrm{cm}^{-2}$, $\epsilon_{220nm} = 120\ \mathrm{L} \cdot \mathrm{mol}^{-1} \cdot \mathrm{cm}^{-2}$ and $\epsilon_{230nm} = 40\ \mathrm{L} \cdot \mathrm{mol}^{-1} \cdot \mathrm{cm}^{-2}$ and the corresponding intensities obtained by our deconvolution. The concentrations given in table 6.1 in the article are obtained by averaging over the values for the different wavelengths.

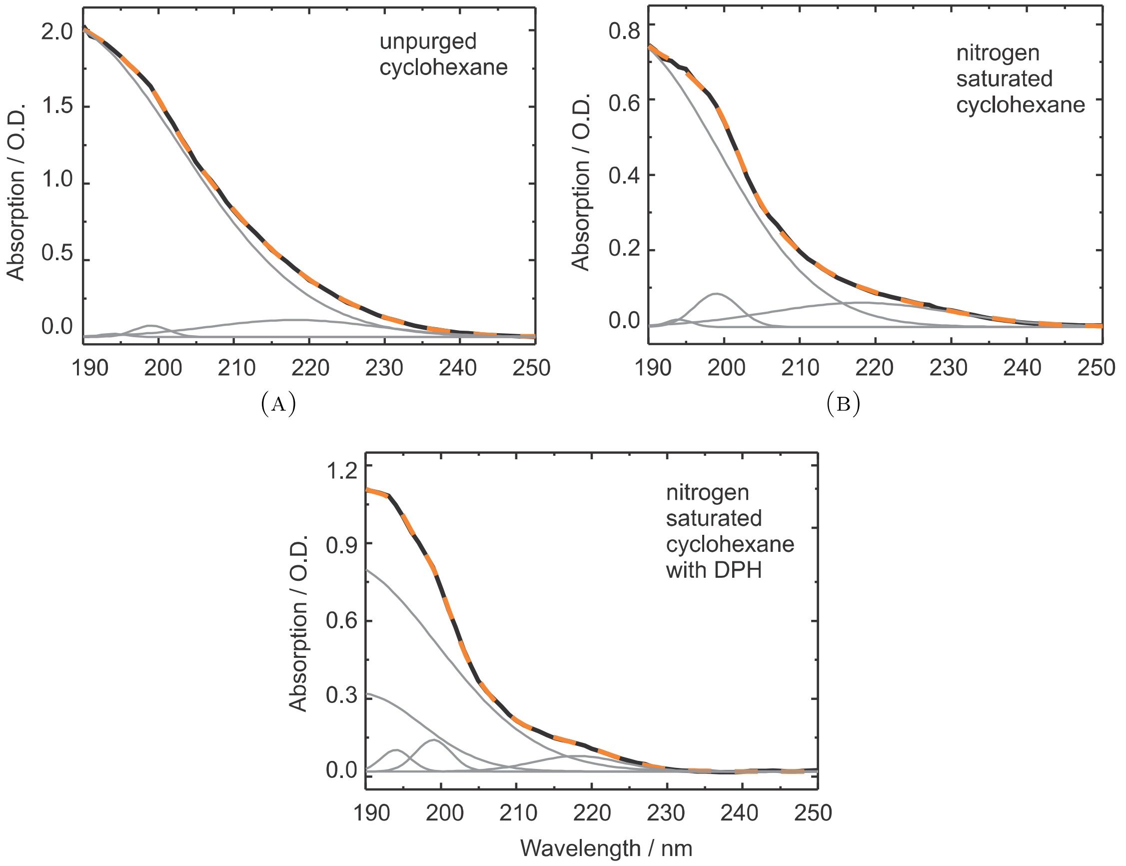

(A)

(B)

(C)

FIGURE 6.9.: Absorption spectra and Gauss deconvolutions of the O_2-CCT complex (a) in unpurged cyclohexane, (b) in cyclohexane saturated with nitrogen, (c) in DPH in cyclohexane ($8.0 \cdot 10^{-6}$ M) purged with nitrogen. The experimental absorbance spectrum is depicted in black, the sum of the Gaussian curves in orange (nearly perfect overlap with the black curve) and the individual Gaussian contributions in grey.

The same analysis was performed for an $8.0 \cdot 10^{-6}$ M DPH solution in cyclohexane. In this case not only the oxygen saturated but also the unpurged solution features an absorption band with intensities above 1 O.D. For the nitrogen saturated solution an additional Gaussian band with $\lambda_{max} = 189$ nm was needed to emulate the CCT complex absorption, which may be due to formation of the O_2-DPH CCT complex. Therefore, the summarized intensities of the Gaussian curves with $\lambda_{max} = 186$ nm and $\lambda_{max} = 189$ nm were used to calculate the combined contact complex concentration. It was assumed that the different CCT complexes exhibit comparable extinction coefficients.

6.1.8. Contributions

Title: Intense long-lived fluorescence of 1,6-diphenyl-1,3,5-hexatriene: Emission from the S_1-state competes with formation of O_2 contact charge transfer complex.

Authors: Katharina Hunger and Karl Kleinermanns.

Accepted by: Open Journal of Physical Chemistry (Impact Factor: 0.17)

All experiments in this work were done by me. I did develop the MATHCAD routine used to simulate the kinetic traces and subsequently performed the simulations. The interpretation of the obtained results was done by me in close collaboration with K. Kleinermanns. The writing was completely done by me.

7. Summary

In this work, three different systems were studied with time-resolved spectroscopy, all of which contained at least one chromophore. The focus of the studies performed lay on the processes which follow electronic excitation.

As first chromophore maleimide was investigated. Upon irradiation this molecule is capable of dimerisation via a [2+2]-cycloaddition mechanism. This can be utilized to embed crosslinks in polymers and thus increase their physical and chemical stability. Polymers modified this way are promising materials for application as pervaporation or gas separation membranes.
The mechanism of this dimerisation reaction was studied *in situ* in PEMAA functionalized with 3-hydroxypropyldimethylmaleimide (MI). Stationary as well as nanosecond transient UV/Vis absorption spectroscopy measurements in solution and polymer films were performed. The polymer itself does not absorb in the UV/Vis spectral region, so that all observed absorption and absorption changes are caused by the maleimide moiety. Absorption at 340 nm with µs lifetime was observed in nitrogen but not in oxygen saturated solutions. This led to the conclusion that after UV irradiation a triplet state is populated. The transient absorption observed PEMAA/maleimide films (λ_{max}=250 nm) was assigned to the maleimide radical anion, on the basis of spectra known from literature. The cation and anion radicals formed this way can then combine to the maleimide cyclobutane dimer.
In cooperation with N. Schmeling (Institute of Organic and Macromolecular Chemistry, University Düsseldorf, Prof. Staudt) it was found that copolyimides show better pervaporation performance than PEMAA. The investigation of copolyimide crosslinking with maleimide derivatives cannot be performed with UV/Vis spectroscopy, since the UV/Vis absorption bands of polymer backbone and crosslinking unit overlap strongly. Therefore this system was studied with FTIR spectroscopy, supported by quantum mechanical calculations for band assignment and photoproduct identification.
IR spectra of films of the 6FDA-ODA/6FDA-DABA 4:1 copolyimide, MI and the copolyimide + MI were measured before and after irradiation. Based on the difference spectra and the DFT calculations it was shown that the *trans*- and the *cis*-cycloadduct as well as the 2-2'-adduct are formed. According to the DFT-calculations the *trans*-cycloadduct is the most stable one, followed by the 2-2'-adduct and the *cis*-cycloadduct. The presence of the 2-2'-adduct was proved by the appearance of the absorption band at 1652 cm^{-1}, which could be assigned to the terminal C=C double bond stretching vibration. The two cycloadducts cannot be easily distinguished from each other by IR spectroscopy, since there are no prominent marker bands. However, the C=O stretching region band pattern after irradiation shows three contributions and thus cannot be explained by the formation of the *trans*-cycloadduct and the 2-2'-adduct alone. Evidence for an oxetane-like photoproduct was not found, which is no surprise considering its much higher energy in respect to the main product.

The cycloadduct accumulates with a shorter time constant than the 2-2'-adduct and it is assumed, that the 2-2'-adduct can be formed by rearrangement of the cycloadduct.
The photocrosslinking yield was determined by spectral deconvolution and kinetic fitting of several marker bands. The calculation was corrected under consideration of photodegradation of the polymer backbone. For the copolyimide synthesized in this work, a maximum crosslinking yield of 6 % was obtained. In the film, not every excited maleimide moiety has a second maleimide in the vicinity to perform the cycloaddition. Rearrangement is impeded by the high stiffness of the 6FDA-ODA/6FDA-DABA 4:1 backbone due to π-π-interactions of the aromatic systems in the copolyimide.

The second chromophore which was investigated within this work, is the nucleobase guanine. The transient UV/Vis absorption of a lipophilic guanine derivative (G) in n-hexane was measured on the nanosecond to microsecond timescale. In N_2 saturated solutions, absorption in the region of 300 - 550 nm was observed, which is completely quenched in the presence of O_2. In the same spectral region, absorption of the G^+ cation and the G(-H)· radical in water is known to occur.
The spectrum observed 100 ns after irradiation was compared with PCM/CAM-B3LYP calculations of a G-trimer in hexane. The structures as well as the singulet and triplet absorption spectra of the G^+G^- ion pair and different radical pairs were calculated by R. Improta (Università Federico II, Napoli). Further insight in the mechanism of H-transfer in G aggregates could be obtained by fs transient UV/Vis absorption spectroscopy (S. Kovalenko, Humboldt University, Berlin). Preceding NMR and IR investigations point to extended G ribbons as prevailing structures with two different H-bond arrangements in hydrocarbon solvents. The calculations indicate that the more stable one is the aggregate which is built by reverse Hoogsteen hydrogen bonding, a motif that is also found *in vivo* in triple-helical DNA structures.
According to the comparison of experiment and calculations, the path upon which electron transfer and proton transfer most likely takes place, is the NH$\cdots$N hydrogen bond between the G moieties. The best agreement with the experiment was obtained with a superposition of the calculated triplet ion pair and triplet radical pair spectra. This assumption is strengthened by the two different lifetimes observed. The absorption in the wavelength region of 335 - 425 nm thus is dominated by the radical pair with $\tau_{rad} = 300$ ns and in the wavelength region of 425 - 540 nm by the ions with $\tau_{ion} = 200$ ns. The observed transient lifetimes are rather long for radicals in a non-polar solvent, however, G^+G^- charge separation via hole transfer is known to occur in large G aggregates. Thus it is suggested that the observed transient spectrum originates from the G ions as well as from the radical pair.
By composition of the conclusions drawn from the different experiments and calculations, the following scheme was developed: After relaxation of the initially excited S_1 state of the GG aggregates and ISC to an energetically nearby triplet $\pi\pi^*$- or $n\pi^*$- state the system internally converts to a triplet charge transfer (^{3}CT) state leading to a G^+G^- ion pair. In competition to this path, charge transfer can take place from the S_1 state, leading to a ^{1}CT state which then converts to the ^{3}CT state. Shortly after the electron follows the proton along the NH$\cdots$N pathway. The (G-H)·/(G+H)· radical pair subsequently dissociates, reacts back or possibly converts to other products like the G enol form. The G^+G^- ion pair also can be separated by hole transfer, whereby proton transfer is inhibited. The G ions + radical pair spectrum was only observed in solutions which are 1-2 days old, which

led to the conclusion that more extended networks of hydrogen bonded G are formed upon aging and that such extended networks are necessary to separate and thus stabilize the radicals.

The last but not least chromophore studied, was 1,6-diphenyl-1,3,5-hexatriene (DPH). The emission characteristics of DPH dissolved in cyclohexane were investigated as a function of temperature, concentration, 355 nm excitation pulse energy as well as oxygen concentration in the solution. In N_2 saturated solutions, long-lived, very intense emission, which appears within less than 5 ns and lasts up to 70 ns, was observed. During the first 50 ns the decay does not follow an exponential but rather a linear behavior. In experiments performed at concentrations below 2.5 µM, excitation energies below 1 mJ or in O_2 saturated solutions, only short-lived fluorescence was detected, which decays with $\tau < 5$ ns, a lifetime corresponding with the used laser pulse width. The spectral pattern was the same under all conditions.
A MATHCAD routine was developed, with which kinetic traces can be simulated on the basis of a postulated mechanism. The rate constants for each process involved in this mechanism can be varied and for each combination of rate constants the deviation of the simulated traces from the experimentally obtained ones is calculated. With the set of rate constants with the lowest deviation, the kinetic traces observed under other experimental conditions are simulated as well, e.g. after variation of initial DPH concentration.
A variety of mechanisms was tested, until a model was found which can explain the unusual emission behavior of DPH: At high pulse energies of the excitation laser the singlet emission of DPH can occur via two different pathways. On the one hand, after excitation to the S_2-state, emission occurs directly from the pumped state. On the other hand, IC into the S_1-state takes place. The fluorescence from the S_1-state features long lifetimes since it is symmetry forbidden and can only occur by intensity borrowing via state mixing with the S_2-state. For the same reason, excitation occurs to the S_2-state. The S_1-state is depopulated by several processes like reverse IC, ISC and fluorescence. The most important competing process is the formation of DPH-O_2-contact charge transfer complexes, which even at very low oxygen concentrations considerably influences the kinetic trace of the long-lived fluorescence and quenches the long-lived fluorescence considerably at high oxygen concentrations. The oxygen concentration is much lower than the excited state DPH concentration. It is not changed upon DPH-O_2 complex formation, due to the equilibrium of free oxygen with cyclohexane-O_2 complexes, which is continuously readjusted. The depopulation of S_1-state DPH thus follows zero order rate law and the observed decay is linear.
This model explains the long-lived emission with the linear decay at high concentrations and/or excitation pulse energies equally good as the short-lived emission at low DPH concentrations and/or high O_2 concentrations. The rate constants obtained with the fit routine are in good agreement with the theoretical rate constants which were already published for some of the implemented processes.

For all three systems which were investigated, the underlying mechanisms could be discovered with the help of time-resolved spectroscopy in combination with simulations and quantum mechanical calculations.

8. Zusammenfassung

Im Rahmen dieser Arbeit wurden drei Systeme untersucht, von denen jedes mindestens einen Chromophor enthält. Der Fokus der Untersuchungen lag dabei auf den Prozessen die einer elektronischen Anregung nachfolgen.

Der Mechanismus der Dimerisierung wurde *in situ* in mit 3-Hydroxypropyldimethylmaleimid (MI) funktionalisiertem PEMAA untersucht. Dazu wurden stationäre und in Nano- bis Mikrosekunden zeitaufgelöste UV/Vis Absorptionsspektren in Lösung und im Film durchgeführt. Da das Polymer selbst nicht im UV/Vis-Spektralbereich absorbiert, werden die beobachtete Absorption und alle Absorptionsänderungen vom Maleimid verursacht. In mit Stickstoff gesättigten Lösungen wurde eine intensive Absorptionbande mit einem Maximum bei 340 nm und einer Lebensdauer im µs-Bereich beobachtet. Nach Sauerstoff-Spülung wird die Absorption gelöscht, woraus geschlossen werden kann, dass durch die UV-Bestrahlung ein Triplett-Zustand des Maleimids populiert wird. In PEMAA + MI-Filmen wurde eine transiente Absorptionsbande bei 250 nm gefunden, die aufgrund von in der Literatur bekannten Spektren dem Maleimid Radikal-Anion zugeordnet wurde. Daraus ergibt sich folgender Mechanismus: Durch ISC wird aus dem elektronisch angeregten Maleimid-Singulettzustand ein Triplett-Zustand populiert. Aus diesem Zustand wird ein Elektron an ein Grundzustands-Molekül abgegeben. Das so entstandene Radikal-Kation und das Radikal-Anion können nun zum Dimer rekombinieren. Bei Anwesenheit von Sauerstoff wird der Triplettzustand gelöscht und der Elektronen-Transfer kann nicht stattfinden.
In Kooperation mit N. Schmeling (Institut für Organische und Makromolekulare Chemie, Universität Düsseldorf, Prof. Staudt) wurde herausgefunden, dass Copolyimide bessere Pervaporationseigenschaften zeigen als PEMAA. Zur Untersuchung der Photovernetzung von Copolyimiden mit Maleimid ist die UV/Vis-Spektroskopie nur bedingt geeignet, da das Polymer und der Vernetzer in diesem Bereich gleichermaßen absorbieren. Deshalb wurde dieses System mit FTIR-Spektroskopie untersucht. Zur Unterstützung der Messungen wurden quantenmechanische Rechnungen durchgeführt, die für die Zuordnung der Absorptionsbanden und damit auch für die Identifikation der Photoprodukte herangezogen wurden.
Es wurden IR-Spektren von Filmen des 6FDA-ODA/6FDA-DABA 4:1 Copolyimids, des MIs und des mit MI funktionalisierten Copolyimids, jeweils vor Bestrahlung und nach verschiedenen Bestrahlungszeiten, gemessen. Mit Hilfe dieser Spektren und den Ergebnissen der DFT-Rechnungen konnte gezeigt werden, dass nach UV-Bestrahlung nicht nur das Cycloaddukt (als *trans*- und als *cis*-Isomer) sondern auch das 2-2'-Addukt entsteht. Den DFT-Rechnungen zufolge ist das *trans*-Cycloaddukt das stabilste, gefolgt vom 2-2'-Addukt und dem *cis*-Cycloaddukt. Der entscheidende Hinweis für die Existenz des 2-2'-Addukt ist die entstandene Absorptionsbande bei 1652 cm^{-1}, die laut den quantenchemischen Rechnungen der Streckschwingung der terminalen C=C Doppelbindung zugeordnet werden kann. Die zwei Isomere des Cycloaddukts können durch IR-Spektroskopie nicht

ohne weiteres unterschieden werden, da sich ihre IR-Spektren nur marginal unterscheiden. Allerdings kann die beobachtete Bande die von den C=O Streckschwingungen nach Bestrahlung herrührt, nur durch drei Gauss-Kurven nachgebildet werden. Ein solches Bandenprofil kann nicht allein vom *trans*-Cycloaddukt und dem 2-2'-Addukt stammen. Es wurde kein Hinweis auf ein Oxetan-Produkt gefunden, was angesichts der im Vergleich zum Hauptprodukt deutlich höheren berechneten Energie keine Überraschung ist.
Das Cycloaddukt wird mit einer kürzeren Zeitkonstante gebildet als das 2-2'-Addukt und es wird vermutet, dass das 2-2'-Addukt durch Umlagerung aus dem Cycloaddukt entstehen kann.
Durch Entfaltung der Absorptionsbanden und anfitten der kinetischen Kurven mehrerer Markerbanden konnte der Grad der Photovernetzung bestimmt werden. Dabei wurde berücksichtigt, dass durch die Bestrahlung eine Photodegradation des Polymers erfolgt. Für das hier untersuchte Copolyimid betrug der maximale beobachtete Vernetzungsgrad 6 %. Aufgrund der π-π-Wechselwirkungen des aromatischen Systems ist das 6FDA-ODA/6FDA-DABA 4:1 Polymer sehr steif. Dadurch wird (insbesondere im Film) verhindert, dass die Maleimid-Gruppen zueinander finden, so dass nicht jede angeregte Maleimid-Einheit ein zweites Maleimid in erreichbarer Nähe findet um die Dimerisierung vollziehen zu können.

Als zweites System wurde ein lipophiles Derivat der Nukleinbase Guanin untersucht. Die UV/Vis-Spektren von 2',3',5'-O-tris -(tert-butyldimethylsilyl)guanosin (G) in Hexan weisen mehrere Nano- bis Mikrosekunden nach dem Anregungspuls eine Absorptionbande bei 300-500 nm auf, die bei Anwesenheit von Sauerstoff komplett gelöscht wird. Es ist bekannt, dass das G^+-Kation und das G(-H)·-Radical in Wasser in diesem Spektralbereich absorbieren.
Das 100 ns nach Anregung gemessene Absorptionsspektrum wurde mit berechneten Absorptionspektren der niedrigsten angeregten Singulett- als auch der niedrigsten Triplettzustände des G^+G^--Ionenpaares und verschiedener Radikal-Paare, die nach H-Transfer enstehen können, verglichen. Die PCM/CAM-B3LYP-Rechnungen des Guanin-Trimers in Hexan wurden von R. Improta (Università Federico II, Napoli) durchgeführt. Weitere unterstützende Informationen wurden durch Femtosekunden UV/Vis Absorptionsspektroskopie erhalten (S. Kovalenko, Humboldt University, Berlin).
In NMR- und IR-Untersuchungen wurden Hinweise darauf gefunden, dass in unpolaren Lösungsmitteln zwei Arten von ausgedehnten G-Aggregaten mit verschiedenen H-Brücken-Motiven gebildet werden. Laut den PCM/CAM-B3LYP-Rechnungen ist die stabilere der beiden Strukturen das sogenannte "Ribbon I"-Aggregat mit dem reverse Hoogsteen Motiv, welches auch *in vivo* in dreisträngigen DNA-Strukturen gefunden werden kann.
Der Vergleich von Rechnungen und Messungen zeigt, dass der Elektronen- und Protonentransfer zwischen zwei G-Molekülen am wahrscheinlichsten entlang der NH···N H-Brückenbindung stattfindet. Die beste Übereinstimmung mit dem 100 ns nach der Anregung gemessenen Absorptionsspektrum wurde mit einer Überlagerung der berechneten Spektren des Triplett-Ionenpaars und des über den NH···N-Pfad entstandenen Triplett-Radikalpaars erzielt. Es wurden zudem zwei verschiedene Lebensdauern gefunden. Im Bereich von 335 - 425 nm dominiert demzufolge die Absorption des Radikalpaares mit τ_{rad} = 300 ns, die Absorption bei 425 - 540 nm stammt hauptsächlich von den G-Ionen mit τ_{ion} = 200 ns. Die für Ionen in einem unpolaren Lösungsmittel untypisch langen Lebensdauern werden durch Ladungstrennung über Lochwanderung im Aggregat verur-

sacht. Neben dem Radikalpaar werden also hauptsächlich die getrennten Ionen und nicht das Ionenpaar beobachtet.
Diese Beobachtungen führen zu folgendem Mechanismus für den H-Transfer in H-Brücken-gebundenen G-Aggregaten: aus dem durch die Anregung populierten Singulettzustand findet ISC in einen energetisch nahegelegenen Triplett-$\pi\pi^*$- oder Triplett-nπ^*-Zustand statt. Aus diesem entsteht über einen ^{3}CT-Zustand das G^+G^- Ionenpaar. Alternativ kann aus dem elektronisch angeregten Singulettzustand der ^{1}CT-Zustand und daraus der ^{3}CT-Zustand populiert werden. Ein Proton folgt dem Elektron entlang dem NH$\cdots$N-Pfad, wodurch das (G-H)·/(G+H)·-Radikalpaar entsteht, welches dann entweder dissoziiert, zu den Edukten zurück reagiert oder möglicherweise in Folgeprodukte wie das G-Enol umgewandelt wird. Das Ionenpaar kann durch Lochwanderung getrennt werden, wodurch der nachfolgende Protonentransfer verhindert wird.
Das beschriebene Spektrum wurde nur in Lösungen beobachtet, die ein bis zwei Tage alt sind. Vermutlich entstehen in dieser Zeit größere über H-Brücken verknüpfte G-Netzwerke, die für die Trennung und damit die Stabilisierung der Ionen notwendig sind.

Der dritte Chromophor der im Rahmen dieser Arbeit untersucht wurde, ist *all-trans*-1,6-Diphenyl-1,3,5-hexatrien (DPH). DPH in Cyclohexan zeigt ein ungewöhnliches Fluoreszenzverhalten, welches durch Änderungen von Temperatur, Konzentration, Energie des Anregungspulses oder des Sauerstoff-Gehalts in der Lösung stark beeinflusst wird.
In mit Stickstoff gesättigten µmolaren DPH Lösungen ist die beobachtete Emission sehr lang (bis zu 70 ns) und intensiv. Sie entsteht innerhalb von 5 ns, was der Pulsbreite des Anregungspulses entspricht. Während der ersten 50 ns ist der Abfall der Emission nicht monoexponentiell, wie zu erwarten wäre, sondern linear. Bei niedrigeren Konzentrationen, Pulsenergien unter 1 mJ oder in O_2-gesättigten Lösungen ist die Fluoreszenz deutlich weniger intensiv und wird nur während der Laserpulsdauer beobachtet. Im Gegensatz zum zeitlichen Verhalten blieb das Spektrum der Emission unter allen untersuchten Bedingungen unverändert.
Um dieses Phänomen zu erklären, wurde eine Mathcad Routine entwickelt mit deren Hilfe anhand eines postulierten Mechanismus' die korrespondierenden kinetische Kurven aller involvierten Zustände simulieren werden können. Die Geschwindigkeitskonstanten für jeden Prozess können variiert werden und für jede Kombination wird die Standartabweichung der erhaltenen kinetischen Kurve von der gemessenen zeitabhängigen Emission berechnet.
Zahlreiche Mechanismen wurden mit dieser Methode getestet, bis ein Modell gefunden wurde, welches das unübliche Emissionsverhalten von DPH erklären kann. Durch den Laserpuls wird DPH in den S_2-Zustand angeregt. Dieser Zustand kann durch Fluoreszenz (mit kurzer Lebensdauer) oder IC in den S_1-Zustand depopuliert werden. Die Emission aus dem S_1-Zustand hat eine lange Lebensdauer, da der S_1-S_0-Übergang symmetrieverboten ist und nur über vibronische Kopplung mit dem S_2-Zustand ermöglicht wird. Aus dem gleichen Grund findet die Anregung nicht in den S_1-Zustand sondern in den S_2-Zustand statt.
Der Haupt-Konkurrenzprozess für die S_1-Fluoreszenz ist die Bildung von DPH-O_2-Charge-Transfer-Komplexen. ISC in den energetisch nahen Triplettzustand, sowie IC zurück in den S_2-Zustand spielen eine untergeordnete Rolle, können allerdings nicht vernachlässigt werden. Durch die Bildung der DPH-O_2-Komplexe wird das zeitliche Verhalten der beobachteten Emission selbst bei geringsten Sauerstoffkonzentrationen gravierend beein-

flusst, bei höheren Konzentrationen wird die Emission durch die Komplexbildung nahezu vollständig verhindert. In Cyclohexan liegt ein Großteil des Sauerstoffs in O_2-Cyclohexan-Komplexen vor, die sich mit freiem Sauerstoff O_{2_f} im Gleichgewicht befinden. In mit Stickstoff gesättigten Lösungen ist die O_{2_f}-Konzentration deutlich geringer als die Konzentration an elektronisch angeregten DPH-Molekülen. Durch ständige Neueinstellung des Gleichgewichts mit den O_2-Cyclohexan-Komplexen wird die O_{2_f}-Konzentration durch die DPH-O_2-Komplexbildung nicht geringer. Daraus resultierend folgt die Depopulation des S_1-Zustandes einem Geschwindigkeitsgesetz 0. Ordnung und der beobachtete zeitliche Verlauf nimmt linear ab.
In mit Sauerstoff gesättigten Lösungen ist die O_{2_f}-Konzentration größer als die DPH-Konzentration und kann damit die Geschwindigkeit der Komplexbildung nicht mehr limitieren. Die beobachtete Emission ist also exponentiell.
Dieses Modell erklärt sowohl die langlebige Fluoreszenz bei hohen Konzentration an elektronisch angeregten DPH-Molekülen (hohe DPH-Konzentrationen oder Anregungspuls-Energien) als auch die kurzlebige Emission bei niedrigen Konzentration an elektronisch angeregten DPH-Molekülen oder bei hohen Sauerstoff-Konzentrationen. Die aus den Simulationen erhaltenen Geschwindigkeitskonstanten stimmen gut mit den bereits für einige der involvierten Prozesse publizierten theoretischen Geschwindigkeitskonstanten überein.

In allen drei untersuchten Systemen konnten also mit Hilfe von zeitaufgelöster Spektroskopie in Kombination mit Simulationen und quantenchemischen Rechnungen die den Beobachtungen zugrunde liegenden Mechanismen aufgeklärt werden.

Bibliography

[1] T. Melin and R. Rautenbach. *Membranverfahren.* Springer, 3rd edition, 2007.

[2] L. Y. Jiang, Y. Wang, T. S. Chung, X. Y. Qiao, and J. Y. Lai. Polyimide membranes for pervaporation and biofuels separation. *Prog. Polym. Sci.*, 34(11):1135–1160, 2009.

[3] M. T. Ravanchi, T. Kaghazchi, and A. Kargari. Application of membrane separation processes in petrochemical industry: a review. *Desalination*, 235(1-3):199–244, 2009.

[4] S. P. Nunes and K.-V. Peinemann. *Membrane Technology: in the Chemical Industry.* Wiley-VCH, 1st edition, 2006.

[5] Directive 98/70/ec of the european parliament and of the council of 13 october 1998 relating to the quality of petrol and diesel fuels and amending council directive 93/12/eec, 1998.

[6] A. Jonquières, R. Clément, P. Lochon, J. Nèel, M. Dresch, and B. Chrétien. Industrial state-of-the-art of pervaporation and vapour permeation in the western countries. *J. Membr. Sci.*, 206(1-2):87–117, 2002.

[7] H. E. A. Brüschke. *State-of-the-Art of Pervaporation Processes in the Chemical Industry*, pages 151–202. Wiley-VCH Verlag GmbH & Co. KGaA, 2006.

[8] D. Beaumelle, M. Marin, and H. Gibert. Pervaporation with organophilic membranes: state of the art. *Food Bioprod. Process.*, 71:77–89, 1993.

[9] J. Z. Ren, C. Staudt-Bickel, and R. N. Lichtenthaler. Separation of aromatics/aliphatics with crosslinked 6FDA-based copolyimides. *Sep. Purif. Tech.*, 22-3(1-3):31–43, 2001.

[10] P. A. Kober. Pervaporation, perstillation and percrystallization. *J. Membr. Sci.*, 100(1):61–64, 1995.

[11] J. P. Garcia Villaluenga and A. Tabe-Mohammadi. A review on the separation of benzene/cyclohexane mixtures by pervaporation processes. *J. Membr. Sci.*, 169(2):159–174, 2000.

[12] T. Graham. XXII.-On the absorption and dialytic separation of gases by colloid septa. *J. Chem. Soc.*, 20:235–288, 1867.

[13] V. S. Cunha, M. L. L. Paredes, C. P. Borges, A. C. Habert, and R. Nobrega. Removal of aromatics from multicomponent organic mixtures by pervaporation using polyurethane membranes: experimental and modeling. *J. Membr. Sci.*, 206(1-2):277–290, 2002.

[14] O. Sae-Khow and S. Mitra. Pervaporation in chemical analysis. *J. Chromatogr. A*, 1217(16):2736–2746, 2010.

[15] S. T. Hwang. Fundamentals of membrane transport. *Kor. J. Chem. Eng.*, 28(1):1–15, 2011.

[16] T. Gittel. *Aufarbeitung mizellarer Lösungen durch organophile Pervaporation.* Dissertation, 2004.

[17] N. Schmeling. *Vernetzbare Polymermaterialien für die Pervaporation - Synthese, Charakterisierung und Anwendungen.* Dissertation, 2013.

[18] R. C. Fettes. Process of polymerizing ester of acrylic or methacrylic acids, 1960.

[19] D. Braun, H. Cherdron, and H. Ritter. *Praktikum der Makromolekularen Stoffe.* Wiley-VCH, 1999.

[20] N. Schmeling, K. Hunger, G. Engler, B. Breiten, P. Rölling, A. Mixa, C. Staudt, and K. Kleinermanns. Photo-crosslinking of poly[ethene-stat-(methacrylic acid)] functionalised with maleimide side groups. *Polym. Int.*, 58(7):720–727, 2009.

[21] H. Domininghaus. *Die Kunststoffe und ihre Eigenschaften.* Springer-Verlag GmbH, 2004.

[22] M. T. Bogert and R. R. Renshaw. 4-Amino-o-phtalic acid and some of its derivatives. *J. Am. Chem. Soc.*, 30(7):1135–1144, 1908.

[23] W. H. Carothers. Linear polyamides and their production, 1938.

[24] C. E. Sroog, A. L. Endrey, S. V. Abramo, C. E. Berr, W. M. Edwards, and K. L. Olivier. Aromatic polypyromellitimides from aromatic polyamic acids. *J. Polym. Sci. Part A*, 3(4PA):1373–1390, 1965.

[25] G. M. Bower and L. W. Frost. Aromatic polyimides. *J. Polym. Sci. A*, 1(10):3135–3150, 1963.

[26] J. H. Petropoulos, M. Sanopoulou, and K. G. Papadokostaki. Physically insightful modeling of non-fickian kinetic regimes encountered in fundamental studies of isothermal sorption of swelling agents in polymeric media. *Eur. Polym. J.*, 47(11):2053–2062, 2011.

[27] S. Matsui and D. R. Paul. Pervaporation separation of aromatic/aliphatic hydrocarbons by a series of ionically crosslinked poly(n-alkyl acrylate) membranes. *J. Membr. Sci.*, 213(1-2):67–83, 2003.

[28] S. Matsui and D. R. Paul. Pervaporation separation of aromatic/aliphatic hydrocarbons by crosslinked poly(methyl acrylate-co-acrylic acid) membranes. *J. Membr. Sci.*, 195(2):229–245, 2002.

[29] N. Schmeling, R. Konietzny, D. Sieffert, P. Rölling, and C. Staudt. Functionalized copolyimide membranes for the separation of gaseous and liquid mixtures. *Beilstein J. Org. Chem.*, 6:789–800, 2010.

[30] D. L. Damian, C. R. S. Patterson, M. Stapelberg, J. Park, R. S. C. Barnetson, and G. M. Halliday. UV radiation-induced immunosuppression is greater in men and prevented by topical nicotinamide. *J. Invest. Dermatol.*, 128(2):447–454, 2008.

[31] M. A. Pathak and K. Stratton. Free radicals in human skin before and after exposure to light. *Arch. Biochem. Biophys.*, 123(3):468, 1968.

[32] K. Jimbow, M. A. Pathak, and Fitzpatrick.T. Effect of ultraviolet on the distribution pattern of microfilaments and microtubules on the nucleus in human melanocytes. *Yale J. Biol. Med.*, 46(5):411–426, 1973.

[33] P. C. Jou, R. J. Feldman, and K. J. Tomecki. UV protection and sunscreens: What to tell patients. *Clevel. Clin. J. Med.*, 79(6):427–436, 2012.

[34] P. Kullavanijaya and H. W. Lim. Photoprotection. *J. Am. Acad. Dermatol*, 52(6):937–958, 2005.

[35] Y. Miyamura, S. G. Coelho, K. Schlenz, J. Batzer, C. Smuda, W. Choi, M. Brenner, T. Passeron, G. F. Zhang, L. Kolbe, R. Wolber, and V. J. Hearing. The deceptive nature of UVA tanning versus the modest protective effects of UVB tanning on human skin. *Pigment Cell Melanoma Res.*, 24(1):136–147, 2011.

[36] E. M. Gil and T. H. Kim. UV-induced immune suppression and sunscreen. *Photodermatol. Photoimmunol. Photomed.*, 16(3):101–110, 2000.

[37] H. Honigsmann. Erythema and pigmentation. *Photodermatol. Photoimmunol. Photomed.*, 18(2):75–81, 2002.

[38] J. H. Rabe, A. J. Mamelak, P. J. S. McElgunn, W. L. Morison, and D. N. Sauder. Photoaging: Mechanisms and repair. *J. Am. Acad. Dermatol.*, 55(1):1–19, 2006.

[39] P. C. Jou, T. S. McCormick, and E. D. Baron. UV immunosuppression and cutaneous malignancies. *Exp. Rev. Dermatol.*, 6(1):61–74, 2011.

[40] J. D. Watson and F. H. C. Crick. Molecular structure of nucleic acids: A structure for deoxyribose nucleic acid. *Nature*, 171(4356):737–738, 1953.

[41] K. Hoogsteen. The crystal and molecular structure of a hydrogen-bonded complex between 1-methylthymine and 9-methyladenine. *Acta Crystallogr.*, 16(9):907–916, 1963.

[42] P. Balagurumoorthy and S. K. Brahmachari. Structure and stability of human telomeric sequence. *J. Biol. Chem.*, 269(34):21858–21869, 1994.

[43] T. M. Bryan and P. Baumann. G-quadruplexes: From guanine gels to chemotherapeutics. *Mol. Biotechnol.*, 49(2):198–208, 2011.

[44] G. P. Pfeifer and A. Besaratinia. UV wavelength-dependent DNA damage and human non-melanoma and melanoma skin cancer. *Photochem. Photobiol. Sci.*, 11(1):90–97, 2012.

[45] J. Cadet, E. Sage, and T. Douki. Ultraviolet radiation-mediated damage to cellular DNA. *Mutat. Res. - Fund. Mol. M.*, 571(1-2):3–17, 2005.

[46] W. J. Schreier, T. E. Schrader, F. O. Koller, P. Gilch, C. E. Crespo-Hernández, V. N. Swaminathan, T. Carell, W. Zinth, and B. Kohler. Thymine dimerization in DNA is an ultrafast photoreaction. *Science*, 315(5812):625–629, 2007.

[47] W. J. Schreier, J. Kubon, P. Clivio, W. Zinth, and P. Gilch. DNA photodamage: Study of cyclobutane pyrimidine dimer formation in a locked thymine dinucleotide. *Spectroscopy*, 24(3-4):309–316, 2010.

[48] G. P. Pfeifer, Y. H. You, and A. Besaratinia. Mutations induced by ultraviolet light. *Mutat. Res. - Fund. Mol. M.*, 571(1-2):19–31, 2005.

[49] D. L. Mitchell and A. A. Fernandez. Different types of DNA damage play different roles in the etiology of sunlight-induced melanoma. *Pigm. Cell Melanoma Res.*, 24(1):119–124, 2011.

[50] A. Besaratinia, S.-i. Kim, and G. P. Pfeifer. Rapid repair of UVA-induced oxidized purines and persistence of UVB-induced dipyrimidine lesions determine the mutagenicity of sunlight in mouse cells. *Faseb Journal*, 22(7):2379–2392, 2008.

[51] D. L. Mitchell and R. S. Nairn. The biology of the (6-4) photoproduct. *Photochem. Photobiol.*, 49(6):805–819, 1989.

[52] L. F. Z. Batista, B. Kaina, R. Meneghini, and C. F. M. Menck. How DNA lesions are turned into powerful killing structures: Insights from UV-induced apoptosis. *Mutat. Res., Rev. Mutat. Res.*, 681(2-3):197–208, 2009.

[53] E. D. Pleasance, R. K. Cheetham, P. J. Stephens, D. J. McBride, S. J. Humphray, C. D. Greenman, I. Varela, M.-L. Lin, G. R. Ordonez, G. R. Bignell, K. Ye, J. Alipaz, M. J. Bauer, D. Beare, A. Butler, R. J. Carter, L. Chen, A. J. Cox, S. Edkins, P. I. Kokko-Gonzales, N. A. Gormley, R. J. Grocock, C. D. Haudenschild, M. M. Hims, T. James, M. Jia, Z. Kingsbury, C. Leroy, J. Marshall, A. Menzies, L. J. Mudie, Z. Ning, T. Royce, O. B. Schulz-Trieglaff, A. Spiridou, L. A. Stebbings, L. Szajkowski, J. Teague, D. Williamson, L. Chin, M. T. Ross, P. J. Campbell, D. R. Bentley, P. A. Futreal, and M. R. Stratton. A comprehensive catalogue of somatic mutations from a human cancer genome. *Nature*, 463(7278):191–U73, 2010.

[54] J. S. Taylor, D. S. Garrett, and M. P. Cohrs. Solution-state structure of the Dewar pyrimidinone photoproduct of thymidylyl-(3'- 5')-thymidine. *Biochemistry*, 27(19):7206–7215, 1988.

[55] B. P. Fingerhut, T. T. Herzog, G. Ryseck, K. Haiser, F. F. Graupner, K. Heil, P. Gilch, W. J. Schreier, T. Carell, R. de Vivie-Riedle, and W. Zinth. Dynamics of ultraviolet-induced dna lesions: Dewar formation guided by pre-tension induced by the backbone. *New J. Phys.*, 14(6):065006, 2012.

[56] H. Ikehata and T. Ono. The mechanisms of UV mutagenesis. *J. Radiat. Res.*, 52(2):115–125, 2011.

[57] J. M. L. Pecourt, J. Peon, and B. Kohler. Ultrafast internal conversion of electronically excited rna and dna nucleosides in water (vol 122, pg 9348, 2000). *J. Am. Chem. Soc.*, 123(21):5166–5166, 2001.

[58] M. K. Shukla and Jerzy Leszczynski. Electronic spectra, excited state structures and interactions of nucleic acid bases and base assemblies: A review. *J. Biomol. Struct. Dyn.*, 25(1):93–118, 2007.

[59] C. T. Middleton, K. de La Harpe, C. Su, Y. K. Law, C. E. Crespo-Hernández, and B. Kohler. *DNA Excited-State Dynamics: From Single Bases to the Double Helix*, volume 60 of *Annu. Rev. Phys. Chem.*, pages 217–239. Annual Reviews, Palo Alto, 2009.

[60] P.-O. Löwdin. Proton tunneling in DNA and its biological implications. *Rev. Mod. Phys.*, 35(3):724–732, 1963.

[61] C. E. Crespo-Hernández, B. Cohen, P. M. Hare, and B. Kohler. Ultrafast excited-state dynamics in nucleic acids. *Chem. Rev.*, 104(4):1977–2019, 2004.

[62] S. Lagerwerf, M. G. Vrouwe, R. M. Overmeer, M. I. Fousteri, and L. H. F. Mullenders. DNA damage response and transcription. *DNA Repair*, 10(7):743–750, 2011.

[63] E. Sage, P. M. Girard, and S. Francesconi. Unravelling UVA-induced mutagenesis. *Photochem. Photobiol. Sci*, 11(1):74–80, 2012.

[64] C. E. Crespo-Hernández, B. Cohen, and B. Kohler. Base stacking controls excited-state dynamics in A-T DNA. *Nature*, 436(7054):1141–1144, 2005.

[65] T. Takaya, C. Su, K. de La Harpe, C. E. Crespo-Hernández, and B. Kohler. UV excitation of single DNA and RNA strands produces high yields of exciplex states between two stacked bases. *Proc. Natl. Acad. Sci. USA*, 105(30):10285–10290, 2008.

[66] A. L. Sobolewski and W. Domcke. Ab initio studies on the photophysics of the guanine-cytosine base pair. *Phys. Chem. Chem. Phys.*, 6(10):2763–2771, 2004.

[67] A. L. Sobolewski, W. Domcke, and C. Hattig. Tautomeric selectivity of the excited-state lifetime of guanine/cytosine base pairs: The role of electron-driven proton-transfer processes. *Proc. Natl. Acad. Sci. USA*, 102(50):17903–17906, 2005.

[68] E. Henderson, C. C. Hardin, S. K. Walk, I. Tinoco, and E. H. Blackburn. Telomeric DNA oligonucleotides form novel intramolecular structures containing guanine guanine base-pairs. *Cell*, 51(6):899–908, 1987.

[69] R. J. Wellinger and D. Sen. The DNA structures at the ends of eukaryotic chromosomes. *Eur. J. Cancer*, 33(5):735–749, 1997.

[70] E. H. Blackburn. Structure and function of telomeres. *Nature*, 350(6319):569–573, 1991.

[71] A. Gualberto, R. M. Patrick, and K. Walsh. Nucleic acid specificity of a vertebrate telomere-binding protein: evidence for G-G base pair recognition at the core-binding site. *Genes & Development*, 6(5):815–824, 1992.

[72] J. L. Battiste, H. Y. Mao, N. S. Rao, R. Y. Tan, D. R. Muhandiram, L. E. Kay, A. D. Frankel, and J. R. Williamson. alpha helix-RNA major groove recognition in an HIV-1 rev peptide RRE RNA complex. *Science*, 273(5281):1547–1551, 1996.

[73] T. Förster. Zwischenmolekulare Energiewanderung und Fluoreszenz. *Ann. Phys.*, 437(1-2):55–75, 1948.

[74] R. van Grondelle, J. P. Dekker, T. Gillbro, and V. Sundstrom. Energy transfer and trapping in photosynthesis. *Biochim. Biophys. Acta*, 1187(1):1–65, 1994.

[75] P. Horton, A. V. Ruban, and R. G. Walters. Regulation of light harvesting in green plants. *Ann. Rev. Plant Physio.*, 47(1):655–684, 1996.

[76] C. König and J. Neugebauer. Quantum chemical description of absorption properties and excited-state processes in photosynthetic systems. *ChemPhysChem*, 13(2):386–425, 2012.

[77] R. Nevo, D. Charuvi, O. Tsabari, and Z. Reich. Composition, architecture and dynamics of the photosynthetic apparatus in higher plants. *Plant J.*, 70(1):157–176, 2012.

[78] R. Croce and H. van Amerongen. Light-harvesting and structural organization of photosystem II: From individual complexes to thylakoid membrane. *J. Photochem. Photobiol. B*, 104(1-2):142–153, 2011.

[79] J. Deisenhofer and H. Michel. The photosynthetic reaction center from the purple bacterium Rhodopseudomonas-viridis. *Embo Journal*, 8(8):2149–2170, 1989.

[80] R. Huber. A structural basis of light energy and electron-transfer in biology (Nobel Lecture). *Nobel Lecture*, 1988.

[81] H. Lokstein, A. Betke, M. Krikunova, K. Teuchner, and B. Voigt. Elucidation of structure-function relationships in plant major light-harvesting complex (LHC II) by nonlinear spectroscopy. *Photosynth. Res.*, 111(1):227–235, 2012.

[82] A. Pandit and H. de Groot. Solid-state NMR applied to photosynthetic light-harvesting complexes. *Photosynth. Res.*, 111(1):219–226, 2012.

[83] K.-H. Tang and R. Blankenship. Neutron and light scattering studies of light-harvesting photosynthetic antenna complexes. *Photosynth. Res.*, 111(1):205–217, 2012.

[84] V. Sundström, T. Pullerits, and R. van Grondelle. Photosynthetic light-harvesting: Reconciling dynamics and structure of purple bacterial LH2 reveals function of photosynthetic unit. *J. Phys. Chem. B*, 103(13):2327–2346, 1999.

[85] R. Berera, R. van Grondelle, and J. T. M. Kennis. Ultrafast transient absorption spectroscopy: principles and application to photosynthetic systems. *Photosynth. Res.*, 101(2-3):105–118, 2009.

[86] A. D. Stahl, M. Di Donato, I. van Stokkum, R. van Grondelle, and M. L. Groot. A femtosecond visible/visible and visible/mid-infrared transient absorption study of the light harvesting complex II. *Biophys. J.*, 97(12):3215–3223, 2009.

[87] J. P. Allen and J. C. Williams. Photosynthetic reaction centers. *Febs Lett.*, 438(1-2):5–9, 1998.

[88] V. A. Boichenko. Photosynthetic units of phototrophic organisms. *Biochem. Moscow*, 69(5):471–484, 2004.

[89] S. Ohashi, T. Iemura, N. Okada, S. Itoh, H. Furukawa, M. Okuda, M. Ohnishi-Kameyama, T. Ogawa, H. Miyashita, T. Watanabe, H. Oh-oka, K. Inoue, and M. Kobayashi. An overview on chlorophylls and quinones in the photosystem i-type reaction centers. *Photosynth. Res.*, 104(2-3):305–319, 2010.

[90] D. Siefermann-Harms. The light-harvesting and protective functions of carotenoids in photosynthetic membranes. *Physiol. Plantarum*, 69(3):561–568, 1987.

[91] B. Demmig-Adams, A. M. Gilmore, and W. W. Adams. Carotenoids 3. In vivo functions of carotenoids in higher plants. *Faseb Journal*, 10(4):403–412, 1996.

[92] F. G. Xiao, L. Shen, and H. F. Ji. On photoprotective mechanisms of carotenoids in light harvesting complex. *Biochem. Biophys. Res. Comm.*, 414(1):1–4, 2011.

[93] S. Takaichi. Carotenoids in algae: Distributions, biosyntheses and functions. *Marine Drugs*, 9(6):1101–1118, 2011.

[94] K. Scharffetter-Kochanek, M. Wlaschek, P. Brenneisen, M. Schauen, R. Blaudschun, and J. Wenk. Uv-induced reactive oxygen species in photocarcinogenesis and photoaging. *Biol. Chem.*, 378(11):1247–1257, 1997.

[95] O. Blokhina, E. Virolainen, and K. V. Fagerstedt. Antioxidants, oxidative damage and oxygen deprivation stress: a review. *Ann. Bot.*, 91(2):179–194, 2003.

[96] M. Ichihashi, M. Ueda, A. Budiyanto, T. Bito, M. Oka, M. Fukunaga, K. Tsuru, and T. Horikawa. Uv-induced skin damage. *Toxicology*, 189(1-2):21–39, 2003.

[97] W. Droge. Free radicals in the physiological control of cell function. *Physiol. Rev.*, 82(1):47–95, 2002.

[98] R. M. Han, J. P. Zhang, and L. H. Skibsted. Reaction dynamics of flavonoids and carotenoids as antioxidants. *Molecules*, 17(2):2140–2160, 2012.

[99] P. Jahns and A. R. Holzwarth. The role of the xanthophyll cycle and of lutein in photoprotection of photosystem II. *Biochim. Biophys. Acta-Bioenerg.*, 1817(1):182–193, 2012.

[100] S. M. Bachilo, C. W. Spangler, and T. Gillbro. Excited state energies and internal conversion in diphenylpolyenes: from diphenylbutadiene to diphenyltetradecaheptaene. *Chem. Phys. Lett.*, 283(3-4):235–242, 1998.

[101] K.W. Hausser. *Z. Tech. Phys.*, 15:10, 1935.

[102] K.W. Hausser, R. Kuhn, A. Smakula, and K.H. Kreuchen. *Z. Phys. Chem. Abt. B*, 29:363, 1935.

[103] K.W. Hausser, R. Kuhn, and A. Smakula. *Z. Phys. Chem. Abt. B*, 29:378, 1935.

[104] K.W. Hausser, R. Kuhn, and A. Smakula. *Z. Phys. Chem. Abt. B*, 29:384, 1935.

[105] K.W. Hausser, R. Kuhn, and G. Seitz. *Z. Phys. Chem. Abt. B*, 29:391, 1935.

[106] K.W. Hausser, R. Kuhn, and E. Kuhn. *Z. Phys. Chem. Abt. B*, 29:417, 1935.

[107] M. T. Allen and D. G. Whitten. The photophysics and photochemistry of α,ω-diphenylpolyene singlet states. *Chem. Rev.*, 89(8):1691–1702, 1989.

[108] B. S. Hudson and B. E. Kohler. A low-lying weak transition in the polyene α,ω-diphenyloctatetraene. *Chem. Phys. Lett.*, 14(3):299–304, 1972.

[109] J. Catalán. The emission of α,ω-diphenylpolyenes: A model involving several molecular structures. *Chem. Phys.*, 335(1):69–78, 2007.

[110] J. Catalán. On the chromism of polyenes. *Chem. Phys. Lett.*, 457(1-3):87–90, 2008.

[111] A. K. Singh and G. R. Mahalaxmi. Excited state properties of alpha,omega-diphenylpolyenes: Photophysical and photochemical studies of donor-acceptor diarylbutadienes. *Photochem. Photobiol.*, 71(4):387–396, 2000.

[112] W. A. Yee, R. H. O'Neil, J. W. Lewis, J. Z. Zhang, and D. S. Kliger. Femtosecond transient absorption studies of diphenylpolyenes. direct detection of S_2 -> S_1 radiationless conversion in diphenylhexatriene and diphenyloctatetraene. *Chem. Phys. Lett.*, 276(5-6):430–434, 1997.

[113] S. M. Bachilo, E. V. Bachilo, and T. Gillbro. Spectral shape of diphenylpolyene fluorescence and mixing of the S_1 and S_2 states. *Chemical Physics*, 229(1):75–91, 1998.

[114] J. G. Calvert and J. N. Jr. Pitts. *Photochemistry.* John Wiley & Sons, Inc., New York, London, Sydney, 2nd edition, 1966.

[115] N.J. Turro, V. Ramamurthy, and J.C. Scaiano. *Principles of Molecular Photochemistry: An Introduction.* University Science Books, Sausalito, 1st edition, 2009.

[116] W. Demtröder. *Molekülphysik: Theoretische Grundlagen und experimentelle Methoden.* Oldenbourg Wissenschaftsverlag, München, Wien, 1st edition, 2003.

[117] P.W. Atkins. *Molecular Quantum Mechanics.* Oxford University Press, 3rd edition, 1996.

[118] J. C. Cramer. *Essentials of Computational Chemistry: Theories and Models.* John Wiley & Sons, 2 edition, 2004.

[119] M. Kasha. Characterization of electronic transitions in complex molecules. *Farad. Discuss.*, 9:14–19, 1950.

[120] G. G. Stokes. On the change of refrangibility of light. *Phil. Trans. R. Soc. Lond.*, 142:463–562, 1852.

[121] J. R. Lakowicz. *Principles of Fluorescence Spectroscopy.* Springer Science + Business Media, New York, 2006.

[122] M. Hesse, H. Meier, and B. Zeeh. *Spektroskopische Methoden in der organischen Chemie*. Thieme, Stuttgart, 7th edition, 2005.

[123] J. Franck and E. G. Dymond. Elementary processes of photochemical reactions. *Trans. Faraday Soc.*, 21(February):536–542, 1926.

[124] E. Condon. A theory of intensity distribution in band systems. *Phys. Rev.*, 28(6):1182–1201, 1926.

[125] E. Condon. Nuclear motions associated with electron transitions in diatomic molecules. *Phys. Rev.*, 32(6):858–872, 1928.

[126] L. Biemann, M. Braun, and K. Kleinermanns. Gas phase infrared spectra and corresponding DFT calculations of alpha, omega-diphenylpolyenes. *J. Mol. Spectrosc.*, 259(1):11–15, 2010.

[127] R. Hoffmann. Building bridges between inorganic and organic chemistry (Nobel lecture). *Angewandte Chemie-International Edition in English*, 21(10):711–724, 1982.

[128] G. W. Goodall and W. Hayes. Advances in cycloaddition polymerizations. *Chem. Soc. Rev.*, 35(3):280–312, 2006.

[129] T. Bach. Stereoselective intermolecular 2+2 -photocycloaddition reactions and their application in synthesis. *Synthesis-Stuttgart*, (5):683–703, 1998.

[130] J.-L. Ravanat, T. Douki, and J. Cadet. Direct and indirect effects of UV radiation on DNA and its components. *J. Photochem. Photobiol. B: Biol.*, 63(1-3):88–102, 2001.

[131] K. Heil, D. Pearson, and T. Carell. Chemical investigation of light induced DNA bipyrimidine damage and repair. *Chem. Soc. Rev.*, 40(8):4271–4278, 2011.

[132] E. Paternò and G. Chieffi. *Gazz. Chim. Ital.*, 39(1):341, 1909.

[133] G. Büchi, C. G. Inman, and E. S. Lipinsky. Light-catalyzed organic reactions .1. the reaction of carbonyl compounds with 2-methyl-2-butene in the presence of ultraviolet light. *J. Am. Chem. Soc.*, 76(17):4327–4331, 1954.

[134] J. Iriondo-Alberdi and M. F. Greaney. Photocycloaddition in natural product synthesis. *Eur. J. Org. Chem.*, 2007(29):4801–4815, 2007.

[135] N. Agmon. Elementary steps in excited-state proton transfer. *J. Phys. Chem. A*, 109(1):13–35, 2005.

[136] L. G. Arnaut and S. J. Formosinho. Excited-state proton transfer reactions i. fundamentals and intermolecular reactions. *J. Photochem. Photobiol. A-Chem.*, 75(1):1–20, 1993.

[137] Z. R. Grabowski and W. Rubaszewska. Generalised Förster cycle. Thermodynamic and extrathermodynamic relationships between proton transfer, electron transfer and electronic excitation. *J. Chem. Soc. Faraday T.*, 73:11–28, 1977.

[138] M. H. V. Huynh and T. J. Meyer. Proton-coupled electron transfer. *Chem. Rev.*, 107(11):5004–5064, 2007.

[139] E. M. Kosower and D. Huppert. Excited-state electron and proton transfers. *Annu. Rev. Phys. Chem.*, 37:127–156, 1986.

[140] S. Scheiner. Theoretical studies of excited state proton transfer in small model systems. *J. Phys. Chem. A*, 104(25):5898–5909, 2000.

[141] A. A. El-Rayyes, H. P. Perzanowski, S. A. I. Barri, and U. K. A. Klein. New insight into the excited-state proton-transfer reactions of 1-naphthylamine in solution. *J. Phys. Chem. A*, 105(45):10169–10175, 2001.

[142] H. Shizuka. Excited-state proton-transfer reactions and proton-induced quenching of aromatic compounds. *Acc. Chem. Res.*, 18(5):141–147, 1985.

[143] L. G. Arnaut and S. J. Formosinho. Excited-state proton-transfer kinetics - a theoretical model. *J. Phys. Chem.*, 92(3):685–691, 1988.

[144] P. O. Löwdin. Isotope effect in tunneling and its influence on mutation rates. *Mutation Res.*, 2(3):218–, 1965.

[145] V. Zoete and M. Meuwly. Double proton transfer in the isolated and DNA-embedded guanine-cytosine base pair. *J. Chem. Phys.*, 121(9):4377–4388, 2004.

[146] S. Takeuchi and T. Tahara. Femtosecond ultraviolet-visible fluorescence study of the excited-state proton-transfer reaction of 7-azaindole dimer. *J. Phys. Chem. A*, 102(40):7740–7753, 1998.

[147] A. Douhal, S. K. Kim, and A. H. Zewail. Femtosecond molecular-dynamics of tautomerization in model base-pairs. *Nature*, 378(6554):260–263, 1995.

[148] Xue-Fang Yu, Shohei Yamazaki, and Tetsuya Taketsugu. Theoretical study of the excited-state double proton transfer in the (3-methyl-7-azaindole)-(7-azaindole) heterodimer. *J. Comput. Chem.*, 33(20):1701–1708, 2012.

[149] A. Abo-Riziq, L. Grace, E. Nir, M. Kabelac, P. Hobza, and M. S. de Vries. Photochemical selectivity in guanine-cytosine base-pair structures. *P. Natl. Acad. Sci. USA*, 102(1):20–23, 2005.

[150] T. Douki, D. Angelov, and J. Cadet. UV laser photolysis of DNA: Effect of duplex stability on charge-transfer efficiency. *J. Am. Chem. Soc.*, 123(46):11360–11366, 2001.

[151] C. E. Crespo-Hernández and R. Arce. Photoionization of DNA and RNA bases, nucleosides and nucleotides through a combination of one- and two-photon pathways upon 266 nm nanosecond laser excitation. *Photochem. Photobiol.*, 76(3):259–267, 2002.

[152] R. G. W. Norrish and G. Porter. Chemical reactions produced by very high light intensities. *Nature*, 164:658, 1949.

[153] G. Porter. Flash photolysis and some of its applications. *Nobel Lecture*, 1967.

[154] D. Löwenich. *Stationäre und transiente UV-Spektroskopie an Cytochrom c und Porphyrin-Modellsystemen.* Dissertation, 2007.

[155] W. Herres and J. Gronholz. Understanding FT-IR data processing. part 1: Data acquisition and Fourier transformation. *Comp. Appl. Lab.*, 216:1–5, 1984.

[156] J. Gronholz and W. Herres. Understanding FT-IR data processing, part 2: Details of the spectrum calculation. *Instrum. & Comp.*, 10:6–12, 1985.

[157] J. Gronholz and W. Herres. Understanding FT-IR data processing, part 3: Further useful computational methods. *Intell. Instrum. Comp.*, 3:13–23, 1985.

[158] O. Treutler and R. Ahlrichs. Effcient molecular numerical integration schemes. *J. Chem. Phys.*, 102(1):346–354, 1995.

[159] M. von Arnim and R. Ahlrichs. Performance of parallel turbomole for density functional calculations. *J. Comput. Chem.*, 19(15):1746–1757, 1998.

[160] A. Schäfer, C. Huber, and R. Ahlrichs. Fully optimized contracted gaussian basis sets of triple zeta valence quality for atoms Li to Kr. *J. Chem. Phys.*, 100(8):5829–5835, 1994.

[161] R. Ahlrichs, M. Bär, M. Häser, H. Horn, and C. Kölmel. Electronic structure calculations on workstation computers: The program system turbomole. *Chem. Phys. Lett.*, 162(3):165–169, 1989.

[162] P. Deglmann, F. Furche, and R. Ahlrichs. An efficient implementation of second analytical derivatives for density functional methods. *Chem. Phys. Lett.*, 362(5-6):511–518, 2002.

[163] P. Deglmann and F. Furche. Efficient characterization of stationary points on potential energy surfaces. *J. Chem. Phys.*, 117(21):9535–9538, 2002.

[164] P. Deglmann, K. May, F. Furche, and R. Ahlrichs. Nuclear second analytical derivative calculations using auxiliary basis set expansions. *Chem. Phys. Lett.*, 384(1-3):103–107, 2004.

[165] F. Jensen. *Introduction to Computational Chemistry.* Wiley & Sons, West Sussex, 1st edition, 1998.

[166] W. Kutzelnigg. *Einführung in die Theoretische Chemie.* Wiley-VCH Verlag GmbH & Co. KGaA, 1st edition, 2001.

[167] M. Born and R. Oppenheimer. Zur Quantentheorie der Molekeln. *Ann. Phys.*, 389(20):457–484, 1927.

[168] T. Ziegler. Approximate density functional theory as a practical tool in molecular energetics and dynamics. *Chem. Rev.*, 91(5):651–667, 1991.

[169] A. D. Becke. Density-functional thermochemistry .4. a new dynamical correlation functional and implications for exact-exchange mixing. *J. Chem. Phys.*, 104(3):1040–1046, 1996.

[170] R. Colle and O. Salvetti. Approximate calculation of the correlation energy for the closed shells. *Theo. Chim. Acta*, 37(4):329–334, 1975.

[171] A. D. Becke. Density-functional thermochemistry. III. the role of exact exchange. *J. Chem. Phys.*, 98(7):5648–5652, 1993.

[172] P. J. Stephens, F. J. Devlin, C. F. Chabalowski, and M. J. Frisch. Ab initio calculation of vibrational absorption and circular dichroism spectra using density functional force fields. *J. Phys. Chem.*, 98(45):11623–11627, 1994.

[173] A. D. Becke. Density-functional exchange-energy approximation with correct asymptotic behavior. *Phys. Rev. A*, 38(6):3098–3100, 1988.

[174] C. T. Lee, W. T. Yang, and R. G. Parr. Development of the Colic-Salvetti correlation-energy formula into a functional of the electron density. *Phys. Rev. B*, 37(2):785–789, 1988.

[175] R. G. Parr and W. Yang. *Density-Functional Theory of Atoms and Molecules.* International Series of Monographs on Chemistry. Oxford University Press USA, 1989.

[176] J. C. Slater. Atomic shielding constants. *Phys. Rev.*, 36(1):57–64, 1930.

[177] S. F. Boys. Electronic wave functions. i. a general method of calculation for the stationary states of any molecular system. *Proc. R. Soc.*, 200(1063):542–554, 1950.

[178] M. W. Schmidt, K. K. Baldrige, J. A. Boatz, J. H. Jensen, S. Koseki, M. S. Gordon, K. A. Nguyen, T. L. Windus, and S. T. Elbert. Berny optimization. *QCPE Bulletin*, 10:52–62, 1990.

[179] W. J. Koros and R. Mahajan. Pushing the limits on possibilities for large scale gas separation: which strategies? *J.Membr. Sci.*, 175(2):181–196, 2000.

[180] K. Inui, T. Noguchi, T. Miyata, and T. Uragami. Pervaporation characteristics of methyl methacrylate-methacrylic acid copolymer membranes ionically crosslinked with metal ions for a benzene/cyclohexane mixture. *J. Appl. Polym. Sci.*, 71(2):233–241, 1999.

[181] K. Okamoto, H. Y. Wang, T. Ijyuin, S. Fujiwara, K. Tanaka, and H. Kita. Pervaporation of aromatic/non-aromatic hydrocarbon mixtures through crosslinked membranes of polyimide with pendant phosphonate ester groups. *J. Membr. Sci.*, 157(1):97–105, 1999.

[182] F. Pithan and C. Staudt-Bickel. Crosslinked copolyimide membranes for phenol recovery from process water by pervaporation. *ChemPhysChem*, 4(9):967–973, 2003.

[183] D. W. Wallace, C. Staudt-Bickel, and W. J. Koros. Efficient development of effective hollow fiber membranes for gas separations from novel polymers. *J. Membr. Sci.*, 278(1-2):92–104, 2006.

[184] D. W. Wallace, J. Williams, C. Staudt-Bickel, and W. J. Koros. Characterization of crosslinked hollow fiber membranes. *Polymer*, 47(4):1207–1216, 2006.

[185] A. Bos, I. G. M. Pünt, M. Wessling, and H. Strathmann. Plasticization-resistant glassy polyimide membranes for CO_2/CO_4 separations. *Sep. Purif. Technol.*, 14(1-3):27–39, 1998.

[186] C. Staudt-Bickel and W. J. Koros. Improvement of CO_2/CH_4 separation characteristics of polyimides by chemical crosslinking. *J. Membr. Sci.*, 155(1):145–154, 1999.

[187] J. D. Wind, C. Staudt-Bickel, D. R. Paul, and W. J. Koros. The effects of crosslinking chemistry on $CO-2$ plasticization of polyimide gas separation membranes. *Ind. Eng. Chem. Res.*, 41(24):6139–6148, 2002.

[188] J. D. Wind, C. Staudt-Bickel, D. R. Paul, and W. J. Koros. Solid-state covalent cross-linking of polyimide membranes for carbon dioxide plasticization reduction. *Macromolecules*, 36(6):1882–1888, 2003.

[189] W. J. Koros, D. Wallace, J.D. Wind, S.J. Miller, C. Staudt-Bickel, and De Q. Vu. Crosslinked and crosslinkable hollow fiber mixed matrix membrane and method of making same, 2004.

[190] D. Katarzynski and C. Staudt-Bickel. Separation of multi component aromatic/aliphatic mixtures by pervaporation with copolyimide membranes. *Desalination*, 189(1-3):81–86, 2006.

[191] U. Beyer, M. Krüger, P. Schumacher, C. Unger, and F. Kratz. Synthese von neuen bifunktionellen Maleinimidverbindungen zur Herstellung von Chemoimmunokonjugaten. *Monatshefte für Chemie / Chemical Monthly*, 128(1):91–102, 1997.

[192] C. Decker and C. Bianchi. Photocrosslinking of a maleimide functionalized polymethacrylate. *Polym. Int.*, 52(5):722–732, 2003.

[193] E. M. Kosower, T. Miyadera, and N. S. Kosower. Receptor site labeling through functional groups. barbital and amphetamine derivatives. *J. Med. Chem.*, 14(9):873–878, 1971.

[194] M.D. Lechner, K Gehrke, and E.H. Nordmeier. *Makromolekulare Chemie*. Birkhäuser Verlag, 3 edition, 2003.

[195] J. von Sonntag and W. Knolle. Maleimides as electron-transfer photoinitiators: quantum yields of triplet states and radical-ion formation. *J. Photochem. Photobiol. A*, 136(1-2):133–139, 2000.

[196] J. von Sonntag, W. Knolle, S. Naumov, and R. Mehnert. Deprotonation and dimerization of maleimide in the triplet state: A laser flash photolysis study with optical and conductometric detection. *Chem. - Eur. J.*, 8(18):4199–4209, 2002.

[197] Y. C. Xiao, B. T. Low, S. S. Hosseini, T. S. Chung, and D. R. Paul. The strategies of molecular architecture and modification of polyimide-based membranes for CO_2 removal from natural gas - a review. *Prog. Polym. Sci.*, 34(6):561–580, 2009.

[198] S. Basu, A. L. Khan, A. Cano-Odena, C. Liu, and I. F. J. Vankelecom. Membrane-based technologies for biogas separations. *Chem. Soc. Rev.*, 39(2):750–768, 2010.

[199] C. T. Wright and D. R. Paul. Gas sorption and transport in UV-irradiated polyarylate copolymers based on tetramethyl bisphenol-A and dihydroxybenzophenone. *J. Membr. Sci.*, 124(2):161–174, 1997.

[200] S. Hess, C. Staudt-Bickel, and R. N. Lichtenthaler. Propene/propane separation with copolyimide membranes containing silver ions. *J. Membr. Sci.*, 275(1-2):52–60, 2006.

[201] A. M. Kratochvil and W. J. Koros. Effects of supercritical CO_2 conditioning on cross-linked polyimide membranes. *Macromolecules*, 43(10):4679–4687, 2010.

[202] F. Santoso, W. Albrecht, M. Schroeter, T. Weigel, D. Paul, and R. Schomäcker. A novel technique for preparation of aminated polyimide membranes with microfiltration characteristics. *J. Membr. Sci.*, 223(1-2):171–185, 2003.

[203] A. Taubert, J. D. Wind, D. R. Paul, W. J. Koros, and K. I. Winey. Novel polyimide ionomers: CO_2 plasticization, morphology, and ion distribution. *Polymer*, 44(6):1881–1892, 2003.

[204] A. A. Lin, V. R. Sastri, G. Tesoro, A. Reiser, and R. Eachus. On the cross-linking mechanism of benzophenone-containing polyimides. *Macromolecules*, 21(4):1165–1169, 1988.

[205] Y. Liu, C. Pan, M. Ding, and J. Xu. Effect of crosslinking distribution on gas permeability and permselectivity of crosslinked polyimides. *Eur. Polym. J.*, 35(9):1739–1741, 1999.

[206] H. Kita, T. Inada, K. Tanaka, and K. Okamoto. Effect of photo-cross-linking on permeability and permselectivity of gases through benzophenone-containing polyimide. *J. Membr. Sci.*, 87(1-2):139–147, 1994.

[207] C. Decker, C. Bianchi, and S. Jonsson. Light-induced crosslinking polymerization of a novel N-substituted bis-maleimide monomer. *Polymer*, 45(17):5803–5811, 2004.

[208] G. Mattson, E. Conklin, S. Desai, G. Nielander, M. D. Savage, and S. Morgensen. A practical approach to crosslinking. *Mol. Biol. Rep.*, 17(3):167–183, 1993.

[209] S. Pfeifer and J. F. Lutz. Development of a library of N-substituted maleimides for the local functionalization of linear polymer chains. *Chem. - Eur. J.*, 14(35):10949–10957, 2008.

[210] M. P. Stevens and A. D. Jenkins. Crosslinking of polystyrene via pendant maleimide groups. *J. Polym. Sci. Pol. Chem.*, 17(11):3675–3685, 1979.

[211] M. Nagarathinam and J. J. Vittal. A rational approach to crosslinking of coordination polymers using the photochemical [2+2] cycloaddition reaction. *Macromol. Rapid Commun.*, 27(14):1091–1099, 2006.

[212] J. Put and F.C. De Schryver. Photochemistry of nonconjugated bichromophoric systems. intramolecular photocycloaddition of N,N'-alkylenedimaleimides in solution. *J. Am. Chem. Soc.*, 95(1):137–145, 1973.

[213] S. Seiffert, W. Oppermann, and K. Saalwächter. Hydrogel formation by photocrosslinking of dimethylmaleimide functionalized polyacrylamide. *Polymer*, 48(19):5599–5611, 2007.

[214] X. Yu, C. Corten, H. Görner, T. Wolff, and D. Kuckling. Photodimers of N-alkyl-3,4-dimethylmaleimides - product ratios and reaction mechanism. *J. Photochem. Photobiol. A*, 198(1):34–44, 2008. J. Photochem. Photobiol., A.

[215] W. Y. Chiang and J. Y. Lu. Preparation and properties of Si-containing copolymer for near-UV resist. 3. maleimide / silylstyrene copolymer. *J. Appl. Polym. Sci.*, 49(5):893–899, 1993.

[216] M. J. Marks, D. C. Scott, B. R. Guilbeaux, and S. E. Bales. Synthesis and thermochemistry of phenylmaleimide- and phenylnadimide-terminated bisphenol A polycarbonates. *J. Polym. Sci. Pol. Chem.*, 35(2):385–390, 1997.

[217] Y. Chen and C. J. Tsay. Preparation and photo-cross-linking behaviors of polyesters derived from trans-2,2'-dihydroxystilbene. *J. Polym. Sci. Pol. Chem.*, 33(8):1319–1327, 1995.

[218] R. Schinner and T. Wolff. Defined photo-cross-linking and viscometric data - II. photo-cross-linking versus coordinative cross-linking. *Colloid Polym. Sci.*, 279(12):1225–1230, 2001.

[219] C. D. Vlad and C. Hulubei. Crosslinked copolymers based on n-(π-carboxyphenyl)-maleimide. *High Perform. Polym.*, 14(1):31–40, 2002.

[220] C. W. Lee, J. M. Kim, D. K. Han, and K. D. Ahn. Photopolymerization of bifunctional maleimides based on electron-donor/acceptor systems. *J. Macromol. Sci. Pure*, A36(10):1387–1399, 1999.

[221] C. J. King. *Separation Processes, Introduction.* Wiley-VCH Verlag GmbH & Co. KGaA, 2000.

[222] J. C. Davis, R. J. Valus, R. Eshraghi, and A. E. Velikoff. Facilitated transport membrane hybrid systems for olefin purification. *Sep. Sci. Tec.*, 28(1-3):463–476, 1993.

[223] M. Kondo, M. Komori, H. Kita, and K. Okamoto. Tubular-type pervaporation module with zeolite NaA membrane. *J. Membr. Sci.*, 133(1):133–141, 1997.

[224] S. M. Holmes, M. Schmitt, C. Markert, R. J. Plaisted, J. O. Forrest, P. N. Sharratt, A. A. Garforth, C. S. Cundy, and J. Dwyer. Zeolite A membranes for use in alcohol/water separations - Part I: Experimental investigation. *Chem. Eng. Res. Des.*, 78(A8):1084–1088, 2000.

[225] A. W. C. van den Berg, L. Gora, J. C. Jansen, M. Makkee, and T. Maschmeyer. Zeolite A membranes synthesized on a UV-irradiated TiO_2 coated metal support: The high pervaporation performance. *J. Membr. Sci.*, 224(1-2):29–37, 2003.

[226] C. A. Scholes, G. W. Stevens, and S. E. Kentish. Membrane gas separation applications in natural gas processing. *Fuel*, 96(1):15–28, 2012.

[227] W. J. Koros and G. K. Fleming. Membrane-based gas separation. *J. Membr. Sci.*, 83(1):1–80, 1993.

[228] R.W. Baker. *Membrane Technology and Applications.* Wiley, Chichester, England, 2nd edition, 2004.

[229] D. R. Paul and Y. P. Yampol'skii. *Polymeric Gas Separation Membranes.* CRC Press, 1994.

[230] A. Mixa and C. Staudt. Membrane-based separation of phenol/water mixtures using ionically and covalently cross-linked ethylene-methacrylic acid copolymers. *Int. J. Chem. Eng.*, 2008, 2008.

[231] H. Strathmann. *Introduction to Membrane Science and Technology.* Wiley-VCH, 2011.

[232] G. Saracco, H. W. J. P. Neomagus, G. F. Versteeg, and W. P. M. van Swaaij. High-temperature membrane reactors: Potential and problems. *Chem. Eng. Sci.*, 54(13-14):1997–2017, 1999.

[233] A Julbe. *Zeolite membranes - synthesis, characterization and application*, page 181. Elsevier B.V., 3rd edition, 2007.

[234] E. Staude. *Membranen und Membranprozesse.* Wiley-VCH, 1992.

[235] G. Maier. Gas separation with polymer membranes. *Angew Chem Int Edit*, 37(21):2961–2974, 1998.

[236] L. G. Lin, Y. Z. Zhang, and Y. Kong. Recent advances in sulfur removal from gasoline by pervaporation. *Fuel*, 88(10):1799–1809, 2009.

[237] B. Bolto, M. Hoang, and Z. L. Xie. A review of membrane selection for the dehydration of aqueous ethanol by pervaporation. *Chem. Eng. Proc.*, 50(3):227–235, 2011.

[238] L. M. Robeson. Correlation of separation factor versus permeability for polymeric membranes. *J. Membr. Sci.*, 62(2):165–185, 1991.

[239] L. M. Robeson. The upper bound revisited. *J. Membr. Sci.*, 320(1-2):390–400, 2008.

[240] K. Ohlrogge and K. Stürken. *The Separation of Organic Vapors from Gas Streams by Means of Membranes*, pages 69–94. Wiley-VCH Verlag GmbH, 2001.

[241] R. W. Baker. Future directions of membrane gas separation technology. *Ind. Eng. Chem. Res.*, 41(6):1393–1411, 2002.

[242] R. W. Spillman. Economics of gas separation membranes. *Chemical Engineering Progress*, 85(1):41–62, 1989.

[243] H. Ohya, V. V. Kudryavtsev, and S. I. Semenova. *Polyimide Membranes - Applications, Fabrications and Properties.* Crc Pr Inc, 1996.

[244] N. Y. Du, H. B. Park, M. M. Dal-Cin, and M. D. Guiver. Advances in high permeability polymeric membrane materials for CO_2 separations. *Energy Environ. Sci.*, 5(6):7306–7322, 2012.

[245] R. W. Baker and K. Lokhandwala. Natural gas processing with membranes: An overview. *Ind. Eng. Chem. Res.*, 47(7):2109–2121, 2008.

[246] A. L. Kohl and R. B. Nielsen. *Gas Purification.* Gulf Publishing, 1997.

[247] R.H. Hugman, E.H. Vidas, and P.S. Springer. Chemical composition of discovered and undiscovered natural gas in the Lower-48 United States. Project Summary. Final report, 1 November 1988-31 March 1990. Technical Report PB-91-144600/XAB, 1990.

[248] N. Tanihara, K. Tanaka, H. Kita, and K. Okamoto. Pervaporation of organic liquid-mixtures through membranes of polyimides containing methyl-substituted phenylenediamine moieties. *J. Membr. Sci.*, 95(2):161–169, 1994.

[249] J. Terada, T. Hohjoh, S. Yoshimasu, M. Ikemi, and I. Shinohara. Separation of benzene/cyclohexane azeotropic mixture through polymeric membranes with microphase separated structures. *Polym. J.*, 14(5):347–353, 1982.

[250] K. Inui, K. Tsukamoto, T. Miyata, and T. Uragami. Permeation and separation of a benzene/cyclohexane mixture through benzoylchitosan membranes. *J. Membr. Sci.*, 138(1):67–75, 1998.

[251] A. Ito and S.-T. Hwang. Permeation of propane and propylene thrugh cellulosic polymer membranes. *J. Appl. Polym. Sci.*, 38(3):483–490, 1989.

[252] A. Shimazu, K. Ikeda, and H. Hachisuka. Method of selectively separating unsaturated hydrocarbon, 1998.

[253] K. Tanaka, A. Taguchi, Jianqiang Hao, H. Kita, and K. Okamoto. Permeation and separation properties of polyimide membranes to olefins and paraffins. *J. Membr. Sci.*, 121(2):197–207, 1996.

[254] K.-R. Lee and S.-T. Hwang. Separation of propylene and propane by polyimide hollow-fiber membrane module. *J. Membr. Sci.*, 73(1):37–45, 1992.

[255] J. J. Krol, M. Boerrigter, and G. H. Koops. Polyimide hollow fiber gas separation membranes: preparation and the suppression of plasticization in propane/propylene environments. *J. Membr. Sci.*, 184(2):275–286, 2001.

[256] A. Shimazu, T. Miyazaki, M. Maeda, and K. Ikeda. Relationships between the chemical structures and the solubility, diffusivity, and permselectivity of propylene and propane in 6FDA-based polyimides. *J. Polym. Sci. B*, 38(19):2525–2536, 2000.

[257] W. J. Koros, G. K. Fleming, S. M. Jordan, T. H. Kim, and H. H. Hoehn. Polymeric membrane materials for solution-diffusion based permeation separations. *Prog. Polym. Sci.*, 13(4):339–401, 1988.

[258] L. M. Robeson, W. F. Burgoyne, M. Langsam, A. C. Savoca, and C. F. Tien. High-performance polymers for membrane separation. *Polymer*, 35(23):4970–4978, 1994.

[259] K. Tanaka, H. Kita, M. Okano, and K. Okamoto. Permeability and permselectivity of gases in fluorinated and non-fluorinated polyimides. *Polymer*, 33(3):585–592, 1992.

[260] S. A. Stern. Polymers for gas separations - The next decade. *J. Membr. Sci.*, 94:1–65, 1994.

[261] K. Tanaka, M. Okano, H. Kita, K.-i. Okamoto, and S. Nishi. Effects of trifluoromethyl side groups on gas permeability and permselectivity in polyimides. *Polym. J.*, 26(10):1186–1189, 1994.

[262] V. M. Kochkodan and V. K. Sharma. Graft polymerization and plasma treatment of polymer membranes for fouling reduction: A review. *J. Environ. Sci. Heal. A*, 47(12):1713–27, 2012.

[263] M. Wessling, S. Schoeman, T. van der Boomgaard, and C. A. Smolders. Plasticization of gas separation membranes. *Gas Sep. Pur.*, 5(4):222–228, 1991.

[264] J. H. Kim, W. J. Koros, and D. R. Paul. Effects of CO_2 exposure and physical aging on the gas permeability of thin 6FDA-based polyimide membranes: Part 1. Without crosslinking. *J. Membr. Sci.*, 282(1-2):21–31, 2006.

[265] C. Staudt-Bickel and W. J. Koros. Olefin/paraffin gas separations with 6FDA-based polyimide membranes. *J. Membr. Sci.*, 170(2):205–214, 2000.

[266] B. Schiewe, C. Staudt-Bickel, A. Vuin, and G. Wegner. Membrane-based gas separation of ethylene/ethylene oxide mixtures for product enrichment in microreactor technology. *ChemPhysChem*, 2(4):211–218, 2001.

[267] D. Q. Vu, W. J. Koros, and S. J. Miller. High pressure CO_2/CH_4 separation using carbon molecular sieve hollow fiber membranes. *Ind. Eng. Chem. Res.*, 41(3):367–380, 2001.

[268] F. Pithan, C. Staudt-Bickel, S. Hess, and R. N. Lichtenthaler. Polymeric membranes for aromatic/aliphatic separation processes. *ChemPhysChem*, 3(10):856–862, 2002.

[269] B. Cao, H. Hinode, and T. Kajiuchi. Permeation and separation of styrene/ethylbenzene mixtures through cross-linked poly(hexamethylene sebacate) membranes. *J. Membr. Sci.*, 156(1):43–47, 1999.

[270] M. S. McCaig and D. R. Paul. Effect of UV crosslinking and physical aging on the gas permeability of thin glassy polyarylate films. *Polymer*, 40(26):7209–7225, 1999.

[271] M. E. Rezac and B. Schöberl. Transport and thermal properties of poly(ether imide)/acetylene-terminated monomer blends. *J. Membr. Sci.*, 156(2):211–222, 1999.

[272] A. Bos, I. G. M. Pünt, M. Wessling, and H. Strathmann. Suppression of CO_2-plasticization by semiinterpenetrating polymer network formation. *J. Polym. Sci., Polym. Phys.*, 36(9):1547–1556, 1998.

[273] M. E. Rezac, E. Todd Sorensen, and H. W. Beckham. Transport properties of crosslinkable polyimide blends. *J. Membr. Sci.*, 136(1-2):249–259, 1997.

[274] C. Janiak and J. K. Vieth. MOFs, MILs and more: concepts, properties and applications for porous coordination networks (PCNs). *New J. Chem.*, 34(11):2366–2388, 2010.

[275] J. R. Long and O. M. Yaghi. The pervasive chemistry of metal-organic frameworks. *Chem. Soc. Rev.*, 38(5):1213–1214, 2009.

[276] K Biradha. Introduction to the themed issue coordination polymers: structure and function. *New J. Chem.*, 34(11):2353–2354, 2010.

[277] M.J. Zaworotko. There is plenty of room in the middle: crystal clear opportunities abound for coordination polymers. *New J. Chem.*, 34(11):2355–2356, 2010.

[278] K. Hindson. Quo vadis MOFs? *Eur. J. Inorg. Chem.*, 2010(24):3683–3683, 2010.

[279] S. Kitagawa and S. Natarajan. Targeted fabrication of MOFs for hybrid functionality. *Eur. J. Inorg. Chem.*, 2010(24):3685–3685, 2010.

[280] H. C. Zhou, J. R. Long, and O. M. Yaghi. Introduction to metal-organic frameworks. *Chem. Rev.*, 112(2):673–674, 2012.

[281] A. I. Skoulidas, D. S. Sholl, and J. K. Johnson. Adsorption and diffusion of carbon dioxide and nitrogen through single-walled carbon nanotube membranes. *J. Chem. Phys.*, 124(5):054708–7, 2006.

[282] D.-Y. Kang, H. M. Tong, J. Zang, R. P. Choudhury, D. S. Sholl, H. W. Beckham, C. W. Jones, and S. Nair. Single-walled aluminosilicate nanotube/poly(vinyl alcohol) nanocomposite membranes. *ACS Appl. Mater. Interfaces*, 4(2):965–976, 2012.

[283] A. Fonseca, S. Reijerkerk, J. Potreck, K. Nijmeijer, Z. Mekhalif, and J. Delhalle. Very short functionalized carbon nanotubes for membrane applications. *Desalination*, 250(3):1150–1154, 2010.

[284] T. Liu, Y. Tong, and W.-D. Zhang. Preparation and characterization of carbon nanotube/polyetherimide nanocomposite films. *Compos. Sci. Technol.*, 67(3-4):406–412, 2007.

[285] A. Pantano, G. Modica, and F. Cappello. Multiwalled carbon nanotube reinforced polymer composites. *Mater. Sci. Eng. A*, 486(1-2):222–227, 2008.

[286] P. S. Goh, B. C. Ng, A. F. Ismail, M. Aziz, and Y. Hayashi. Pre-treatment of multi-walled carbon nanotubes for polyetherimide mixed matrix hollow fiber membranes. *J. Colloid Interface Sci.*, 386(1):80–87, 2012.

[287] D.-Y. Kang, C. W. Jones, and S. Nair. Modeling molecular transport in composite membranes with tubular fillers. *J. Membr. Sci.*, 381(1-2):50–63, 2011.

[288] H. Cong, J. Zhang, M. Radosz, and Y. Shen. Carbon nanotube composite membranes of brominated poly(2,6-diphenyl-1,4-phenylene oxide) for gas separation. *J. Membr. Sci.*, 294(1-2):178–185, 2007.

[289] H.-K. Jeong, W. Krych, H. Ramanan, S. Nair, E. Marand, and M. Tsapatsis. Fabrication of polymer/selective-flake nanocomposite membranes and their use in gas separation. *Chem. Mater.*, 16(20):3838–3845, 2004.

[290] J. R. Johnson and W. J. Koros. Utilization of nanoplatelets in organic-inorganic hybrid separation materials: Separation advantages and formation challenges. *Taiwan Inst. Chem. Eng*, 40(3):268–275, 2009.

[291] C. Yang, W. H. Smyrl, and E. L. Cussler. Flake alignment in composite coatings. *J. Membr. Sci.*, 231(1-2):1–12, 2004.

[292] J. A. Sheffel and M. Tsapatsis. A model for the performance of microporous mixed matrix membranes with oriented selective flakes. *J. Membr. Sci.*, 295(1-2):50–70, 2007.

[293] J. Choi and M. Tsapatsis. MCM-22/silica selective flake nanocomposite membranes for hydrogen separations. *J. Am. Chem. Soc.*, 132(2):448–449, 2009.

[294] C. Rubio, C. Casado, P. Gorgojo, F. Etayo, S. Uriel, C. TÃ©llez, and J. Coronas. Exfoliated titanosilicate material UZAR-S1 obtained from JDF-L1. *Eur. J. Inorg. Chem.*, 2010(1):159–163, 2010.

[295] A. Galve, D. Sieffert, E. Vispe, C. T éllez, J. Coronas, and C. Staudt. Copolyimide mixed matrix membranes with oriented microporous titanosilicate JDF-L1 sheet particles. *J. Membr. Sci.*, 370(1-2):131–140, 2011.

[296] Q. Hu, E. Marand, S. Dhingra, D. Fritsch, J. Wen, and G. Wilkes. Poly(amide-imide)/TiO_2 nano-composite gas separation membranes: Fabrication and characterization. *J. Membr. Sci.*, 135(1):65–79, 1997.

[297] C. M. Zimmerman, A. Singh, and W. J. Koros. Tailoring mixed matrix composite membranes for gas separations. *J. Membr. Sci.*, 137(1-2):145–154, 1997.

[298] R. Mahajan and W. J. Koros. Factors controlling successful formation of mixed-matrix gas separation materials. *Ind. & Eng. Chem. Res.*, 39(8):2692–2696, 2000.

[299] L. Y. Jiang, T. S. Chung, C. Cao, Z. Huang, and S. Kulprathipanja. Fundamental understanding of nano-sized zeolite distribution in the formation of the mixed matrix single- and dual-layer asymmetric hollow fiber membranes. *J. Membr. Sci.*, 252(1-2):89–100, 2005.

[300] T. S. Chung, L. Y. Jiang, Y. Li, and S. Kulprathipanja. Mixed matrix membranes (MMMs) comprising organic polymers with dispersed inorganic fillers for gas separation. *Prog. Polym. Sci.*, 32(4):483–507, 2007.

[301] T. C. Merkel, B. D. Freeman, R. J. Spontak, Z. He, I. Pinnau, P. Meakin, and A. J. Hill. Ultrapermeable, reverse-selective nanocomposite membranes. *Science*, 296(5567):519–522, 2002.

[302] P. Bernardo, E. Drioli, and G. Golemme. Membrane gas separation: A review/state of the art. *Ind. Eng. Chem. Res.*, 48(10):4638–4663, 2009.

[303] T. T. Moore, R. Mahajan, D. Q. Vu, and W. J. Koros. Hybrid membrane materials comprising organic polymers with rigid dispersed phases. *Angew. Chem. Int. Ed.*, 50(2):311–321, 2004.

[304] G. Langhendries and G. V. Baron. Mass transfer in composite polymer zeolite catalytic membranes. *J. Membr. Sci.*, 141(2):265–275, 1998.

[305] P. Gorgojo, D. Sieffert, C. Staudt, C. Tellez, and J. Coronas. Exfoliated zeolite nu-6(2) as filler for 6FDA-based copolyimide mixed matrix membranes. *J. Membr. Sci.*, 411:146–152, 2012.

[306] T. T. Moore and W. J. Koros. Non-ideal effects in organic-inorganic materials for gas separation membranes. *J. Mol. Struct.*, 739(1-3):87–98, 2005.

[307] R. Mahajan and W. J. Koros. Mixed matrix membrane materials with glassy polymers. part 1. *Polym. Eng. Sci.*, 42(7):1420–1431, 2002.

[308] J. M. Duval, A. J. B. Kemperman, B. Folkers, M. H. V. Mulder, G. Desgrandchamps, and C. A. Smolders. Preparation of zeolite filled glassy polymer membranes. *J. Appl. Polym. Sci.*, 54(4):409–418, 1994.

[309] T. W. Pechar, S. Kim, B. Vaughan, E. Marand, M. Tsapatsis, H. K. Jeong, and C. J. Cornelius. Fabrication and characterization of polyimide-zeolite L mixed matrix membranes for gas separations. *J. Membr. Sci.*, 277(1-2):195–202, 2006.

[310] M. Moaddeb and W. J. Koros. Gas transport properties of thin polymeric membranes in the presence of silicon dioxide particles. *J. Membr. Sci.*, 125(1):143–163, 1997.

[311] J. Ahn, W.-J. Chung, I. Pinnau, and M. D. Guiver. Poly sulfone/silica nanoparticle mixed-matrix membranes for gas separation. *J. Membr. Sci.*, 314(1-2):123–133, 2008.

[312] T. C. Merkel, Z. J. He, I. Pinnau, B. D. Freeman, P. Meakin, and A. J. Hill. Sorption and transport in poly(2,2-bis(trifluoromethyl)-4,5-difluoro-1,3-dioxole-co-tetrafluoroethylene) containing nanoscale fumed silica. *Macromolecules*, 36(22):8406–8414, 2003.

[313] F. Yan and W. A. Goedel. Polymer membranes with two-dimensionally arranged pores derived from monolayers of silica particles. *Chem. Mater.*, 16(9):1622–1626, 2004.

[314] B. Bolto, T. Tran, M. Hoang, and Z. L. Xie. Crosslinked poly(vinyl alcohol) membranes. *Prog. Polym. Sci.*, 34(9):969–981, 2009.

[315] S. Peter, N. Hese, and R. Stefan. Phenol-selective, highly resistant RO-membranes made from PVA for the purification of toxic industrial wastes. *Desalination*, 19(1â“3):161–167, 1976.

[316] A. S. Hickey and N. A. Peppas. Mesh size and diffusive characteristics of semicrystalline poly(vinyl alcohol) membranes prepared by freezing/thawing techniques. *J. Membr. Sci.*, 107(3):229–237, 1995.

[317] R.F. Ofstead and C.I. Poser. *Semicrystalline poly (vinyl alcohol) hydrogels*, pages 61–72. 1989.

[318] C. E. Reid and E. J. Breton. Water and ion flow across cellulosic membranes. *J. Appl. Polym. Sci.*, 1(2):133–143, 1959.

[319] Y. Xianda, W. Anlai, and C. Suqin. Water-vapor permeability of polyvinyl alcohol films. *Desalination*, 62(0):293–297, 1987.

[320] R. D. Sanderson, E. Immelman, D. Bezuidenhout, E. P. Jacobs, and A. J. Vanreenen. Polyvinyl-alcohol and modified polyvinyl-alcohol reverse-osmosis membranes. *Desalination*, 90(1-3):15–29, 1993.

[321] E. Immelman, D. Bezuidenhout, R. D. Sanderson, E. P. Jacobs, and A. J. Vanreenen. Poly(vinyl alcohol) gel sublayers for reverse-osmosis membranes .3. Insolubilization by cross-linking with potassium peroxodisulfate. *Desalination*, 94(2):115–132, 1993.

[322] R. Konietzny, I. Bettermann, and C. Staudt. Removal of sulfur aromatics from jet fuel using membrane technology. *Annu. B. Aust. Inst. High En. Mater.*, 1(1):57–62, 2010.

[323] D. Sieffert and C. Staudt. Preparation of hybrid materials containing copolyimides covalently linked with carbon nanotubes. *Sep. Pur. Technol.*, 77(1):99–103, 2011.

[324] D. M. Sterescu, D. F. Stamatialis, E. Mendes, M. Wubbenhorst, and M. Wessling. Fullerene-modified poly(2,6-dimethyl-1,4-phenylene oxide) gas separation membranes: Why binding is better than dispersing. *Macromolecules*, 39(26):9234–9242, 2006.

[325] F. Peng, C. Hu, and Z. Jiang. Novel poly(vinyl alcohol)/carbon nanotube hybrid membranes for pervaporation separation of benzene/cyclohexane mixtures. *J. Membr. Sci.*, 297(1-2):236–242, 2007.

[326] F. Peng, F. Pan, H. Sun, L. Lu, and Z. Jiang. Novel nanocomposite pervaporation membranes composed of poly(vinyl alcohol) and chitosan-wrapped carbon nanotube. *J. Membr. Sci.*, 300(1-2):13–19, 2007.

[327] R. Srivastava, S. Banerjee, D. Jehnichen, B. Voit, and F. Böhme. In situ preparation of polyimide composites based on functionalized carbon nanotubes. *Macromol. Mat. Eng.*, 294(2):96–102, 2009.

[328] B. Han, J. Li, C. Chen, C. Xu, and S. R. Wickramasinghe. Effects of degree of formaldehyde acetal treatment and maleic acid crosslinking on solubility and diffusivity of water in PVA membranes. *Chem. Eng. Res. Des.*, 81(A10):1385–1392, 2003.

[329] C. T. Chen, Y. J. Chang, M. C. Chen, and A. V. Tobolsky. Formalized poly(vinyl alcohol) membranes for reverse osmosis. *J. Appl. Polym. Sci.*, 17(3):789–796, 1973.

[330] N. Durmaz-Hilmioglu, A. E. Yildirim, A. S. Sakaoglu, and S. Tulbentci. Acetic acid dehydration by pervaporation. *Chem. Eng. Proc.*, 40(3):263–267, 2001.

[331] S. Jian and S. Xiao Ming. Crosslinked PVA-PS thin-film composite membrane for reverse osmosis. *Desalination*, 62(0):395–403, 1987.

[332] T. A. Peters, C. H. S. Poeth, N. E. Benes, H. C. W. M. Buijs, F. F. Vercauteren, and J. T. F. Keurentjes. Ceramic-supported thin pva pervaporation membranes combining high flux and high selectivity; contradicting the flux-selectivity paradigm. *J. Membr. Sci.*, 276(1-2):42–50, 2006.

[333] M. Ungerank and G. Baumgarten. Polyimide membranes made of polymerization solutions, 2011.

[334] G. A. Delzenne. Synthesis and photocrosslinking of light-sensitive polymers. *Eur. Polym. J.*, S:55, 1969.

[335] A. M. W. Hillock and W. J. Koros. Cross-linkable polyimide membrane for natural gas purification and carbon dioxide plasticization reduction. *Macromolecules*, 40(3):583–587, 2007.

[336] W. S. Kim, K. H. Um, S. C. Shin, Y. J. Lee, and K. H. Hong. Synthesis and properties of photocrosslinkable polymers with maleimide moiety. *Polym.-Korea*, 23(4):502–506, 1999.

[337] W. S. Kim, K. H. Seo, and W. S. Chang. Synthesis and photocrosslinking of maleimide-type polymers. *Macromol. Rapid Commun.*, 17(11):835–841, 1996.

[338] D. M. He, H. Susanto, and M. Ulbricht. Photo-irradiation for preparation, modification and stimulation of polymeric membranes. *Prog. Polym. Sci.*, 34(1):62–98, 2009.

[339] J. S. Kang, J. Won, H. C. Park, U. Y. Kim, Y. S. Kang, and Y. M. Lee. Morphology control of asymmetric membranes by uv irradiation on polyimide dope solution. *J. Membr. Sci.*, 169(2):229–235, 2000.

[340] J. Guthrie, M. B. Jeganathan, M. S. Otterburn, and J. Woods. Light screening effects of photoinitiators in uv curable systems. *Polym. Bull.*, 15(1):51–58, 1986.

[341] C. N. Dudley, B. Schöberl, G. K. Sturgill, H. W. Beckham, and M. E. Rezac. Influence of crosslinking technique on the physical and transport properties of ethynyl-terminated monomer/polyetherimide asymmetric membranes. *J. Membr. Sci.*, 191(1-2):1–11, 2001.

[342] E. Andrzejewska. Photopolymerization kinetics of multifunctional monomers. *Prog. Polym. Sci.*, 26(4):605–665, 2001.

[343] L. M. Tedaldi, A. E. Aliev, and J. R. Baker. [2+2] photocycloadditions of thiomaleimides. *Chem. Comm.*, 48(39):4725–4727, 2012.

[344] B. Tieke. *Makromolekulare Chemie: Eine Einführung.* Wiley-VCH Verlag GmbH & Co. KGaA, 1997.

[345] D. Katarzynski. *Pervaporation komplexer Aromaten am Beispiel von Naphthalin/n-Decan-Mischungen.* Dissertation, 2008.

[346] V. Talrose, A.N. Yermakov, A.A. Usov, A.A. Goncharova, A.N. Leskin, N.A. Messineva, N.V. Trusova, and M.V. Efimkina. *UV/Visible Spectra.* National Institute of Standards and Technology, Gaithersburg MD, 2012. http://webbook.nist.gov.

[347] K. Hunger, L. Buschhaus, N. Schmeling, C. Staudt, A. Pfeifer, and K. Kleinermanns. Characterization of maleimide dimers in photo-cross-linked copolyimide films. *PhysChemChemPhys*, 14(13):4538–4547, 2012.

[348] F. Masson, C. Decker, T. Jaworek, and R. Schwalm. UV-radiation curing of water-based urethane-acrylate coatings. *Prog. Org. Coat.*, 39(2-4):115–126, 2000.

[349] L. Lin, Y. Kong, J. Yang, D. Shi, K. Xie, and Y. Zhang. Scale-up of pervaporation for gasoline desulphurization: Part 1. simulation and design. *J. Membr. Sci.*, 298(1-2):1–13, 2007.

[350] R. D. Noble. Perspectives on mixed matrix membranes. *J. Membr. Sci.*, 378(1-2):393–397, 2011.

[351] J. R. Li, Y. G. Ma, M. C. McCarthy, J. Sculley, J. M. Yu, H. K. Jeong, P. B. Balbuena, and H. C. Zhou. Carbon dioxide capture-related gas adsorption and separation in metal-organic frameworks. *Coordination Chemistry Reviews*, 255(15-16):1791–1823, 2011.

[352] D. H. Liu and C. L. Zhong. Understanding gas separation in metal-organic frameworks using computer modeling. *Journal of Materials Chemistry*, 20(46):10308–10318, 2010.

[353] S. T. Meek, J. A. Greathouse, and M. D. Allendorf. Metal-organic frameworks: A rapidly growing class of versatile nanoporous materials. *Adv. Mater.*, 23(2):249–267, 2011.

[354] T. H. Bae, J. S. Lee, W. L. Qiu, W. J. Koros, C. W. Jones, and S. Nair. A high-performance gas-separation membrane containing submicrometer-sized metal-organic framework crystals. *Angew. Chem. - Int. Edit.*, 49(51):9863–9866, 2010.

[355] Y. F. Zhang, I. H. Musseman, J. P. Ferraris, and K. J. Balkus. Gas permeability properties of matrimid (R) membranes containing the metal-organic framework Cu-BPY-HFS. *J. Membr. Sci.*, 313(1-2):170–181, 2008.

[356] S. Basu, A. Cano-Odena, and I. F. J. Vankelecom. Asymmetric matrimid (R)/ Cu-3(BTC)$_2$ mixed-matrix membranes for gas separations. *J. Membr. Sci.*, 362(1-2):478–487, 2010.

[357] S. Basu, A. Cano-Odena, and I. F. J. Vankelecom. MOF-containing mixed-matrix membranes for CO_2/CH_4 and CO_2/N_2 binary gas mixture separations. *Sep. Purif. Technol.*, 81(1):31–40, 2011.

[358] J. Hu, H. P. Cai, H. Q. Ren, Y. M. Wei, Z. L. Xu, H. L. Liu, and Y. Hu. Mixed-matrix membrane hollow fibers of $Cu_3(BTC)_2$ MOF and polyimide for gas separation and adsorption. *Ind. Eng. Chem. Res.*, 49(24):12605–12612, 2010.

[359] B. Zornoza, B. Seoane, J. M. Zamaro, C. Tellez, and J. Coronas. Combination of mofs and zeolites for mixed-matrix membranes. *Chemphyschem*, 12(15):2781–2785, 2011.

[360] E. V. Perez, K. J. Balkus, J. P. Ferraris, and I. H. Musselman. Mixed-matrix membranes containing MOF-5 for gas separations. *J. Membr. Sci.*, 328(1-2):165–173, 2009.

[361] M. J. C. Ordonez, K. J. Balkus, J. P. Ferraris, and I. H. Musselman. Molecular sieving realized with ZIF-8/matrimid (R) mixed-matrix membranes. *J. Membr. Sci.*, 361(1-2):28–37, 2010.

[362] K. Diaz, L. Garrido, M. Lopez-Gonzalez, L. F. del Castillo, and E. Riande. CO_2 transport in polysulfone membranes containing zeolitic imidazolate frameworks as determined by permeation and PFG NMR techniques. *Macromol.*, 43(1):316–325, 2010.

[363] J. A. Thompson, K. W. Chapman, W. J. Koros, C. W. Jones, and S. Nair. Sonication-induced ostwald ripening of ZIF-8 nanoparticles and formation of ZIF-8/polymer composite membranes. *Micropor. Mesopor. Mater.,*, 158(0):292–299, 2012.

[364] B. Seoane, J. M. Zamaro, C. Tellez, and J. Coronas. Insight into the crystal synthesis, activation and application of ZIF-20. *Rsc Advances*, 1(5):917–922, 2011.

[365] A. Car, C. Stropnik, and K.-V. Peinemann. Hybrid membrane materials with different metal-organic frameworks (mofs) for gas separation. *Desalination*, 200(1-3):424–426, 2006.

[366] H. B. Tanh Jeazet, C. Staudt, and C. Janiak. A method for increasing permeability in O_2/N_2 separation with mixed-matrix membranes made of water-stable MIL-101 and polysulfone. *Chem. Commun.*, 48(15):2140–2142, 2012.

[367] H.B. Tanh Jeazet, C. Staudt, and C. Janiak. unpublished results. -.

[368] S. K. Henninger, F. Jeremias, H. Kummer, and C. Janiak. MOFs for use in adsorption heat pump processes. *Eur. J. Inorg. Chem.*, (16):2625–2634, 2012.

[369] F. Jeremias, A. Khutia, S. K. Henninger, and C. Janiak. MIL-100(Al, Fe) as water adsorbents for heat transformation purposes - A promising application. *J. Mat. Chem.*, 22(20):10148–10151, 2012.

[370] J. Ehrenmann, S. K. Henninger, and C. Janiak. Water adsorption characteristics of MIL-101 for heat-transformation applications of MOFs. *Eur. J. Inorg. Chem.*, (4):471–474, 2011.

[371] J. J. Low, A. I. Benin, P. Jakubczak, J. F. Abrahamian, S. A. Faheem, and R. R. Willis. Virtual high throughput screening confirmed experimentally: Porous coordination polymer hydration. *J. Am. Chem. Soc.*, 131(43):15834–15842, 2009.

[372] S. Aguado, J. Canivet, and D. Farrusseng. Engineering structured MOF at nano and macroscales for catalysis and separation. *J. Mat. Chem.*, 21(21):7582–7588, 2011.

[373] S. Aguado, C.-H. Nicolas, V. Moizan-Basle, C. Nieto, H. Amrouche, N. Bats, N. Audebrand, and D. Farrusseng. Facile synthesis of an ultramicroporous MOF tubular membrane with selectivity towards CO_2. *New J. Chem.*, 35(1):41–44, 2011.

[374] J. Gascon and F. Kapteijn. Metal-organic framework membranes-high potential, bright future? *Angew. Chem. - Int. Edit.*, 49(9):1530–1532, 2010.

[375] H. Bux, F. Liang, Y. Li, J. Cravillon, M. Wiebcke, and J. Caro. Zeolitic imidazolate framework membrane with molecular sieving properties by microwave-assisted solvothermal synthesis. *J. Am. Chem. Soc.*, 131(44):16000–16001, 2009.

[376] Y.-S. Li, F.-Y. Liang, H. Bux, A. Feldhoff, W.-S. Yang, and J. Caro. Molecular sieve membrane: Supported metal-organic framework with high hydrogen selectivity. *Angew. Chem. - Int. Edit.*, 49(3):548–551, 2010.

[377] T. Giorgi, F. Grepioni, I. Manet, P. Mariani, S. Masiero, E. Mezzina, S. Pieraccini, L. Saturni, G. P. Spada, and G. Gottarelli. Gel-like lyomesophases formed in organic solvents by self-assembled guanine ribbons. *Chem.-Eur. J.*, 8(9):2143–2152, 2002.

[378] R. Zain and J. S. Sun. Do natural DNA triple-helical structures occur and function in vivo? *Cell. Mol. Life Sci.*, 60(5):862–870, 2003.

[379] F. A. Buske, J. S. Mattick, and T. L. Bailey. Potential in vivo roles of nucleic acid triple-helices. *Rna Biology*, 8(3):427–439, 2011.

[380] G. Gottarelli, S. Masiero, E. Mezzina, S. Pieraccini, J. P. Rabe, P. SamorÃ, and G. P. Spada. The self-assembly of lipophilic guanosine derivatives in solution and on solid surfaces. *Chem. Eur. J.*, 6(17):3242–3248, 2000.

[381] L. Biemann, T. Häber, D. Maydt, K. Schaper, and K. Kleinermanns. Fourier transform infrared spectroscopy of 2 '-deoxycytidine aggregates in $CDCl_3$ solutions. *J. Chem. Phys.*, 134(11), 2011.

[382] V. Karunakaran, K. Kleinermanns, R. Improta, and S. A. Kovalenko. Photoinduced dynamics of guanosine monophosphate in water from broad-band transient absorption spectroscopy and quantum-chemical calculations. *J. Am. Chem. Soc.*, 131(16):5839–5850, 2009.

[383] L. Biemann, S. A. Kovalenko, K. Kleinermanns, R. Mahrwald, M. Markert, and R. Improta. Excited state proton transfer is not involved in the ultrafast deactivation of guanine-cytosine pair in solution. *J. Am. Chem. Soc.*, 133(49):19664–19667, 2011.

[384] R. Improta and V. Barone. Interplay between "neutral" and "charge-transfer" excimers rules the excited state decay in adenine-rich polynucleotides. *Angew.Chem., Int. Ed.*, 50(50):12016–12019, 2011.

[385] F. Santoro, V. Barone, and R. Improta. Excited states decay of the A-T DNA: A PCM/TD-DFT study in aqueous solution of the (9-methyl-adenine)(2)center dot(1-methyl-thymine)(2) stacked tetramer. *J. Am. Chem. Soc.*, 131(42):15232–15245, 2009.

[386] M. Dargiewicz, M. Biczysko, R. Improta, and V. Barone. Solvent effects on electron-driven proton-transfer processes: adenine-thymine base pairs. *Phys. Chem. Chem. Phys.*, 14(25):8981–8989, 2012.

[387] A. W. Lange and J. M. Herbert. Both intra- and interstrand charge-transfer excited states in aqueous B-DNA are present at energies comparable to, or just above, the $^1\pi\pi^*$ excitonic bright states. *J. Am. Chem. Soc.*, 131(11):3913–3922, 2009.

[388] R. Improta, V. Barone, G. Scalmani, and M. J. Frisch. A state-specific polarizable continuum model time dependent density functional theory method for excited state calculations in solution. *J. Chem. Phys.*, 125(5), 2006.

[389] R. Improta, G. Scalmani, M. J. Frisch, and V. Barone. Toward effective and reliable fluorescence energies in solution by a new state specific polarizable continuum model time dependent density functional theory approach. *J. Chem. Phys.*, 127(7), 2007.

[390] J. Tomasi, B. Mennucci, and R. Cammi. Quantum mechanical continuum solvation models. *Chem. Rev.*, 105(8):2999–3093, 2005.

[391] Y. Tawada, T. Tsuneda, S. Yanagisawa, T. Yanai, and K. Hirao. A long-range-corrected time-dependent density functional theory. *J. Chem. Phys.*, 120(18):8425–8433, 2004.

[392] J. D. Gu, Y. M. Xie, and H. F. Schaefer III. Electron attachment to DNA single strands: gas phase and aqueous solution. *Nucleic Acids Res.*, 35(15):5165–5172, 2007.

[393] K. Kobayashi and S. Tagawa. Direct observation of guanine radical cation deprotonation in duplex DNA using pulse radiolysis. *J. Am. Chem. Soc.*, 125(34):10213–10218, 2003.

[394] E. Nir, K. Kleinermanns, and M. S. de Vries. Pairing of isolated nucleic-acid bases in the absence of the DNA backbone. *Nature*, 408(6815):949–951, 2000.

[395] B. Giese, J. Amaudrut, A.-K. Kohler, M. Spormann, and S. Wessely. Direct observation of hole transfer through DNA by hopping between adenine bases and by tunnelling. *Nature*, 412(6844):318–320, 2001.

[396] F. D. Lewis. DNA molecular photonics. *Photochem. Photobiol.*, 81(1):65–72, 2005.

[397] C. Sheu and C. S. Foote. Reactivity toward singlet oxygen of a 7,8-dihydro-8-oxoguanosine ("8-hydroxyguanosine") formed by photooxidation of a guanosine derivative. *J. Am. Chem. Soc.*, 117(24):6439–6442, 1995.

[398] K. K. Ogilvie. The tert-butyldimethylsilyl group as a protecting group in deoxynucleosides. *Can. J. Chem.*, 51(22):3799–3807, 1973.

[399] M. J. Frisch, J. A. Pople, and J. S. Binkley. Self-consistent molecular-orbital methods. 25. supplementary functions for gaussian basis sets. *J. Chem. Phys.*, 80(7):3265–3269, 1984.

[400] M. Cossi and V. Barone. Time-dependent density functional theory for molecules in liquid solutions. *J. Chem. Phys.*, 115(10):4708–4717, 2001.

[401] G. Scalmani, M. J. Frisch, B. Mennucci, J. Tomasi, R. Cammi, and V. Barone. Geometries and properties of excited states in the gas phase and in solution: Theory and application of a time-dependent density functional theory polarizable continuum model. *J. Chem. Phys.*, 124(9):094107, 2006.

[402] H. A. Frank, R. Farhoosh, M. L. Aldema, B. DeCoster, R. L. Christensen, R. Gebhard, and J. Lugtenburg. Carotenoid-to-Bacteriochlorophyll singlet energy transfer in carotenoid-incorporated B850 light-harvesting complexes of Rhodobacter sphaeroides R-26.1. *Photochem. Photobiol.*, 57(1):49–55, 1993.

[403] M. Ricci, S. E. Bradforth, R. Jimenez, and G. R. Fleming. Internal conversion and energy transfer dynamics of spheroidene in solution and in the LH-1 and LH-2 light-harvesting complexes. *Chem. Phys. Lett.*, 259(3-4):381–390, 1996.

[404] S. Yamashita, A. G. Szabo, and P. Cavatorta. Temperature-dependence and decay kinetics of the high-energy band in DPH fluorescence. *Bull. Chem. Soc. Jpn.*, 62(9):2849–2853, 1989.

[405] S. J. Strickler and R. A. Berg. Relationship between absorption intensity and fluorescence lifetime of molecules. *J. Chem. Phys.*, 37(4):814–822, 1962.

[406] E. D. Cehelnik, R. B. Cundall, J. R. Lockwood, and T. F. Palmer. 1,6-Diphenyl-1,3,5-hexatriene as a fluorescence standard. *Chem. Phys. Lett.*, 27(4):586–588, 1974.

[407] B. S. Hudson and B. E. Kohler. Linear polyene electronic-structure and spectroscopy. *Annu. Rev. Phys. Chem.*, 25:437–460, 1974.

[408] B. S. Hudson and B. E. Kohler. Polyene spectroscopy: The lowest energy excited singlet state of diphenyloctateratene and other linear polyenes. *J. Chem. Phys.*, 59(9):4984–5002, 1973.

[409] P. C. Alford and T. F. Palmer. Photophysics of derivatives of all-trans-1,6-diphenyl-1,3,5-hexatriene (DPH); Part 1.- Model involving fluorescence from S_2 and S_1 excited states. *J. Chem. Soc., Faraday Trans. 2*, 79:433–447, 1983.

[410] B. E. Kohler and T. A. Spiglanin. Saturation kinteics of the S_0 to S_2 optical-transition in isolated diphenylhexatriene. *J. Chem. Phys.*, 82(7):2939–2941, 1985.

[411] M. Kleinschmidt, C. M. Marian, M. Waletzke, and S. Grimme. Parallel multireference configuration interaction calculations on mini-β-carotenes and β-carotene. *J. Chem. Phys.*, 130(4):044708, 2009.

[412] B. Küpper, M. Kleinschmidt, K. Schaper, and C. M. Marian. On the photophysics of 1,6-diphenyl-1,3,5-hexatriene isomers and rotamers. *Chemphyschem*, 12(10):1872–1879, 2011.

[413] T. Itoh. Franck-Condon analysis of the absorption and fluorescence spectra of all trans α,ω-diphenylpolyenes with one to seven polyene double bonds. *J. Chem. Phys.*, 123(6):6, 2005.

[414] J. Saltiel, D. F. Sears, Y. P. Sun, and J. O. Choi. Evidence for ground-state s-cis conformers in the fluorescence spectra of all-trans-1,6-diphenyl-1,3,5-hexatriene. *J. Am. Chem. Soc.*, 114(10):3607–3612, 1992.

[415] J. Saltiel, S. Wang, D.-H. Ko, and D. A. Gormin. Cis-trans photoisomerization of the 1,6-diphenyl-1,3,5-hexatrienes in the triplet state. The quantum chain mechanism and the structure of the triplet state. *J. Phys. Chem. A*, 102(28):5383–5392, 1998.

[416] J. Saltiel, S. Wang, L. P. Watkins, and D.-H. Ko. Direct photoisomerization of the 1,6-diphenyl-1,3,5-hexatrienes. Medium effect on triplet and singlet contributions. *J. Phys. Chem. A*, 104(48):11443–11450, 2000.

[417] J. Saltiel, G. Krishnamoorthy, Z. Huang, D.-H. Ko, and S. Wang. Photoisomerization of all-trans-1,6-diphenyl-1,3,5-hexatriene. Temperature and deuterium isotope effects. *J. Phys. Chem. A*, 107(18):3178–3186, 2003.

[418] J. Saltiel, D. Papadimitriou, T. S. R. Krishna, Z.-N. Huang, G. Krishnamoorthy, S. Laohhasurayotin, and R. J. Clark. Photoisomerization of all-cis-1,6-diphenyl-1,3,5-hexatriene in the solid state and in solution: A simultaneous three-bond twist process. *Angew. Chem. - Int. Edit.*, 48(43):8082–8085, 2009.

[419] J. Catalán and J. L. G. de Paz. On the photophysics of all-trans polyenes: Hexatriene versus octatetraene. *J. Chem. Phys.*, 124(3):034306–11, 2006.

[420] A. M. Turek, G. Krishnamoorthy, D. F. Sears, I. Garcia, O. Dmitrenko, and J. Saltiel. Resolution of three fluorescence components in the spectra of all-trans-1,6-diphenyl-1,3,5-hexatriene under isopolarizability conditions. *J. Phys. Chem. A*, 109(2):293–303, 2005.

[421] J. C. del Valle, N. Tarkalanov, and J. Saltiel. Distortion of the fluorescence spectrum of all-trans-1,6-diphenyl-1,3,5-hexatriene with increasing laser pulse excitation energies. *J. Phys. Chem. B*, 103(43):9350–9355, 1999.

[422] C. M. Marian and N. Gilka. Performance of the density functional theory/multireference configuration interaction method on electronic excitation of extended π-systems. *J. Chem. Theory Comput.*, 4(9):1501–1515, 2008.

[423] A. Hager. Ausbildung von Maxima im Absorptionsspektrum von Carotinoiden im Bereich um 370 nm; Folgen für die Interpretation bestimmter Wirkungsspektren. *Planta*, 91(1):38–53, 1970.

[424] A. V. Ruban, P. Horton, and A. J. Young. Aggregation of higher plant xanthophylls: Differences in absorption spectra and in the dependency on solvent polarity. *J. Photochem. Photobiol., B*, 21(2-3):229–234, 1993.

[425] S. K. Chattopadhyay, P. K. Das, and G. L. Hug. Photoprocesses in diphenylpolyenes - oxygen and heavy-atom enhancement of triplet yields. *J. Am. Chem. Soc.*, 104(17):4507–4514, 1982.

[426] Y. Hirata, K. Mashima, H. Fukumoto, K. Tani, and T. Okada. Energy gap dependence of the S_2 -> S_1 internal conversion of α,ω-diphenylpolyenes (N=3-8) in solution phase. *Chem. Phys. Lett.*, 308(3-4):176–180, 1999.

[427] Z. Wang and W. G. McGimpsey. Time-resolved evidence for isomerization of diphenylpolyene cation radicals in solution. *J. Phys. Chem.*, 97(13):3324–3327, 1993.

[428] J. Saltiel and B. W. Atwater. *Spin-statistical factors in diffusion-controlled reactions*, volume 14 of *Advances in Photochemistry.* John Wiley & Sons, Inc., 1988.

[429] J. Saltiel, J. M. Crowder, and S. J. Wang. Mapping the potential energy surfaces of the 1,6-diphenyl-1,3,5-hexatriene ground and triplet states. *J. Am. Chem. Soc.*, 121(5):895–902, 1999.

[430] R. Bensasson, E. J. Land, J. Lafferty, R. S. Sinclair, and T. G. Truscott. The triplet state of 1,6-diphenyl-1,3,5-hexatriene and 1,8-diphenyl-1,3,5,7-octatetraene. *Chem. Phys. Lett.*, 41(2):333–335, 1976.

[431] M. Klessinger and E. Gunkel. The electronic structure of polyenes and unsaturated carbonyl compounds. *Tetrahedron*, 34(24):3591–3598, 1978.

[432] K. C. Wu and A. M. Trozzolo. Production of singlet molecular-oxygen from the oxygen quenching of the lowest excited singlet-state of aromatic molecules in n-hexane solution. *J. Phys. Chem.*, 83(24):3180–3183, 1979.

[433] J. T. Brownrigg and J. E. Kenny. Fluorescence intensities and lifetimes of aromatic hydrocarbons in cyclohexane solution: Evidence of contact charge-transfer interactions with oxygen. *J. Phys. Chem. A*, 113(6):1049–1059, 2009.

[434] R. Schmidt. Photosensitized generation of singlet oxygen. *Photochem. Photobiol.*, 82(5):1161–1177, 2006.

[435] C. Schweitzer and R. Schmidt. Physical mechanisms of generation and deactivation of singlet oxygen. *Chem. Rev.*, 103(5):1685–1757, 2003.

[436] E. A. Gooding, K. R. Serak, and P. R. Ogilby. Ground-state benzene-oxygen complex. *J. Phys. Chem.*, 95(20):7868–7871, 1991.

[437] K. Kikuchi, C. Sato, M. Watabe, H. Ikeda, Y. Takahashi, and T. Miyashi. New aspects on fluorescence quenching by molecular oxygen. *J. Am. Chem. Soc.*, 115(12):5180–5184, 1993.

[438] L. Rodrìguez, J. C. Lima, F. Pina, R. Cacciapaglia, S. Di Stefano, and A. Ruggi. Photophysical study of naphthalenophanes: Evidence of adduct formation with molecular oxygen. *J. Phys. Chem. A*, 115(2):123–127, 2011.

[439] T. Kamisuki and C. Hirose. Photoionization mechanism of α,ω-diphenylpolyenes in polar solvents investigated by using coherent Raman spectroscopy. *J. Photochem. Photobiol. A*, 99(1):13–21, 1996.

[440] S. Nath, D. K. Palit, and A. V. Sapre. Photoinduced charge transfer interaction between fullerene[60] and diphenylpolyenes in solution: Evidence for photocycloaddition reaction. *Chem. Phys. Lett.*, 330(3-4):255–261, 2000.

[441] J. F. Ye, H. Chen, R. Note, H. Mizuseki, and Y. Kawazoe. Excess polarizabilities upon excitation from the ground state to the first dipole-allowed excited state of diphenylpolyenes. *Int. J. Quantum Chem.*, 107(10):2006–2014, 2007.

[442] G. Hunger. *Mechanische Eigenschaften metallischer Gläser*. Dissertation, 1983.

A. Simulation of Kinetic Traces

The simulation of kinetic traces and the calculation of the deviation of those simulations to the experimental data was performed with Mathcad 2001 SE with the following code:

Definitions

Vectorization:

```
vec(z):=  $v_0 \leftarrow 0$
          for $e \in z$
              $v \leftarrow$ stack(v,vec(e)) if IsArray(e)
              $v_{\mathrm{rows(v)}} \leftarrow$ e otherwise
          submatrix(v,1,last(v),0,0)
```

Number of iterations 1:
N:=10
Increment of iterations 1:
i1:=vec(1,1.01..N)
Number of iterations 2:
M:=5
Increment of iterations 2:
i2:=vec(1,2..M)
...

Time interval in ps:
T:=99999
Time increment in ps:
t:=0,1..T

Rate constants in ps^{-1}:
vkfl$_2$:=$8.0\cdot10^{-4}\cdot$ vec(i1) *in case of variation of this value*
vkfl$_1$:=$1.1\cdot10^{-7}\cdot$ vec(i2) *in case of variation of this value*
vkQ:=$1.7\cdot10^{-3}$
vkT:=$5.0\cdot10^{-8}$
vkisc:=$1.4\cdot10^{-5}$
vic20:=$1.0\cdot10^{-2}$
vic10:=$2.8\cdot10^{-7}$
vic21:=$7.3\cdot10^{-1}$
vic12:=$4.1\cdot10^{-4}$

Fit Routine

```
(res kvals):=
    $\mathrm{S0}_T \leftarrow 0$
    $\mathrm{S1}_T \leftarrow 0$
    $\mathrm{S2}_T \leftarrow 0$
    $\mathrm{T1}_T \leftarrow 0$
    $\mathrm{O2}_T \leftarrow 0$
    $\mathrm{res} \leftarrow 0$
    $\mathrm{kvals} \leftarrow 0$
    for $\mathrm{kfl}_2 \in \mathrm{vkfl}_2$
      for $\mathrm{kfl}_1 \in \mathrm{vkfl}_1$
        for $\mathrm{kQ} \in \mathrm{vkQ}$
          for $\mathrm{kT} \in \mathrm{vkT}$
            for $\mathrm{kisc} \in \mathrm{vkisc}$
              for $\mathrm{kic20} \in \mathrm{vkic20}$
                for $\mathrm{kic10} \in \mathrm{vkic10}$
                  for $\mathrm{kic21} \in \mathrm{vkic21}$
                    for $\mathrm{kic12} \in \mathrm{vkic12}$
                        $\mathrm{S0}_0 \leftarrow 6$
                        $\mathrm{S1}_0 \leftarrow 0$
                        $\mathrm{S2}_0 \leftarrow 2$
                        $\mathrm{T1}_0 \leftarrow 0$
                        $\mathrm{O2}_0 \leftarrow 0.002$
                        for $\mathrm{t} \in 0,1..\mathrm{T}$
                            $\mathrm{S0}_{t+1} \leftarrow$ insert argument 1
                            $\mathrm{S1}_{t+1} \leftarrow$ insert argument 2
                            $\mathrm{S2}_{t+1} \leftarrow -\mathrm{kfl}_2\cdot\mathrm{S2}_t-\mathrm{kic21}\cdot\mathrm{S2}_t+\mathrm{kic12}\cdot\mathrm{S1}_t-\mathrm{kic20}\cdot\mathrm{S2}_t+\mathrm{S2}_t$
                            $\mathrm{T1}_{t+1} \leftarrow \mathrm{kisc}\cdot\mathrm{S1}_t-\mathrm{kT}\cdot\mathrm{T1}_t+\mathrm{T1}_t$
                            $\mathrm{O2}_{t+1} \leftarrow \mathrm{O2}_t$
                        $\mathrm{res}_{\mathrm{rows(res)}} \leftarrow \begin{pmatrix} S0 \\ S1 \\ S2 \\ T1 \\ O2 \end{pmatrix}$
                        $\mathrm{kvals}_{\mathrm{rows(kvals)}} \leftarrow \mathrm{stack}(\mathrm{kfl}_2,\mathrm{kfl}_1,\mathrm{kQ},\mathrm{kT},\mathrm{kisc},\mathrm{kic20},\mathrm{kic10},\mathrm{kic21},\mathrm{kic12})$
    (res kvals)
```

Arguments for fit routine:
argument 1:
if($\mathrm{S1}_t \le \mathrm{x}\cdot\mathrm{O2}_t$, $\mathrm{kfl}_2\cdot\mathrm{S2}_t+\mathrm{kfl}_1\cdot\mathrm{S1}_t+\mathrm{kQ}\cdot\mathrm{S1}_t\cdot\mathrm{O2}_t+\mathrm{kT}\cdot\mathrm{T1}_t+\mathrm{kic20}\cdot\mathrm{S2}_t+\mathrm{kic10}\cdot\mathrm{S1}_t+\mathrm{S0}_t$,
$\mathrm{kfl}_2\cdot\mathrm{S2}_t+\mathrm{kfl}_1\cdot\mathrm{S1}_t+\mathrm{kQ}\cdot\mathrm{O2}_t+\mathrm{kT}\cdot\mathrm{T1}_t+\mathrm{kic20}\cdot\mathrm{S2}_t+\mathrm{kic10}\cdot\mathrm{S1}_t+\mathrm{S0}_t$)
argument 2:
if($\mathrm{S1}_t \le \mathrm{x}\cdot\mathrm{O2}_t$, $\mathrm{kic21}\cdot\mathrm{S2}_t-\mathrm{kfl}_1\cdot\mathrm{S1}_t-\mathrm{kQ}\cdot\mathrm{S1}_t\cdot\mathrm{O2}_t-\mathrm{kisc}\cdot\mathrm{S1}_t-\mathrm{kic12}\cdot\mathrm{S1}_t-\mathrm{kic10}\cdot\mathrm{S1}_t+\mathrm{S1}_t$,
$\mathrm{kic21}\cdot\mathrm{S2}_t-\mathrm{kfl}_1\cdot\mathrm{S1}_t-\mathrm{kQ}\cdot\mathrm{O2}_t-\mathrm{kisc}\cdot\mathrm{S1}_t-\mathrm{kic12}\cdot\mathrm{S1}_t-\mathrm{kic10}\cdot\mathrm{S1}_t+\mathrm{S1}_t$)
The parameter x has to be adjusted empirically, so that the change from zero order (linear) decay to first order (exponential) decay in simulated and experimental kinetic traces happens after the same time interval.

Determination of Deviation:

Import experimental data:
messdaten:= *path to ascii-file*

Calculate deviations:

```
writeres(kvals,res):=  for i ∈ 0..last(kvals)
                           kv ← $kvals_i$
                           S0 ← $(res_i)_0$
                           S1 ← $(res_i)_1$
                           S2 ← $(res_i)_2$
                           S12 ← S1+S2
                           RQ ← mean[$(messdaten-S12)^2$]
                           fbasename ←  s ← (num2string($kv_0$))
                                        for j ∈ 1..last(kv)
                                          s ← concat(s,"_",num2str($kv_j$))
                           fname ← concat("S0_",fbasename,".dat")
                           WRITEPRN(fname,S0)
                           fname ← concat("S1_",fbasename,".dat")
                           WRITEPRN(fname,S1)
                           fname ← concat("S2_",fbasename,".dat")
                           WRITEPRN(fname,S2)
                           fname ← concat("S12_",fbasename,".dat")
                           WRITEPRN(fname,S12)
                           fname ← concat("RQ_",fbasename,".dat")
                           WRITEPRN(fname,RQ)
```

Export simulated kinetic curves:
writeres(kvals,res)=

B. Symbols and Abbreviations

6FDA	4,4'-hexafluoroisopropylidene diphthalic anhydride
6FpDA	4,4'-hexafluoroisopropylidene dianiline
α	selectivity
A	absorption, difference absorbance adenine
a. u.	arbitrary units
B3LYP	a DFT functional[171]
BAPE	benzoic acid propylester
BASF	Chemical Company, formerly known as Badische Anilin- und Soda-Fabrik
BBO	BaB_2O_4
BDC	benzene-1,4-dicarboxylate, terephthalate
BPY	4,4'-bipyridine
BTC	benzene-1,3,5-tricarboxylate
c	light velocity, 299 792 458 m/s
C	cytosine carbon Coulomb
°C	degree Celsius, K - 273.15
CA	cycloadduct
CAM	Coulomb-attenuating method
cm	centimeter, 10^{-2} m
CASPT2	complete-active-space second-order perturbation theory
$CDCl_3$	chloroform
CPD	cyclobutane pyrimidine dimer
CNT	carbon nanotubes
CT	charge transfer
CCT	contact charge transfer
CH	cyclohexane
CH_4	methane
CO_2	carbon dioxide
DABA	3,5-diamino benzoic acid
DAM	diaminomesitylene
DFT	density functional theory
DMAc	dimethyl acetamide
DNA	deoxyribonucleic acid
DPB	1,4-diphenyl-1,3-butadiene
DPE	diphenyl ether
DPH	1,6-diphenyl-1,3,5-hexatriene
DPO	1,8-diphenyl-1,3,5,7-octatetraene

ϵ	extinction coefficient
e	elementary charge, 1.602176565(35) $\cdot 10^{-19}$ C
E	energy
$\mathrm{E_A}$	electron affinity
ESPT	excited state proton transfer
EU	European Union
eV	electron volt, 1eV=1.602 176 565(35) $\cdot 10^{-19}$ J
ϕ	quantum yield
F	fluorine
fl	fluorescence
fs	picosecond, 10^{-15} s
FTIR	Fourier transform infrared
G	guanine, guanosine, 2’,3’,5’-O-tris (tert-butyldimethylsilyl) guanosine
GCMS	gas chromatography - mass spectroscopy
GGA	gradient approximated exchange and correlation functional
GMP	guanosine monophosphate
GTO	Gaussian type orbitals
h	hour
h	Planck constant, h=6.626 069 57(29) $\cdot 10^{-34}$ Js
$\hbar$	$h/2\pi$
H	hydrogen
ΔH_0	standard enthalpy change
$\mathrm{H_2}$	molecular hydrogen
HF	Hartree Fock
HFS	hexafluorosilicate
Hg	mercury
HH	headt-to-head
HOMO	highest occupied molecular orbital
HPLC	high-performance liquid chromatography
HT	head-to-tail
HWHM	half width at half maximum
I	emission or absorption intensity
IC	internal conversion
IP	ionisation potential
IR	infrared
IR-ATR	infrared attenuated total reflection
ISC	intersystem crossing
J	Joule, 1 kg·m^2/s^2
k	force constant rate constant
kJ	kilojoule, 10^3 J
λ	wavelength
LHC	light-harvesting complex
LR	Linear Response
LSDA	local spin density approximated functional
LUMO	lowest unoccupied molecular orbital

μ	dipole moment
µm	micrometer, 10^{-6} m
µM	10^{-6} mol/L
µs	microsecond, 10^{-6} s
m	meter
M	mol/L
	molecule
MCT	
mbar	millibar, 10^{-3} bar
MCT	$\mathrm{Hg_xCd_yTe_z}$
MHz	megahertz, 10^6/s
m_i	mass of the particle i
MI	maleimide
MIL	asymmetric MMM of Matrimid ® 9725 and ZIF-8
MIOH	3-hydroxypropyldimethylmaleimide
mJ	millijoule, 10^{-3} J
mm	millimeter, 10^{-3} m
MMM	mixed-matrix membrane
MOF	metal-organic framework
MRCI	multi reference configuration interaction
MPD	2,3,5,6-tetramethylbenzene-1,4-diamine
ν	frequency
N	nitrogen
N_2	molecular nitrogen
N_A	Avogadro constant, $6.02214129(27) \cdot 10^{23}$ mol^{-1}
NaCl	natrium chloride
Nd:YAG	an yttrium aluminium garnet doped with Nd^{3+}
nm	nanometer, 10^{-9} m
NMR	nuclear magnetic resonance
ns	nanosecond, 10^{-9} s
O	oxygen
O_2	molecular oxygen
O.D.	optical density, absorbance
ODA	4,4'-diaminodiphenyl ether
ψ	wave function
P	permability
PCM	polarizable continuum model
PE	potential energy
PES	potential energy surface
PEM	photoelectron multiplier
PEMAA	poly[ethene-*stat*-(methacrylic acid)]
ph	phosphorescence
PHI	N-methyl phthalimide
pK_a	acid dissociation constant
PI	polyimide
PMDA	pyromellitic dianhydride
PMMA	polymethyl methacrylate

PPEES	poly-(1,4-phenylene ether-ether-sulfone)
ps	picosecond, 10^{-12} s
PSF	MMA of Cu-BTC combined with S1C
PVA	poly(vinyl alcohol)
Q	quenching
Q_i	normal coordinate i
r	distance
R	gas constant, 8.3144621(75) J/mol·K
ROS	reactive oxygen species
s	second
S1C	silicalite-1
S_0	electronic ground singlet state
S_1	first electronically excited singlet state
S_2	second electronically excited singlet state
SS	state specific
STO	Slater type orbitals
τ	lifetime
T	thymine
T	temperature
T_1	first electronically excited triplet state
TFMP	2,2-bis-trifluoromethyl propane
TD	time dependent
THF	tetrahydrofuran
tRNA	transfer ribonucleic acid
TTA	triplet-triplet annihilation
TZVP	triple-zeta split valence basis set
UV	ultraviolet
V	volume
Vis	visible light
W	Watt, 1 kg·$\mathrm{m}^2/\mathrm{s}^3$
WC	Watson-Crick
ZIF	zeolitic imidazolate frameworks

C. Danke

An erster Stelle danke ich meinem Doktorvater Prof. Dr. Karl Kleinermanns für die Aufnahme in seine Arbeitsgruppe und für all die konstruktiven Anmerkungen und Diskussionen. Ganz besonders danke ich ihm für das in mich gesetzte Vertrauen und dass er mir bei der Erarbeitung der hier präsentierten Ergebnisse so oft freie Hand gelassen hat. Herrn Prof. Michael Schmitt danke ich für sein Interesse an meiner Arbeit, für die Übernahme des Korreferats und für die vielen Diskussionen - ob mündlich oder schriftlich. Für die freundliche Übernahme des dritten Gutachtens danke ich Herrn Prof. Köhler.

Großer Dank gebührt Nadine Schmeling, die alle Polymere für mich synthetisiert hat und mit der eine so fruchtbare Kooperation möglich war. Auch Frau Prof. Claudia Staudt, Herrn Prof. Janiak, Dr. Roberto Improta und Dr. Sergey Kovalenko danke ich für die gute Zusammenarbeit.

Außerdem danke ich meinen aktuellen und ehemaligen Kollegen: Lars Biemann, Thomas Häber, Dieter Marx, Brigitte Müller, Olivia Oeltermann, Dominika Radziejewski, Thorsten Wilke - sowie insbesondere Gernot Engler, der mir beigebracht hat wie ich mit dem ns-Transientenspektrometer und mit Turbomole umgehen muss; Michalina Braun, die mich bei beruflichen und privaten Problemen immer wieder aufgebaut hat; Benjamin Stuhlmann, der immer so hilfsbereit war; Daniel Ogermann und Markus Böning, die - auch wenn wir fachlich nicht viel miteinander zu tun hatten - die Arbeit für mich dennoch angenehm gemacht haben; Christian Brand, der mir meine unzähligen Fragen immer so geduldig beantwortet hat; Klaus Kelbert, der jegliches technische Problem wie durch Handauflegen beheben konnte; Andrea Lotzwick, die sich all meiner Anliegen stets mit ihrer freundlichen Art angenommen hat; den Mitarbeitern der Mechanischen Werkstätten, die jede meiner Zeichnungen in reale Objekte verwandelt haben; meinen Bürokollegen (in chronologischer Reihenfolge): Kai Seefeld, Gernot Engler, Matthias Busker, Markus Böning, Anna Pfeifer, Josy Rolf und Laura Buschhaus, die von meiner Diplomandin erst zur Kollegin und dann zur Freundin geworden ist. Euch allen danke ich für die freundschaftliche Atmosphäre und für die vielen großen und kleinen Hilfen!
Benjamin Stuhlmann, Laura Buschhaus und Christian Brand danke ich zudem für das Korrekturlesen und die konstruktive Kritik. Der Fürstin, dem Baron, Herrn Vogel, Herrn Berger und Herrmann danke ich dafür dass sie es immer wieder geschafft haben, allen Horror mit ihrem grenzenlosen Humor im Keim zu ersticken.
Ausserdem möchte ich mich bei meinen Freunden aus Aachener Zeiten bedanken, dafür dass wir uns nicht aus den Augen verloren haben, obwohl wir in alle Lande verstreut sind!

Ganz besonders danke ich meinen Eltern und meinem Bruder, dafür dass sie immer hinter mir standen, mich unterstützt und an mich geglaubt haben!

Abschließen möchte ich mit den Worten von Dr. Hunger (sen.): "Das war's!"[442]